GROWTH AND CHARACTERIZATION OF CdTe-BASED MULTIJUNCTION HOLE-BLOCKING SOLAR CELL

By

RANVEER SINGH

PHYS07201304010

INSTITUTE OF PHYSICS, BHUBANESWAR

A thesis submitted to the

Board of studies in physical sciences

In partial fulfilment of requirements

For the degree of

DOCTOR OF PHILOSOPHY

of

HOMI BHABHA NATIONAL INSTITUTE

January, 2019

Homi Bhabha National Institute

Recommendations of the Viva Voce Committee

As members of the Viva Voce Committee, we certify that we have read the dissertation prepared by Mr Ranveer Singh entitled "Growth and characterization of CdTe-based multijunctoion hole-blocking solar cell", and recommend that it may be accepted as fulfilling the dissertation requirement for the Degree of Doctor of Philosophy.

AmJayannavar

Chairman - Prof. A. M. Jayannavar Date: 08/04/19

Guide /Convener - Prof. Tapobrata Som Date: 08/04/19

Co-guide (if any) — Date: —

Examiner - Prof. O. P. Sinha Date: 08/04/2019

Satyam 08/04/2019

Member 1 - Prof. P. V. Satyam Date:

08/04/2019

Member 2 - Prof. S. K. Patra Date:

Final approval and acceptance of this thesis is contingent upon the candidate's submission of the final copies of the dissertation to HBNI.

I/We hereby certify that I/we have read this thesis prepared under my/our direction and recommend that it may be accepted as fulfilling the thesis requirement.

Date: April 08, 2019
Place: IOP, Bhubaneswar

Co-guide (if applicable)

08/04/19
Guide
(T. SOM)

STATEMENT BY AUTHOR

This dissertation has been submitted in partial fulfillment of requirement for an advanced degree at Homi Bhabha National Institute (HBNI) and is deposited in the Library to be made available to borrowers under rules of HBNI.

Brief quotation from this dissertation are allowable without special permission, provided that accurate acknowledgement of source is made. Requests for permission for extended quotation from the reproduction of this manuscript in whole or in part may be granted by the Competent Authority of HBNI when in his or her judgement the proposed use of the material is in the interests of scholarship. In all other instances, however, permission must be obtained from the author.

Ranvir Singh

RANVEER SINGH

DECLARATION

I, hereby declare that the investigation presented in the thesis has been carried out by me. The work is original and has not been submitted earlier as a whole or in part for a degree / diploma at this or any other Institution / University.

Ranvir Singh

Ranveer Singh

List of Publications arising from Thesis

Journal

1. “Experimental and simulation studies on temporal evolution of chemically etched Si surface: Tunable light trapping and cold cathode electron emission properties”, **R Singh**, S A Mollick, M Saini, P Guha, and T Som, *J. Appl. Phys.* (in press).

2. “White light-driven photoresponse of TiO_2 thin film: Influence of substrate texturing, R Singh, M Kumar, M Saini, B Satpati, and T Som”, *Solar Energy*, **2018**, 174, 231-239.

3. “Growth of TiO_2 thin films on chemically textured Si for solar cell applications as a hole-blocking and antireflection layer”, R Singh, M Kumar, A. Singh, M Saini, B Satpati, and T Som, *Appl. Surf. Sci.*, **2017**, 418, 225-231.

4. “Influence of grain size on local work function and optoelectronic properties of *n*-ZTO/*p*-Si heterostructures”, R Singh, A Dutta, P Nandi, S K Srivastava, and T Som, *Appl. Surf. Sci.* (under review).

To be communicated

1. “Local probe microscopic studies on zinc tin oxide: Work function tuning and band mapping across a metal-semiconductor junction”, R Singh and T Som.

2. “Hole-blocking molybdenum-oxide/silicon heterojunction: Carrier selective contact”, R Singh, R Sivakumar, S K Srivastava, and T Som.

3. “Role of Cu-doping and annealing temperature in CdTe: An experimental and first principle study”, R Singh, M Vallet, V Kumar, S K Srivastava, A Claverie, and T Som.

4. “Growth angle-dependent tunable structural, optical, work function, and electrical properties of MoO_3 thin film”, R Singh, R Sivakumar, and T Som.

5. “Improved photovoltaic performance of CdTe solar cell with hole-blocking layer: Nanoscale imaging of barrier height at the interface”, R Singh, A Dutta, and T Som.

Conferences

[1] **Ranveer Singh**, Mohit Kumar, Mahesh Saini, B. Satpati, and T. Som ─ “Growth of TiO_2 thin films on chemically textured Si for solar cell applications as a hole-blocking and antireflection layer” POSTER: Asian Consortium on Computational Materials Science (ACCMS) Theme

Meeting on First Principle Analysis and Experiment : Role in Energy Research, Chennai on September 22-24, 2016.

[2] **Ranveer Singh**, M. Muneeswaran, Mohit Kumar, and T. Som ─ "An efficient hole-blocking property in $BiFeO_3$ thin films grown by PLD" ORAL: International Conference on Functional Oxides and Nanomaterials (ICFONM), Rajkot on November 11-13, 2016.

[3] **Ranveer Singh**, Mohit Kumar, Mahesh Saini, and Tapobrata Som ─ "Thickness-dependent photoresponse in *n*-TiO_2/*p*-Si heterostructure" ORAL: 2nd International Conference on Solar Energy Photovoltaic (ICSEP), Bhubaneswar on December 17-19, 2016.

[4] **Ranveer Singh**, Mohit Kumar, R. Shivakumar, and Tapobrata Som ─ "Growth angle-dependent tunable structural, optical, and electrical properties of MoO_3 thin films" ORAL: International Conference on Advances in Biological Systems and Materials Science in NanoWorld (ABSMSNW-2017), Varanasi on February 19-23, 2016.

[5] **Ranveer Singh**, Mohit Kumar, R. Shivakumar, and Tapobrata Som ─ "Thickness-dependent tunable optoelectronic properties of *n*-MoO_3/*p*-Si heterojunction" ORAL: 9th International Conference on Materials for Advanced Technologies (ICAMT-2017), Singapore on June 18-23, 2017.

[6] Mahesh Saini, **Ranveer Singh**, and Tapobrata Som ─ "Photoresponse study of Pulsed Laser Deposited ZnO:Cu thin films" POSTER: 9nd International Conference on Materials for Advanced Technologies (ICAMT-2017), Singapore on June 18-23, 2017.

[7] **Ranveer Singh** and Tapobrata Som ─ "Influence of grain size on local work function and optoelectronic properties of *n*-ZTO/*p*-Si heterostructures" POSTER: Annual Condensed Matter Physics Meeting, Bhubaneswar (India) on February 26-27, 2018.

[8] **Ranveer Singh**, Sanjeev K Srivastava, and Tapobrata Som ─ "Influence of grain size on local work function and optoelectronic properties of *n*-ZTO/*p*-Si heterostructures" POSTER: International Conference on Microscopy – EMSI 2018, Bhubaneswar (India) on July 18-20, 2018.

[9] **Ranveer Singh**, Maxime Vallet, Sanjeev K Srivastava, Alain Claverie, and Tapobrata Som ─ "Effect of annealing temperature on the microstructure, optical, and electrical properties of polycrystalline CdTe for solar cell applications" POSTER: International Conference on Microscopy – EMSI 2018, Bhubaneswar (India) on July 18-20, 2018.

[10] **Ranveer Singh**, Maxime Vallet, Sanjeev K Srivastava, Alain Claverie, and Tapobrata Som ─ "Effect of Cu-doping on the different physical properties of polycrystalline CdTe for solar cell

applications” ORAL: International Conference on Efficient Solar Power Generation and Energy Harvesting (ESPGH-2019)-An Industry – Academia Meet, Noida (India) on February 12-14, 2019.

Ranvir Singh

Ranveer Singh

To my parents and grandparents

Acknowledgements

First and foremost, I would like to thank Professor Tapobrata Som for his tireless efforts in ensuring the continued success of the SUNAG Laboratory. He has fostered an excellent place for work and science. The challenging journey of my Ph. D. life and all the achievements that I have accomplished during my stay at Institute of Physics, Bhubaneswar won't be possible without the support, help, and guidance of my advisor, Prof. T. Som. Under his tutelage, I have learned valuable scientific and occupational lessons. I take this opportunity to express my sincere and deep gratitude to him for his constant encouragement and enormous energy towards my cause. His advice was sage and always appreciated. His innovative ways of looking into the problem with an admixture of professionalism and perfectionism will remain as assets for the rest of my life. I sincerely thank him and his family for their care and hospitality which never let me feel to be away from home during my stay at IOP. It has been truly a life time privilege for me to work under his guidance.

I would like to thank Prof. A. Claverie, CEMES-CNRS, France, Dr. R. Sivakumar, Alagappa University, Tamil Nadu, Dr. S. K. Srivastava, IIT Kharagpur, Dr. B. Satpati, SINP, Kolkata, Dr. P. K. Sahoo, NISER, Bhubaneswar, Prof. J. Lahiri, University of Hyderabad, Hyderabad, Dr. V. Kumar, University of Illinois, Chicago, and Dr. S. Chatterjee, IMMT, Bhubaneswar for extending their facilities and precious time towards my research and relevant discussion.

I would also like to acknowledge my senior group members Dr. Sandeep K. Garg, Dr. Tanmoy Basu, Dr. Mohit Kumar, Dr. Debi P. Datta, and Dr. Safiul A. Mollick for their valuable suggestions and providing me a chance to work with them. In particular, I express my heartfelt thanks to Dr. Mohit Kumar, Incheon National University, South Korea for his valuable time and useful discussions with me at various points. I have learned a lot from him in personal life as well as in research. He always treats me like a younger brother. My special thanks go to Dr. S. Nandy, Dr. S. K. Hazra, and Mr. Sudheer for valuable discussion and their helps during various stages of my research life.

I would like to thank my other lab mates, Mr. Mahesh Saini, Mr. Alapan Dutta, Ms. Dilruba Hasina, and Mr. Rupam Mondal for their helps and creating a nice ambience in the laboratory. I wish to thank Mr. Nilanjan Basu (University of Hyderabad, Hyderabad) for his help in carrying out micro-Raman and SEM measurements.

I thank all my teachers who taught me during the pre-doctoral course work and all the experimental condensed matter group faculties of IOP, Bhubaneswar for their generous support. I also thank to scientific staff of IOP, especially Mr. S. K. Choudhury and Mr. Arun Dash, for making themselves available wherever their expertise was required for the lab. In fact, I have learnt a lot about various experimental systems from Mr. S. K. Choudhury.

I am grateful to the present director, Prof. S. Panda, Dean HBNI at IOP, Prof. Pankaj Agrawal, members of my Doctoral committee: Prof. A. M. Jayannavar, Prof. S. K. Patra, and Prof. P. V. Satyam and other members of the Institute (academic and non-academic) for their timely helps, cooperation, and support whenever I needed the same.

I have enjoyed the company of all my colleagues. Thanks to all the senior and junior scholars of IOP for their direct or indirect assistance on many occasions during my stay at IOP. A special acknowledgement goes to my friends who have been invaluable to the success of my research and to my happiness during these Ph. D. days. In particular, I would love to thank my batch mates Mahesh, Bharat, Paramita, and Pronoy for all their helps. Some special words of gratitude go to Praveen among the best friends that I can ever have. He has always been a major source of support when things would get a bit discoursing.

Most importantly, I have always been fortunate in being able to count on continuous support received from my parents and extended family as a whole. They have always believed in me and their love and affection have kept me going during all these years. I am extremely grateful to my dearest grandparents who supported me all throughout my life and have allowed me to pursue whatever I wanted. You have been role models of the highest calibre as a hero, as a protector, as a matriarch, and as a macher. I have great memories and spending time with you. Today, although my grandfather is not there with me, I always believe that your blessings will be there with me and show me the right path to achieve my goals. It is because of both of you that I was able to become the person I am today.

Date: 25/01/2019

RanvirSingh

Place: Bhubaneswar Ranveer Singh

Summary

In the present thesis, we have fabricated an efficient multijunction CdTe-based, chlorine-free hole-blocking solar cells. In order to do this, multilayers are grown to make the junction using dc/rf sputtering technique and to separate out the photo-generated charge carries. For instance, ZTO is used as a transparent conducting oxide layer, MoO_3 is used as a hole-blocking layer, Cu-doped CdTe is employed as the main absorbing layer, and Mo is used as the metal back contact. In addition, we have prepared pyramidally textured Si substrates (which show a very low surface reflectance, <0.4%, in the wide wavelength range of 300 to 2400 nm) to use as a template for the fabrication of PV cell. Before fabricating full solar cells, we have studied the role of each layer and characterized their different properties using XRD, AFM, SEM, TEM, EDX, XPS, UV-Vis, *I-V*, *C-V*, and photoresponsitivity. It is found that ZTO films grown at RT and an incidence angle of 50° and having thickness of 180 nm exhibits excellent optoelectronic properties to use it as a TCOs. In addition, we have studied the role of grains and grain boundaries on charge transport at nanoscale as well as at bulk and it is observed that grains are more conductive than grain boundaries. CdTe films grown at normal incidence show the lowest resistivity and work function among others. Further, Cu-doping in CdTe reduces work function and resistivity to use it as an absorber layer where it shows reflectance <15% in the visible region. The introduction of hole-blocking layer in between the main absorbing layer and the top TCO layer helps in enhancing the efficiency of the CdTe:Cu-based solar cells. Among various thicknesses of hole-blocking layer, it is observed that 10 nm-thick MoO_3 film efficiently allow the transport of electrons but block the transport of holes. In case of metal back contact, it is observed that the optical reflectivity decreases with increasing growth angles and both Al and Mo films deposited under normally incident flux show the highest reflectivity and the lowest resistivity. Thus, those Al and Mo growth conditions

are used to grow the back contacts for different chosen configurations of the CdTe:Cu-based solar cell. We have fabricated following configrations: (i) ZTO/CdTe:Cu/Mo/*pris*-Si, (ii) ZTO/CdTe:Cu/Mo/*txt*-Si, (iii) ZTO/MoO_3/CdTe:Cu/Mo/*pris*-Si, (iv) ZTO/MoO_3/CdTe:Cu/Mo/*txt*-Si, (v) ZTO/CdTe:Cu/Al/*pris*-Si, (vi) ZTO/CdTe:Cu/Al/*txt*-Si, (vii) ZTO/MoO_3/CdTe:Cu/Al/*pris*-Si, and (viii) ZTO/MoO_3/CdTe:Cu/Al/*txt*-Si. Using photo-KPFM, real time photo-induced charge dynamics across grains is measured and it is shown that local band-bending takes place at the interface which reduces under illumination. Finally, we have measured the efficiency of all the configurations and it is observed that the CdTe:Cu-based solar cell fabricated on *pris*-Si substrate using a MoO_3 hole-blocking layer shows 7.01% efficiency and it further increase to 8.2% by replacing the *pris*-Si by a *txt*-Si substrate. To the best of our knowledge, this is the first demonstration of a CdTe-based hole-blocking solar cell where we have achieved the best efficiency for any CdTe-based cell configuration fabricated without any $CdCl_2$ vapor treatment.

Table of contents

List of figures

CHAPTER 1

1. Introduction

1.1 Preamble

Energy demand is one of the most fundamental necessities in today's world and it is increasing at a rapid rate [1,2]. As the world is observing more modernization, per capita consumption of energy has increased because energy lits our cities, powers our vehicles, trains, planes, and rockets as well as drives our household etc. While on one hand growth brings prosperity to a nation it also puts immense pressure on earth's natural resources. Thus, to fulfil the demand of energy for the world's population, it is becoming a more and more critical challenge [3]. Therefore, there is a demand of an environment-friendly, abundant, safe, and sustainable energy sources.

Natural resources like fossil fuels – coal, petroleum, etc. have been the main energy sources for the mankind over the last two centuries. However, these energy resources are depleting very fast [4]. Moreover, their increased usage creates a number of challenges including pollution, rising prices, security of supply, and so on [5]. Pollution by carbon dioxide is the biggest problem because it causes the greenhouse effect. As a result, radiations from planet's atmosphere warms the planet's surface temperature, leading to the global warming [5]. Thus, the increased usage of above mentioned natural resources generates a vast amount of greenhouse gases that put the nature at risk. Therefore, use of alternative forms of energy is the need of the hour.

Alternative energy sources like fuel from biomass, solar, geothermal, wind power, nuclear power, and hydroelectric power are eco-friendly and do not deplete as opposed to fossil fuels [6], albeit some of them have serious issues. Hydro-power is indirectly obtained from solar energy and has the advantage of being a renewable source of energy. However, many environmental concerns are now being raised when big projects involving the storage of large amount of water is being considered [7]. On the other hand, nuclear power is obtained from fission reactions in pressurized heavy water reactors which utilize only the U^{235} isotope. This isotope is available to the extent of less than 1% in naturally occurring uranium [8]. It is thus fairly evident that a need exists for developing alternative energy sources. Among the other renewable energy sources, solar energy has a great focus as an inexhaustible source of energy. The power from the sun intercepted by the earth is approximately 1.80×10^{11} MW which is thousands of times larger than the present consumption rate on the earth of all commercial energy sources [9]. Currently the total global energy consumption is estimated to be approximately 1.35×10^{7} MW and will increase up to 2.7×10^{7} MW by the year 2050 [3]. Thus, solar energy could provide all the present and future energy needs of the world on a continuing basis. This makes it one of the most promising among all the unconventional energy sources. In addition to its available amount, solar energy has two other factors in its favour. First, unlike nuclear power and fossil-fuels, it is an environmentally clean source of energy and second, it is free and abundant all over the world. However, there are many issues associated with its use which need to be addressed as well. For instance, the main problem is that it is a dilute source of energy and its availability varies widely with time. To meet the world’s energy demand, solar energy conversation with photovoltaics (PV) will have to reach the terawatt (TW) scale which is still far away [4]. In addition, cost reduction with respect to other conventional energy sources is still a big challenge. Further, the solar energy industry is still not fully equipped to handle the environmental pollution, arising out of the toxic elements/compounds which are used in the constituent layers in PV cells.

1.2 Physics of solar Cells

A photovoltaic cell, or a solar cell, is a device that converts light energy from the sun into electrical energy through the photoelectric effect [10]. In all solar cells, light absorbing materials are required which absorb photons and generate electron-hole pairs via the photoelectric effect. In fact, light (photons) is absorbed by the cell and converted to electron-hole pairs which must be separated for the electrons to work on a connected external load or to generate electric current or voltage across the device [11]. This is achieved by semiconducting materials in the form of a *p-n* junction or which under illumination of light results in the charge separation across the junction through the existing built-in potential in the depletion region as is shown in Fig. 1.1 [12]. When photons carrying energy more than a certain threshold energy (being the band gap of the materials on which photons are incident) are incident on *p-n* junction,

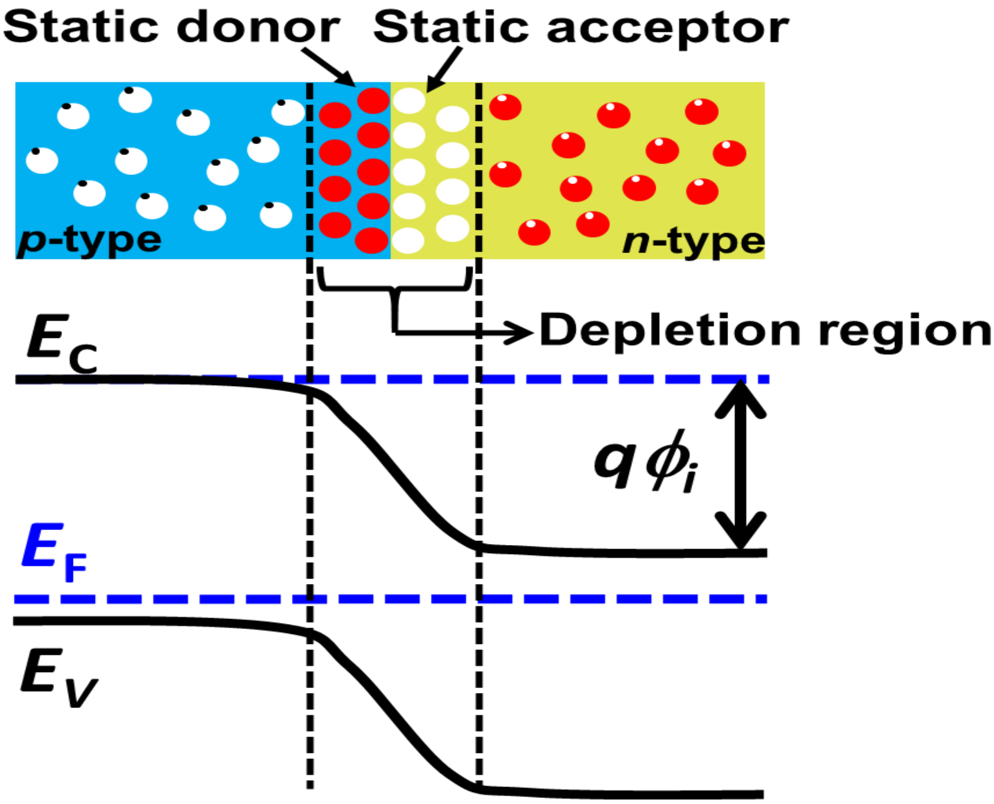

Figure 1.1: Schematic diagram of a *p-n* junction and its band diagram [8].

electrons are excited from the valance band to the conduction band, leaving behind positively charged vacancies (i.e. holes) in the valance band and electron-hole pairs are created in this process. These photo-generated charge carriers exist only for a short time which is equal to the minority carrier lifetime and thereafter they recombine [13]. Thus, before the recombination of photo-generated charge carriers or electron-hole pairs, they should be separated out and collected at the suitable electrode. In doing so, the strong internal electric field is required which is created at the interface of the *p*-*n* junction. Since both sides of the junction have different concentrations of mobile carriers, diffusion takes place across the junction. Thus, static charges build up both in *p*- and *n*-type materials close to the junction as diffusion of holes and electrons take place. This static charged area is known as space charge region or the depletion region and it gives rise to an electric field in semiconductors close to the junction region [13]. Thus, this electric field sweeps out the photo-generated charge carriers in the opposite direction which leads to the generation of potential difference at both the electrodes of the device (Fig. 1.2). The magnitude of this potential drop is called open circuit voltage (V_{oc})

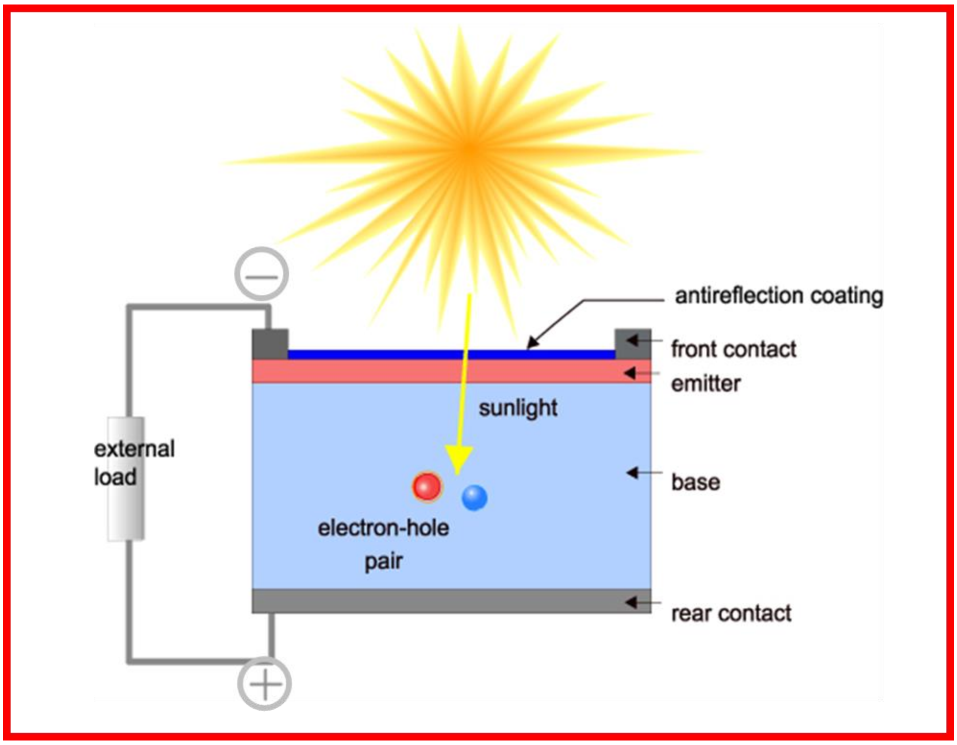

Figure 1.2: Schematic diagram of a solar cell.

and it depends on the intensity of the incident light. When the two ends of a *p-n* junction are connected together without any load the resultant current is called short circuit current (I_{sc}) [11]. A more common parameter is the current per unit area or current density (J), which will be used in later the following chapters.

To explain the *I-V* characteristics of a practical solar cell, the resistance due to semiconductor material and metallic contacts cannot be neglected. Besides, this leakage path across a *p-n* junction cannot be overlooked. Therefore, an actual solar cell is represented by an equivalent circuit shown in Fig. 1.3. In this equivalent circuit R_{SH} stands for the leakage resistance across the *p-n* junction, known as shunt resistance and R_S represents the series resistance of the solar cell consisting of resistances of the front region, base region, as well as front and back metal contacts [14].

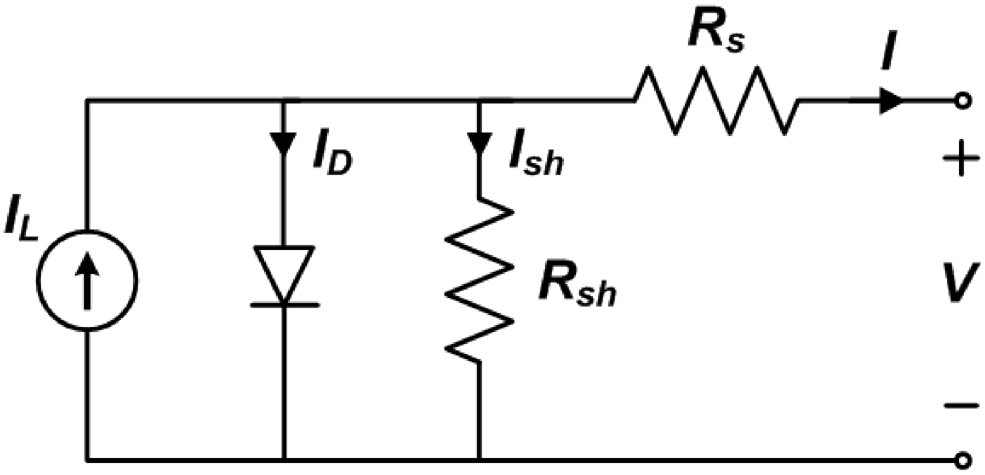

Figure 1.3: Equivalent circuit diagram of a solar cell.

As a matter of fact, R_{SH} accounts for the leakage currents and recombination of charge carriers from one terminal to the other due to a poor insulation. Thus, to reduce the recombination and leakage currents, a larger R_{SH} value is required. On the other hand, R_S is the total Ohmic resistance of the solar cell. A smaller R_S is required to construct a better efficient solar cell. From this equivalent circuit, the current density produced by the cell can be written as:

$$J = J_L - J_D - J_{SH}, \tag{1.1}$$

where J, J_L, J_D, and J_SH are output current density, photo-generated current density, diode current density, and shunt current density, respectively. The current in solar cell is governed by the voltage drop across them:

$$V_J = V + IR_{SH}, \tag{1.2}$$

where V_J and V are voltages across both diode and the resistor R_SH and voltage across the output terminals. By the Shockley diode Eq., the current density through the diode is:

$$J_D = J_0 \left[\exp\left(\frac{qV_J}{nk_\mathrm{B}T}\right) - 1\right], \tag{1.3}$$

where J_0, n, q, k_B, and T are reverse saturation current, diode ideality factor (1 for an ideal diode), elementary charge, Boltzmann's constant (at RT, $k_\mathrm{B}T/q$ is approximated to 25.9 mV), and absolute temperature, respectively [13]. The ideal Shockley diode Eq. for the solar cell without any loss can be described as:

$$J = J_L - J_0 \left[\exp\left(\frac{qV_J}{nk_\mathrm{B}T}\right) - 1\right]. \tag{1.4}$$

On the other hand, the current diverted through the shunt resistor is:

$$J_{SH} = V_J/R_{SH}. \tag{1.5}$$

Summing up the Eqs. from (1.1) to (1.5), one obtains the total output current density (J) Eq. for the solar cell in the following manner:

$$J = J_L - J_0[exp\{q\left(V + \frac{JR_S}{nk_BT}\right)\} - 1] + (V + JR_S)/R_{SH}. \tag{1.6}$$

The load current density J is given by Eq. (1.6) which includes an empirical factor n, known as the diode ideality factor. Basically n depends on the quality of the material used and recombination of the minority carriers in the material. A value of n more than unity leads to deterioration in the efficiency of the cell. On the other hand, low value of R_SH has an adverse effect on the performance of the solar cell and a higher value of the R_S drastically reduces the efficiency. For an ideal solar cell R_SH is equal to infinity and R_S equal to zero. However, practically good quality solar cell is associated with shunt and series resistance of the order of

10 kΩ and 0.01 Ω, respectively. In fact, R_S is parasitic in nature and difficult to study its effect independently. It influences other important parameters of solar cell, viz. short current density (J_{sc}), open circuit voltage (V_{oc}), fill factor etc. [13].

The other parameters of a solar cell such as short circuit current density (J_{sc}), open circuit voltage (V_{oc}), fill factor (*FF*), power (*W*), and conversion efficiency (η) can be obtained by carrying out *I-V* measurements in the presence of light [14]. V_{oc} is the voltage across the solar cell when the current through the solar cell is zero and it is the maximum voltage available from the cell. Eq. (1.4) under the condition of open circuit voltage (J=0) gives

$$V_{oc} = \frac{nk_{\mathrm{B}}T}{q} \ln\left(\frac{J_L}{J_0}\right) + 1] \tag{1.7}$$

and J_{sc} (or J_L) is the current density through the solar cell when the voltage across the solar cell is zero (V_J=0). The fill factor (*FF*) and conversion efficiency (η) are two other important parameters which are used to characterize the performance of the solar cell. The *FF* is defined as the ratio of the maximum power output (P_{max}) of the cell to the product of open circuit voltage and short circuit current. *FF* is a measure of the quality of the solar cell. P_{max} is the maximum power generated by the solar cell and V_{max} and I_{max} are voltage and current at maximum power point, respectively [Fig. 1.4]. *FF* is expressed by following Eq.:

$$F.F. = \frac{Maximum\ power}{I_{sc} \times V_{oc}} = \frac{I_{max} \times V_{max}}{I_{sc} \times V_{oc}} \,. \tag{1.8}$$

The conversion efficiency (η) of the solar cell is the ratio of P_{max} to the product of the solar cell area (*A*) and incident light irradiance (*E*). The product of *A* and *E* is known as input power (P_{in}). Thus, η is expressed by following Eq.:

$$\eta = \frac{P_{max}}{E \times A} = \frac{P_{max}}{P_{in}} \,. \tag{1.9}$$

The other important parameter of a solar cell is the quantum efficiency (*QE*). *QE* is defined as the ratio of the number of carriers collected by the solar cell to the number of photons of a given energy incident on the solar cell. *QE* can be expressed either as a function of the

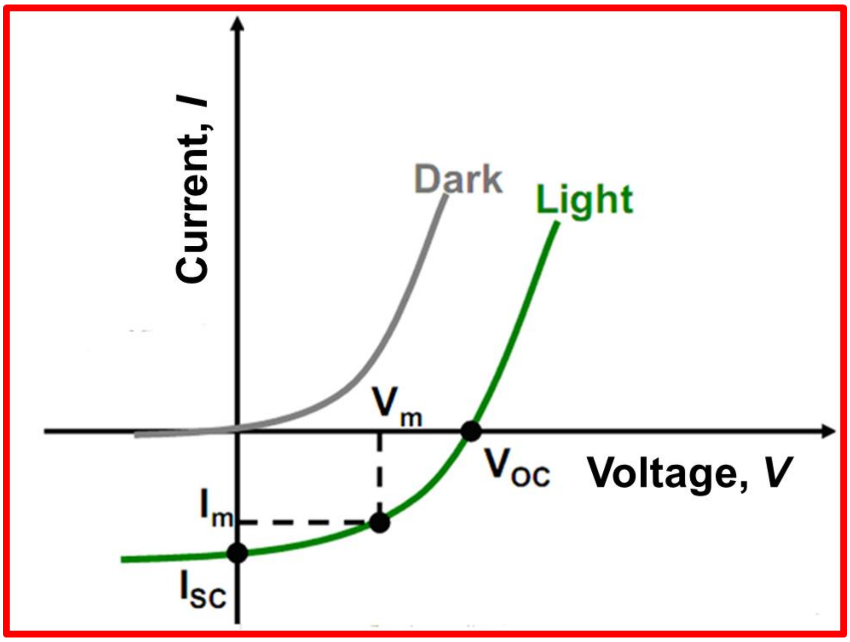

Figure 1.4: Schematic *I-V* characteristics of a solar cell.

wavelength or the energy [12,13]. If all photons of a certain wavelength are absorbed and the resulting minority carriers are collected, *QE* becomes unity at that particular wavelength. On the other hand, *QE* for photons with energy below the band gap of the main absorbing layer is zero. Theoretically, *QE* for an ideal solar cell has the square shape but experimentally, it is found between 0 and 1 due to recombination of photo-generated charge carriers and they are not able to move into the external circuit as depicted in Fig. 1.1. This loss in charge carriers affect the collection probability which also affects the efficiency of a solar cell. Thus, the front surface recombination and diffusion length impact on the collection probability reduces the *QE* [11-13]. The better cell efficiency can be achieved by using a *p-n* junction closer to the surface rather than the bulk so that the separated charge carriers have a shorter diffusion length to reach at the electrode, resulting a less probability of recombination. The low diffusion lengths have no effect on the recombination of carriers at rear surface.

1.3 History of photovoltaic cells and current status: A brief literature survey

Currently, there are several different types of materials and technologies used in solar cells which are commercially available. As discussed, the operation of the solar cells depends upon the photovoltaic effect. Becquerel, who observed a light-dependent voltage between electrodes immersed in an electrolyte, reported this effect initially in 1839 [15]. But, Fritts was the first person who made functional PV device in 1883 [15]. He melted selenium into a thin sheet on a metal substrate having 30 cm^2 area and used an Au-leaf film as the top contact. He stated, “the current, if not wanted immediately, can be either stored where produced, in storage batteries, …or transmitted a distance and there used.” The modern era of photovoltaics started in 1954 when accidentally scientists at Bell Laboratories in the USA discovered that a *p-n* junction diode generated a voltage when the room lights were on and they produced 6% efficiency with a Si *p-n* junction solar cell within one year [16]. In 1960, Shockely *et al*. developed a theoretical relation between band gap, incident spectrum, temperature, thermodynamics, and efficiency [17]. At the same time, solar cells based on GaAs and CdTe thin films were also fabricated. In the era of 1980s, PV industry began to mature as the emphasis grew on manufacturing and costs. Presently, the high cost and relatively low power conversion efficiency are the two main issues with the utilization of solar energy which need to be resolved before solar energy can become a major contributor in the energy market [2,3,13]. To date, there are three major PV technologies for large-scale production. These are based on amorphous Si (a-Si), multi-crystalline compounds like cadmium telluride (CdTe) and copper indium gallium diselenide ($Cu(In, Ga)Se_2$ or CIGS) along with GaAs-based solar cells for both single and multijunction [15,18]. Multiple layers are used to absorb the maximum light of different portions of the solar spectrum in a multijunction solar cell for enhancing the efficiency of cell. GaAs-based solar cells exhibit highest efficiency but generally limited to space applications because of their relatively high cost [18].On the other hand, silicon-based solar cells have more than 85% market. Thus, PV industry mainly depends on the Si-based solar cells because silicon is found to be abundant in nature. The monocrystalline silicon cell has 23% efficiency but the cost of producing the materials causes the cells price to be high. They are made of single crystal silicon grown at high temperature [15]. Thus, crystalline and multicrystalline silicon solar cells have still high cost to be considered as a reasonable competitor to the energy production using conventional routes. In an effort to address the issues of cost minimization of solar cell and materials utilization, very thin layers of semiconductor materials are the subject of intensive PV research. Therefore, thin film solar cells have gained a prominence and to have cost effective solar cells, thin films having high absorption coefficients are used to ensure the maximum absorption of light (from the solar spectrum) within the films [20]. These films are grown on any kind of substrates even at lower temperatures. The band gap (E_g) of the materials should also be close to their theoretically calculated values ($1.1 \leq E_g \leq 1.8$) to produce the maximum efficiency. In this regard, various types of thin film-based solar cells have been fabricated such as *a*-Si, CIGS, GaAsInP, dye sensitized, CdS/CdTe etc. albeit all of them are still facing various challenges [21]. For instance, *a*-Si thin film solar cells exhibit >10% efficiency but have a low absorption coefficient due to the fact that it has an indirect band gap. CIGS offers the highest efficiency (14%) thin film modules but the limited amount of indium reserves poses a long-term issue. On the other hand, the optical properties of GaAsInP, CdS/CdTe, and its family strongly depends on the growth processes and are very difficult to control them [15,21]. For dye-sensitized solar cells, the development of absorbing materials is a major issue and still not completed [21]. Dye-sensitized solar cells exhibit ~11% efficiency and work slightly differently to conventional cells. Dye-sensitized solar cells use an organic dye to absorb light and form an exciton (an electron-hole pair). The exciton moves to an interface where electron and hole get separated. The use of a liquid electrolyte in the dye-sensitized cells has a source of reliability issues [22]. In case of organic solar cells, the chemical, electrical, and optical properties of organic semiconductors can be tailored by numerous methods and can allow new processing methods. Using organic semiconductors flexible solar cells can be fabricated on flexible substrates such as polyethylene terephthalate (PET). The technology of manufacturing flexible solar cells was developed by a group of researchers from the Massachusetts Institute of technology [23]. The solar cells fabricated using printing processes (from dye) can be much cheaper than conventional solar panels [23]. However, organic semiconductors are still not very well studied and the best-known highest efficiency for an organic thin film solar cell is only ~8% [22]. Figure 1.5 summarizes the highest efficiencies achieved by many groups in various solar cell technologies over the years [24]. There are also hybrid approaches such as combined crystalline silicon-perovskite, crystalline silicon- amorphous silicon, amorphous silicon-perovskite cells, etc. [21]. However. Still lot of efforts need to be put in these directions to make these solar cells commercially viable since stability is a big issue for the perovskite layers.

Thin film solar cells based on CdTe received much attention as an absorber material for fabricating efficient and low cost solar cells. After 2010, the efficiency of CdTe thin film solar cells increase from 16% to 22% as shown in Fig. 1.5 at the laboratory scale. It is observed that the commercially available solar cells have lower efficiency compared to laboratory solar cells because of additional complexities during manufacturing on a large scale.

1.4 Motivation: The aim and objectives of work

Photovoltaics has the potential to become a major source of energy and has significant and beneficial effects on the global environment. To fulfil this requirement, the search for an ideal PV material is being actively pursued at many fronts. The following discussion describes the status and prospects of one major PV material, e.g. CdTe [25].

Thin film solar cells based on binary compound CdTe has received much attention as an absorber material for efficient and low-cost solar cell because of its attractive properties. The optoelectronic properties of CdTe provides an ideal match to the solar spectrum towards high

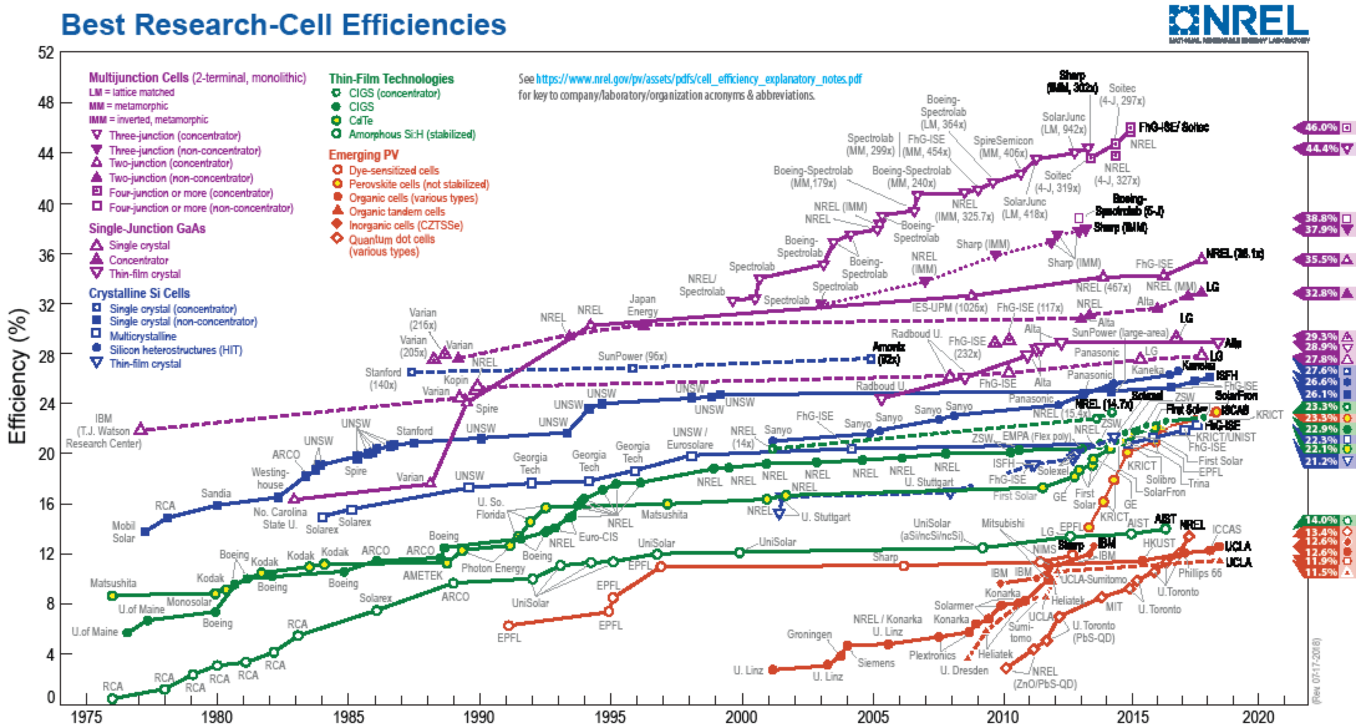

Figure 1.5: Comparison in efficiencies of various solar cells with time (obtained from NREL, USA).

conversion efficiency [15]. CdTe has a band gap of 1.45 eV (at room temperature) which is well suited to absorb the solar light spectrum and the band gap between conduction and valance levels in CdTe is direct. The absorption coefficient of CdTe in the visible region is greater than 10^5 cm^{-1} which means 90% of the light is absorbed in the first few microns [26-28]. To fabricate solar cells with single-crystal *p*-type CdTe, heterojunctions using oxides, such as In_2O_3:Sn (ITO), Al-doped ZnO, tin oxide (SnO_2), and CdS have been investigated [15]. In these devices, the short wavelength spectral response is influenced by transmission of used window layer and low-resistance contact. CdTe solar cells based on a CdS/CdTe heterojunction exhibits 16.5% efficiency at laboratory scale, which is 65% of their theoretical values and module efficiencies greater than 10% have been demonstrated for widely used different CdTe deposition technologies [15]. Recently, First Solar has announced a record 22.1% conversion efficiency for CdS/CdTe solar cell in 2016 whereas in 2014 they had achieved 21.1% conversion efficiency. On the other hand, in the case of solar module, the efficiency has increased from 16.1% to 17.0% by the First Solar. But, in CdS/CdTe solar cell, there will be access Cd due to used CdS layer which is toxic and have serious environmental issues at the end-of-life and during recycling [29]. Thus, the major concern with CdTe-based devices is the toxicity of cadmium and tellurium. The European Union has recently brought in legislation (2006/66/EC) to reduce the amount of hazardous materials released in the environment; this includes that no more than 0.002% of cadmium (% by weight) incorporated into portable batteries with some exceptions [30]. Thus, to reduce the cadmium in the CdTe-based solar cells, doping of different elements such as Cu, Na, etc. have been done [31]. CdTe offers flexibility in device design and allowing tunability in optical and electrical properties of the absorber layer.

To further increase the efficiency, chlorine treatment of CdS/CdTe solar cell using cadmium chloride ($CdCl_2$) is used. Chlorine treatment increases the grain boundary passivation and lifetime of minority charge carriers, resulting CdS/CdTe solar exhibits high efficiency [29]. Recently, it has also demonstrated that after a $CdCl_2$ treatment Cl is incorporated in the CdTe grain boundaries. The presence of Cl, an *n*-dopant for CdTe, results in local doping, which affect the efficiency of the device. The maximum achieved efficiency of CdTe solar cell without any CdS layer and $CdCl_2$ treatment is <6%. Thus, in the present thesis, we have revisited the problem and use Cu doping to decrease the toxicity, which also helps to increase the power conversion efficiency. However, use of $CdCl_2$ vapour incorporates toxic element like Cl which is considered to environmentally hazardous, although $CdCl_2$ vapour treatment improves efficiency to a large extent [29]. In order to overcome the Cl-related environmental issue, it will be desirable to fabricate a chlorine-free CdTe-based PV cell, albeit one has to comprise with the conversion efficiency. However, this loss may be possibly compensated to some extent, by using a hole-blocking layer in between the absorber layer and the transparent conducting layer [32]. Thus, to fabricate such a Cl-free CdTe-based hole-blocking PV cell, the present thesis deals with optimization of growth of the constituent layers and their nanoscale and/or bulk characterizations by studying their electrical, optical, structural, and compositional aspects towards achieving a superior cell efficiency (>8%). Theoretically, the efficiency of this type of solar cell without any CdS layer should be around 30% [33], albeit the experimentally achieved efficiency is still less than 4% [34]. This low efficiency is due to the high work function of CdTe layer and lack of charge transport properties in the constituent layers. On the other hand, a higher temperature is also required to fabricate a high efficiency solar cell [13-15]. As a consequence, all kind of material interactions between the CdTe absorber and the other materials (contacts, buffer, window, and substrate) are possible, reducing the efficiency of same. After annealing at a high temperature, it is also difficult to measure the properties of CdTe on a complete solar cell because of the presence of the other layers which influence the standard characterizations. Thus, in order to improve the efficiency of CdTe-based solar cells, a relatively low temperature processing is needed along with an in-depth understanding of the charge transport in this layer and the other constituent layers. Figure 1.6(a) shows a schematic diagram of a CdTe-based hole-blocking solar cell used in this thesis work. Here $ZnO:SnO_2$ (ZTO) is used as the transparent conducting oxide (TCO) layer, MoO_3 is used as the hole-blocking layer , and Mo is the back contact. (ZTO) is used as the transparent conducting oxide (TCO) layer, MoO_3 is used as the hole-blocking layer, and Mo is the back contact.

For the sake of comparison in terms of performance of the same layer structures towards enhancing the cell efficiency, we have constructed another set of sample on *txt*-Si substrate [Fig. 1.6(b)]. In doing so, all the constituent layers are grown simultaneously on *pris*- and *txt*-Si substrates.

(a) Growth of zinc tin oxide (ZTO) films and understanding the charge transport: The top most layer of the studied solar cell is a ZTO film. Various deposition techniques such as sol-gel, thermal evaporation, sputtering, and pulsed laser deposition are generally used to grow a high quality ZTO films in terms of low resistivity and high transmittance [35]. But, in most of the deposition techniques, a high substrate temperature or post annealing process is needed to meet the desired level of transparency and conducting properties. In doing so, diffusion and interface mixing in the underlying layers become an eventuality. To get rid of this problem, room temperature (RT) processing is needed. In fact, achieving a low resistivity (metal-like) and a high transmittance (glass-like) in ZTO films at RT is still challenging [36]. In addition, in order to understand the transparent contact properties, it is necessary to understand not only the bulk but also the nanoscale electrical properties of ZTO thin films which are also considered to be quite challenging. As a matter of fact, nanoscale conductivity in ZTO films depends on the carrier concentration. Moreover, the top metal electrical contact with ZTO films creates a schottky barrier which affects collection of charge carriers at the electrode, leading to a poor cell performance. This can be addressed by directly studying the nanoscale charge transport in ZTO films. In this thesis, we focus on these issues and demonstrate how one can make a TCO based on ZTO films for solar cell applications.

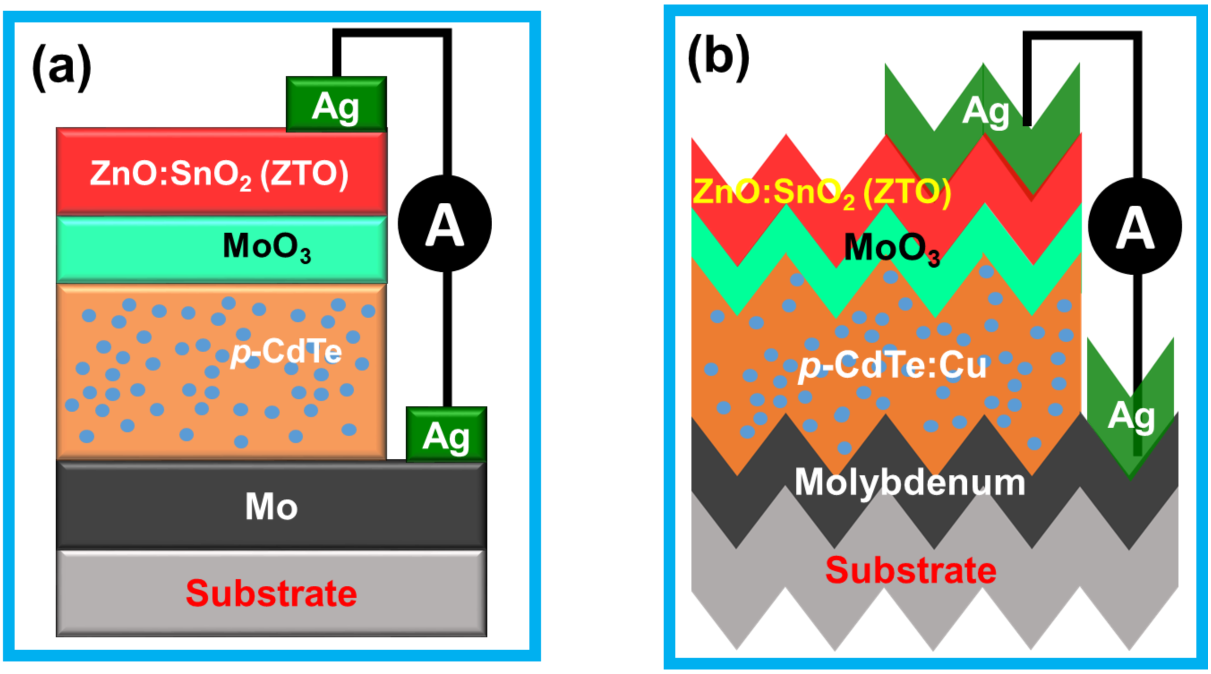

Figure 1.6: Schematic representation of a CdTe:Cu based solar cells fabricated on *pris*-substrate (a) and *textured*-substrate (b).

(b) Understanding the hole-blocking nature of MoO$_3$:

The presently proposed solar cell configuration that we have fabricated as a part of this thesis, uses a hole-blocking layer in the form of MoO_3, between the ZTO and the absorber layer. The concept of hole-blocking is explained here: when a *p*- and an *n*-type semiconductors are brought together, depending on the difference in their band gaps, the formation of an interfacial barrier is due to form. Subsequently band-bending takes place at the interface which in turn leads to the blocking of charge carriers [37]. This blocking of charge carriers decrease the recombination of charge carriers in a solar cell, resulting efficiency increase. Thus, one of the motivations to take up this study is to make use of this concept to employ a hole-blocking layer (e.g. MoO_3) in the solar cells studied in this thesis. In fact, such a layer can be sandwiched between the absorber and the transparent conducting layer (i.e. between the *p*-*n* junction) in a solar cell to reduce the recombination of carriers and in turn increases the efficiency of the cell. Although MoO_3 is grown by e-beam evaporation and sputtering, in this thesis, we have optimized the growth of the MoO_3 layer by using RF magnetron sputtering and show that it works as a good hole-blocking. We have employed both bulk and nanoscale characterization tools.

(c) Growth of CdTe:Cu layer and the role of annealing on its work function: Since in this work, CdTe is the main absorbing layer, it should have a low resistivity and a high absorption of light for a smooth charge transport across this layer. However, the growth of low resistive films of CdTe at RT is a challenging task [31]. In general, CdTe films are grown by various methods with CdS as a window layer. But, there are several challenges: (1) short minority carrier lifetime due to recombination of electron-hole pairs at the defect centers in CdTe films and at the interface between CdS/CdTe, (2) insufficient transparency of transparent conductive oxide (TCO) and the CdS layer, (3) stability of *p*-type CdTe films, and (4) lack of good Ohmic contact between the CdTe film and the back contact [13,14]. To enhance the conductivity, doping of a suitable candidate is required and this doping can change the defect concentration

[31]. This should lead to a shift in the Fermi level position and in turn change the work function of the absorber layer as well which has a one-to-one correspondence with its electrical conductivity. However, optimization of the growth of CdTe films at RT having a low resistivity and the influence of annealing on the work function in the same is still lacking. In this thesis, we have addressed all these above issues in detail. In particular, we have studied the effect of Cu-doping in CdTe and its effect on the work function of this layer by studying nanoscale charge transport across this layer.

(d) Growth of back contact: A back contact in a solar cell plays an important role to enhance its efficiency. In general, a back contact should have a high reflectivity and a low resistivity. In the present work, we have chosen two back contact layers (e.g. Al and Mo) to achieve the best cell performance. As a matter of fact, the use of a Mo layer yields the best result.

1.5 Background of the used layers

CdTe-based solar cells have huge potential to fulfil the world's energy requirement and are known to a have low cost, abundant in nature, etc. and thus various combinations of CdTe such as ZnO/CdTe, CdS/CdTe, SnO_2/CdS/CdTe, etc. have been tested to design an efficient solar cell [21]. As mentioned above, this thesis deals with a ZTO/MoO_3/CdTe:Cu/Mo heterostructure hole-blocking solar cell (Fig. 1.6). In this section, we will provide layer-by-layer description (from the top towards the battom as is seen in Fig. 1.6) and address their various physical properties.

1.5.1 ZnO:SnO_2 (ZTO)

In thin film PV cells, a window layer is required to prevent an unfavorable conduction band alignment and for smooth collection of photo-generated charge carriers from the absorber layer known as transparent conducting oxide (TCO) and used as a top electrical contact. In principle, a TCO layer should have high optical transmittance and low resistivity for the top contact [38].

Ham *et al*. have predicted the minimum theoretical resistivity limit for TCOs as 4×10^{-5} Ω–cm [39]. This limit is a consequence of transport that is constrained by ionized impurity scattering and carrier concentration limitations due to increasing optical reflection with increasing carrier concentration [38]. Sn-doped In_2O_3 (ITO) is commonly employed in all solar cell applications as a transparent contact. Unfortunately, the availability of indium is limited as it is not as abundant as other metals (there is 1000 times more zinc than indium in the earth's crust). In addition, due to its toxicity and high cost, researchers are looking for an alternative of ITO. In this regard, amorphous oxide semiconductors are considered to be suitable replacements of ITO as TCOs [38,40]. Amorphous oxides composed of heavy-metal cations with $(n\text{-}1)d^{10}\ ns^0$ ($n\geq4$) electronic configurations constitute an interesting class of transparent conductors since they are often transparent in the visible region of the electromagnetic spectrum with low electrical resistivity [41]. One promising material is zinc-tin-oxide (ZTO), which consists of naturally abundant and non-toxic elements.

ZTO thin films typically exhibit a direct optical band gap of 3.3-3.9 eV (at RT) and generally, its stoichiometry is described as $(ZnO)_x(SnO_2)_{1-x}$ ($0<x<1$) [42]. This wide band gap range likely arises from a combination of Burstein-Moss (BM) shift and compositional or structural variation in ZTO films. The fundamental band gap of ZTO has been reported to be 3.35 eV [42]. ZTO exists in two crystalline forms: trigonal ilmenite known as zinc stannate or metastannate ($ZnSnO_3$) and cubic spinal also known as zinc orthostannate (Zn_2SnO_4). Metastannate is face-centered perovskite with polar $LiNbO_3$ (L-N)–type structure having a space group of $R3c$, while orthostannate forms an inverse spinal structure (AB_2O_4-type) having a space group of $Fd3m$ as is shown in Fig. 1.7. The metastannate phase exhibits limited thermal stability [43]. Low-temperature synthesis of $ZnSnO_3$ via solid-state reactions are energetically unfavorable and typically forms mixed oxide phases below a temperature of 700°C due to the positive formation enthalpies [44]. In $ZnSnO_3$ crystal structure, each Zn and Sn octahedron shares corners with another Zn and Sn octahedron structure and during crystallization (typically above 500°C) it transforms from a metastable phase to thermodynamically stable zinc orthostannate phase. On the other hand, the inverse spinel structure of Zn_2SnO_4 consists of a Zn atom that is centered at alternating tetrahedral of ZnO_4 with four nearest-neighbor oxygen (O) atoms, while equal numbers of Zn and Sn atoms are located at the center of octahedral ZnO_6 or SnO_6 with six nearest-neighbors O atoms in the lattice. The polar structure of $ZnSnO_3$ is highly metastable in nature and is responsible for several unique and astonishing properties such as high mobility, piezoelectric property, etc. [42,43]. Generally, ZTO exhibits *n*-type conductivity which can be attributed to the presence of oxygen vacancies and/or donor levels arising from interstitial zinc or tin atoms and high mobility [42]. The high mobility is likely, a consequence of a conduction band derived from spherically symmetric *n*s orbitals of transition metal cations. Such orbitals have large radii which lead to a high degree of overlapping between adjacent orbitals and considerable band dispersion. Moreover, the delocalized electron transport is less sensitive to local and extended structural order due to the spherical symmetry of high mobility comes from an increase in the population of charge carriers (electrons), originating from the oxygen vacancies. However, too many deep trap levels within the band gap can lead to an instability in the device during operation, giving rise to a non-stoichiometric nature of the film. This non-stoichiometric nature not only changes the conductivity of the ZTO film but also gives rise to a shift in the optical band gap of the same known as BM effect [41,43]. In addition, attractive attributes of ZTO include its physical robustness, chemically stable with respect to oxidation and etching, and smooth surface in thin films. In fact, the presence of defects and oxygen vacancies in ZTO films play an important role in tuning the physical properties. Thus, it is important to understand the formation of oxygen-vacancies and deep states for high performance and stable device operation. In order to understand the role these defects and to make a superior TCO in terms of low resistivity and high transmittance, ZTO films have been grown by various deposition techniques such as sol-gel, thermal evaporation, sputtering, and pulsed laser deposition [43,44]. In most cases, they exhibit a wide variety of microstructures in terms of grain size, surface morphology, composition, lattice defects, and form grain boundaries (GBs) in the films. GBs present in the film give rise to a large number of defects which can influence the physical properties such as charge transport, resistivity, optical band gap, work function, band-bending, etc. of ZTO thin films.

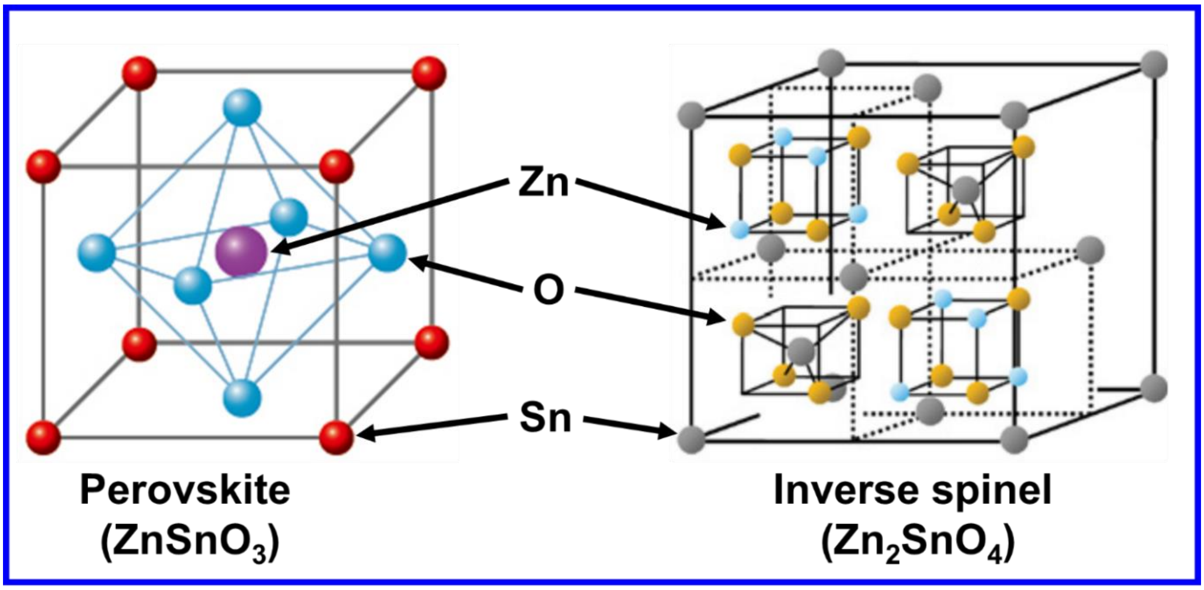

Figure 1.7: Crystal structures of face-centered perovskite metastannate ($ZnSnO_3$) and inverse spinal orthostannate (Zn_2SnO_4) [43].

1.5.2 MoO_3: The hole-blocking layer

As a wide band gap *n*-type semiconducting material, molybdenum tri-oxide (MoO_3) thin films have received a considerable attention in various applications such as photochromic and electrochromic devices, erasable optical storage media, chemical sensor, energy-efficient window technology, optical switching coatings, high-density memory devices, lithium ion batteries, etc. because of their excellent chemical stability, high dielectric constant, mechanical hardness, crystal structure, high work function, and optical transmittance with a high refractive index [45]. In addition, recently, due to its high work function, MoO_3 thin films are used as a carrier selective and window layer in organic and inorganic solar cells to improve the efficiency and lifetime [46]. Generally, MoO_3 is found to be in three main phases, e.g. α-MoO_3, β-MoO_3, and *h*-MoO_3 [45]. It is known that out of these phases, *α*-MoO_3 is found to be thermodynamically most stable which has a two-dimensional layered orthorhombic crystal structure with unit cell parameters a=3.96 Å, b=13.85 Å and c=3.71 Å in *Pbnm* space group [47]. Along [010] direction of *α*-MoO_3, two distorted bilayer of MoO_6 octahedral are connected by weak van der Waals forces and the interaction between the atoms within the MoO_6 octahedral double layer are dominated by strong covalent bond and ionic bonds, as is shown in Fig. 1.8 [46,47]. The second phase is metastable monoclinic *β*-MoO_3 with unit cell parameters: a=7.12 Å, b=5.37 Å and c=5.57 Å in $P2_1/c$ space group. The crystal structure of *β*-MoO_3 is quite different from *α*-MoO_3 phase as depicted in Fig. 1.8 [47]. It can be related to three dimensional ReO_3 structure like WO_3. It is formed only by the corner sharing MoO_6 octahedron. The external parameters like temperature, pressure, and impurities lead to the arrangement of the MoO_6 octahedron. Pham *et al.* have shown that there is a phase transformation from the metastable *β*-MoO_3 to the stable *α*-MoO_3 at 433°C [48]. The highest known phase transition temperature from *β*- to *α*-MoO_3 is 450°C, whereas the lowest one is 387°C [48,49]. The last one is a metastable hexagonal MoO_3 (*h*-MoO_3) with unit cell parameters: a=10.53 Å, and c=14.97 Å in $P6_3/m$ space group as shown in Fig. 1.8 [49]. Depending on the oxygen concentration and oxidation states of Mo, molybdenum oxide exists in different forms like MoO_3, Mo_4O_{11}, Mo_8O_{23}, Mo_9O_{26}, and MoO_2 [48]. This allows the band gap engineering of MoO_3 over a wide range. A number of techniques, such as chemical vapor deposition, atomic layer deposition, electron beam evaporation, and magnetron sputtering are used to grow MoO_3 thin films onto several substrate materials [45]. Out of these, sputtering is considered to be an attractive technique to grow MoO_3 thin films because it has the advantages of producing high-quality contamination-free films over a large area with a large uniformity at lower substrate temperatures. In addition, the morphology, microstructure, grain size, nature of crystallinity, and planar orientation of the MoO_3 layers can be controlled by various process parameters such as sputtering gases, growth angle, oxygen partial pressure, substrate temperature, substrate-to-target distance, substrate rotation speed, deposition power, deposition time, and/or annealing process. However, α-MoO_3, β-MoO_3, and h-MoO_3 phases have generally been observed through the high temperature sputter deposition of MoO_3 [45, 48]. In addition, amorphous MoO_3 films are often observed if the substrate temperature is low during deposition (e.g. at room temperature) [47]. In fact, all the physical properties of MoO_3 films grown by reactive sputtering technique, strongly depend on the above-mentioned parameters.

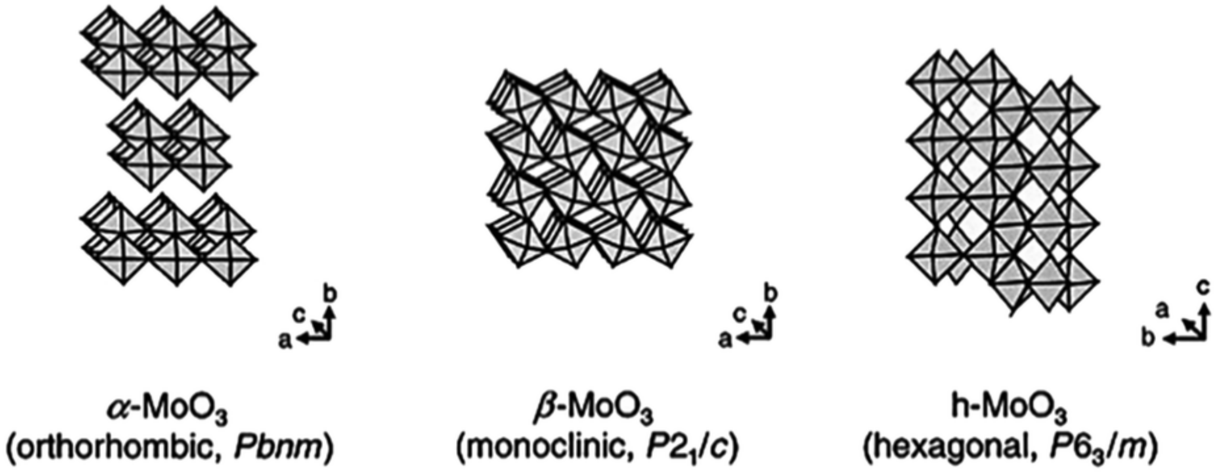

Figure 1.8: Crystal structures of different phases of MoO_3 [46,47].

Generally, MoO_3 behaves as an *n*-type semiconductor due to oxygen vacancies or reduced oxidation state of Mo [50], resulting in the formation of defect levels below the conduction band which yields a large band gap (3.0-3.7 eV at room temperature). In addition, MoO_3 has a very high work function, ranging from 5.1 to 6.5 eV. Recently, Battaglia *et al.* have shown a high work function of MoO_3 (practically causing it to act as a metal) and extended its application to solar cell [50]. This high work function depends on the deposition technique and oxidation state of Mo. The main advantage of MoO_3 is that it can be used to make a heterojunction where it shows the ability to selectively block the flow of either electrons (via the conduction band barrier) or holes (via the valence band barrier). In this work, we have used this property to employ MoO_3 as a hole-blocking layer.

1.5.3 Cu-doped CdTe: The main absorbing layer

CdTe thin film solar cells are the basis of PV technology with major commercial impact on solar energy production. CdTe is considered as an attractive material for photovoltaic applications because of its novel properties such as high absorption coefficient (higher than *a*-Si, much higher than crystalline-Si), band gap, low cost, thermal stability, high minority carrier diffusion length (of the order of 1 μm) [15]. Tetrahedral atomic coordination, with the four nearest neighbors of the other element and the twelve next-nearest neighbors, leads to the diamond structure in monatomic solids and zinc blende and wurtzite structures of binary compounds. The most stable crystal structure is zinc blende with unit cell dimension (a) of 6.481 Å and bond length of 2.806 Å in $F\bar{4}3m$ space group as is shown in Fig. 1.9. The natural crystal lattice of CdTe is cubic but actually it is hexagonal if viewed perpendicular to the direction of the cubic (111) axis. It appears to consist stacking planes of hexagonally packed alternative Cd and Te [21,31].

CdTe is the only stable Cd-Te compound in the Cd-Te phase diagram. This advantageous property allows the growth of near stoichiometric CdTe films [15]. In addition, a primary production advantage of CdTe, relative to other known thin film absorber layers, is that it can be deposited very fast using vacuum techniques. A variety of physical and chemical vapour deposition techniques have been used to deposit CdTe thin films such as sputtering, thermal evaporation, pulsed laser deposition, close spaced sublimation, vapour transport deposition, electrodeposition, screen printing, spray techniques [21]. However, one of the main problems in CdTe solar cell research is the achievement of a high hole density in the CdTe layer. As-grown CdTe thin films can exhibit *n*- or *p*-type electrical conductivity. CdTe is a II-VI binary compound and physical properties of this semiconducting material can be improved by doping with some other suitable materials [51]. For instance, first- principle based calculations suggest that Cu dopants can occupy the Cd atomic site in CdTe which act as an acceptor. Thus, it is possible to tune the electrical and optical properties of CdTe by Cu doping. Cu dopants in CdTe work as a donor at interstitial positions and can increase the hole-density or *p*-type conductivity of the CdTe layer [51]. Usually, Cu is added to the back contact to improve the contact properties of CdTe solar cells [31]. But high-temperature processing for the device fabrication leads to an excessive diffusion of Cu atoms into the adjacent layers and deteriorate the device performance [15]. It is also possible that excess Cu atoms may lead to an increase in the resistivity.

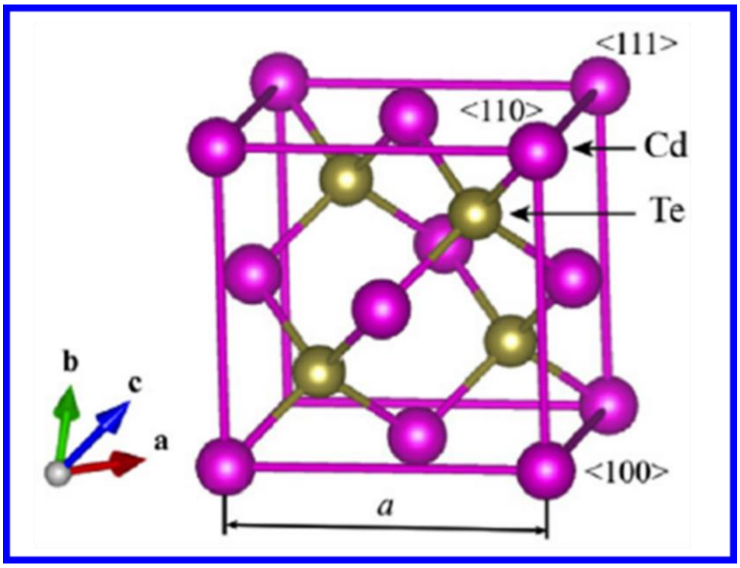

Figure 1.9: Zinc blende crystal structure of cadmium telluride.

1.5.4 Back contact for solar cell: Mo

The need of high efficiency solar cell requires a good back contact in terms of (high) reflectance and (low) resistivity. Aluminum has been used widely employed as a reflective layer with high electrical conduction. Al is one of the most abundant metals on the earth. Al has about one-third the density and stiffness of steel and is ductile. Generally, Al is found to have the face centered cubic crystal structure as is shown in Fig. 1.10(a) [52]. Al thin films show low resistivity and high reflectivity and are, thus used as back electrical contacts in solar cells [52]. On the other hand, Mo is also considered to be a suitable electrical contacts for various optoelectronic applications [52]. Most Mo-based compounds have low oxidation rate as well as low solubility in water due to its electronegativity. Mo has body-centered cubic crystal structure as is shown in Fig. 1.10(b). Mo thin films have good electrical conductivity and high thermal stability and used in fabricating electrical contacts [53]. In addition, it is also used as a back electrode in solar cells [53].

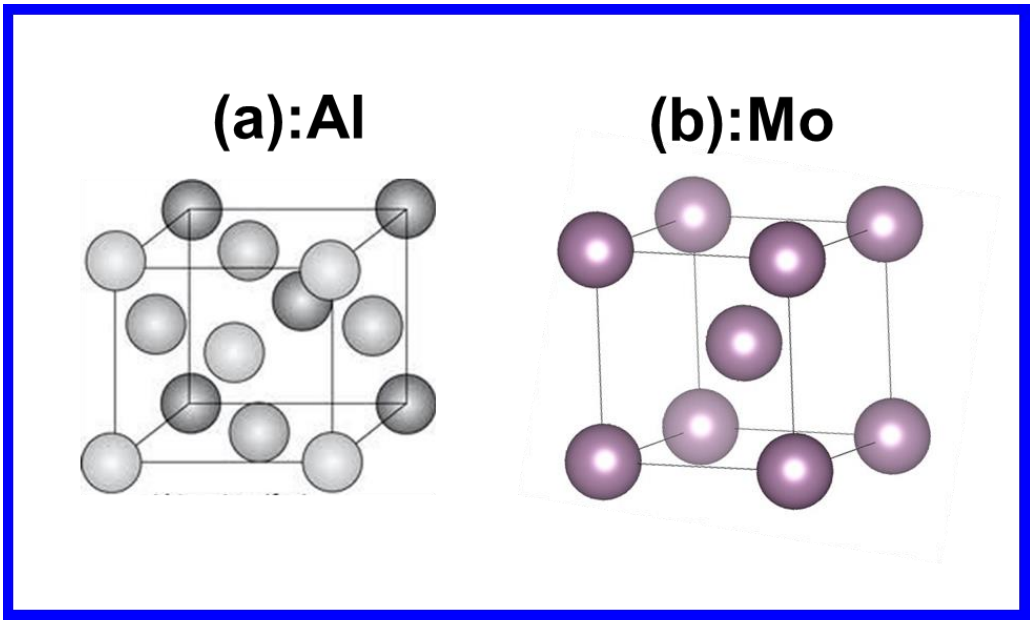

Figure 1.10: Crystal structures of Aluminum and Molybdenum [46].

1.6 Outline of the thesis

Chapter 1: In this chapter a brief review of solar cells and related issues are covered in the studies are presented. The chapter also includes basics and history of solar cells with detail literature survey along with motivation behind our study. In addition, the physical properties of all the layers (which are used in our study) are described in detail. In fact, we describe the crystal structures, optical properties, and explain the role of each used layer.

Chapter 2: This chapter deals with the experimental techniques employed for carrying out the studies presented in this thesis. To start with, it may be mentioned that in this work, all the films are grown by radio frequency (RF) magnetron sputtering technique, whereas *txt*-silicon substrates are fabricated by chemically etching. Silicon substrates are etched in a 30 wt.% NaOH solution (in H_2O) at 348±2 K for 180 s during which both the top and the rear surfaces were cleaned through the removal of 3-4 μm-thick Si from each side. Afterwards, controlled chemical etching was executed at 353±2 K for 2400 s in 3 wt.% NaOH solution in the presence of 10% IPA. In addition, the working principle of various characterization techniques deployed to evaluate the used layers, such as surface profilometer, atomic force microscopy (AFM), field-emission scanning electron microscopy (FESEM), high-resolution transmission electron microscopy (HRTEM), x-ray photoelectron spectroscopy (XPS), Rutherford backscattering spectrometry (RBS), x-ray diffraction (XRD), micro-Raman spectroscopy, ultraviolet-visible-near infrared (UV-Vis-NIR) spectroscopy, Kelvin probe force microscopy (KPFM), conductive atomic force microcopy (cAFM), electrostatic force microscopy (EFM), current-voltage (*I*-*V*), and capacitance-voltage (*C*-*V*) spectroscopies, and spectral response are also discussed.

Chapter 3: In this chapter, we demonstrate that how an optimum quality ZTO film can be deposited at room temperature, yielding high transmittance and low resistivity which are essential for a top transparent electrode in solar cells. In doing so, we show the effect of deposition angle on the structural, optical, and electrical properties of ZTO films. Following this, we explore the role of grain boundaries in local and bulk charge transport across this layer. Our experimental results are explained in the framework of oblique angle deposition process and thickness-dependent variation in grain size of ZTO films which in turn leads to charge trapping at the grain boundaries and influence the transport of carrier transport across the adjacent grains.

In addition, we demonstrate an experimental evidence of band-bending at grain boundaries of ZTO film and metal-semiconductor (i.e. ZTO) interface using Kelvin probe force microscopy and conductive atomic force microscopy. In particular, charge trapping at grain boundaries is observed through the electrostatic force microscopy measurements. The charge trapping at grain boundaries will open a new avenue to control the charge transport which corroborates well with the measured nanoscale charge transport using conductive atomic force microscopy.

Chapter 4: In this chapter, optimizing the growth of CdTe films is carried out by varying the deposition angle during RF magnetron sputtering at RT. Following this, we demonstrate the effect of growth angle on various physical properties. For instance, XRD is used to investigate the crystalline nature and structural properties of CdTe films, optical studies, e.g. reflectance and band gap are performed. In addition, we have used Kelvin probe force microscopy to show the work function of the layers.

Further, we will show how annealing temperature for Cu-doping in CdTe film can influence its physical properties such as structural, morphology, compositional, microstructural, work function, optical, and resistivity. XRD is used to investigate the crystalline nature and to evaluate the particle size, strain, and dislocation density in the films. AFM shows granular nature of the films whereas SEM and XSEM confirm the formation of tightly packed and elongated nanostructures. EDX spectrum, STEM-EDX mapping, and XPS studies rule out the presence of any impurities. We have also made use of optical absorption spectroscopy before and after annealing which shows a reduction in the band gap of CdTe:Cu films. In addition, we have used KPFM to measure the work function of the films before and after Cu-doping.

Chapter 5: This chapter provides the discussion on two processes to increase the efficiency of the PV cell. Generally, the efficiency of a solar cell can be enhanced by maximum absorption of light and separation of photo-generated charge carriers before recombination. The absorption of light can enhanced by using anti-reflection coating, graded-index surfaces, textured surfaces, etc. Here, we demonstrate the fabrication of randomly distributed pyramidal structures on Si surfaces by the help of anisotropic alkaline etching. This leads to the reduction in surface reflectance and can be brought down to 0.4% over a broad spectral range, viz. from 300-3000 nm. Further to check the efficacy of these pyramidal structures for solar cell applications and to reduce the recombination rate of photo-generated charge carriers, titanium oxide (TiO_2) thin film is grown on these textured substrates by RF sputtering. It is interesting to note that the average specular reflectance of conformally grown TiO_2 thin films on chemically prepared pyramidally *txt*-Si substrates can be brought down to ~0.2 % (in the wavelength range of 300 to 800 nm), which increases up to ~0.53 % after annealing at 673 K in air for 1 h. In addition, bulk current-voltage (*I-V*) characteristics show that the leakage current increases after annealing which corroborates well with change in the band gap. Moreover, TiO_2/Si heterojunction allows the transport of electrons but blocks the transport of holes. The present study paves the way to design hole-blocking solar cells having wide range of photo-absorption. However, in the present thesis CdTe is the main absorber layer which has a high work function (5.3 eV) in comparison to that of TiO_2 (4.7 eV) and thus, to minimize the conduction barrier height, we need a higher work function preferably in the form of a transition metal oxide such as MoO_3.

Thus, the sandwiched layer between the CdTe:Cu (absorber layer) and the ZTO (window layer) is MoO_3 which is used to block the flow of holes and we study the growth and hole-blocking behaviour of RF magnetron sputter deposited grown amorphous MoO_3 thin films. Initially, we demonstrate the role of deposition angle on the structural, physical, optical, and electrical properties of MoO_3 films. Following this we have tried to understand the charge transport across this layer. In fact, we have carried out thickness-dependent (*I-V*) measurements of MoO_3/Si heterojunction for carrier-selective contact in solar cells. Using KPFM and thickness-dependent *I-V* characteristics, we have studied the hole-blocking property as well as charge transport across MoO_3/Si heterojunctions. In particular, KPFM results show a variation in the work function at the film surface for all thicknesses. Further, thickness-dependent *I-V* characteristics depict non-ideal hole-blocking behavior. In addition, the measured barrier height is found to increase with thickness. The observed results corroborate well with the KPFM maps and the measured barrier heights. Following this, we also confirm the hole-blocking nature of MoO_3 layer for CdTe:Cu substrate.

Chapter 6: For the present studies, we have used two different metal electrodes Al and Mo to check the role of bottom electrode on the CdTe-based PV cell efficiency. For a better efficiency, the bottom electrode should have low barrier height and high optical reflectivity with high charge collection efficiency. Thus, first we have optimized the growth of Al and Mo thin films at various deposition angles by RF sputtering and studied their structural, electrical, and optical properties. It is observed that the films deposited under normal incidence exhibit the highest reflectivity (greater than 95%) and lowest resistivity (less than 10^{-7} Ω-cm) for Al whereas for Mo the highest reflectivity and lowest resistivity are ~65% and ~10^{-6} Ω-cm, respectively. Further, these films grown under normal incidence are used to fabricate the full solar cells towards having a comparative results so that the most efficient cell can be produced.

Chapter 7: Finally, we have fabricated full solar cells based on the above mentioned metal bottom electrodes and based on our experimental findings on individual layers. First, we have discussed the results on constructing full solar cells which are fabricated using Mo and Al a back contacts on *pris*-Si substrates. Theoretically, it is well known that the interface at the each layer in solar cell plays an important role in determining the efficiency. To the best of our knowledge, there is no experimental evidence on band-bending at the each interface of a multijunction solar cell. Thus, using photo-KPFM, we have measured the band-bending at the interface of each layer and photoinduced charge carrier dynamics across the heterojunctions. Finally, we have measured the efficiency of all solar cells and found that PV cells fabricated with Mo as a back contact exhibits the highest efficiency (7.05%). Based on these findings, we have demonstrated that the efficiency of the CdTe-based solar cell based on Mo electrode offers the highest efficiency (>7%). However, we observe a cell efficiency of ~8.2% by replacing the *pris*-Si substrate by a *txt*-Si substrate.

Chapter 8: In chapter 8, we provide a summary of the present thesis work which deals with the growth and characterization of different heterostructures towards constructing a highly efficient Cl-free CdTe-based hole-blocking solar cell. In doing so, we have studied the bulk and nanoscale charge transport properties across all the used layers in the present PV cell. For the optimization of grown layers, a large angular window, ranging from 0° to 87°, is used. In addition, different properties such as morphological, structural, microstructural, compositional, and electrical properties of all the different layers are critically examined. Before fabricating the full solar cells, we have optimized the growth conditions by varying thickness, growth angle, working pressure, etc. at RT for the individual layers, viz. ZnO:SnO_2, MoO_3, CdTe, Mo, and Al. After optimization, we have constructed several fully functioning CdTe:Cu based hole-blocking solar cells using different bottom electrodes (e.g. Al, Mo etc.) and measured the efficiency of these cells. To the best of our knowledge, this is the maximum achieved efficiency of the simplest CdTe-based solar cell without $CdCl_2$ vapour treatment. It further enhances the cell efficiency when the *pris*-Si substrate is replaced by a chemical etching induced textured-Si substrates.

Overall, the present thesis incorporates a variety of experimental works performed using various bulk and local probe microscopic techniques. In addition, we have summarized our studies presented in this thesis. Further, we have outlined the future scope of studies based on the present results and their importance towards a deeper understanding of the CdTe based solar cells.

References

[1] World Wildlife Fund, (2010) http://wwf.panda.org/ what_we_do/footprint/ climate_carbon_energy/energy_solutions/renewable_energy/sustainable_energy_report

[2] T. B. Johansson, H. Kelly, A. K. N. Reddy, R. Williams, T. E. Drennen, Renewable energy: sources for fuels and electricity. 1992: Washington (D.C.).

[3] M. Asif, T. Muneer, Rene. Sus. En. Rev. 11 (2007) 1388.

[4] J. Twidell, T. Weir, Renewable Energy Resources. 1986: London, UK.

[5] G. Bahgat, International Affairs 82 (2006) 961.

[6] http://www.ecology.com/2011/09/06/fossil-fuels-renewable-energy-resources/

[7] http://www.envirothonpa.org/documents/19bHydropowerAdvantagesandDisadvantages.pdf

[8] https://en.wikipedia.org/wiki/Nuclear_power

[9 T. Jackson, RE. Renewable energy sources. Background paper for the Royal Commission on Environmental Pollution, Centre for Environmental Strategy. 1998: University of Surrey, UK.

[10] https://en.wikipedia.org/wiki/Solar_cell

[11] http://www.pveducation.org/pvcdrom/solar-cell-operation/solar-cell-structure

[12] M. Buresch, Photovoltaic energy systems: design and installation. 2008: McGraw-Hill, New York, USA.

[13] P. Würfel, U. Würfel, Physics of Solar Cells: From Basic Principles to Advanced Concepts. 2009: John Wiley & Sons.

[14] R. K. Kotnala, N. P. Singh, Essentials of Solar cell. 1986: Allied Publishers Private Limited.

[15] Antonio Luque, Steven Hegedus, Handbook of Photovoltaic Science and Engineering. 2003: John Wiley & Sons.

[16] D. Chapin, C. Fuller, G. Pearson, J. Appl. Phys. 25 (1954) 676.

[17] W. Shockely, H. Queisser, J. Appl. Phys. 32 (1961) 510.

[18] H. Cotal, C. Fetzer, J. Boisvert, G. Kinsey, R. King, P. Hebert, H. Yoon, and N. Karam, Energy Environ. Sci. 2 (2009) 174.

[19] M. S. Leite, R. L. Woo, J. N. Munday, W. D. Hong, S. Mesropian, D. C. Law, and H. A. Atwater, Appl. Phys. Letts. 102 (2013) 033901.

[20] S. Kim, J.-W. Chung, H. Lee, J. Park, Y. Heo, H.-M. Lee, Sol. Ener. Mater. Sol. Cells 119 (2013) 26

[21] J. Poortmans, V. Arkhipov, Thin Films Solar cell Fabrication, Characterization, and Applications. 2006: John Wiley & Sons.

[22] T. W. Hamann, J. W. Ondersma, Energy Environ. Sci, 4 (2011) 370.

[23] https://en.wikipedia.org/wiki/Flexible_solar_cell_research

[24] http://www.nrel.gov/ncpv/

[25] A. Bosio, G. Rosa, N. Remo, Sol. Ener., XX (2018) XXX.

[26] J. L. Loferski, J. Appl. Phys. 27 (1956) 777.

[27] S. Lalitha, R. Sathyamoorthy, S. Senthilarasu, A. Subbarayan, K. Natarajan, Sol. Ener. Mater. Sol. Cells 82 (2004) 187–199.

[28] H. R. Moutinho, F. S. Hasoon, F. Abulfotuh, L. L. Kazmerski, J. Vac. Sci. Technol. A 13 (1995) 2877.

[29] https://en.wikipedia.org/wiki/Cadmium_telluride_photovoltaics

[30] http://ec.europa.eu/environment/waste/pdf/Legal%20proposal%20review%20targets.pdf.

[31] A. J. Nozik, G. Conibeer, M. C. Beard, Advanced Concept in Photovoltaics. 2014: Royal Society of Chemistry.

[32] Mohit Kumar (Ph. D. Thesis, Institute of Physics, Bhubaneswar)

[33] A. Bosio, N. Romeo, S. Mazzamuto, V. Canevari, Progress Crys. Growth and Character. Of Materials 52 (2006) 247.

[34] R. W. Crisp, M. G. Panthani, W. L. Rance, J. N. Duenow, P. A. Parilla, R. Callahan, M. S. Dabney, J. J. Berry, D. V. Talapin, J. M. Luther, ACS Nano 9 (2014) 9063.

[35] Sofie Bitter, P. Schlupp, M. Bonholzer, H. von Wenckstern, M. Grundmann, ACS Comb. Sci. 18 (2016) 188.

[36] S. F. Tseng, W. T. Hsiao, K. C. Huang, D. Chiang, M. F. Chen, C. P. Chou, Appl. Surf. Sci. 2576 (2010) 1487.

[37] R. Singh, M. Kumar, M. Saini, B. Satpati, T. Som, Appl. Sur. Sci. 258 (2018) 225.

[38] D. S. Ginley, H. Hosono, D. C. Paine, Handbook of Transparent Conductors. 2010: Springer.

[39] J. R. Bellingham, W. A. Phillips, C. J. Adkins, J. Phys.: Condens. Matter 2 (1990) 6207.

[40] R. Guo, Y. Guo, H. Duan, H. Li, H. Liu, ACS Appl. Mater. Interfaces. 9 (2017) 8271.

[41] R.D. Chandra, M. Rao, K. Zhang, R.R. Prabhakar, C. Shi, J. Zhang, S.G. Mhaisalkar, N. Mathews, ACS Appl Mater Inter. 6 (2014) 773.

[42] T. Minami, S. Takata, H. Sato, H. Sonohara, J. Vac. Sci. Technol. A Vacuum, Surfaces, Film. 13 (1995) 1095.

[43] T. Bora, M.H. Al-Hinai, A.T. Al-Hinai, J. Dutta, J. Am. Ceram. Soc. 98 (2015) 4044.

[44] M. B. Ali, F. B.-Bouaifel, H. Elhouichet, B. Sieber, A. Addad, L. Boussekey, M. Férid, R. Boukherroub, Journal of Colloid and Interface Science 457 (2015) 360.

[45] P. Ashrit, Transition Metal Oxide Thin Film-based Chromogenics and Devices. 2017: Elsevier.

[46] P. Qina, G. Fang, W. Ke, F. Cheng, Q. Zheng, J. Wan, H. Lei, X. Zhao,J. Mater. Chem. C 2 (2014) 2742.

[47] I. A. Castro, R. S. Datta, J. Z. Ou, A. C. Gomez, S. Sriram, T. Daeneke, K. Kalantar-zadeh, Adv. Mater. (2017) 1701619.

[48] T. T. P. Pham, P. H. D. Nguyen, T. T. Vo, H. H. P. Nguyen, C. L. Luu, Adv. Nat. Sci.: Nanosci. Nanotechnol. 6 (2015) 045010.

[49] P. Guha, A. Ghosh, R. Thapa, E. M. Kumar, S. Kirishwaran, R. Singh, P. V. Satyam, Nanotechnology 28 (2017) 415602.

[50] C. Battaglia, X. Yin, M. Zheng, I. D. Sharp, T. Chen, S. McDonnell, A. Azcatl, C. Carraro, B. Ma, R. Maboudian, R. M. Wallace, A. Javey, Nano Letts. 14 (2014) 967.

[51] U. V. Desnica, Prog. Cryst. Growth Charact. Mater. 36 (1998) 291.

[52] https://en.wikipedia.org/wiki/Aluminium

[53] https://en.wikipedia.org/wiki/Molybdenum

[54] https://en.wikipedia.org/wiki/Gold

CHAPTER 2

2. Experimental techniques

The experimental results presented in this thesis cover the growth of various thin films and their characterizations such as morphological, structural, compositional, optical, and electrical properties. The deposition was carried out using radio frequency (RF) magnetron sputtering technique using various deposition parameters, viz. power, working pressure, growth angle, etc. The surface morphology of the deposited films were investigated by *ex-situ* atomic force microscopy (AFM) and scanning electron microscopy (SEM). On the other hand, x-ray diffraction (XRD) and micro-Raman spectroscopy were employed to check the crystallinity and vibrational properties of the layers. Transmission electron microscopy (TEM) was used to check the microstructure, nature of the interface, and crystallinity of the films, whereas energy dispersive x-ray spectrometry (EDX) and x-ray photoelectron spectroscopy (XPS) were employed for compositional analyses. Specular reflectance, absorption, transmittance, and in turn optical band gap measurements were carried out using ultra-violet-visible (UV-Vis) spectroscopy. In addition, the bulk charge transport in the films was studied by current-voltage (*I*-*V*), capacitance-voltage (*C*-*V*), and photoresponsivity measurements. Further, nanoscale modes of AFM-based charge transport properties were also studied using various local probe microscopic techniques. In this chapter, we briefly introduce the basic principle of these experimental techniques and describe the instruments. This chapter also describes the experimental procedures employed in the sample preparation. The fabrication details of *txt*-Si will be elaborated.

2.1 Sample preparation

2.1.1 Chemically etching

Textured-silicon (*txt*-Si) is prepared by chemical etching. Prior to chemical etching, using an ultrasonicator bath, Si substrates were cleaned by trichloroethylene, isopropyl alcohol, and acetone, followed by de-ionized water (Milli-Q Gradient water purification system, Millipore) for 300 s each. Following this, Si substrates were etched in a 30 wt.% NaOH solution (in H_2O) at 348±2 K for 180 s during which both the top and the rear surfaces were cleaned through the removal of 3-4 μm thick-Si from each side. Afterwards, controlled chemical etching was executed at 353±2 K for different times starting from 30 to 2400 s in 3 wt.% NaOH solution in

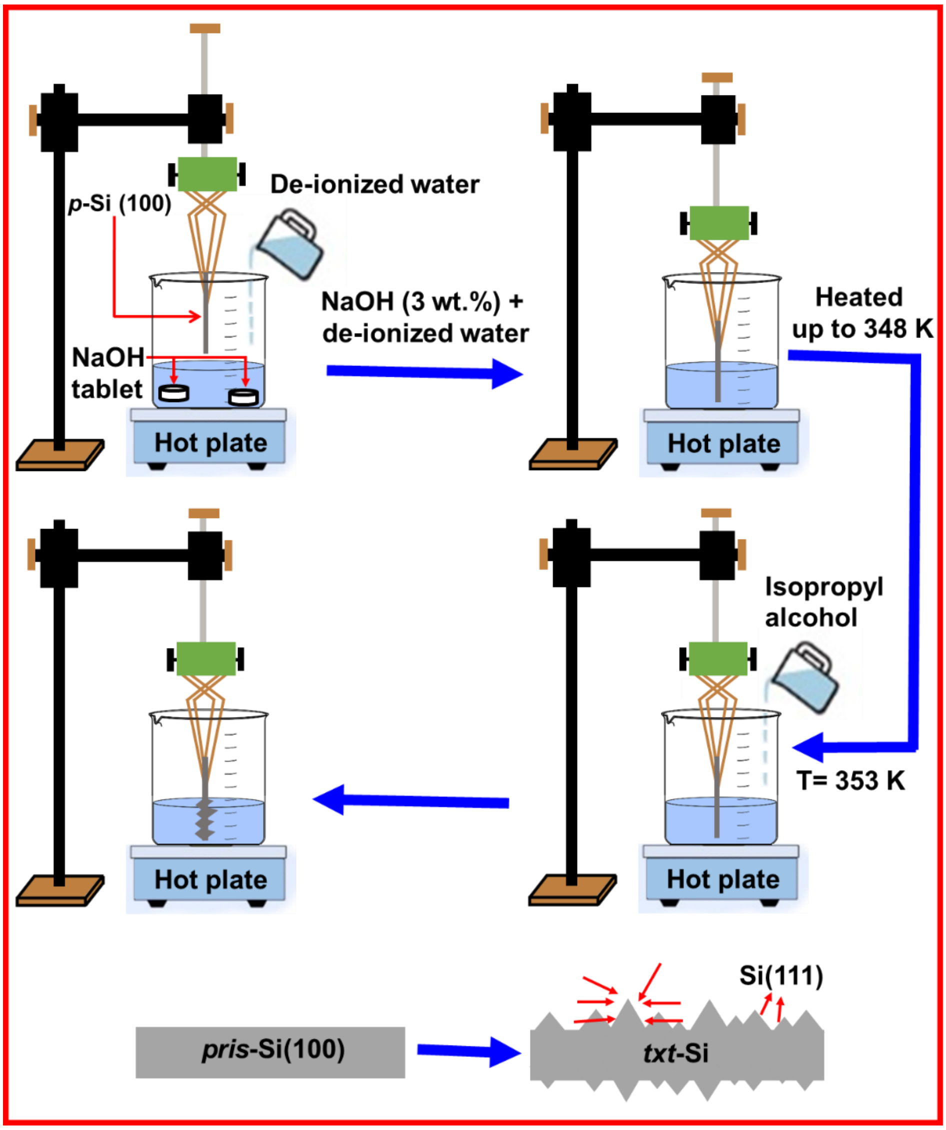

Figure 2.1: Schematic of the experimental setup used for chemical etching of Si(100) substrates.

the presence of 10% IPA. A schematic diagram of the etching setup is shown in Fig. 2.1. After completion of the chemical etching, Si substrates were further immersed in 20% HCl for 60 s followed by rinsing in de-ionized water to remove the Na residues. Finally, they were cleaned in 10% HF for 20 s to remove the native SiO_x layer and neutralize the residual chemicals which was followed by multiple washing by de-ionized water [1].

2.1.2 RF magnetron sputtering

Sputtering was first observed in a DC gas discharge tube by Grove in 1852 [2]. He discovered that the cathode surface of the discharge tube was sputtered by energetic ions in the gas discharge, and cathode materials were deposited on the inner wall of the discharge tube. Sputter deposition is a physical vapour deposition (PVD) process where atoms are sputtered from a target material by collision of gas ions and gets deposited on a sample surface [2]. During this process, a plasma is generated and positively charged ions from plasma are accelerated towards a negatively charged electrode or “target”. Upon striking the positively charged ions with target, these ions possess sufficient energy to dislodge the surface atoms of the target. The sputtered atoms which are getting ejected from the surface of the target, condense on substrate surfaces that are placed in the proximity of the magnetron sputtering cathode [3].

In addition, to enhance the efficiency of the initial ionization process a magnetron sputter deposition technique is used. Magnetron sputter deposition uses a closed magnetic field near the target to trap electrons [4]. It also allows a plasma to be generated at lower pressures which reduces both background gas incorporation in the growing film and energy loss of the sputtered atoms through gas collisions. In the early 1960’s, magnetron sputtering was reconsidered as an attractive process for thin film deposition.

Arcing is a common source of numerous issues in magnetron sputtering. In contrast to the preferred uniform glow for stable sputtering, arcs are characterized as intense, localized concentrations of plasma supported by collective emission of electrons from the sputtered surface. Multiple mechanisms promote the formation of arcs in the sputtering process [5]. Reactive sputtering of dielectrics is particularly problematic because of the formation of insulating regions that can promote severe arcing [6]. It is well established in reactive sputtering that the use of reverse-voltage pulsing can dramatically reduce arcs in even the most arc-prone reactive processes. Thus, properly chosen pulsing parameters are necessary to optimize the output, but once implemented, the result can be a significant reduction of the arc activity [6]. From the schematic (Fig. 2.2), it is seen that a main deposition chamber coupled with a load lock chamber, manipulator, and gate valve is the heart of the sputtering system. A turbo molecular pump (Varian, USA) backed by a rotary pump is used to maintain the high vacuum ($\sim 3\times10^{-7}$ mbar) condition. A small gas inlet is fixed to the main chamber (Excel Instruments, India) which is required to inject the sputtering gas into the main chamber as is shown in Fig. 2.3. In general, a sample manipulator is required to align the substrate position at different growth angles with respect to the incoming incident flux. This enables us to deposit films at different oblique angles other than the normal incidence. Different important parts of the setup are shown in Fig. 2.2. The pulsed DC/RF magnetron sputtering setup (Fig. 2.3) has a spherical vacuum chamber.

A 2 inch diameter target can be used for the present setup. A continuous chilled-water flow is ensured to maintain the temperature of the sputtering target holder below 20˚C. Different films, used in the present thesis, are prepared using the present setup (Fig. 2.3) at room temperature (RT).

The substrates were mounted on the top of the rotating substrate holder kept at a distance of 80 mm from the target. This substrate holder is equipped with a glancing angle deposition (GLAD) attachment. Prior to sputtering, a base vacuum of $\leq 3\times10^{-7}$ mbar was achieved. Ultra-pure (99.999%) Ar gas is injected into the chamber at a flow rate of 30/40 sccm (standard cubic centimetres per minute) until it reaches a working pressure of 5×10^{-3} mbar. In order to generate

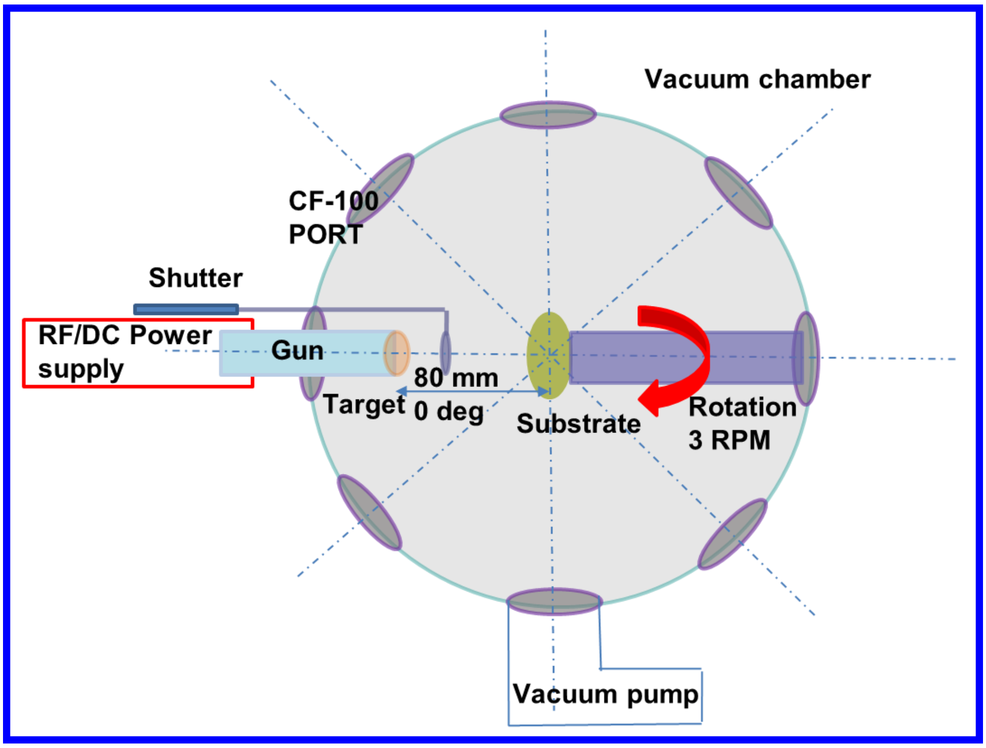

Figure 2.2: A schematic diagram of a DC/RF magnetron sputtering process.

the plasma of Ar gas, an RF power of 100 W (Cesar, Advanced energy, USA) was supplied to the targets [7]. In addition, prior to each deposition, pre-sputtering for a time duration of 10 min was carried out to remove the contaminations and trapped impurities from the surface of the target. In this setup the substrate is generally rotated at a speed of 3 rpm to achieve a uniform film thickness and during this process, a movable shutter is used to protect the substrate from getting contaminated.

2.2 Thickness profilometer

Surface profilometry is one of the most common techniques to measure the film thickness. A stylus/probe is a small tool similar to a modern ball point pen which is used to measure the thickness. In a surface profilometer, to measure the vertical displacement corresponding to the studied feature a diamond stylus moves across the surface. This process involves some mechanical and electronic devices in order to perform the measurement [8]. For film thickness measurement, the sample is mounted on a stage which can move in both X- and Y- directions.

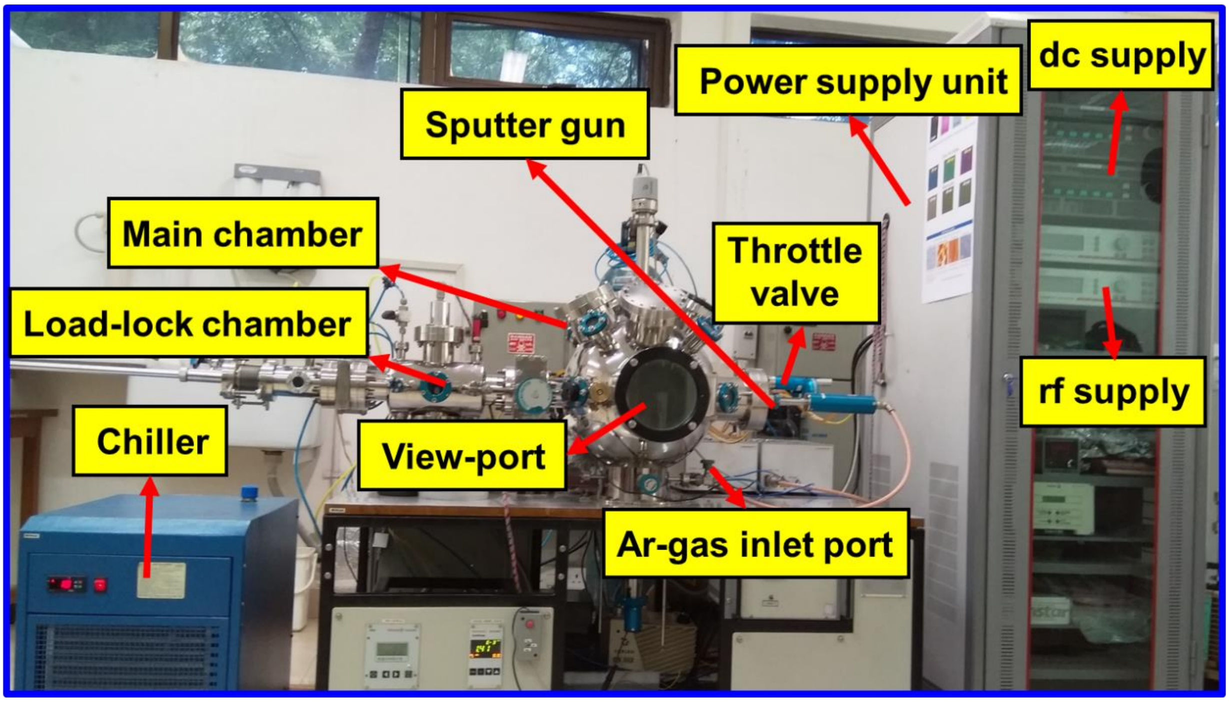

Figure 2.3: A digital photograph of pulsed DC/RF magnetron sputtering set up at SUNAG laboratory.

On the other hand, the measurement of the height or Z-axis is done by the stylus in contact with the surface. The stylus is situated at the end of a cantilever arm. The opposite end of the cantilever is counter-balanced by a weight that is mounted in a screw system actuated by a motor; the motor can move the counter-weight closer or further according to the loaded force from the pivoting centre of the cantilever, regulating the pressure of the tip. The cantilever moves along the Z- direction (up/down) by dragging the stylus over the surface and the force that the stylus impinges over the sample is controlled by the counter-weight system. Finally, the linear Z displacement is converted into an electric signal and processed by software.

Thickness measurement of all the deposited films, used in this thesis work, was carried out by using a surface profilometer (Ambios XP-200, USA) and image of the setup is depicted in Fig. 2.4. The stylus is located in an acoustic isolation hood to reduce vibrational noise during scanning and placed on a large vibration damped sandstone stage. The vertical or Z- direction movement range of the profilometer is 400 μm and its vertical resolution is 0.1 nm at a 10 μm scan length, 1.5 nm at 100 μm scan length, and 6.2 nm at 400 μm scan length [9]. The XP-200 profilometer's stylus is diamond coated one and has a tip radius of 2.0 ± 0.1 μm with an adjustable force range between 0.05–10 mg.

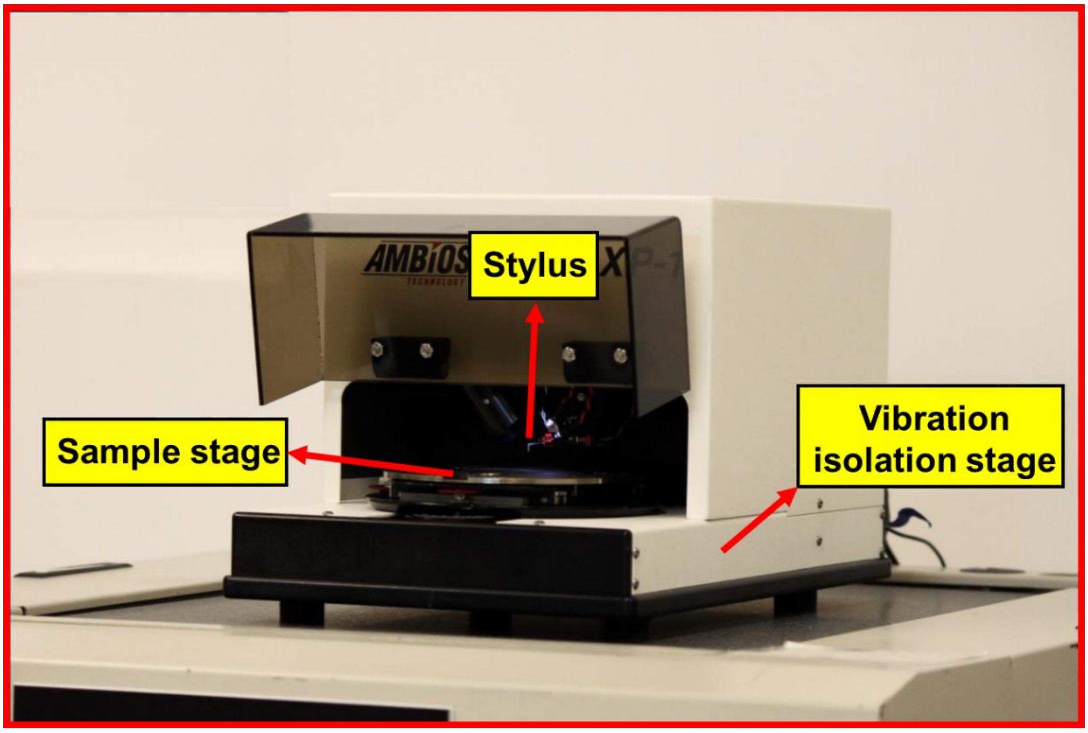

Figure 2.4: A picture of the surface profilometer at the SUNAG Laboratory.

The surface profilometer XP-200 can also calculate surface roughness, waviness, and perform stress analysis on thin films [10]. The film thickness is measured with respect to the substrate which is partially masked prior to the film growth.

2.3 Atomic force microscopy (AFM)

The invention of scanning tunnelling microscopy (STM) by Binning and Rohrer in 1981, triggered a tremendous development of scanning probe microscopy (SPM) techniques [11]. SPM has a family of techniques for studying surface morphology and various nanoscale physical properties [12]. The basic principle that all SPMs have in common involves a sharp probe which is moved mechanically over the surface and records the probe-surface interaction as a function of position [13]. This interaction can be manifested in different forms, e.g. tunnelling current, inter-atomic, magnetic, electrical, and frictional force, etc. which actually decides the required mode of microscopy [13]. The most important among the SPM based techniques is the atomic force microscope (AFM) [13]. AFM was invented in 1985 by Binning, Quate, and Gerber which is based on the measurements of different forces (e.g. attractive, repulsive, magnetic, electrostatic, van der Waals) between a sharp probe and sample surface [14]. AFM is applicable to all types of materials, viz. insulators, semiconductors, conductors as well as polymers. This technique measures nanoscale variation in the surface topography by measuring the deflection of a tip (10-30 nm in diameter) attached to the end of a cantilever, as the tip is brought to a close proximity of the surface to be probed.

Figure 2.5 depicts a schematic diagram on the working principle of an AFM setup. Here, a laser beam is focused on the tip of a highly reflective cantilever head such that the laser beam is reflected onto the surface of a position-sensitive photodetector and provides maximum signal in it. Piezoelectric scanner made of lead zirconium titanate (PZT) helps to scan the sample surface via a tip/probe. As the tip scans the sample surface, a feedback loop is used to maintain either a constant deflection (contact mode) or oscillatory amplitude (tapping mode) of the cantilever. The force between the tip and the sample during scanning is the inter-atomic van der Waals force. The dependence of this van der Waals force upon the distance between the tip

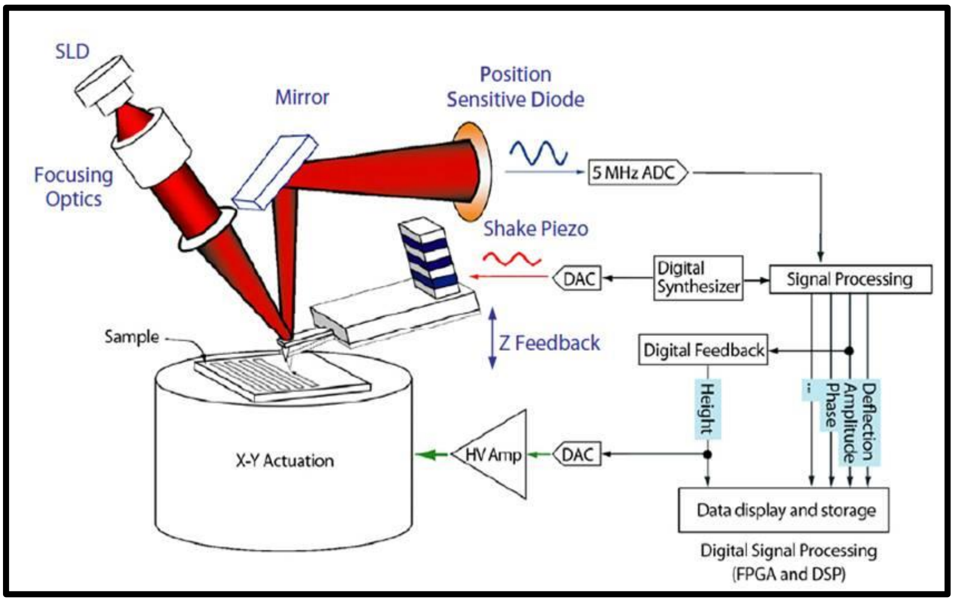

Figure 2.5: Schematic diagram of an AFM setup [12].

and the sample can be described by force-distance curve, as is shown in Fig. 2.6 where three regimes of tip-surface distance are labelled: the contact regime, the non-contact regime, and the tapping regime. At large tip-surface distance, there is no interaction and the observed force is zero. When the tip moves towards the sample it jumps into contact due to attractive van der Waals interaction and the tip moves further towards the sample and the total force acting on the cantilever becomes repulsive. When the tip retracts again, the force is reduced and the net force acting on the cantilever becomes attractive. Thus, based on this tip-surface interaction or force between the tip and the sample, AFM is known to operate in three different modes: contact or repulsive, non-contact or attractive, and tapping or intermediate mode.

AFM System and measurements: All AFM images in this thesis were acquired with the help of an AFM setup from Asylum Research, USA (Model: MFP-3D), in different modes according to requirement. The resonant frequency of the cantilevers used for tapping mode is 300 kHz and the spring constant is 42 N m^{-1}. On the other hand, a conductive tip (AC240 TM, Electric-lever, Olympus) having a radius of curvature of ~30 nm, a stiffness of ~2 N m^{-1}, and a resonance frequency of ~70 kHz was used for the electrical measurements. Special attention

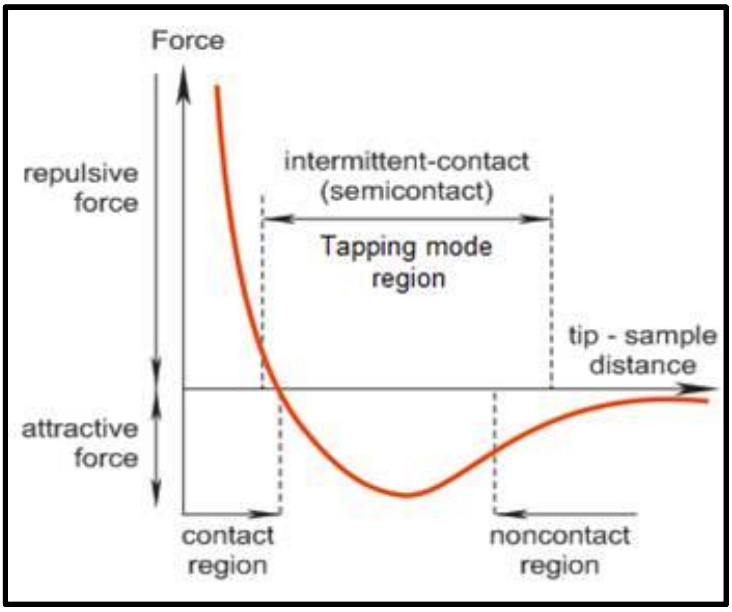

Figure 2.6: van der Waals force as a function of tip-to-surface distance [12,13].

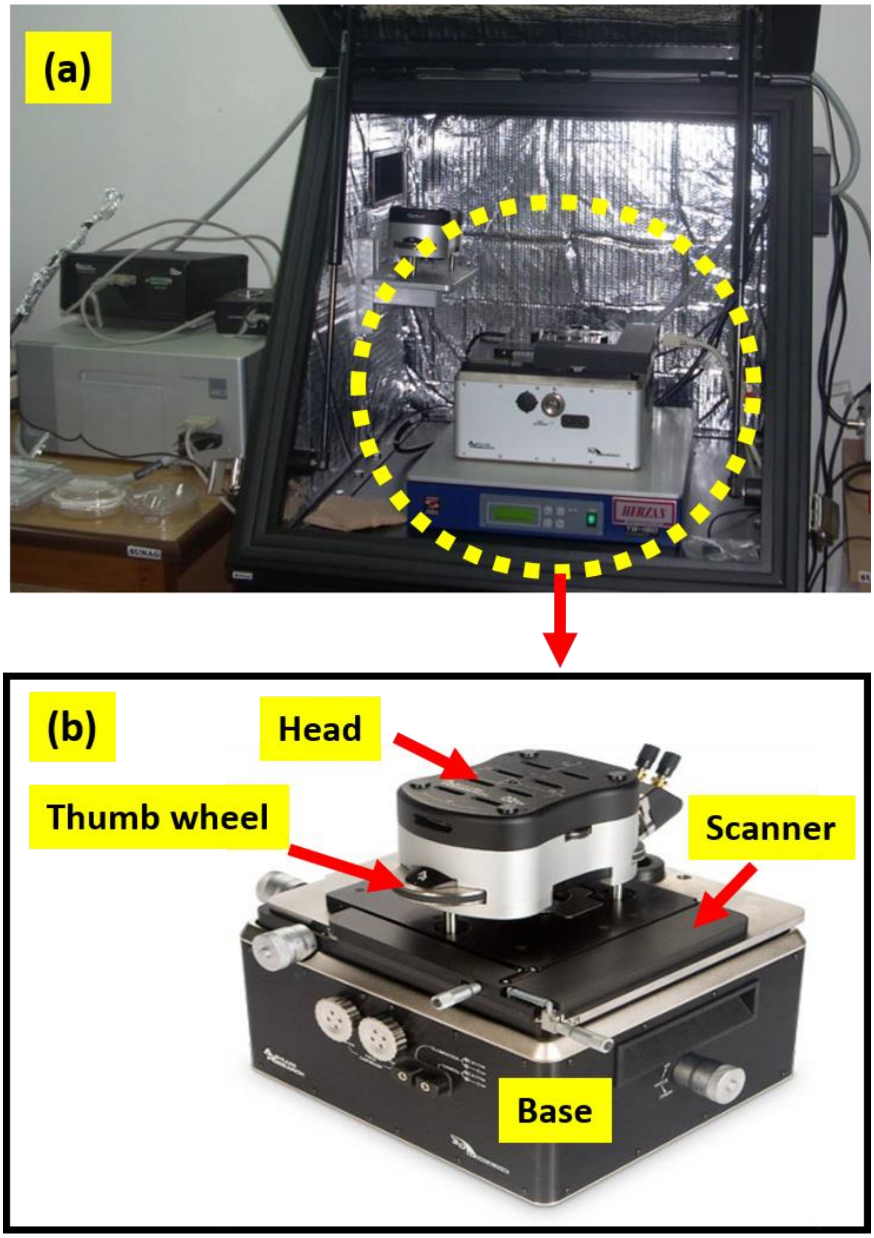

Figure 2.7: (a) AFM set up and (b) shows the various parts of the AFM.

was given to prevent artefacts in the measurements. Among many advantages of this setup, an important one is its large area-high precision facility because of which we can scan areas up to 90×90 μm^2 with very high accuracy. Figure 2.7(a) shows different parts of the present AFM setup. A zoomed image of the main part of this AFM setup is also shown in Fig. 2.7(b) which shows the scanner, head, base, and thumbwheel. Initially, the head is used to manually bring the tip near the surface. In the next stage, close approach to the surface (separation between the tip and sample remains 80 nm) is controlled by the software to prevent the damage in the tip.

A XY-motorized sample stage, attached with the AFM, helps in precise positioning of a sample and checking large scale uniformity in surface morphology within a precision of 500 μm. In addition, a low humidity environment has always maintained surrounding the AFM system. For AFM image processing, WSxM [15], Gwyddion [16], and SPIP [17] softwares were used. The SPIP (Scanning Probe Image Processor) software package has specialized tools for correcting and analyzing SPM data.

2.3.1 Contact and non-contact modes

Contact or repulsive mode: Contact mode was the first mode developed for AFM. It is the simplest mode conceptually and was the basis for the development of other AFM modes. Therefore, understanding contact mode helps to understand the working principle of other modes. In contact-AFM mode, also known as repulsive mode (due to the repulsive nature of the force in this regime), an AFM tip makes soft 'physical contact' with the sample by bringing the tip very close to a surface (a few angstroms) [14]. The tip is attached to the end of a cantilever with a low spring constant. As the scanner gently traces the tip across the sample (or the sample under the tip), the contact force causes the cantilever to bend to accommodate changes in the topography. This mode is usually used for hard crystalline surface because in the case of weakly absorbed samples, or sort, easily deformed samples. This can lead to problems of sample distortion, damage, or even removal from the substrate surface [14].

Non-contact mode or attractive mode: Non-contact mode AFM is one of several vibrating cantilever techniques in which an AFM cantilever vibrates near the surface of the sample keeping the tip-to-surface distance in the range of tens to hundreds of angstroms [14]. Therefore, non-contact mode is carried out in the attractive regime as shown in Fig. 2.7. The major advantage of the non-contact mode AFM is its truly non-invasive character.

2.3.2 Tapping or intermediate mode

Tapping mode: This mode is also known as intermittent-contact mode [11,14]. In this case the vibrating cantilever is brought closer to the sample surface so that it just barely hits or ‘taps’ the sample. This mode is a compromise between the contact and the non-contact mode where the cantilever is made to oscillate with or near to the resonant frequency using an additional piezoelectric element so that the tip remains very close to the sample for a short time and then goes far away for a short time. When the oscillating probe approaches the sample surface, the cantilever oscillation changes due to the interaction between the probe and the force field from the sample. As a result, there is damping of the cantilever oscillation, which leads to a reduction in the frequency and amplitude of the oscillation. The cantilever oscillation is monitored by the force transducer (i.e. by the optical lever), and the scanner adjusts the Z height via a feedback loop to maintain the probe at a fixed distance from the sample, just like it is done in the case of contact-mode AFM. The reduction in the amplitude of oscillation is used to identify and measure the surface features. This mode allows one to scan soft adsorbates on a substrate with a better resolution than in the non-contact mode but with a small interaction (and consequently less modification of the samples) between the tip and adsorbate as is done in the case of non-contact mode AFM. Thus, the tapping mode overcomes certain problems associated with conventional AFM scanning method, viz. friction, adhesion, electrostatic forces, etc. [12].

2.3.3 Conductive atomic force microscopy (cAFM)

Conductive atomic force microscopy (cAFM) is most powerful current sensing technique that can simultaneously map the topography and current distribution on a sample surface [18]. In fact, it can be used for electrical characterization of conductivity variations at nanoscale even in low conductive samples. cAFM allows to measure the current in the range of few picoamps (pA) to tens of nanoamps (nA) [19]. It is useful for characterization of a wide variety of materials including thin dielectric films, ferroelectric films, nanotubes, conductive polymers, and others [19].

The present cAFM system has an ORCA module to measure the current map that consists of a specially-designed cantilever holder and includes a transimpedance amplifier. The gain of the amplifier can be chosen by the user while the standard values range from 5×10^7 to 5×10^9 V A^{-1}. A conductive AFM tip/probe is used to measure the current map with the help of the cantilever holder. This technique is combined with the contact mode AFM imaging for measuring the localized conductivity of a sample. All cAFM images used in this thesis were acquired using the contact mode with a Pt-Ir coated Electri-Lever tip (AC240TM), having a tip radius of 15 nm with a nominal spring constant of 1-2 N m^{-1} and good wear characteristics.

In addition, this system is equipped with nanopositioning closed loop sensors (NPS™) which make it possible to reproduce the position of the cantilever at a point of interest [19]. The tip is positioned in the centre of the using the MFP-3D's "pick a point" force curve interface and one can measure the *I-V* characteristics at any chosen points at nanoscale. In fact, the ORCA conductive AFM option for the MFP-3D provides low-noise, flexible transport measurements at the nanoscale. Further, the flexible software environment enables a variety of standard measurements to be made, as well as allowing the researcher to define their own experiments.

2.3.4 Kelvin probe force microscopy (KPFM)

Kelvin probe force microscopy (KPFM) is a scanning probe microscopy technique which enables in nanoscale imaging of potential difference between the tip and the sample of a material with nanometer scale resolution [20]. The name "Kelvin probe force microscope" originates from the macroscopic method developed by Lord Kelvin in 1898 using a vibrating parallel plate capacitor arrangement, where a voltage applied to one vibrating plate was controlled such that no current was induced by the vibration [21]. Therefore, in KPFM the electrostatic force is used. With the steadily increasing variety of applications and materials being investigated, the increasing trend of research performed applying this techniques is foreseen to continue. In general, the data collected from a sample will represent a combination of three contributing factors: the difference in work function, trapped charge, and any permanent or applied voltage between the tip and the sample. It is based on the non-contact AFM and minimizes the electrostatic interaction between the scanning tip and the surface. The technique relies on an AC bias applied to the tip to produce an electric force on the cantilever that is proportional to the potential difference between the tip and the sample [21]. In this mode, the tip is moved at a lift height (>40 nm) and thus, there is no mechanically induce drive. In fact, the only oscillations that the probe will have is going to induced by an applied AC bias. An AC bias applied between the tip and the sample produces an electrostatic force between them. If they are considered as a parallel plate capacitor (C), then the force between the two plates is proportional to the square of the applied voltage (V):

$$F = -\frac{1}{2}\frac{\partial C}{\partial Z}V^2. \tag{2.1}$$

The magnetic forces are only relevant if the top/or sample material are magnetic. Generally, for KPFM this is not the case and therefore, these forces will not be considered here. However, instead of the current as the controlling parameter, the electrostatic force is used. The total potential difference between the probe and the sample is the sum of the applied AC bias (V_{ac}), the potential difference we are trying to measure (V_{sp}), and any DC bias we wish to apply (V_{dc}).

$$V = V_{sp} + V_{dc} + V_{ac}\sin(\omega t), \tag{2.2}$$

where ω is the angular frequency of the applied ac signal. If we substitute this into Eq. 2.1 and do some rearrangements, we get the following [21, 22]:

$$F = -\frac{1}{2}\frac{\partial C}{\partial z}\left([(V_{dc} - V_{sp}) + \frac{1}{2}V_{ac}^2] + 2[(V_{dc} - V_{sp})V_{ac}\sin(\omega t)] - [\frac{1}{2}V_{ac}^2\cos(2\omega t)]\right). \tag{2.3}$$

Note that there are three force terms which are summed together: The first force is the static one which has no frequency dependence, the second occurs at the ac signal drive frequency, while the third force oscillates at twice the drive frequency. The most important term here, as far as the surface potential is concerned, is the second one since it depends not on the square of the voltage but rather on the potential difference between the tip and the sample and is multiplied by the magnitude of the applied AC voltage. This means that if there is a potential difference between the tip and the sample, then when an AC bias is applied, there will be an oscillatory force at the frequency of the drive and it will be proportional to the magnitude of the applied bias and to the potential difference. In addition, $\frac{\partial C}{\partial z}$ is the capacitance gradient of the tip-sample system and the SP is the difference in work function between sample and tip:

$$V_{SP} = \frac{\Delta\phi}{e} = \frac{(\phi_{sample} - \phi_{tip})}{e}, \tag{2.4}$$

where e is the elementary charge. The probes used for KPFM measurements are generally conductive or heavily-doped semiconductors. Insulating tips/probes do not work on the MFP-3D, as the bias is applied to the tip. To implement this technique on an MFP-3D setup, a two pass technique is used where the first pass is used to determine the topography of the surface (and is done exactly like a standard tapping mode scan line), whereas the second one is used to find the surface potential and the tip is raised above the surface. To do this, a technique called '*nap*^{TM} *mode'* is implemented. During a nap scan, the tip is raised over the surface on a point-by-point basis, while the potential feedback loop is implemented.

One issue that influences the interpretation of results of KPFM measurements is the physical limitations of their lateral resolution. This is very important as the physical size of electronic devices become smaller and smaller. Following this, one of the basic and an important structure is *p-n* junction. The predicated built-in potential across the junction can be measured using KPFM technique and in turn band-bending at the interface can be directly probed.

2.3.5 Electrostatic force microscopy (EFM)

Electrostatic force microscopy (EFM) measures the electrostatic force gradient between the AFM tip and a sample surface [23]. It is a tapping mode technique which works in dual pass mode using a conductive probe and an applied tip-sample bias. In the first pass, after measuring the topography, the probe retraces each line at a fixed distance (typically 50 nm) above the surface ("*nap mode*") in the second pass. During this *nap mode* pass, the cantilever is still driven mechanically with the tapping piezo, while the electrostatic force between the tip and the sample surface shifts the resonance frequency of the probe, resulting in a change in both the amplitude and phase of the cantilever. This can either be directly probed or by applying a phase lock loop (PLL) in order to track the resonance frequency. EFM is very useful for measuring conductors embedded near the surface in insulating and semiconducting materials [23]. It can also be used to measure variations in gradient of the capacitance between the tip and the sample.

2.4 Scanning electron microscopy (SEM)

The electron microscopes are meant for high resolution imaging. A scanning electron microscope (SEM) is a microscope that uses electrons instead of light to form an image. In SEM, a tightly focused electron beam is scanned over the sample surface in vacuum [24-26]. The novelty of SEM lies in its capability of producing 10-1,00,000 times magnified image of surface features of length scale starting from µm down to nm scale in two dimensions. For SEM measurements, the sample needs to be conducting to prevent charging of the sample surface during scanning. In case of non-conducting samples, a very thin metal (normally gold) layer is coated over the sample surface or special beam conditions are applied such as low beam energy or high beam spot size and special detectors are used to prevent only the surface charging. In a typical SEM, an energetic beam of electrons interacts with substrate and transfer its kinetic energy to the electrons present in the sample. As a result, energetic electrons undergo a series of elastic and inelastic scattering events inside the sample which generate different signals like emission of secondary electrons, backscattering of electrons, production of characteristic x-rays, etc. In the standard imaging mode the secondary electrons are used. Secondary electrons produce topographic contrast with high resolution and large depth of field.

The secondary electron depends strongly on the electron beam energy; at lower energies, they are generated closer to the surface and thus, they have a higher escape possibility.

Figure 2.8: Scanning electron microscopy setup used in this thesis.

At higher electron beam energies, the number of secondary electrons increases but they are excited deeper in the specimen. The secondary electron yield depends also on the surface gradient and increases with the increasing tilt angle. Thus, more secondary electrons are produced from the tilted regions of the specimen. The electrons, ejected through these phenomena are collected by a special detector connected to the system and this provides an important mechanism for the surface topographic imaging.

A scanning electron microscope (Fig. 2.8) contains an electron column containing an electron gun and a demagnification system which consists of electromagnetic lenses to focus the electrons from the electron gun to a nm size spot on the sample mounted in the sample chamber below the electron column. Mainly, two types of electron gun are used; viz. thermionic- and field emission-electron gun. In a typical thermionic electron gun, electrical heating of the filament induces the emission of electron from the filament. However, the low thermal drifting during the measurement, relatively low brightness, and a high temperature requirement for electrons hinder the use of thermionic electron gun. On the other hand, field electron emission gun in SEM yields high spatial resolution with bright contrast and low electrostatic distortion, small spot diameter, and coherent emission. Detectors for electrons and x-rays emitted from the sample are also equipped inside the sample chamber and a computer interface is coupled with the detectors for displaying the image. In a field emission gun, the cathode is a very sharp tungsten tip attached to a hairpin-shaped tungsten wire. A high voltage bias applied on the cathode causes the development of an intense electric field around the tip, which results in electron emission from the sharp tip. The source size of the electron beam can be of the order of 20 nm in a field emission gun, offering a better resolution in SEM. For the studies presented in this thesis, a GEMINI Carl Zeiss SEM was used for morphological imaging [27]. The SEM works with a probe current up to 100 nA at 0.2 to 30 kV acceleration voltages. For imaging, the chamber was maintained at a vacuum range between 5×10^{-6} to 5×10^{-7} mbar, whereas the base pressure was always maintained around 2×10^{-9} mbar for the gun chamber.

2.5 Transmission electron microscopy (TEM)

TEM is used to study microstructure, layer thickness, crystalline nature, distance between atomic planes (*d*-spacing), and defects in materials [28, 29]. The ideal thickness of the sample may be of the order of 100 nm or even less [29] which transmits electrons and leads to the formation of an image/diffraction pattern. In order to obtain selected area electron diffraction (SAED) pattern of the sample, an aperture is placed around the selected area of the specimen above the intermediate lens, whereas for conventional imaging, the SAED aperture is replaced by an objective aperture. The configuration of a TEM is shown schematically in Fig. 2.9. The electron gun with a LaB_6 crystal filament is commonly used in TEMs which produces a stream of energetic electrons [29]. The sample to be examined is placed at the object plane of the objective lens of the TEM. To obtain a well resolved image on the phosphor screen, the sample is required to be electron-transparent. The transmitted portion of the electron beam is focused by the objective lens. An electron diffraction pattern of the sample area is formed at the focal plane of the objective lens, as is indicated in Fig. 2.9. The electron diffraction pattern or the image formed at the image plane is magnified on the viewing screen by intermediate and the projector lens assembly. In diffraction mode, the first intermediate lens is adjusted in such a way that the back focal plane of the objective lens becomes the object plane of the first intermediate lens. In this case, an electron diffraction pattern is seen on the viewing screen which consists of a bright central spot on the optic axis and spots due to the diffracted electrons. An area of interest on the specimen can be selected from the sample image formed on the first image plane by the selected area aperture. This selected area acts as a virtual source for the intermediate lens assembly so that only electron diffraction from this area can be observed in the viewing screen and is known as selected area electron diffraction [30]. To obtain an image of the sample, the first intermediate lens is adjusted so that the first image plane becomes its object plane. If the central spot on the optic axis is chosen for imaging by the objective aperture then the TEM image is called a bright field image, whereas if any other diffraction spot is chosen for imaging then the image is called a dark field image. In this thesis, TEM measurements were carried out using a field emission gun based 300 keV FEI Tecnai G2 S-Twin machine with LaB_6 thermionic emission based electron source. TEM column was kept at high vacuum ~10^{-8} mbar in order to get a collimated electron beam. The images were recorded in a charge-coupled device (CCD) based detector with 40 ms time resolution and having 4008 × 2672 pixels (Model 832, Orius CCD detector, Gatan). The pole piece of objective lens has an ultra-high resolution with a spherical aberration coefficient of 0.5 mm which allows achieving point-to-point resolution of 0.194 nm.

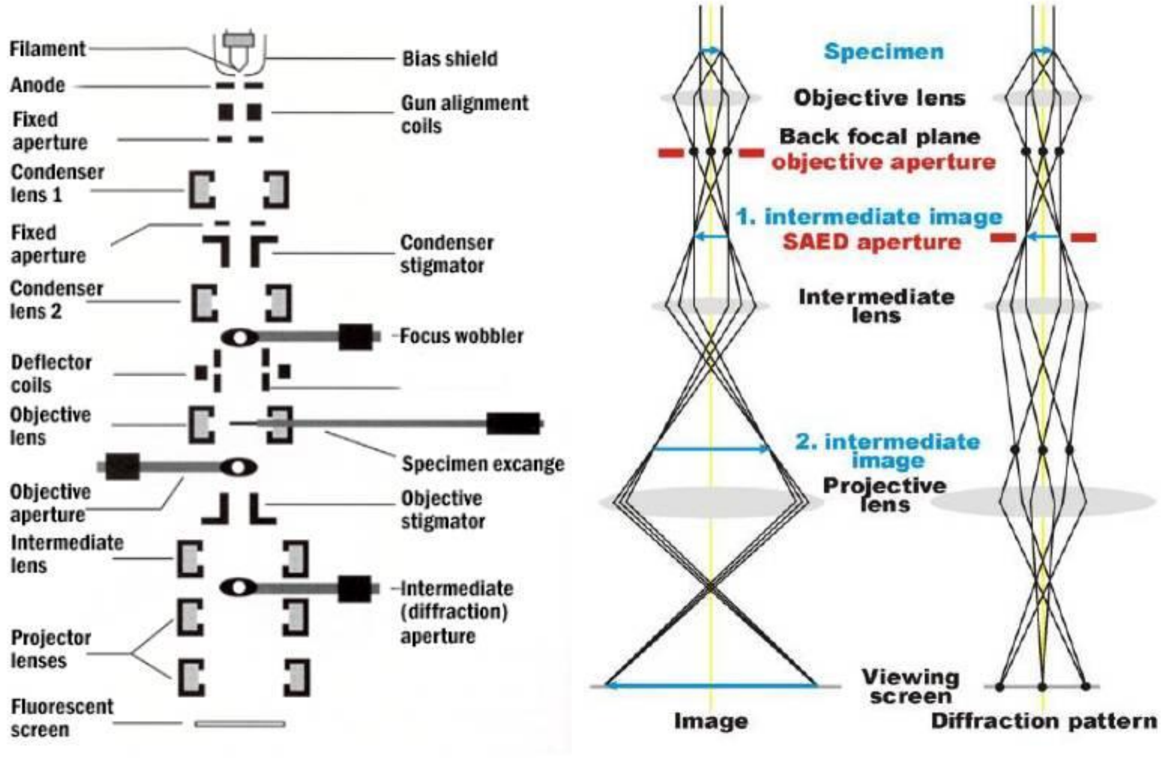

Figure 2.9: Schematic diagram of TEM parts, image formation, and diffraction pattern formation process [28].

2.6 X-ray diffraction (XRD)

X-ray, being an electromagnetic radiation, undergoes the phenomenon of diffraction, as is observed for visible light. However, unlike visible light, x-rays cannot be diffracted by ordinary optical grating because of their very short wavelengths. The phenomenon of x-ray diffraction (XRD) is employed to determine the nature of crystallinity, presence of strain, average particle size, and phase identification of materials [31]. Since all the atoms in a single crystal are regularly arranged with interatomic spacing of the order of a few angstroms, a crystal can act as a three-dimensional natural grating for x-rays. Interestingly, the wavelength of x-rays (1-10 nm) are similar in size to interatomic spacing of materials and thus the waves diffract and scatter upon falling on them. The scattered waves contain information of the atoms and their arrangement in a material.

When a target is exposed to a beam of monochromatic x-rays, atomic electrons start vibrating with a frequency equal to that of the incident beam. Since an accelerating charge emits radiations, the vibrating electrons become a source of secondary radiation having the same frequency as the incident x-ray. This phenomenon may also be regarded as the scattering of x-rays by atomic electrons. If the wavelength of the incident radiation is quite large compared to the atomic dimension, the radiation emitted by electrons should be in phase with each other. However, the incident x-rays have the same order of wavelength as that of the atomic dimensions. Hence, the radiations emitted by electrons are out of phase with each another. Therefore, these radiations undergo constructive and destructive interferences and this condition of interference is defined by Bragg's law (Fig. 2.10) [32]:

$$2d\sin\theta = n\lambda, \tag{2.5}$$

where θ is half the angle between the diffracted beam and the original beam direction, λ is the wavelength of the x-rays, and d is the inter-planar spacing between the planes that cause constructive reinforcement of the beam. The reflections take place for those values of d, θ, and λ which satisfy the above Eq. The average crystallite size is given by the Scherrer's formula [33]:

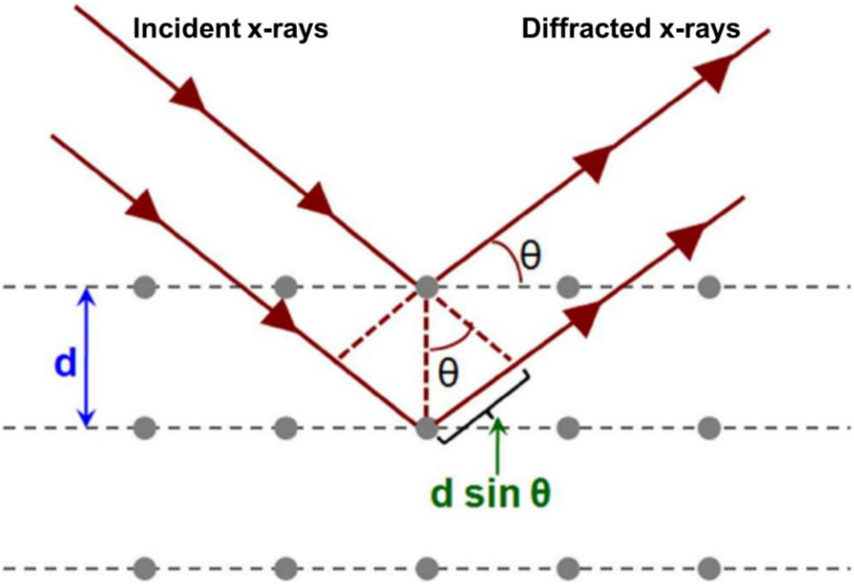

Figure 2.10: Schematic diagram of Bragg's reflection.

$$D = \frac{k\lambda}{\beta \cos\theta}, \tag{2.6}$$

where D is the average crystallite size, β is the FWHM of the diffraction peak, and k=0.9 has been chosen according to the literature [33]. Additionally, the relative strain in polycrystalline materials can be measured – based on the shift in the central location of the reflection peak.

A Bruker D8 Discover diffractometer (Fig. 2.11) with Cu-K_α radiation source has been used for the studies presented in this thesis. The x-ray source is operated at a voltage of 40 kV and a current of 40 mA. A Göbel mirror attachment is used to produce a parallel beam of x-rays, whereas single bounce Ge (220) monochromator is used for high-resolution measurements.

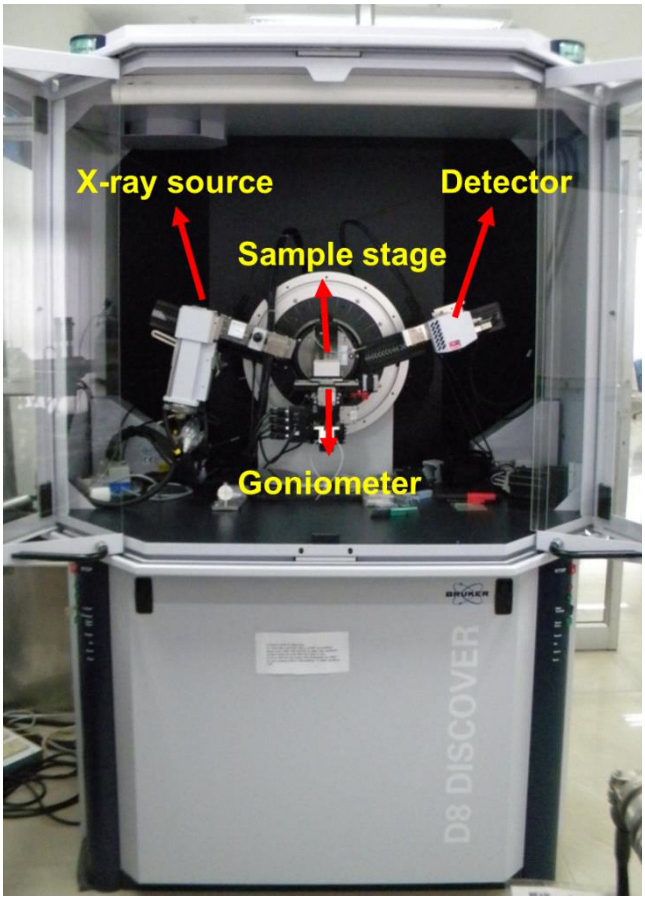

Figure 2.11: XRD setup used in this thesis work.

2.7 Compositional analysis

Energy dispersive x-ray spectroscopy and x-ray photoelectron spectroscopy are used for the compositional analysis of the samples. Generally, photons with energies of up to 10 KeV interact with atomic electrons. The photoelectric process is a direct signature of the photon interaction with the atoms and is the basis of photoelectron spectroscopy. In materials analysis, the photon energy range extends from 10 eV, close to binding energy of the electron in the hydrogen atom (13.6 eV), to energies of 100 KeV. At these energies, photons can penetrate within the solid and interact with the inner-shell electrons. The basic principles and a brief description of these two techniques are presented in the following paragraphs.

2.7.1 Energy dispersive x-ray spectrometry

Energy dispersive x-ray (EDX) spectrometry is an analytical technique used for the elemental analysis or chemical characterization of a sample [34, 35]. In EDX measurements, characteristic x-rays are emitted from a material due to the interaction of energetic electron beam which are used to identify the elements present in the material and their relative amounts. All elements from atomic number 4 (Be) to 92 (U) can be detected in principle, albeit all instruments are not equipped for 'light' elements ($Z<10$) [35]. During interaction, an incident electron gets inelastically scattered and knocks out a core electron from the atom. An electron from a higher orbital fills the empty state (hole) in lower (core) orbital. The characteristic x-rays are results of electronic transitions from the outer to the inner orbits. The energy difference between two such orbitals is released in the form of photons (when the core level electron of high enough atomic number is knocked out, the emitted photons have energy in the x-ray regime), whose energy is characterized for the transition in the respective target atom by following the Mosley's law [34]:

$$\sqrt{v} = a\,(Z-b)\,, \tag{2.7}$$

where v is the characteristic x-ray frequency, a and b are constants, and Z is the atomic number(s) of the target atom(s). The emitted x-rays are detected by a spectrally resolved (the number of counts in a given energy width of typically few eV/channel) appropriate energy dispersive detector like Si(Li) or SDD (Si drifted detector).When an incident x-ray photon strikes the detector crystal, its energy is absorbed by electrons in the valence band of the semiconductor and electrons are raised in the conduction band, creating holes in the valence band. A high bias voltage at the front and back face of the detector sweeps these electrons and holes producing a charge signal. The size of the charge signal is proportional to the energy of the incident x-ray photon. The resolution of the x-ray detector (given by the FWHM of the peak of a characteristic x-ray line) is 132 eV as is measured for Mn-K_α line (5.9 keV) [35]. An EDX spectrum displays peaks corresponding to the energy levels for which the most x-rays are received. Each of these peaks is unique to an atom, and therefore, corresponds to a single element. The higher is the intensity of a peak in a spectrum, the more concentrated the element is in the specimen. An EDX spectrum not only identifies the element corresponding to each of its peaks but the type of x-ray to which it corresponds as well. For example, a peak corresponding to the amount of energy possessed by x-rays emitted by an electron in the *L*-shell going down to the *K*-shell is identified as a K_α peak. In the present thesis, the compositional analysis of selective samples were examined by EDS unit coupled with the SEM (Carl Zeiss) setup.

2.7.2 X-ray photoelectron spectroscopy (XPS)

X-ray photoelectron spectroscopy (XPS) is one of the most widely used spectroscopic techniques which quantitatively measures the elemental composition, chemical state, and charge state of elements present in a material. Since the discovery of photoelectric effect by Heinrich Rudolf Hertz in 1887, it has become the most interesting light-matter interaction phenomenon which was successfully explained later in 1905 by Albert Einstein [36]. Siegbahn and his group developed and recorded the first high-energy-resolution XPS spectrum of the cleaved sodium chloride (NaCl) material [37]. XPS spectra are obtained by exposing a material to a beam of x-rays and simultaneously measuring the kinetic energy and number of electrons that escape from the top 1 to 10 nm of the material being analyzed. XPS requires ultra-high vacuum (UHV) conditions.

The surface to be analyzed is irradiated with soft x-rays. When x-ray photons, having energy $h\nu$, interact with a solid, it leads to ionization and the emission of a core (inner shell) electron from the atoms of the solid. Because the energy of the incoming x-ray photon is known, the binding energy of the emitted electrons can be determined by

$$E_{\text{binding}} = E_{\text{photon}} - (E_{\text{kinetic}} + \varphi), \tag{2.8}$$

where E_{photon} is the energy of the x-ray photons, E_{kinetic} is the kinetic energy of the electron and is measured by an electron analyzer, and φ is the work function of the material [36]. Obviously, $h\nu$ must be greater than E_{binding}. The ejected electron may come from a core level or from the occupied portion of valance level, but in XPS most attention is focused on the electrons of core levels. In XPS measurement, analyzers use electrostatic and/or magnetic lens units focused through apertures to effectively separate out electrons in a desired narrow band of energies from the wide range of energies contained in all other electrons entering the spectrometer [37]. In principle, XPS can be used to analyze all elements in the periodic table, however, in general hydrogen and helium cannot be detected due to their low cross-sections of interaction. For every element there will be a characteristic binding energy associated with each core atomic orbital. This gives rise to a characteristic set of peaks in the photoelectron spectrum at kinetic energies, determined by the photon energy and the respective binding energies. The presence of peaks at particular energies therefore, indicates the presence of a specific element in the specimen under investigation. Intensity of the peaks is related to the concentration of the element within the sampled region.

In the present thesis, the XPS measurements were carried out using a setup procured from VG Instruments (the schematic of the system setup is shown in Fig. 2.12). The base pressure of the main chamber is maintained at 1×10^{-11} mbar. The load-lock chamber is maintained at a base

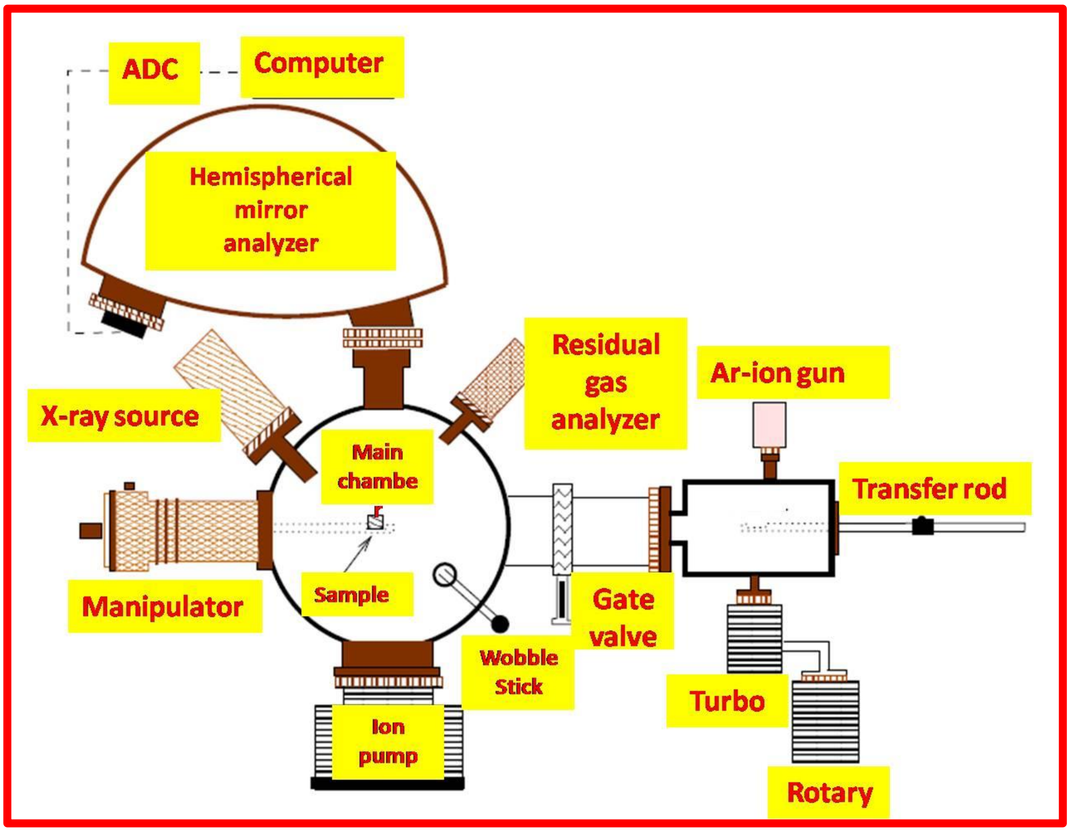

Figure 2.12: Schematic diagram of the XPS setup displaying different components.

pressure of 1×10^{-8} mbar which is equipped with a low energy Ar-ion gun for pre-sputtering the sample surface. The XPS system is equipped with twin Mg/Al anodes, a hemispherical analyzer, and a channeltron detector unit. The dual anodes generate non-monochromatic x-ray emission of energies 1253.6 eV for Mg-K_α and 1486.6 eV for Al-K_α lines. The analyzer is operated with the pass energy of 200 eV for the large survey scans in the range of 1-1200 eV and 20 eV for the high-resolution scans. The instrumental resolution of the system is 0.9 eV. The data are acquired at an angle of 45° between the sample normal and the analyzer axis. Shirley background correction is used to subtract the background from the XPS spectra. C 1*s* peak position is used as the reference for binding energy. The final spectra are fitted using the VGX-900 and peak fit CASA software to get the composition and binding energy positions of the elements.

2.8 Optical studies

Optical spectroscopy is one of most powerful characterization techniques in material science. It measures the attenuation of beam of light after reflection from the sample surface or after transmission through a sample. All these measurements can be carried out using a single wavelength or over an extended range. When an electromagnetic radiation interacts with the matter, a series of events occurs like scattering, reflection, transmission, and absorption. The optical spectra help us to determine the electronic property of materials. There is a linear relationship between absorbance and absorber concentration, known as the Beer-Lambert law [38]. In the present thesis, transmittance, absorbance, and reflectance measurements have been carried out for various heterojunctions. The working principles of these techniques are described below.

2.8.1 Reflectance

Reflectance is the amount of incident light that is reflected by a surface [39]. Optical reflectance measurements have been carried out using a Shimadzu (Model: UV 3101PC) –make ultra-violet-visible-near infrared (UV-Vis-NIR) spectrophotometer (Fig. 2.13) equipped with a specular reflectance measurement accessory. The spectral range that can be studied with this instrument is 200 to 3200 nm. It contains two light sources to produce photons of different energies using deuterium (for UV region) and tungsten halogen lamp (for visible and IR region). However, in the present thesis, most of the spectra have been collected over a wavelength range of 300–800 nm using 1 nm increment. The reflectance mode works in the specular reflection geometry arrangement with 45^0 incidence angle of light. Interestingly, system is designed in such a way that it rejects all the stray light coming from the outer environment which can affect the measurements.

2.8.2 Transmittance

Transmission is the process of passage of a radiant flux through a medium through diffusion and scattering. Both processes can undergo scattering, which is the deflection of the unidirectional beam of radiation into other directions [40]. When no diffusion occurs, the beam of radiation obeys the laws of geometrical optics and the unidirectional beam results in unidirectional beam called specular (or regular) reflection and direct (or regular) transmission. The wavelength of radiation is unchanged in these processes if the medium is stationary. The transmittance, T, of a medium is defined by the ratio of transmitted radiant flux to the incident radiant flux. The total transmittance T is subdivided into specular transmittance, T_r, and diffuse transmittance, T_d.

2.8.3 Absorbance

The absorbance, A, of a medium is defined by the ratio of absorbed radiant flux to the incident radiant flux [40]. According to the conservation of energy principle, the following relationship holds: $R+T+A= 1$, where R is reflectance, T is transmittance, and A is absorbance. The emittance (also called emissivity) of a body at a given temperature is equal to the absorbance. Therefore, based on the above expression, the emittance of a body can be deduced in principle by measuring R and T. For opaque materials, no transmission takes place and T is zero. In such cases, the absorbance /emittance can be derived from the measurement of reflectance, R, alone. These quantities are defined using an independent vocabulary to account for the effects of geometry and other parameters such as polarization and temperature of the material, etc. The interaction between absorbing species can lead to deviations in the absorption coefficient as a function of concentration. The relationship between A and measured T is:

$$A = -logT = -log\frac{P}{P_o}, \tag{2.9}$$

where P is the radiant power after passing through the sample and P_o is the initial radiant power

Figure 2.13: UV-Vis spectrophotometer used for the present thesis work.

known as band bap of semiconductor material. The band gap value can be calculated using absorbance data.

2.8.4 Vibrational properties

Raman spectroscopy is a versatile, convenient, non-destructive characterization technique that can be used for quantitative and qualitative analysis of semiconductors. It is based on inelastic scattering process of photons which is sensitive to the vibrational and rotational modes of atomic/molecular species [36]. Since it probes lattice vibrations which are sensitive to internal and external perturbations such as the changes in the vibrational frequencies induced by the microstructures and/or by the strain in the lattice, it can be used to study the compositional and microstructural analysis. When an electromagnetic radiation interacts with a molecule or a crystal, photons lose energy which excite molecules/crystal from its ground electronic state to a virtual state that is lower in energy than the first excited state. Most of the time, this light is elastically scattered and the molecule returns to its initial state. This effect is known as Rayleigh scattering [40]. On the other hand, some light can go under a process of inelastic scattering and

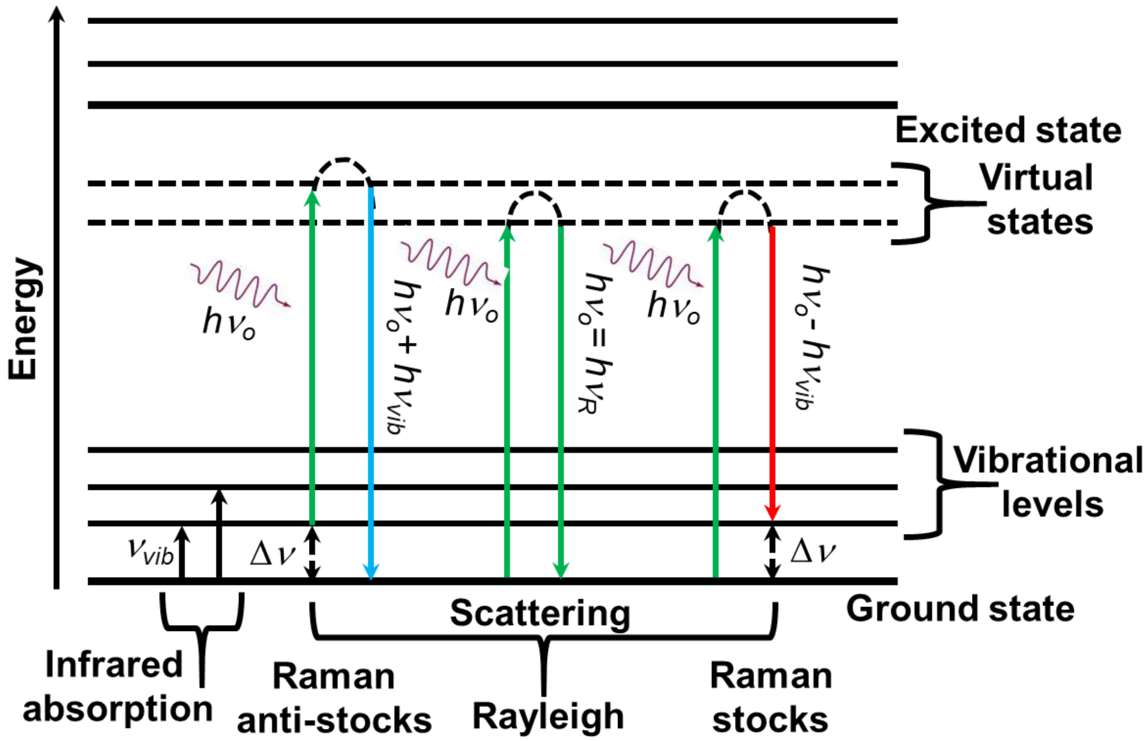

Figure 2.14: Vibrational transitions between energy levels during Raman scattering phenomena.

the molecule can end up in a vibrational state that is different than from where it is originate. The light that is scattered from the sample after this process will be shifted in frequency by an amount equal to the energy spacing between the vibrational states. Transitions to a higher vibrational state ($\Delta\nu$=+1) give rise to Stokes scattering, while ($\Delta\nu$=-1) transitions to lower states result in anti-Stokes scattering, as shown in Fig 2.14 [36].

The intensity of stoke lines is higher than anti-stoke lines. Both of these stokes and anti-stokes shift have equal distance from the Rayleigh scattered photons. Stokes shift is taking into consideration in Raman spectroscopy because of their high intensity.

In the present thesis, micro-Raman scattering measurements were performed at room temperature in the backscattering geometry using a Raman spectrometer (Horiba Jobin Yvon T64000) having a triple monochromator system with a liquid nitrogen cooled Charged Coupled Device (CCD) detecctor, as is shown in Fig 2.15. A 100x objective was used to acquire the micro Raman to spectra which provides ~1 μm^2 laser spot on the sample surface. A green line

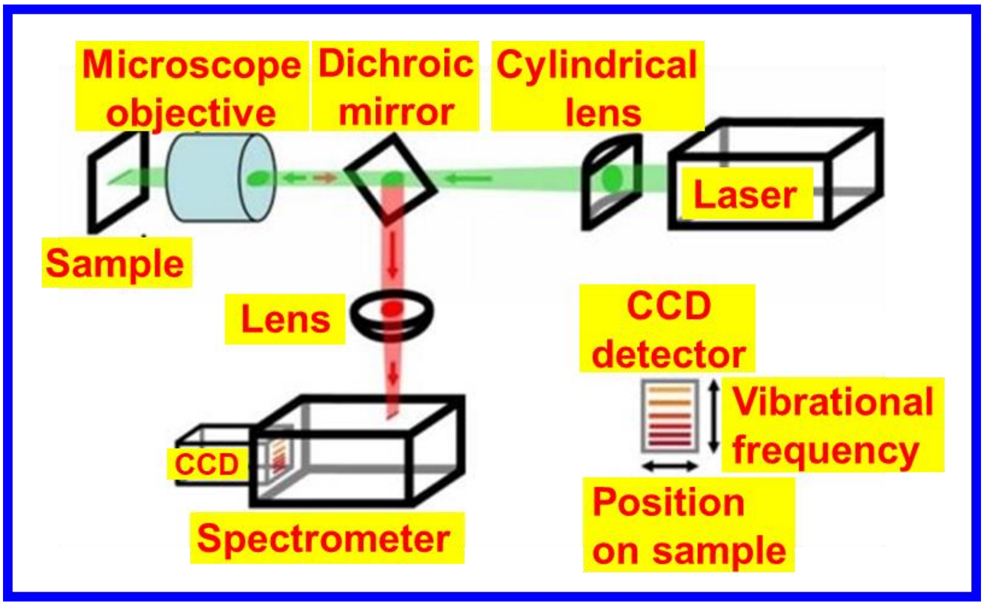

Figure 2.15: Schematic diagram of the Raman setup displaying different components.

(514 nm) from Argon ion laser was used with very low power to avoid any damage to the sample due to laser heating.

2.9 Electrical measurements

In many applications, one of the most important properties of materials is their response to the electric field. The basic electrical parameters which are characterized for a thin film, are generally electrical resistivity, carrier concentration, mobility, and type of charge carriers. Although various methods are used to measure these parameters of a semiconducting thin films but a proper care should be taken in the selection of methods to ensure that these measured parameters are of the grown film and are not being influenced by the substrate underneath. The electrical conductivity and/or resistivity measurement(s) are most commonly performed in the semiconductor industry using a four-point probe and by invoking van der Pauw method [41]. As a matter fact, van der Pauw method is a very effective and widely used method for the determination of electrical conductivity of the films. Interestingly, in contrast, two-point probe systems must take into account contact resistance and therefore, it makes the measurements much more difficult and erroneous [Fig. 2.16].

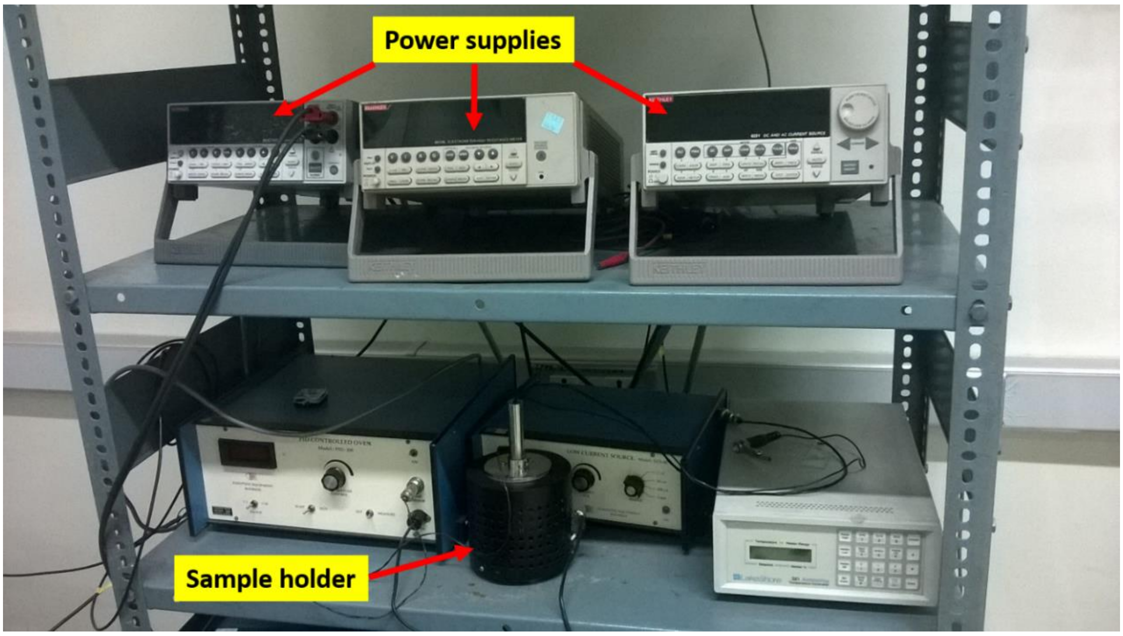

Figure 2.16: Resistivity measurements setup used in the present thesis.

2.9.1 Resistivity

Resistivity is important for devices because it contributes to the device series resistance, capacitance, threshold voltage, etc. In the present thesis, the resistivity of the films were determined by the four-probe method with the electrodes in the planar geometry [43]. The simplest arrangement consists of four in-line and equispaced point probes separated by a distance. For making electrical contacts, high conductivity silver paste (SPI Supplies) was used. The Ohmic nature of these contacts was confirmed from the current-voltage (I-V) measurements which showed a linear behaviour. The resistivity (ρ) of the films was then calculated by applying Ohm's law, using the relation: $\rho = RA/L$. Here R is the resistance given by the slope of the current-voltage characteristics, A is the area of the film in the planar geometry given by the product of the film thickness and the width of the film, and L is the spacing between the electrodes. The current voltage measurements were carried out using a Keithley source meter unit (Model 2410).

2.9.2 *I-V* characteristics

Current-voltage characteristics, apart from enabling one to explain the electrical conduction mechanism, are generally used to determine the built-in potential, ideality factor, leakage current, series resistance, and energy discontinuities in the conduction and valance band edges at the interface of a heterojunction. The measurement of an *I-V* characteristics consists of application of a voltage between two probes in the sample and measuring the current by the other two probes that flows through the sample. Depending on the polarity of the applied voltage, these characteristics can be classified as either forward or reverse biased one. It is conventional to define the forward bias characteristics as one in which the applied voltage is of such a polarity that it reduces the built-in potential. *I-V* measurements are carried out using a Keithley 2410 source meter. Each source meter instrument is equipped with both a highly stable DC power source and a true instrument-grade 6½-digit multimeter. The power source characteristics include low noise and precision. The result is a compact, single-channel, DC parametric tester. To do the characterization, we have used a computer program (Lab Tracer 2.0) which scans the voltage at a constant rate up to the maximum desired voltage.

2.9.3 *C-V* characteristics

Capacitance-voltage measurements are a powerful tool for the characterization of carrier concentration, interface quality, junction barrier height, and dielectric properties of thin films. *C-V* measurements provide a wealth of information about devices and materials characteristics [Fig. 2.17]. The procedure for carrying out taking *C-V* measurements involves the application of a DC bias voltage across the capacitor while making the measurements with an AC signal. Commonly, AC frequencies ranging from 10 kHz to 10 MHz are used. In this technique, the applied voltage is varied and the corresponding capacitance (across a junction) is measured and plotted as a function of the applied voltage. Generally, a metal-semiconductor junction or a *p-n* junction are characterized using this technique where the formed depletion region (with its ionized charges) behaves like a capacitor. By varying the applied voltage, one can vary the width of the depletion region. *C-V* measurements can be carried out using a DC or an AC signal. A strong DC bias causes majority carriers in the substrate to accumulate near the insulator interface. Since, they cannot cross the insulating layer, capacitance is maximum in the accumulation region as the charges stack up near that interface. The dependence of the depletion width on the applied voltage provides information about the doping profile, defect densities, and junction barrier height, etc. In the present thesis, the capacitance measurements are useful in determining the built-in voltage (V_{bi}) using the following Eq. [42]:

$$C^2 = \frac{q(N_n N_p \varepsilon_n \varepsilon_p)}{2(N_n \varepsilon_n + N_p \varepsilon_p)}(V_{bi} - V_A)^{-1}, \tag{2.10}$$

where N_n and N_p are the donor and acceptor concentrations, ε_{n} and ε_{p} are the dielectric constant of, *n*- and *p*-type semiconductor, respectively, *V* is the applied voltage, and *q* is the electronic charge. Eq. 2.10 is the depletion capacitance Eq. for a metal-semiconductor. In an ideal system, plotting $1/C^2$ versus V_{A}, the applied voltage, yields a straight line intercepting at $1/C^2 = 0$ on the voltage axis. Following the above Eq., the slope of this line is proportional to the carrier density and therefore, a straight line is indicative of a uniform doping distribution.

Figure 2.17: Capacitance-Voltage measurement setup used in the present thesis.

Capacitance measurements, which are ideally frequency independent, indicate the capacitance of the space charge layer. It is however, often the case that these plots are frequency dependent. Two types of plots are possible: curves that are parallel to each other and therefore, having different built-in voltages and curves that have different slopes, converging to the same built-in voltage. The latter behaviour is attributed to the presence of surface irregularities and/or surface states in the semiconductor.

According to the Eq., a nonlinear relationship between $1/C^2$ and V are expected when deep levels are present and exposed and when their sites are ionized. Concentration levels increase in a nonlinear fashion as a result of bias changes. Nonlinearity in $1/C^2$ versus V curves is therefore, a direct result originating from the effect of deep level charges [43]. The studies presented in this thesis have been carried out using a precision LCR meter (HP 4284A) as shown in Fig. 2.17.

2.9.4 Spectral response

In general, optoelectronic property of a heterojunction is categorized in two groups, viz. the generation of photocurrents due to absorption of photons and the emission of photons as a result of electronic excitation in the heterojunction. In this thesis, we concentrate on the former one. Photoresponsitity in semiconductors works on the general principle of the creation of electron-hole pairs under the action of light or absorption of incident light by a semiconductor may increase the number of free electrons and holes and thus, the electrical conductivity of the sample. In this way the separation of electron-hole pairs generated by the absorption of light gives rise to a photocurrent. The current–voltage characteristics of a heterojunction gets changed under the presence of a light source. The expression can be written as [42]:

$$J = J_S\left[\exp\left(\frac{qV}{k_BT}\right)-1\right]-J_R, \qquad (2.11)$$

where J_S is the dark reverse saturation current density, J_R is the photocurrent density, V is the applied voltage, q is electronic charge, k_B is the Boltzmann’s constant, and T is the sample temperature. In absence of recombination or generation of carriers, J_R is voltage independent and is equal to the short-circuit photocurrent density (J_{SC}). The open circuit voltage (V_{OC}) across the heterojunction (J=0) can be expressed as:

$$V_{OC} = \frac{k_B T}{q} \ln\left[1 + \frac{J_R}{J_S}\right], \tag{2.12}$$

The saturation current (J_S) depends on the heterojunction structure, while J_R depends on the geometrical dimension of the heterojunction.

The most commonly used mode of illumination for a heterojunction is the perpendicular illumination where the photons are incident on the front surface of the wide–band gap material and are perpendicular to the plane of the junction. In this case high energy photons are absorbed in the wide band gap materials, whereas, the low energy photons pass through the wide band gap materials and are absorbed in the underneath narrow band gap materials. This phenomenon is called the ‘window effect’ [42].

A heterojunction which responds to the incident photons is known as ‘photo detectors’. A photo detector measures the rate of arrival of quanta and shows a selective wavelength dependence of the response (in the form of current or voltage) per unit incident radiation power. Photovoltaic (PV) cell (solar cell) is a type of photo detector where the energy of sun light is directly converted into electricity.

A solar cell under illumination is characterized by the following parameters: responsivity, short-circuit current, open-circuit voltage, fill factor, and the power conversion efficiency. In the following paragraphs these parameters are clarified [44].

Responsivity: Responsivity (R_λ) measures the amount of output electrical signal [voltage or current (I_{ph})] generated by the incident radiation power (P_{in}). The responsivity for monochromatic light of wavelength, λ, incident normally is given by [45]:

$$R_\lambda = \frac{I_{ph}}{P_{in}}, \tag{2.13}$$

Detectivity: The normalized detectivity (D) is the most important parameter for characterizing a photo detector because it allows direct comparison of the performance of photo detectors. The detectivity is given by [38]:

$$D = \frac{R_\lambda}{I_b}, \tag{2.14}$$

where I_b is the noise current. The photovoltaic testing system (PTS, Sciencetech, Canada), used in the present case, includes a 150 W Xe lamp and a monochromator to tune the light source. A setup is shown in Fig. 2.18 for better realization. A source meter is used as an active load which permits the operation of a test cell at various load conditions, including short-circuit current, compensating for a series resistor required to sense the current produced by the modulated monochromatic light. This sensed current plus a reference signal at the frequency of the light modulation are both fed into the precision lock-in amplifier to allow measurement of the photocurrent generated by the modulated monochromatic light. PTS1 software, provided by the supplier, allows us to measure the spectral response (SR) and I-V characteristics of the cell. It includes a SCIRUNSR I-V-Test measurement system, precision lock-in amplifier, and the system software. The software

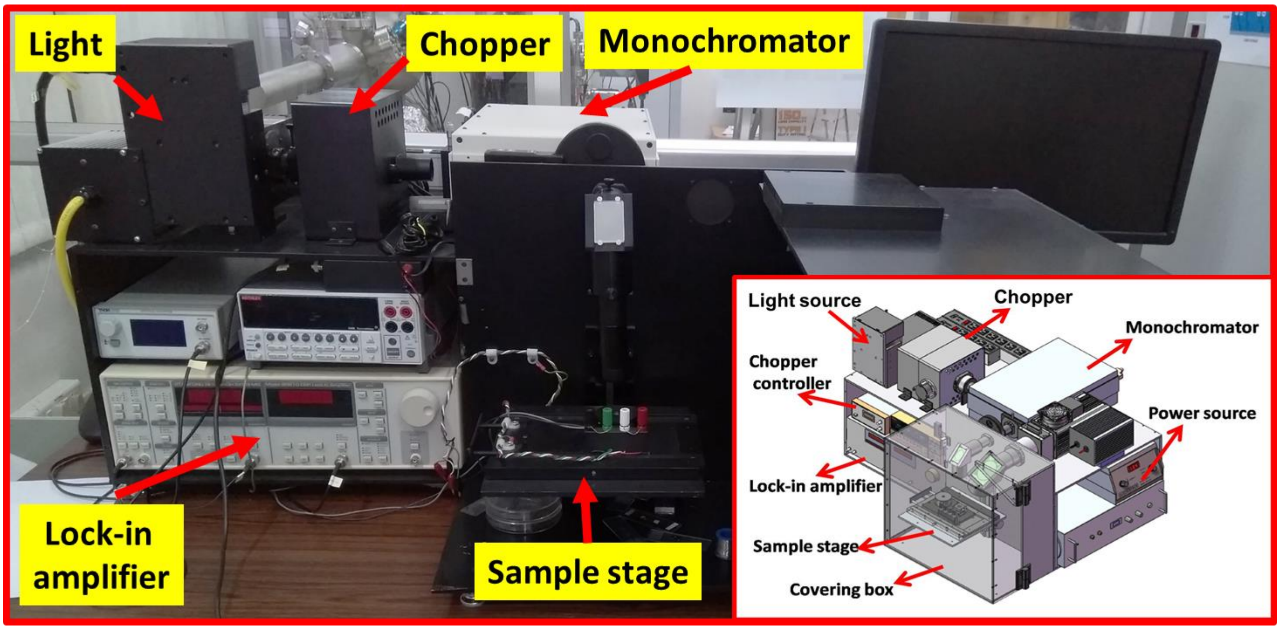

Figure 2.18: Experimental setup for the spectral response.

controls the monochromator, the source meter, and lock-in amplifier to automatically measure the *I-V* characteristics and *SR* versus wavelength, plotting the results on the screen and providing the calculated values of V_{OC}, I_{SC}, P_{max}, and fill factor (*FF*). Key features of this instrument are listed below:

- monochromator with automated order sorting filters
- monochromatic probe light area adjustable from 2 mm to 5 mm diameter
- monochromatic probe light power of 125 mW total (white light)
- Keithley 2400 source meter
- bias voltage ranging from 0-200 V
- calibrated reference detector
- optical chopper and drive
- stanford SR800 series lock-in amplifier
- photocurrents measurable from 1 pA to 1 μA
- automated switching of lock-in input signals from the reference detector to the sample current measurement
- target table with dual cell holder having a150 mm height adjustment.

References

[1] R.V. Stuart, Vacuum technology, thin film, and sputtering, Academic Press, Inc. (1985).

[2] J.B. Webb, Thin films for free atoms and particles, Chapter 6, Academic Press, Inc. (1985).

[3] A. Anders, Thin solid Films 502 (2006) 22.

[4] P.J. Kelly, P.S. Henderson, R.D. Arnell, G. A. Roche, D. Carter, J. Vac. Sci. Technol. A 18 (2000) 6.

[5] K. Seshan, Handbook of thin film deposition process and techniques, Noyes publications Norwich, New York, USA (2002).

[6] www.advanced-energy.com.

[7] D-H Lee and N-G Cho, Meas. Sci. Technol. 23 (2012) 105601.

[8] http://www.rochester.edu/urnano/facilities/Ambios_profilometer/index.html.

[9] http://imel.demokritos.gr/docs/Facilities/SURFACE-PROFILER-EQUIPMENT.pdf

[10] P. Eaton and P. West, Atomic force microscopy (Oxford university press, New York, 2010).

[11] G. J. Legget, "Scanning Tunneling Microscopy and Atomic Force Microscopy", in Surface Analysis: The Principal Techniques, edited by J C Vickerman (John Wiley & Sons, Chichester, 1997), pp. 393.

[12] K. S. Birdi, Scanning Probe Microscopes: Applications in Science and Technology. (CRC Press, Boca Raton, 2003).

[13] Y. Sugawara, "Atomic Force Microscopy", in Roadmap of Scanning Probe Microscopy, edited by S. Morita (Springer, Berlin - Heidelberg, 2007).

[14] http://www.wsxm.es/download.html

[15] http://gwyddion.net/

[16] https://www.imagemet.com/products/spip/

[17] https://www.asylumresearch.com/Applications/Orca/Orca.shtml.

[18] http://asylumresearch.com/Applications/ElectricalCharacterization/ElectricalSuite.pdf

[19] Laurent Nony. Principles of Kelvin Probe Force Microscopy and applications. DEA. Laurent NONY, 1st German-French Summer School on noncontact -AFM Porquerolles, 6th-11th 2013, France, 2013, pp.80.

[20] S. Sadewasser and T. Glatzel, Kelvin probe force microscopy (Springer, Berlin - Heidelberg, 2011).

[21] Wilhelm Melitz, Jian Shena, Andrew C. Kummel, Sangyeob Lee, Surface Science Reports 66 (2011) 1–27

[22] http://www.parkafm.com/images/spmmodes/dielectric/Electrostatic-Force-Microscopy-(EFM).pdf?ver=1.2

[23] D. K. Schroder, Semiconductor material and device characterization. (John Wiley & Sons, Inc., Hoboken, New Jersey, 2006), 3rd ed.

[24] B. G. Yacobi, D. B. Holt, and L. L. Kazmerski, "Scanning Electron Microscopy", in Microanalysis of solids, edited by B. G. Yacobi, D B Holt, and L. L. Kazmerski (Plenum Press, New York, 1994).

[25] P. S. Turner, C. E. Nockolds, and S. Bulcock, "Electron Microscope Techniques for Surface Characterization", in Surface Analysis Methods in Materials Science, edited by D J O'Connor, B A Sexton, and R St C Smart (Springer-Verlag, Berlin Heidelberg, 2003).

[26] http://www.zeiss.de.

[27] A. J. Garrat-Reed, "Transmission Electron Microscopy", in Microanalysis of Solids, edited by B. G. Yacobi, D. B. Holt, and L. L. Kazmerski (Plenum Press, New York, 1994).

[28] N. Yao and Z. L. Wang (eds), Handbook of microscopy for nanotechnology. (Kluwer Academics Publishers, New York, 2005).

[29] B. Satpati (Ph. D. Thesis, Institute of Physics, Bhubaneswar)

[30] B. Fultz and J. M. Howe, Transmission electron microscopy and diffractometry of

materials (Springer, Berlin - Heidelberg, 2007) 3rd ed.

[31] http://www.bruker.com/products

[32] T. L. Alford, L. C. Feldman, and J.W. Mayer, Fundamentals of nanoscale film analysis (Springer-Verlag, Berlin Heidelberg, 2007).

[33] A.L. Patterson, Phys. Rev. 56 (1939) 978.

[34] D. K. Schroder Semiconductor material and device characterization, second edition, A Wiley-interscience publication, New York, 1998.

[35] P.E.J. Flewit and R.K. Wild, Physical methods for material characterization, second edition, IOP publishing, London, 2003.

[36] G. Friedbacher and H. Bubert, Surface and thin film analysis (John Wiley & Sons, Inc., Hoboken, New Jersey, 2011), 2nd ed.

[37] K. Siegbahn, and K. I. Al. Edvarson, Nuclear Physics 1 (1956) 137.

[38] J. I. Pankove, Optical process in semiconductors (Prentice-Hall, Inc., Englewood Cliffs, New Jessey, 1971).

[39] Fabricio L Forgerini and Roberto Marchiori, Biomatter. 2014; 4: e28871.

[40] I. Chambouleyron, E. G. Birgin and J. M. Martínez, in Optical Interference Coatings 9, OSA Technical Digest Series (Optical Society of America, Washington, DC, 1998), p. 132.

[41] Smits, F. M. (1958), Measurement of Sheet Resistivities with the Four-Point Probe. Bell System Technical Journal, 37: 711–718. doi: 10.1002/j.1538-7305.1958.tb03883.x

[42] B. Sharma and R. Purohit, First edition Vol. 5, (1974).

[43] http://www.evaluationengineering.com/articles/200812/fundamentals-of-semiconductor-c-v-measurements.php

[44] A. Tom, Organic Bulk Heterojunction Solar Cells from Single Cell towards Full Flexible Photovoltaic Module, (2006).

[45] http://www.nrel.gov/docs/legosti/fy98/23878.pdf.

CHAPTER 3

3. Study on electrical transport properties in ZnO:SnO$_2$ (ZTO) thin films: Roles of grain boundaries and growth angle

Amorphous transition metal oxide semiconductors have attracted much attention over the past decades as a suitable candidate materials for transparent conductive oxide (TCO) layer in photovoltaic devices [1]. Also, these materials have wide range applications in integrated multi-layered electronics, flat panel display, etc. Currently, great efforts have been made to enhance the performance and stability of TCOs. In particular, amorphous zinc tin oxide (ZTO) has been extensively investigated for TCO applications due to its favourable properties, including high mobility, high transmittance in the visible region, and long term stability [2]. In addition, ZTO exhibits *n*-type conductivity with a large band gap (3.4 eV) which makes it more attractive TCO than commercially used indium tin oxide [2,3]. As we have discussed in the chapter 1, ZTO is used as top transparent electrical electrode in order to fabricate the CdTe-based solar cell. In order to use as a TCO and to achieve the better cell efficiency, it should have smooth charge transport and small barrier height at the interface of the underneath layer with the minimum loss of photo-generated charge carriers which means it have comparable work function with the underneath layer to minimize the band-bending at the interface. Thus, in this chapter, we optimize the growth of ZTO films and demonstrate the role of grain boundaries in transport of electrical charges in these films. In particular, we study room temperature (RT) diode characteristics of *n*-ZTO/*p*-Si heterostructures by current-voltage and capacitance-voltage measurements. In addition, resistivity and transmittance measurements performed on granular ZTO thin films grown on glass as well as silicon substrates having different thicknesses show that the films have good electrical conductivity and highly transparent nature. Following this, using Kelvin probe force microscopy, we study the work function of ZTO thin films and demonstrate that it is highly dependent on the grain size of these films. In order to understand the charge transport in ZTO films, the true nature of the potential barrier at GBs should be understood.

In doing so, we have undertaken the studies on bulk and nanoscale charge transport properties of ZTO films (grown on Si substrates) using cAFM, EFM, and KPFM techniques. Here we make use of these local probe techniques to show the charge conduction process from one grain to the next and how the barrier forms at the GBs due to defects. In fact, we show the local band-bending at the grain boundaries of ZTO thin films and metal-semiconductor interface.

In addition, we show the charge trapping at the grain boundaries and using KPFM studies, the work function of a ZTO film is mapped which is found to be spatially inhomogeneous. As a matter of fact, the charge trapping at grain boundaries will open a new avenue to control the charge transport in the ZTO films. In particular, using KPFM we demonstrate the mapping band-bending at the junction in ZTO film. Further to this, the role of electric field-induced doping in nanoscale charge transport is also demonstrated by performing the local *I-V* measurements by employing cAFM technique. The present study will be useful to understand the roles of grain boundaries in charge transport at nano- and bulk-scale as well as to fabricate a TCOs based on ZTO.

3.1 Growth of low resistive and highly transparent ZTO thin films at room temperature

3.1.1. Experimental details

A film thickness of 120 nm was deposited on ultrasonically cleaned soda lime glass (SLG) and Si substrates at RT using an RF magnetron sputtering system (Excel Instruments; Cesar, Advanced energy, USA). Commercially available (Testbourne Ltd. UK), 99.99% pure

ZnO:SnO$_2$ (ZTO) sputtering target (50 mm dia.×6.2 mm thick) was used to grow ZTO thin films. Ultra-pure (99.99%) argon gas was injected into the chamber with a flow rate of 30 sccm to maintain the working pressure of 5×10^{-3} mbar during sputtering. An RF power of 100 W was supplied to the ZTO target and the substrate was rotated at a constant speed of 3 rpm to achieve uniform film thickness, whereas the target-to-substrate distance was maintained at 80 mm. The deposition was carried out at various angles (θ) in the range of 0°-85° where the angle of incident flux was measured with respect to the target normal. The optical properties of as-deposited ZTO films were measured by an ultra-violet-visible-near infrared (UV-Vis-NIR) spectrophotometer in the wavelength range of 300-800 nm. In addition, linear four-probe technique was used to measure the growth angle-dependent change in resistivity of ZTO films. Kelvin probe force microscopy was employed to measure the work function of ZTO films in lift-mode using an Ir/Pt-coated silicon tip (Nano world) with a resonant frequency of about 75 kHz and force constant of about 2.8 N nm^{-1}. Simultaneously, the surface topography also recorded by atomic force microscopy in tapping mode. The commercial software (IGOR PRO 6.05) together with the Asylum Research code (version 080501-1804C) were used to get the statistical distribution of contact potential.

3.1.2. Results and discussion

Figures 3.1(a)-(c) depict the AFM topography images of ZTO films grown at 0°, 50°, and 80° growth angles, respectively. These images clearly show the granular nature of the films and gradual change in the topography with increasing growth angle. RMS roughness and average grain size increase with the growth as shown in Fig. 3.1(d). The inset of Figs. 3.1(a)-(c) show the digital photographs of samples grown at 0°, 50°, and 80° growth angles, respectively, confirming the colour change of the films with the growth angle [4]. On the other hand, Fig. 3.1(e) depicts the XRD spectrum of ZTO films, confirming the amorphous nature of films as reported in the literature [5]. Normally, ZTO films grown by sputtering are found

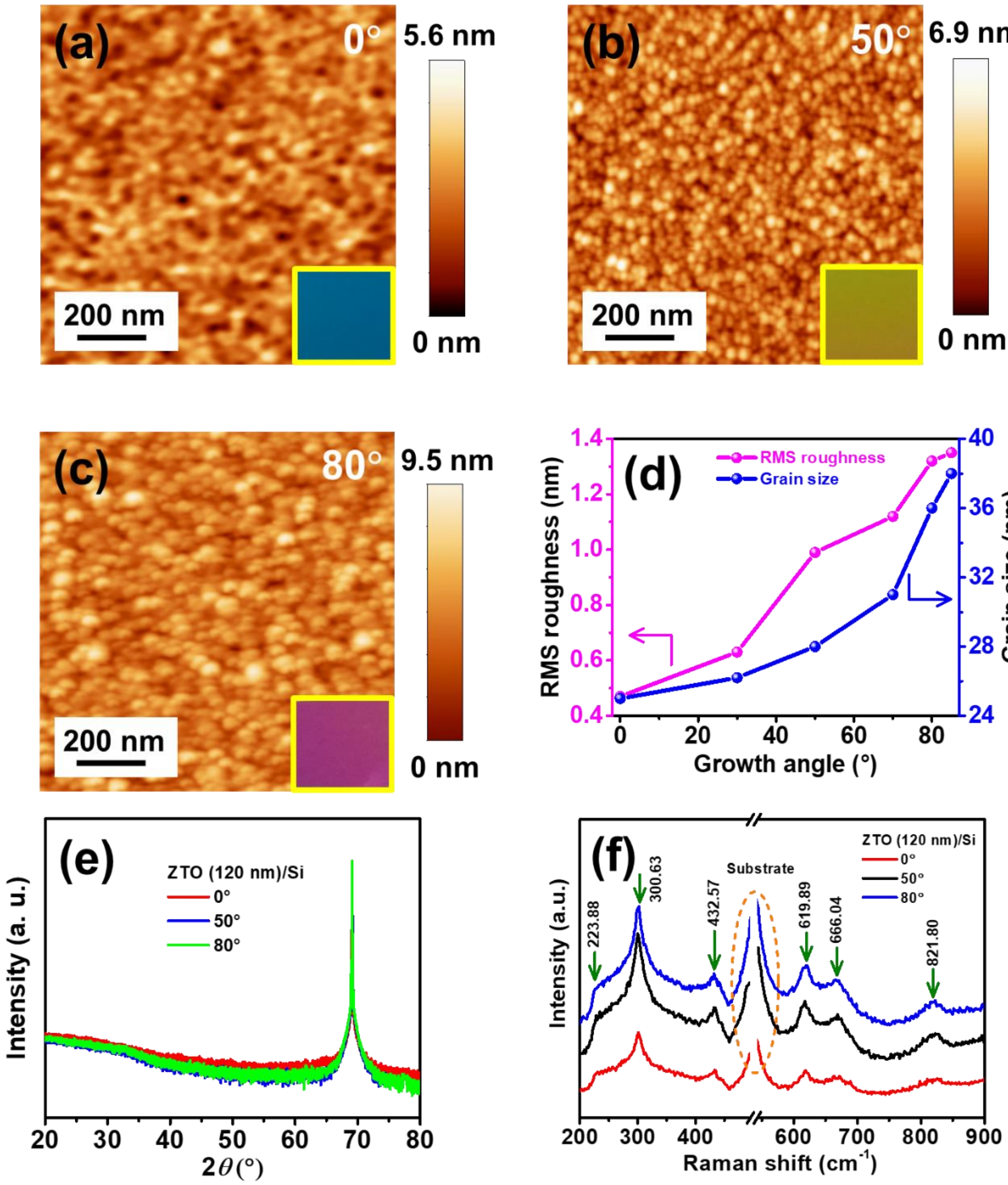

Figure 3.1: (a)-(c) depict the AFM images of ZTO films grown at 0°, 50°, and 80°, respectively, (d) shows the change in RMS roughness and grain size with the growth angle, (e) and (f) depict XRD and Raman spectrum of ZTO films, respectively.

to amorphous in nature [5,6]. Further to confirm the presence of ZTO films, micro-Raman measurement were carried out. The micro-Raman spectrum show a series of Raman lines around the following frequencies: 223.38 cm^{-1}, 300.63 cm^{-1}, 432.57 cm^{-1}, 619.89 cm^{-1}, 666.04 cm^{-1}, and 821.80 cm^{-1}. The strong Raman peak at 521 cm^{-1} is attributed to the Si substrate [4]. The above observed Raman modes can be understood by considering the different vibrational modes $1A_{1g}$, $1E_g$, E(LO), and $3F_{2g}$ of ZTO films. In the spectrum, the Raman line around 223.38 cm^{-1} is quite weak, which may be caused by the overlapping effect and can be reasonably assigned to F_{2g} [6]. On the other hand, the Raman peak at 300.63 cm^{-1} is associated to E(LO) symmetries in $ZnSnO_3$, whereas the Raman mode at 432.57 cm^{-1} belongs to E_g symmetries of ZTO films. The Raman peak appears at 666.04 cm^{-1} which is signature of amorphous phase of ZTO and can be assigned to A_{1g} vibrational mode. The bending mode of M-O-M bonds, where M represent the either Zn or Sn atoms present in the ZTO, appears at 619.89 cm^{-1}, whereas the Raman mode at 821.80 cm^{-1} corresponds to the stretching mode of M-O-M bonds [7,8]. The obtained results match well the XRD results and literature.

Figure 3.2(a) depicts the optical transmittance spectra of all the ZTO films deposited at different deposition angles. From this figure, it is observed that the average transmittance of all the ZTO films (in the visible range) is greater than 90% till the growth angle of 80°, whereas it reduces a bit (<85°) for the films grown at an angle of 87°. In addition, the observed sharp decrease in the transmittance around 365 nm was observed which can be attributed to the fundamental absorption edge or band gap of ZTO [9]. The optical band gap of ZTO films is calculated from Tauc's Eq. [10]:

$$\alpha = \frac{k(hv-E_g)^{\mathrm{n}}}{hv}, \tag{3.1}$$

where α is the optical absorption coefficient, k is a constant, hv is the photon energy in (eV), and n may have different values. By extrapolating the straight line portion of $(\alpha hv)^{1/2}$ versus hv plot, one can find the value of the optical band gap. A clear change in the band gap is noticed for the films grown at different growth angles as shown in Fig. 3.2(b). For instance, a close inspection shows that the optical band gap of thin films deposited under the normally incident flux is 3.82 eV [9,11]. There onwards, a systematic red shift is observed up to the growth angle of 50°, whereas it increases for the film deposited at 85° which can be attributed to the shadowing effect, influencing at higher growth angles [4].

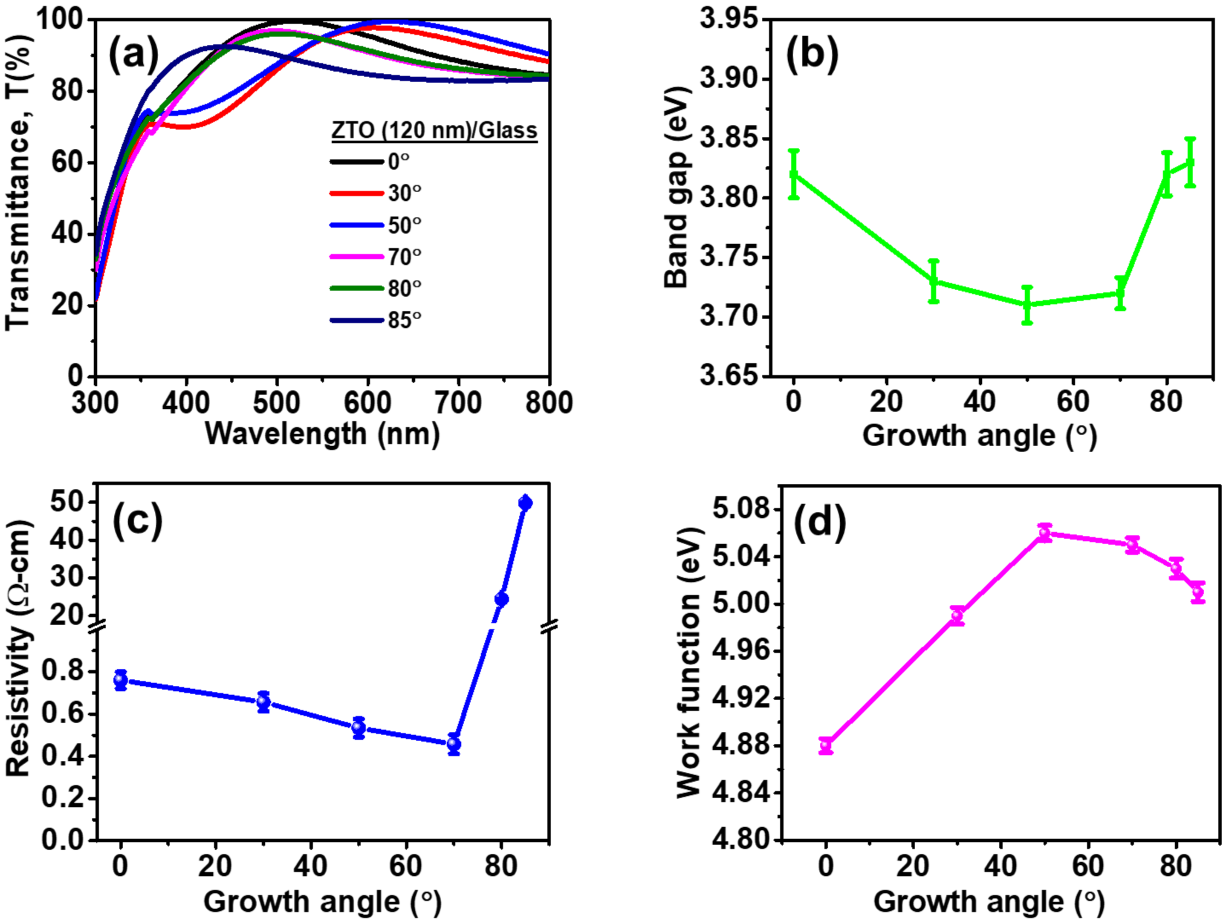

Figure 3.2: (a) and (b) show the optical transmittance data and band gap for ZTO films grown at different angles (c) Variation in the resistivity of ZTO films as a function of deposition angle, and (d) shows the growth angle-dependent variation in the work function of the ZTO films.

Figure 3.2(c) shows the growth angle-dependent variation in resistivity measured by the linear four-probe technique. A decrease in the resistivity is evident with an increase in the deposition angle from 0° to 70°, whereas a sharp increment is observed corresponding to the higher growth angles. The minimum resistivity is found to be in the range of 0.53-0.45 Ω-cm corresponding to the growth angles of 50°-70°. On the other hand, a sharp increase in the resistivity at higher growth angles can be attributed to the presence of porosity in the films at higher angles. It is known that the nanoscale electrical properties are strongly influenced by the film growth angle [12]. In order to address this issue, KPFM measurements are employed to extract the work function of the ZTO films. It is known that the observed V_{CPD} can be converted into the work function of the material, using the following relation [13]: $W_{\mathrm{sample}} = W_{\mathrm{tip}} - qV_{\mathrm{CPD}}$, where W_{sample}

and W_{tip} are the work function of a sample and the tip, respectively and q is the electronic charge. The measured work function is seen to increase up to 50° (5.06 eV), whereas it decreases slightly for the films deposited up to an angle of 85° [Fig. 3.2(d)]. Since for a better electrical contact, a higher work function is desired for CdTe based-solar cells, it is inferred that ZTO films grown at an angle of 50° can be considered to have optimized physical properties of its use (as a TCO) in the present work. The observed results also indicate that not only the bulk but also the nanoscale properties can be tuned by changing the growth angle.

The experimental results described above can be attributed to the growth dynamics of the films in oblique angle deposition (OAD) technique. Kumar *et al*. have shown that grain growth in a thin film is governed by the surface diffusion [4]. In fact, grain size increases with surface diffusion and in general surface diffusion increases with increasing substrate temperature [13]. Thus, our experimental results can also be understood in light of surface diffusion. For instance, the atoms have an equal probability of diffusion with a diffusion energy (D) in all directions [Fig. 3.3(a)] for the film grown at 0° [13,14]. In this case, the presence of a large number of grain boundaries in the film will give rise to a large number of defects produced due to incomplete atomic bonding, resulting in an increase in the scattering centres (or resistivity) of the same. On the other hand, for an OAD, the incident atoms on the substrate will undergo an

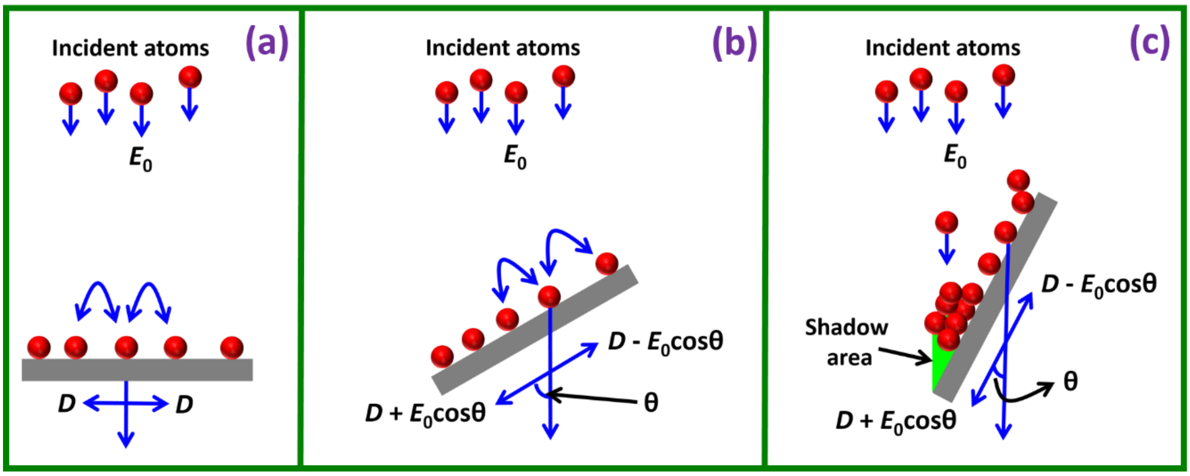

Figure 3.3: Schematic representation of films deposited at normal incidence, an arbitrary oblique angle, and a grazing incidence angle are presented in (a), (b) and (c), respectively [4].

asymmetric diffusion probability [Fig. 3.3(b)]. In fact, initially incident atoms have an energy (E_0) where a component of this energy ($E_0 \cos\theta$) at an oblique angle, θ, enhances the atomic diffusion [Fig. 3.3(b)] on the surface and gives rise to an improvement in the grain growth. On the other hand, films grown at higher angles (>80°) are mainly governed by the shadowing effect and the surface diffusion increases [Fig. 3.3(c)]. This causes an increase in the porosity of the film, which in turn increases the resistivity of the film. In fact, there is an interplay between the surface diffusion and shadowing effect in case of OAD process [13,15]. Thus, one can infer that the formation of nanostructures are governed by the surface diffusion for the films grown at lower oblique incidence angles, whereas shadowing will be the dominating factor for the films grown at higher incident angles.

3.1.3 Conclusions

In conclusion, we have demonstrated that low resistive ZTO films can be obtained corresponding to the growth angle of 50° and a continuous change in the work function takes place with growth angle, whereas it becomes the highest (5.06 eV) corresponding to the growth angle of 50°. Thus, it can be concluded that ZTO films grown at 50° shows the best optimized optoelectronic and physical properties for its use as a transparent conductive contact for the present work on the fabrication of a CdTe-based solar cell and thus, for further studies, we have used this growth angle for the deposition of ZTO films.

3.2 Influence of grain size on local work function and optoelectronic properties of *n*-ZTO/*p*-Si heterostructures

3.2.1 Introduction

Transition metal oxides have been widely investigated for their use in passive devices such as transistors, dielectrics, capacitors, and transparent conducting oxides (TCOs) [1]. TCO thin films, such as tin-doped indium oxide (ITO), fluorine-doped tin oxide (FTO), zinc oxide (ZnO), zinc tin oxide (ZTO), aluminium-doped zinc oxide (AZO), and gallium-doped zinc oxide

(GZO) exhibit many unique properties and are extensively used for flat panel displays, light emitting diodes (LEDs), solar cells, gas sensors, and other optoelectronic devices due to their high transparency and low resistivity [5,16–20]. However, ITO has several known problems which include scarcity of indium and its high cost. Consequently, due to need for indium and gallium free TCOs, Zn-Sn-O systems are attractive because they are composed of non-toxic and inexpensive elements [2,3]. One of the attractive compounds of Zn-Sn-O is amorphous $ZnSnO_3$ (ZTO).

Of further interest is the fact that ZTO has high electron mobility and in turn exhibits an efficient electron transport [5]. Because this oxide comprises of large metal cations with $(n-1)d^{10}ns^0$ electronic configuration and its conduction band is derived from large spherically-symmetrical metal *s*-orbitals so that the degree of overlap between adjacent metal orbitals is relatively insensitive to the bond angle distortion associated with the amorphous structure, resulting in a high mobility [5]. In addition, ZTO has a large band gap (3.4 eV at RT) and hence, exhibits a high transparency in the visible region which makes it a more attractive TCO than commercially used indium tin oxide. Moreover, ZTO shows physical and chemical stability with respect to oxidation and etching [2,21]. Recently, Saini *et al*. have shown the broadband antireflection property of ZTO films grown of different kind of substrates for their use in the light absorption applications [22].

Various deposition techniques and conditions, including sol-gel, thermal evaporation, sputtering, and pulsed laser deposition (PLD) are used to make superior TCOs in terms of low resistivity and high transmittance [5,9,19,23]. Nevertheless, they exhibit a wide variety in microstructures of TCOs in terms of grain size, surface morphology, composition, lattice defects, etc. However, conventional TCOs having high conductivity and transmittance are deposited at high substrate temperature or needed post annealing process [16]. In turn, underlying layers diffusion would take place. To get rid of this problem, room temperature processing is needed to achieve good TCOs properties. Among the above mentioned numerous deposition techniques, magnetron sputtering technique has the following advantages: it is able to produce uniform coatings over a large area with accurate composition and high reproducibility, and uniform morphology of the films [10,24]. Minami *et al*. explored the stability of ZTO films by varying its composition which were deposited by RF sputtering [2]. Likewise, the effects of sub-band gaps and post-annealing were studied to enhance the optoelectronic properties of ZTO films [9]. It was demonstrated that amorphous ZTO films grown by co-sputtering of ZnO and SnO_2 target at RT, could be successfully employed as a TCO after post-annealing [24]. To further improve the optical and electrical properties at RT, a thickness-dependent detailed study is needed as well as their effect on the optoelectronic properties because thickness plays an important role for TCO-related applications [19]. Tsai *et al.* have reported that carrier mobility and visible transmittance are strongly influenced below a critical thickness [30].

In this work we demonstrate the dependencies of the morphological, structural, optical, electrical, and work function properties on the thickness of amorphous ZTO films grown by RF sputtering at RT and how they are affected by grains and grain boundaries. In fact, with increasing ZTO film thickness a systematic reduction in the turn-on potential, barrier height, and electrical resistivity is observed. In order to explain the change in these properties, atomic force microscopy (AFM) and scanning electron microscopy (SEM) measurements are employed to check the thickness-dependent structural evolution of grains in the ZTO films, while their nature of crystallinity and vibrational properties are determined by X-ray diffraction (XRD) and micro-Raman studies. The chemical composition of the films is determined by X-ray photoelectron spectroscopy (XPS). In addition, we have carried out Kelvin probe force microscopy (KPFM) studies on ZTO films to evaluate change in surface potential induced by their change in the grain size. The present study will be extremely useful to make a TCO using

ZTO at RT.

3.2.2 Experimental

In order to grow ZTO thin films a *p*-Si(100) wafer was cut into small slices (1 cm×1cm). Prior to deposition, Si substrates were cleaned by trichloroethylene, acetone, propanol, and de-ionized water (Milli-Q Gradient water purification system, Millipore) for 5 min. each to remove the organic contaminations and further air dried. ZTO thin films were grown on as-obtained *p*-Si substrates at RT using an RF magnetron sputtering setup (Excel Instruments, India). Commercially available 99.99% pure $ZnO:SnO_2$ (ZTO) target (50 mm dia×6.2 mm thick) (Testbourne Ltd. UK) was used for the growth of ZTO films in a vacuum chamber with a base pressure of 2×10^{-7} mbar. Prior to ZTO film deposition, a pre-sputtering was done for (20 min in each experiment). To maintain the working pressure of 5×10^{-3} mbar, ultra-pure (99.99%) argon gas was injected into the deposition chamber with a flow rate of 30 SCCM. An RF power of 100 W (Cesar, Advanced energy, USA) was applied to the target and the substrate was rotated at a speed of 3 rpm to achieve a uniform film thickness, where the substrate-to-target distance was kept at 80 mm and the deposition angle was 50° with respect to the target normal. Four different thicknesses 60, 120, 180, and 240 nm of ZTO films were deposited on Si (viz. S1, S2, S3, and S4, respectively) and glass substrates with an average deposition rate of 3.2 nm/min. The thicknesses were measured using a surface profilometer (Ambios, XP-200). To check the uniformity in the film thickness, many films were deposited before making the devices. Surface morphology and microstructure of the films were examined by atomic force microscopy (Asylum Research, USA) in tapping mode and a field emission gun-based scanning electron microscope (FEGSEM) using 5 KeV electrons (Carl-Zeiss, Germany) under both plan-view and cross-sectional geometries. For every sample, several images were collected from randomly chosen regions to check the uniformity of the film microstructures. AFM images were analysed by WSxM software [25]. Phase identification and nature of the crystallinity of

ZTO films were evaluated by x-ray diffraction (XRD) (Bruker, Germany) under the Bragg-Brentano geometry using a Cu-K$_\alpha$ radiation (λ=0.154 nm) over a 2θ scan range of 20°-80°. Micro-Raman measurements were performed on ZTO films (using the back scattering geometry) to check their vibrational properties using a spectrometer (Horiba Jobin Yvon, Japan) which is equipped with triple monochromators and liquid nitrogen cooled charge-coupled device (CCD) detector. To collect micro-Raman spectra, an argon-ion laser of 514.5 nm wavelength and 100× objective lens were used which provided 1 μm^2 laser spot on the sample surface. Compositional analysis on selective ZTO films were also performed using a x-ray photoelectron spectroscopy (XPS) system (PHI 5000 Versa probe II, ULVAC-PHI, Japan) having a base pressure of $<5\times10^{-10}$ mbar with a microfoused (100 µm, 25 W, 15 KV) monochramatic Al-K$_\alpha$ source ($h\nu$=1486.6 eV), a hemispherical analyzer, and a multichannel detector to check the chemical oxidation state of the zinc and tin.

Work function of the ZTO films was extracted by Kelvin probe force microscopy technique using an *ex-situ* atomic force microscopy setup (Asylum Research, USA) in tapping mode with a lift height of 50 nm and using a conductive tip (AC240 TM, Electric-lever, Olympus) having a radius of curvature of ~30 nm, a stiffness of ~2 N m^{-1}, and a resonance frequency of ~70 kHz. It may be mentioned that a large number of places were randomly chosen to check the uniformity of the films morphology and contact potential difference with different scan speeds, ranging from 0.2 to 1 Hz at various scan angles by rotating the samples. However, no noticeable change was found in the results which confirms that there are no tip-related artefacts in the results. In addition, it is also mentioned that the samples were kept in a silica gel-filled vacuum desiccator and the samples were taken out from this box just before the KPFM measurements. In fact, the present AFM setup is placed in a closed and a low-vibration environment (equipped with silica-gel filled packets) to create a low-humidity level. The room temperature photoluminescence spectra of ZTO films were recorded in the spectral range of 325 to 550 nm using a spectrometer (Edinburgh Instruments, UK) with a Xe lamp as the excitation source. The transmittance and absorbance data were recorded by ultraviolet (UV)-visible (vis)-near infrared (NIR) spectrometer (Shimadzu-3101 PC, Japan), using an unpolarized light. The performance of the Ag/ZTO/Si/Ag heterostructure diodes was evaluated by *I-V* characteristics using a source meter (Keithley, 2410). The barrier height at junction was measured by performing the capacitance-voltage (*C-V*) measurements at a frequency of 1 MHz using a precision LCR meter (HP 4284A).

3.2.3 Results and discussion

Figures 3.4(a)-(d) show AFM images of four samples, viz. S1, S2, S3, and S4, respectively, exhibiting a gradual change in the surface morphology with increasing film thickness and the films are found to be granular in nature. It observed that the average grain size increases with increasing film thickness and the measured grain size turns out to be 23, 28, 38, and 47 nm for S1, S2, S3, and S4, respectively. In addition, RMS roughness of the ZTO films is also observed to increase with increasing film thickness and all these quantities are summarized in Table 3.1. These important differences in the morphology of ZTO films lead to their different appearances as is observed in the respective digital photographs as shown in Figs. 3.4(e)-(f). As a matter of fact, one can see a clear change in the film colours (digital photographs) of the ZTO films with increasing film thickness from 60 to 240 nm which should be related to change in the band gap with increasing film thickness. To investigate more on the morphology of ZTO films, plan-view and cross-sectional SEM measurements are performed. Figures 3.5(a) and (b) depict plan-view FESEM images of S1 and S3, respectively. From the SEM images, granular nature of the ZTO films is further confirmed along with the fact that they consist of uniformly distributed grains and the average grain size increases with increasing film thickness.

On the other hand, Figs. 3.5(c) and (d) show the corresponding cross-sectional SEM images of S1 and S3, respectively, depicting the formation of ZTO films having the thickness of 61.5 and

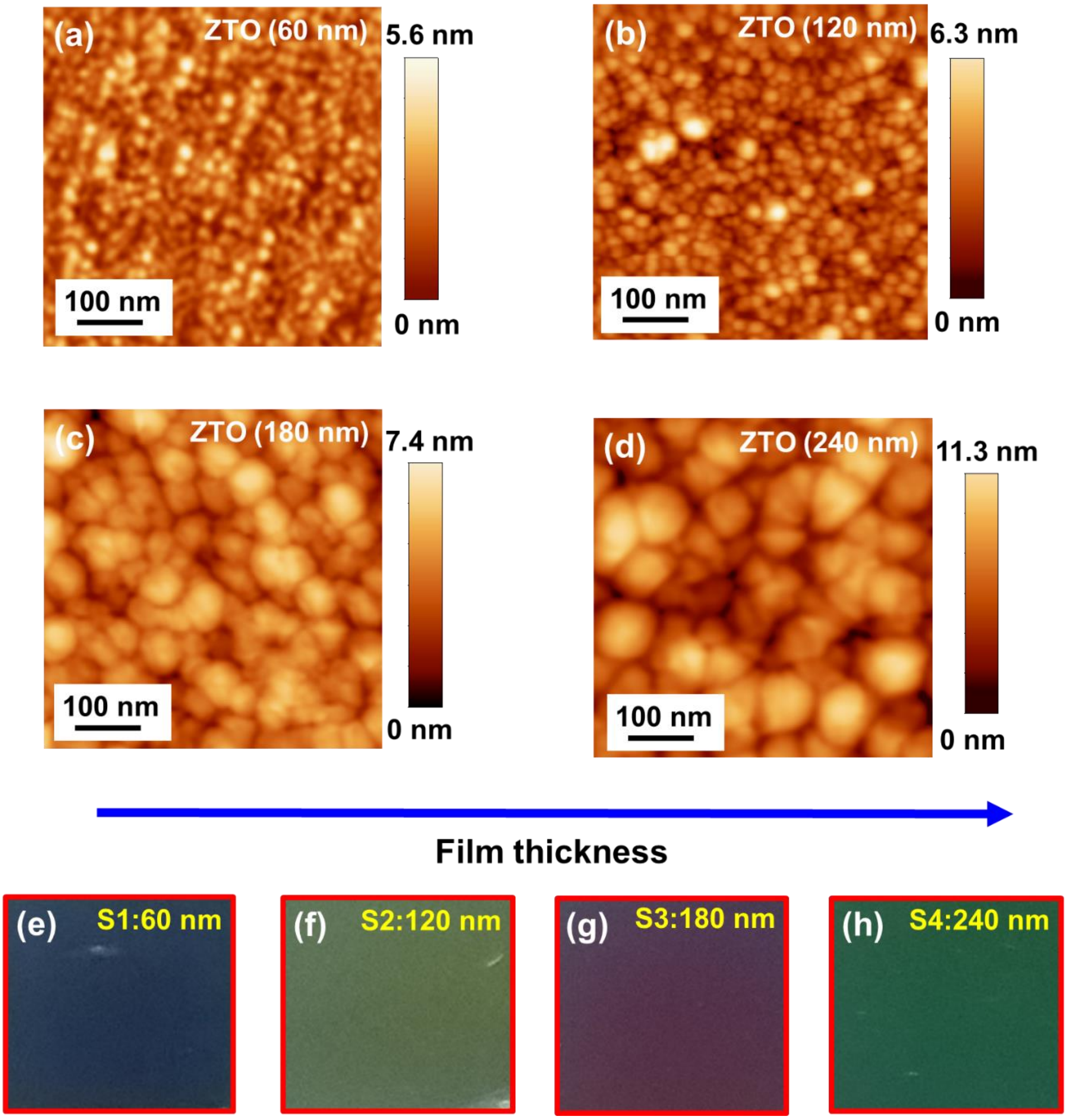

Figure 3.4: AFM images of ZTO films deposited on Si: (a) S1, (b) S2, (c) S3, and (d) S4, respectively. (e)-(h) The corresponding digital photographs of the films having a thickness of 60, 120, 180, and 240 nm, respectively.

182 nm (which is close to the corresponding thickness values measured by the surface profilometer) for S1 and S3, respectively with uniformly distributed grains throughout the layers. Since structural properties of a thin film play a vital role in determining its optical and electrical properties, we now go on to describe the results obtained from the structural properties of the films along with their optical band gap and *I-V* characteristics.

XRD studies are performed on ZTO films under similar conditions to study their crystalline

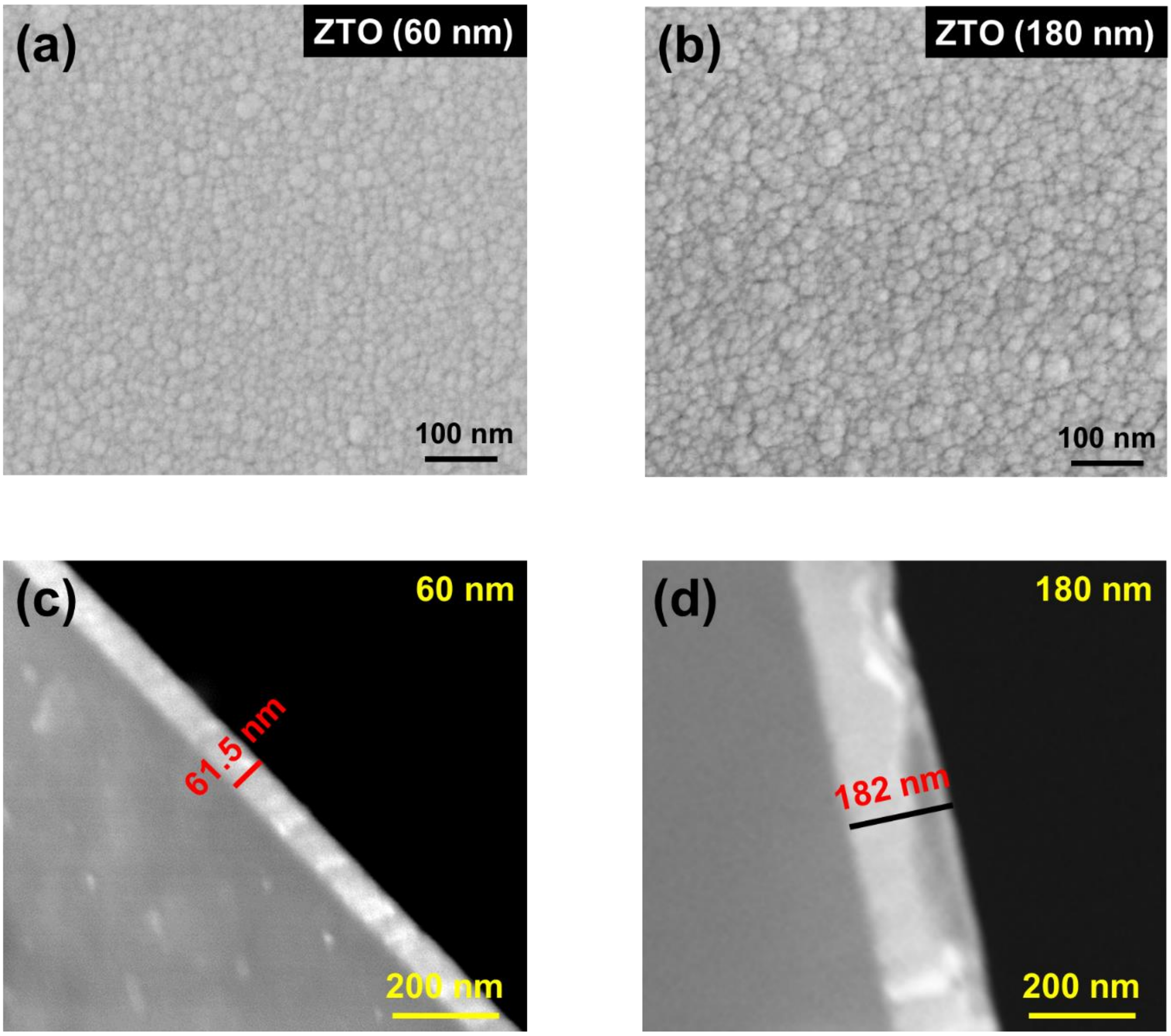

Figure 3.5: (a) and (b) Depict plan-view SEM images of 60 and 180 nm, respectively where (c) and (d) show cross-sectional SEM images of S1 and S3, respectively.

nature. From Fig. 3.6(a), the absence of any peak corresponding to ZTO, SnO_2, or ZnO phase(s), it can be inferred that all ZTO films are amorphous in nature [5,6]. Further, micro-Raman spectroscopy is used to study the structural property of ZTO films. Room temperature micro-Raman spectra of all the ZTO films are depicted in Fig. 3.6(b). These spectra show the presence of a series of vibrational modes around 229.45 cm^{-1}, 302.50 cm^{-1}, 434.6 cm^{-1}, 620.27 cm^{-1}, 669.36 cm^{-1}, and 826.01 cm^{-1}, whereas the Raman peak at 521 cm^{-1} is attributed to the Si substrate [4]. The observed Raman lines can be understood by considering the different vibrational modes $1A_{1g}$, $1E_g$, E (LO), and $3F_{2g}$ of ZTO [8]. In all the spectra, the Raman mode around 229.45 cm^{-1} is quite weak which may be appearing due to the overlapping effect of

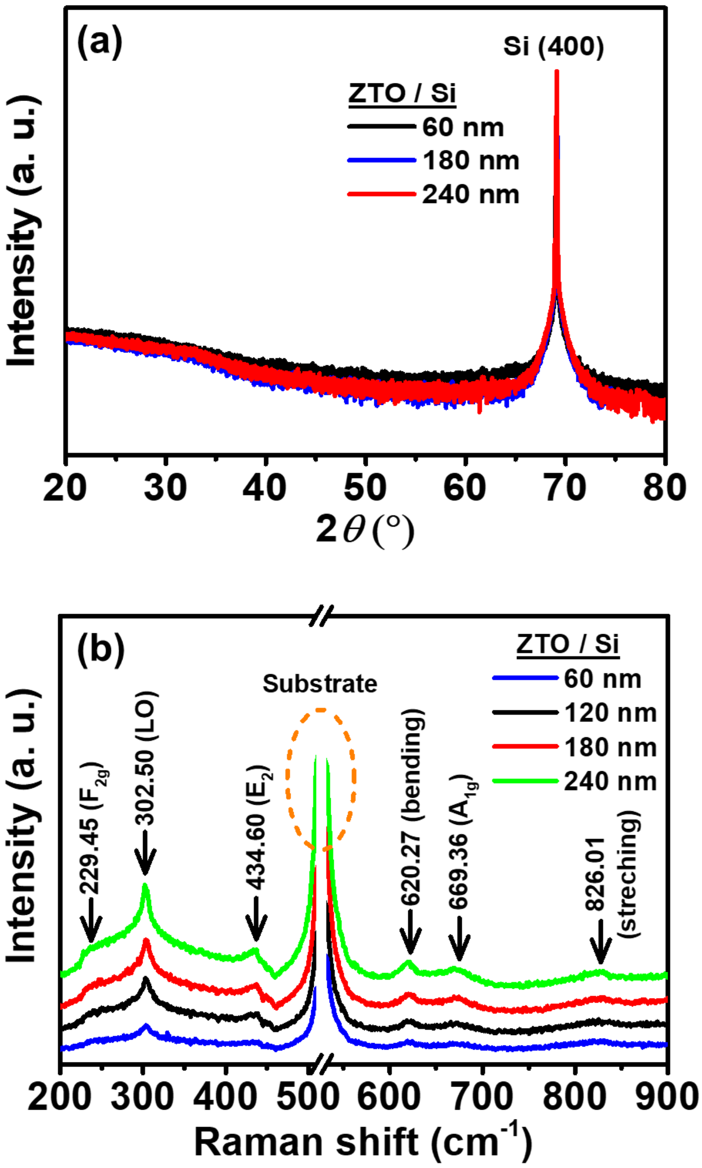

Figure 3.6: (a) and (b) depict XRD and micro-Raman spectra of ZTO films, respectively grown at 50° and at room temperature.

laser-induced plasma and can be reasonably assigned to F_{2g} [6]. On the other hand, The Raman band at 302.50 cm^{-1} can be assigned to E(LO) symmetries in $ZnSnO_3$, whereas the peak at 434.6 cm^{-1} belongs to E_g symmetries in ZTO. The main characteristics Raman peak of ZTO appears at 669.36 cm^{-1} which is a signature of its amorphous nature and can be assigned to A_{1g} vibrational mode. The bending mode of M-O-M bonds, where M represents either Zn or Sn atoms present in the ZTO, appears at 620.27 cm^{-1}, whereas the Raman mode at 826.01 cm^{-1} corresponds to the stretching mode of M-O-M bonds [7,8]. Notably, the peak intensities increase with increasing film thickness. This attributes to the minimization of point defects in the film. The broadening of the peaks indicate the typical feature of nanoscale materials. The observed results are consistent with the XRD results mentioned above. In addition, no Raman modes corresponding to any other phase such as ZnO, SnO_2, SnO is observed [6].

In order to identify the surface valance states, XPS measurements are carried out on selective samples. All high-resolution XPS spectra are deconvoluted with Gaussian curve fitting with the Shirley-type baseline corrections [26]. The survey spectra (not shown) of all the ZTO films reveal the presence of only Zn, Sn, O, and C, indicating the absence of any impurity in the samples. For instance, Fig. 3.7(a)-(c) depict high-resolution XPS data for S1 corresponding to Zn 2*p*, Sn 3*d*, and O 1*s* core level spectra grown on Si substrate, respectively. The emission from Zn 2*p* core levels exhibit two intense peaks at 1044.96 and 1021.85 eV for Zn $2p_{1/2}$ and Zn $2p_{3/2}$, respectively as seen in Fig. 3.7(a) and is highly consistent with the highest oxidation state of Zn (Zn^{2+}) [5,22]. The difference in the binding energies of Zn $2p_{1/2}$ and Zn $2p_{3/2}$ is found to be 23.11 eV which is the characteristics value of ZTO [22,27]. On the other hand, in Fig. 3.7(b), the energy levels located at 495.07 and 486.67 eV correspond to Sn $3d_{3/2}$ and Sn $3d_{5/2}$, respectively, which is in accordance with the Sn^{4+} oxidation state of Sn. It is important to note that Sn can exist in two oxidation states, viz. Sn^{2+} or Sn^{4+} corresponding to *p*-SnO and *n*-SnO_2 [22]. However, in the present case, Sn $3d_{5/2}$ shows only one component at 486.67 eV, ruling out the coexistence of SnO and SnO_2 phases. Likewise, individual O 1*s* peak is deconvoluted to have two distinct curves centered around the binding energies of 530.29 and531.64 eV. The lower binding energy peak at 530.29 eV is attributed to O atoms at regular sites (O_L) associated with Zn-O or Sn-O bonds [11]. On the other hand, the peak at higher binding energy of 531.64 eV is associated with the oxygen-deficient states (O_V). The percent concentration of O_L and O_V turns out to be 61.67% and 38.33%, respectively for S1 film. Moreover, the atomic ratio of Sn/O is calculated from the Sn 3*d* and O 1*s* peaks by taking into

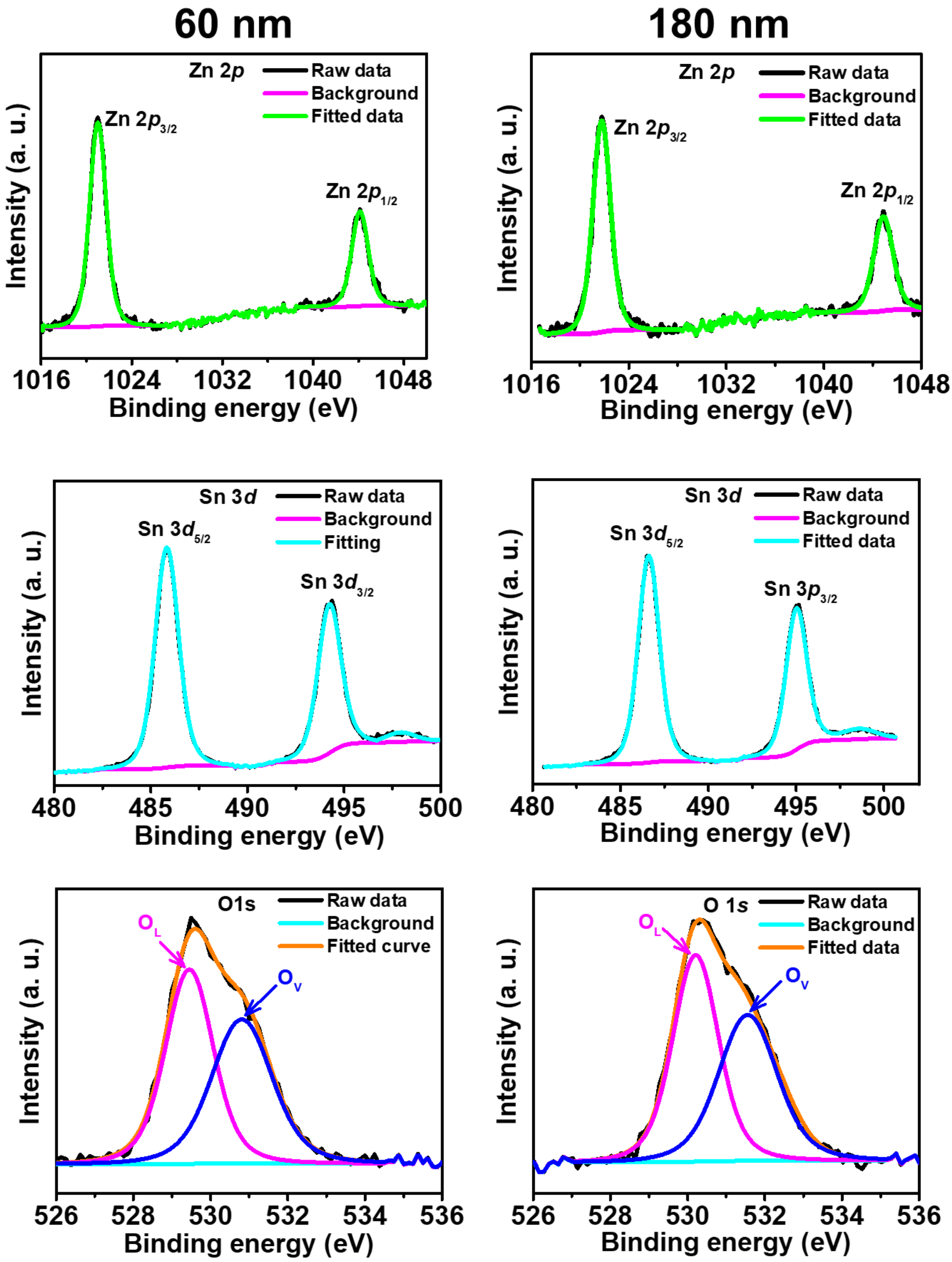

Figure 3.7: (a)-(c) and (d)-(f) present XPS spectra of Zn 2*p*, Sn 3*d*, and O 1*s* core level spectra of S1 and S3, respectively.

consideration atomic sensitivity factors and is found to be 1:1.31 which implies that the ZTO sample is oxygen-deficient. The XPS results are summarized in Table 3.2.

In case of S3, it is observed that the binding energies of Zn 2$p_{1/2}$ and Zn 2$p_{3/2}$ peaks are centred around 1044.88 and 1021.77 eV, respectively as depicted in Fig. 3.7(d). On the other hand, in Fig. 3.7(e), Sn 3d core level exhibits two peaks at binding energies of 495.01 and 486.61 eV for Sn 3$d_{3/2}$ and Sn 3$d_{5/2}$, respectively and it is also important to note that there is no coexistence of SnO and SnO_2 due to one component at 486.61 eV, resulting in the Sn^{4+} oxidation state of Sn [5,22]. In oxide materials, oxygen vacancies act as trap states and change the electrical properties. Following this, Fig. 3.7(f) depicts the XPS data of O 1s line and fitting of two distinct curves centered around the binding energies of 530.20 and 531.53 eV which correspond to O_L and O_V, respectively. The percent concentration of O_L and O_V in case of S3 turns out to be 51.44% and 48.56%, respectively and the atomic ratio of Sn/O is calculated from Sn 3d and O 1s peaks by taking into consideration atomic sensitivity factors and is found to be 1:1.34 which implies that the specimen S3 is also oxygen-deficient [11,22]. From the above discussion, it is observed that there are nominal shifts in the binding energies corresponding to Zn and Sn peaks for 180 nm-thick with respect to 60 nm-thick film, as is tabulated in Table 3.2. This shift in the binding energy may be due to a change in the grain size of these ZTO films as is observed from our AFM and SEM data. In addition, it is observed that the relative concentration of oxygen vacancies decrease with increasing film thickness, probably resulting in a decrease in the carrier concentration and the thicker films have more oxygen vacancies than the thinnest one [5,28].

Further to the above measurements, transmittance and optical band gap of ZTO films are carried out for all ZTO films (i.e. S1-S4) thicknesses as shown in Fig. 3.8(a) (in the wavelength range of 300 to 1200 nm). From Fig. 3.8(a), it is observed that the average transmittance of all ZTO films is greater than 80% (in the visible region). In addition, a sharp decrease in the transmittance around 370 nm can be attributed to the fundamental absorption edge of ZTO [9]. It is interesting to note that the average transmittance decreases slightly with increasing film

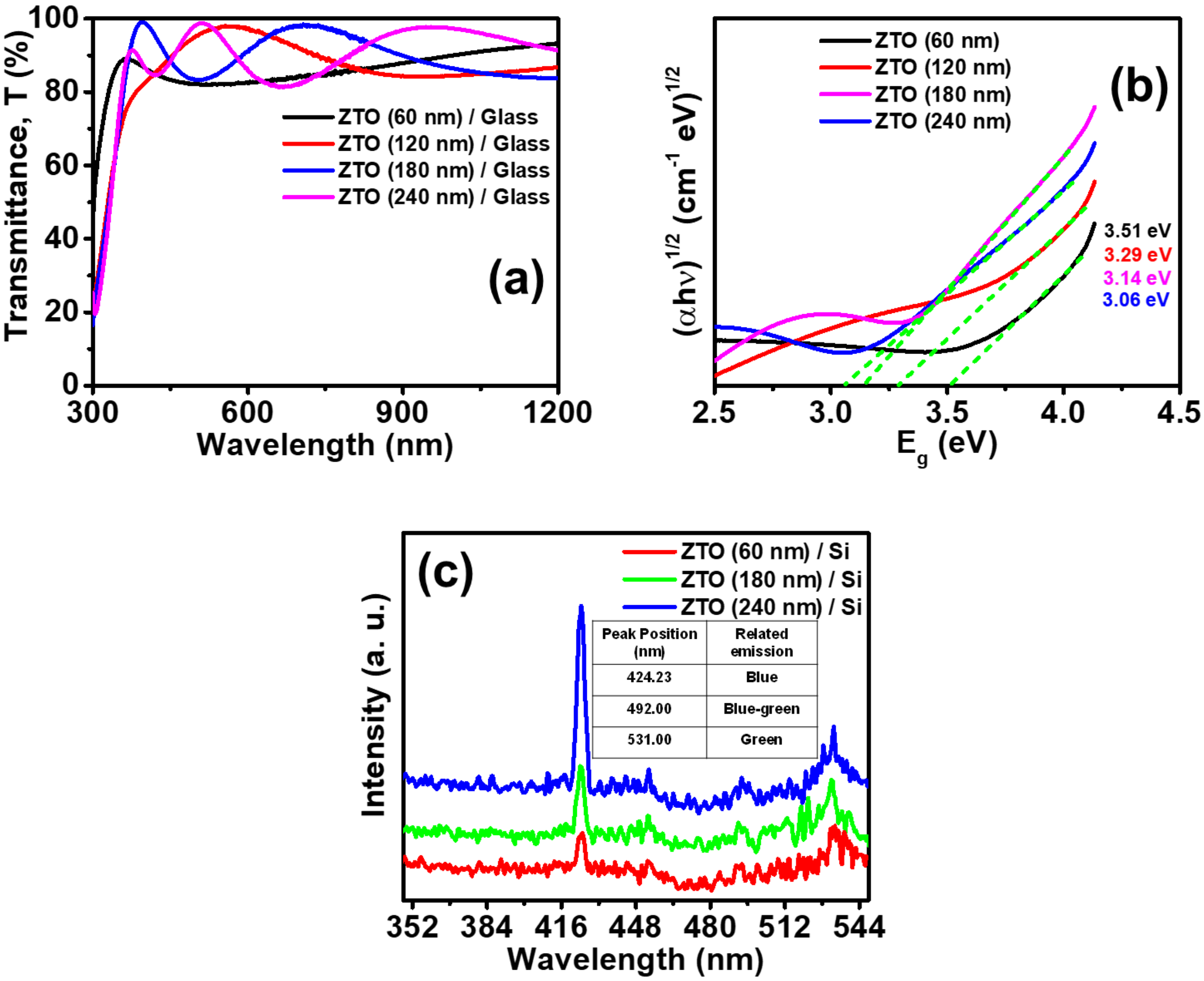

Figure 3.8: (a) and (b) Show the optical transmittance spectra and Tauc's plot of ZTO thin films, respectively, whereas (c) shows the selective PL spectra of ZTO films.

thickness in the visible region. This observed result is due to typical thickness effect (Beer-Lambert's Law) [29]. According to this, due to longer optical paths lengths, the absorption of light increases in films having higher thickness values [30]. In addition, the optical band gap of ZTO films is calculated using Tauc's Eq. (3.1). As a matter of fact, the optical band gap is extracted by extrapolating the straight line portion of $(\alpha h\nu)^{1/2}$ verses $h\nu$ plot, where is α is the optical absorption coefficient and $h\nu$ is the photon energy [10]. Figure 3.8(b) shows the optical band gap data of S1, S2, S3, and S4 grown on glass substrates. It is found that the 60 nm-thick ZTO film has a band gap of 3.51 eV which reduces to 3.3 eV in case of 240 nm-thick film [11]. Firdausa *et al*. have shown that the band gap of TiO_2 decreases with increasing oxygen vacancies [28,31]. In the present case, the band gap of ZTO films decreases with an increase in the film thickness because thicker films have more oxygen vacancies than the thinner ones. In fact, from XPS studies, it is observed that the 180 nm-thick film (i.e. S3) have more oxygen vacancies than that of the 60 nm-thick film (i.e. S1).

Figure 3.8(c) shows the photoluminescence spectrum of ZTO films with an excitation wavelength of 320 nm. As seen from the spectra, a strong and stable blue peak appears which is centered at around 424.23 nm [32]. In addition, the broad peaks, ranging from 480 to 500 and 520 to 540 nm with a maximum at 492 and 531 nm, respectively belong to the blue-green and green emission, respectively [6]. It has been reported that the optical band gap of bulk ZTO is 3.6 eV (at RT) [9]. So, the blue, blue-green, and green emission lines observed here are not associated to band-to-band emission peak (~360 nm). In the previous reports on ZTO films, the PL peaks have generally been attributed to other luminescence centers such as oxygen vacancies and growth induced strain [6,32–34]. From our XPS studies (Table 3.2), it is observed that oxygen vacancies are present in the film which increases with increasing film thickness. These oxygen vacancies induce the formation of new energy levels in the band gap of ZTO films. Thus, the observed emissions are generated from the recombination of photo excited holes with an electron occupying an oxygen vacancy. Moreover, from the deep energy levels the emission moves to a longer wavelength and hence the blue, blue-green, and green light emissions are observed [33,35]. However, the absence of any band-to-band transition in the PL spectra may be due to the thermal quenching effect and the UV emission, related to the band-to-band transition, is too weak to be detected at RT [34]. This clearly indicates that the PL emission in ZTO films originates from oxygen vacancies. In order to investigate the possibility of potential barrier formation at the metal electrode and the grains as well as the grain boundaries present in the ZTO films (which can affect the performance of the devices), KPFM measurements are carried out.

Contact potential difference (V_{CPD}) of the ZTO films are measured using KPFM. Figures 3.9(a) and (b) depict the V_{CPD} map of the ZTO films having thickness of 60 and 180 nm, respectively. The samples exhibit a distinct variation in the V_{CPD} maps as a function of film thickness. It is quite interesting to note that with increasing film thickness V_{CPD} increases. The KPFM technique is used to measure the V_{CPD} of the ZTO films which can be converted into the work function of the films using following Eq.: $V_{\mathrm{CPD}}=(\phi_{\mathrm{tip}}-\phi_{\mathrm{sample}})/e$, where ϕ_{tip} is the work function of tip, ϕ_{sample} is the work function of sample, and e is the electronic charge. The measured work function of ZTO films is seen to decrease from 5.04 to 4.94 eV with increasing film thickness from 60 to 240 nm, respectively as shown in Fig. 3.9(c) [5]. Abbott *et al*. have observed the similar trend between grain size and work function. They have reported that with increasing grain size, work function of the film decreases due to the increasing fractional defect area in bigger grains [36].

For resistivity measurements, ZTO films are deposited on commercial soda lime glass slides under similar conditions (as on silicon substrates). Figure 3.9(d) shows the thickness-dependent variation in resistivity of ZTO films measured by the linear four probe method. The measured resistivity is 12.8×10^{-1} Ω-cm for S1 which drastically reduces to 2.0×6^{-1} Ω-cm for the S2, whereas it remains almost constant for the thicker films, viz. S3 and S4 [37,38].

In general thickness-dependent resistivity for the conventional ITO and AZO TCOs are attributed to a change in the grain size and grain boundary density with increasing thicknesses[19]. However, in the present study this interpretation is inappropriate because all ZTO films are amorphous. Because amorphous materials possess short-range ordering due to variations in bond length, bong angle, and other factors and can increase the carrier scattering [1]. At the same time, oxygen vacancies can increase the number of charge carriers and in turn improve the resistivity of ZTO films [39]. On the other hand, the *I-V* characteristics of all Ag/ZTO/Si/Ag heterojunction diodes show a rectifying behaviour, as are shown in Fig. 3.9(e).

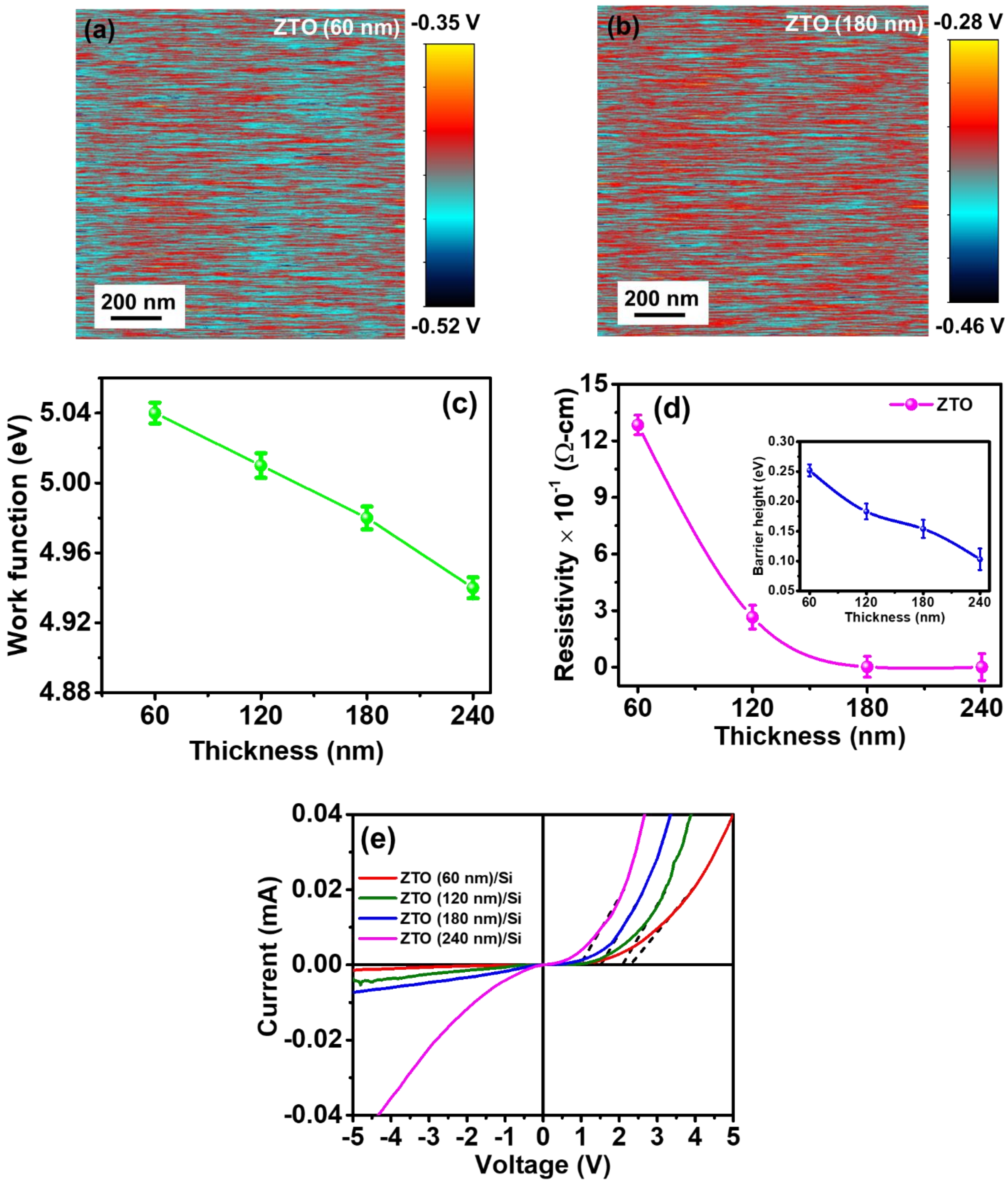

Figure 3.9: (a) and (b) The V_{CPD} map of the ZTO films having thickness 60 and 180 nm, respectively. (c) The thickness-dependent variation in the work function of the ZTO films. (d) Variation in the resistivity of ZTO films as a function of thickness whereas the inset depicts the variation of barrier height. (e) Show thickness-dependent current-voltage plot of all ZTO/Si heterojunctions.

The diode parameters such as ideality factor, leakage current, and turn-on potential are calculated using the respective *I*-*V* characteristics. As a matter of fact, the ideality factor and leakage current can be obtained from the following Eq. [10]:

$$I = I_s\left[exp\left(\frac{qv}{\eta k_B T}\right) - 1\right], \tag{3.2}$$

where q is the electronic charge, V is the applied voltage, η is the ideality factor of the heterojunction, k_B is the Boltzmann constant, T is the absolute temperature, and I_S is the reverse saturation current. Eq. (3.2) can be written as [10]:

$$\frac{dV}{d(\ln I)} = IR_s + \eta\frac{k_B T}{q}, \tag{3.3}$$

where R_S is the series resistance. The y-axis intercept of $[dV/d(\ln I)]$ versus I plot provides $\eta k_B T/q$. The calculated values of ideality factor, reverse saturation current, and the turn-on potential for all the films (i.e. S1-S4) are summarized in Table 3.1. The high value of ideality factor (e.g. 3.20 corresponding to S4) can be attributed to the presence of native oxide layer between ZTO and Si interface. In addition, a large lattice mismatch between the ZTO layer and Si substrate can also lead to an increase in the ideality factor [19]. As the ZTO/Si interface plays a vital role in carrier injection, ZTO thickness-dependent increase in ideality factor is most likely associated with the minority carrier injection and recombination [19]. This is also consistent with the increase in the reverse saturation current with increasing ZTO film thickness which in turn supresses the turn-on voltage by decreasing the barrier height at the ZTO/Si interface. In order to determine the barrier height, we have performed *C-V* measurements at 1 MHz under a forward and reverse bias sweep of -2 to 2 V. The inset of Fig. 3.9(d) depicts the ZTO film thickness-dependent change in barrier height where it decreases from 0.25 to 0.10 V as the film thickness increases from 60 to 240 nm. From the above results, it can be inferred that the ZTO/Si heterojunction diode parameters are strongly influenced by the thickness of ZTO films. As a matter of fact, a decrease in the barrier height with film thickness can enhance the minority carrier recombination probability, leading to an increase in the reverse saturation current. In case of ZnO:Al/Si heterojunction, Kumar *et al.* have shown that with increasing grain size barrier height decreases and in turn trap density reduces [19]. In addition, the mean free path of electrons increase with increasing grain size which in turn reduces the scattering loss and trapping of charge carriers [5,19]. In the present case, the grain size of ZTO films increases with increasing film thickness which reduces the scattering loss and trapping of charge carriers, leading to a decrease in the resistivity of ZTO films with increasing film thickness.

3.2.4 Conclusions

In conclusion, we have undertaken RT growth of ZTO films having different thicknesses and demonstrated the effect of grain size on their optoelectronic properties. The variation in the grain size with increasing ZTO film thickness is obtained from AFM and SEM data, whereas XRD results show the amorphous nature of ZTO films and micro-Raman measurements exhibit the presence of different Raman modes of amorphous ZTO. On the other hand, XPS data reveal the presence of zinc and tin along with oxygen vacancies and it is seen that the oxygen vacancy increases with increasing film thickness. In addition, the optical transmittance of all ZTO films, in the visible region, is found to be more than 85%, while PL measurements exhibit three different emissions, viz. blue, blue-green, and green. A continuous change in the work function with film thickness is also observed. This follows a sharp decrease in the resistivity was found with increasing ZTO thickness due to a change in scattering of charge carriers from grain boundaries. Further, the *I-V* characteristics of ZTO/Si heterojunctions exhibit rectifying properties and a systematic reduction is observed in the turn-on potential with increasing ZTO film thickness which corroborates well with the observed thickness-dependent behaviour of barrier height of the heterojunctions.

3.3 Local probe microscopic studies on zinc tin oxide: Band mapping across a metal-semiconductor junction

3.3.1 Introduction

Zinc tin oxide has attracted considerable attention because of its unique electrical and optical properties [40,41]. Its unique properties make it suitable for a variety of applications such as transparent conducting oxide, active layer in transparent thin film transistor, anode material for Li-ion batteries, photoelectrical devices, sensors, photocatalysts, etc. [42–47]. The above mentioned all applications need a high mobility material with large area uniformity and good environment stability at a low cost. ZTO offers high electron mobility (> 10 cm^2 V^{-1} s^{-1}) due to its inherent electronic configuration $(n\text{-}1)d^{10}ns^{0}$ ($n \geq 4$) [48]. Thus, in order to realize the universal applications of ZTO, the key point is to fabricate on large scale at low cost and understanding the charge transport in the device. ZTO thin films are grown by various methods such as thermal evaporation, sputtering, pulsed laser deposition, and sol-gel [40,45,49,50]. In most of the growth techniques, during the film growth, isolated islands coalesce and the formation of grain boundaries (GBs) take place depending on the thermodynamic driving forces [51–53]. These GBs produce a large number of defects or create band-bending at the interface [54]. However, too many defects or trap levels can influence the physical properties of a device and in turn lead to instability during its operation [55,56].

For high performance and stable device operation, it is important to understand the charge transport within the layer and the nature of an interface/junction [57,58]. In general, the interface/junction between two dissimilar materials creates a band offset due to a difference in the work function of contact and active material, which in turn generates an electrostatic potential barrier at the interface [10,59]. This potential barrier opposes the charge transport across the interface and as a result the performance of the device deteriorates. Hence, the offset at the interface of a heterostructure is important from the point of engineering of nanostructures and it strongly depends on the Fermi level or the work function of the same. In addition, it is also known that defects at the GBs create local band-bending which can further influence the performance of a device [51,54]. In fact, Azulay *et al*. have shown that the presence of potential barrier at GBs enhances the performance of CIGS solar cells by collecting the minority carriers at GBs [53]. The band-banding at GBs in oxide materials has been investigated by various direct/indirect methods [54,58,60,61]. For instance, Kumar *et al*. have studied the effect of polarization on charge transport and shown a direct evidence of band-banding at the GBs of Al-doped ZnO thin films [54]. Thus, ZTO being a suitable candidate for PV industry, a direct evidence of band mapping across the junction and the experimental determination of the barrier height at the ZTO-metal interface is yet to be explored. This study is not only important from a fundamental point of view but also to design advanced functional electronic devices.

To probe the local properties at GBs and band mapping across the junction scanning tunneling microscopy have so far been the most powerful technique [54,58,62–64]. For instance, Bera *et al*. have demonstrated the mapping of band-edges across a single junction between *p*-type Cu_2S and *n*-type CdS using scanning tunneling microscopy, which requires ultrahigh vacuum conditions [58]. In another report, the authors have shown the accumulation of carriers at GBs which creates a defect state below the conduction band, affecting the electron transport in the device [65]. Thus, the growing need of spatially resolved charge transport and band-bending at GBs for semiconductor materials has led to the requirement of another technique. In this regard, various modes of scanning probe microscopy have made it suitable to study the above mentioned properties at nanoscale under ambient conditions [66]. One can build up information on the local charge transport, band-banding at GBs, and band mapping across the junction using different modes of scanning probe microscopy such as Kelvin probe force microscopy (KPFM), electrostatic force microscopy (EFM), and conductive atomic force microscopy (cAFM) [66]. Recently, Kumar *et al*. have shown the impact of GBs on local charge transport properties in Al-doped ZnO films using scanning probe microscopy [54].

In this work, we show the roles of charge trapping in the local band-bending of ZTO thin films at grain boundaries. Since the overall charge transport is controlled by defects at the grain boundaries**,** to understand nanoscale transport properties in ZTO films, we have used KPFM, EFM, and cAFM. Further to this, the role of charge trapping in nanoscale charge transport at grains and grain boundaries is also demonstrated by performing local *I-V* measurements using cAFM. Apart from this, we have used these local probe techniques to understand the nature of potential barrier at the metallic-semiconductor interface and have experimentally measured band mapping across the junction. The present study helps to understand the barrier formation at GBs and the nature of potential barrier at the interface of ZTO films.

3.3.2 Experimental

ZTO thin films were grown on ultrasonically cleaned Pt/TiO_2/SiO_2/Si (Platinized-Si, Radiant Technology, UK) and Si substrates at RT using an RF magnetron sputtering setup (Excel Instruments, India). Similar experimental conditions and the same commercially available target (as described earlier) was used for the growth of ZTO thin films. Phase identification and the nature of crystallinity of the films were carried out by x-ray diffraction (XRD) (Bruker, D8-Discover, Germany) under the Bragg-Brentano geometry using a Cu-K_α radiation (λ=0.154 nm) over a 2θ scan range of 20°-80°. To check the vibrational properties, micro-Raman measurements were performed using micro-Raman spectrometer (Horiba Jobin Yvon, Japan) under the back scattering geometry, as described earlier. Surface morphology and local electrical measurements of ZTO films were examined by an *ex-situ* AFM (MFP-3D, Asylum Research, USA) in different modes using conductive tips (AC240TM, Electro-Lever, Olympus) having ~20 nm radius of curvature, ~2 N m^{-1} stiffness, and a resonance frequency of 70 kHz. Further, KPFM and EFM measurements were performed at RT in the lift mode with a lift height of 50 nm from the surface of the film, whereas cAFM was performed in the contact mode. It is important to mention here that the local electric transport properties at nanoscale, performed by cAFM measurements, strongly depend on the applied force. Hence, the spring constant of the tip and the detector sensitivity were calibrated with the help of a quartz crystal.

These helped us to find out a relation between the set points and the applied force and we used a fixed set point (applied force ∼20 nN) during all cAFM measurements. In fact, the use of a constant force set point reduced the possibility of introducing tip-related artefacts to a significant extent [54]. It may be mentioned that KPFM, EFM, and cAFM measurements were performed at large number of randomly chosen places with different scan speeds, ranging from 0.2 to 1 Hz at various scan angles by rotating the samples. However, no noticeable change was found in the results, confirming the absence of tip-related artefacts in the present data. On the other hand, band mapping across the junction was carried out in KPFM mode.

It is observed that the electrical transport properties at nanoscale strongly depend on the environment. Therefore, a low humidity environment was always maintained surrounding the main AFM setup [54]. In fact, the used AFM system was kept in a closed, low-vibration, and low-humidity enclosure filled with sufficient amount of humidity absorber (silica gel bead-filled packets), which reduced the humidity level (close to 15%, as was measured by a commercially available and calibrated humidity meter) within the same. Such a low humidity level was comparable to the one created by dry nitrogen (≈8–10%) and thus, in this study, humidity-related issues might be safely considered as negligible to induce adsorbed water molecule-related artefacts during current measurements and alter their lateral resolution [67]. To perform the local *I-V* measurements, a Pt-coated conductive tip was used as the top electrode, whereas Platinized-Si substrate was used as the bottom electrode. This led to the formation of Pt/ZTO/Platinized-Si heterojunctions. All recorded images were analyzed using WSxM [25] and commercially available SPIP [68] softwares.

3.3.3 Results and discussion

It is well-known that nanoscale electrical transport properties of a material strongly depend on its morphology and structural properties [54,57]. Thus, besides local probe measurements, SEM and micro-Raman measurements are also recorded. Figure 3.10(a) shows the plan-view

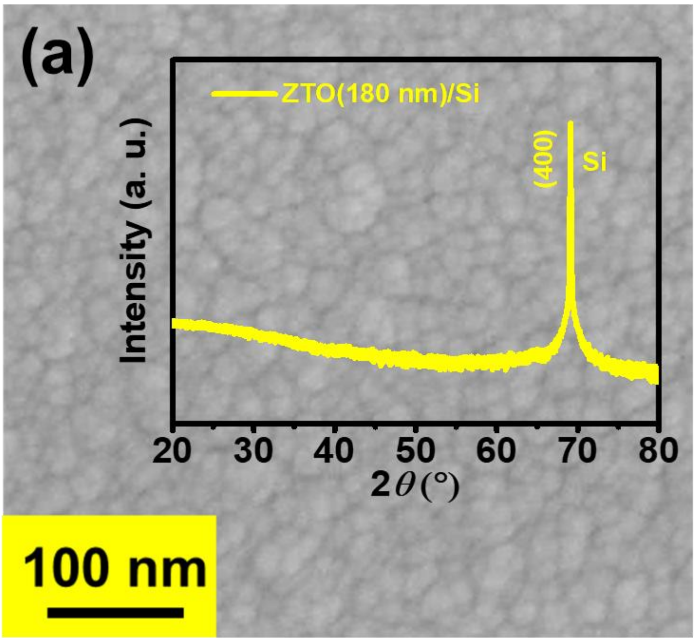

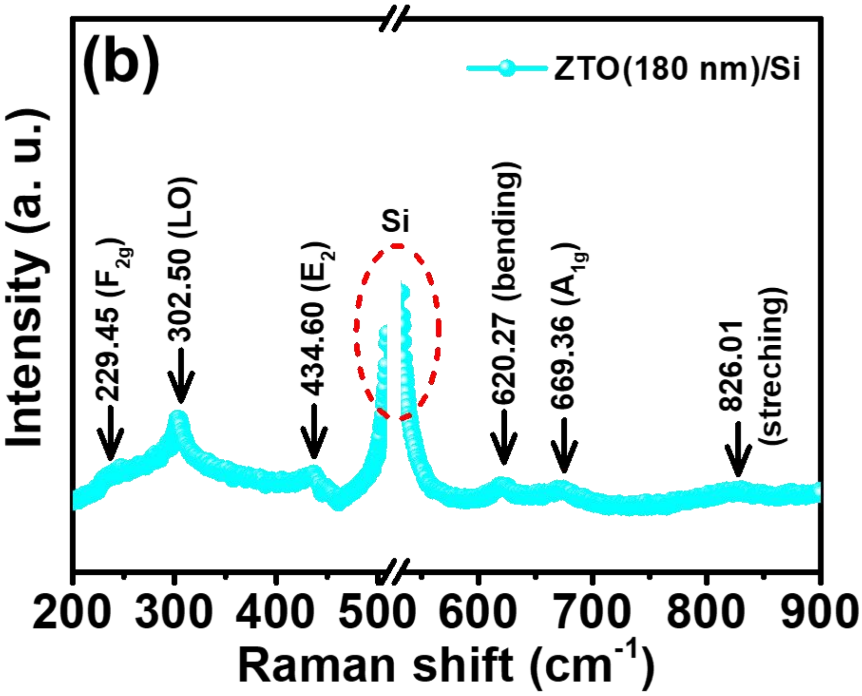

Figure 3.10: (a) Depicts plan-view SEM image of a 180 nm-thick ZTO film deposited on platinized-Si, (b) Micro-Raman spectrum of the same ZTO film whereas the inset shows the XRD data.

SEM image of a ZTO film (180 nm-thick) which clearly depicts the uniformly distributed grains where the average grain size is found to be 54 nm. In addition, XRD data [the inset of Fig. 3.10(a)] reveal the amorphous nature of ZTO films [5]. On the other hand, Fig. 3.10(b) shows the micro-Raman spectrum, confirming the growth of the ZTO film. Figure 3.10(b) shows a series of Raman lines centered around the following frequencies: 229.45, 302.50, 434.6, 620.27, 669.36, and 826.01 cm^{-1}. The strong Raman mode at 521 cm^{-1} is attributed to the Si substrate [4]. The other observed Raman lines belong to different vibrational modes $1A_{1g}$, $1E_g$, E(LO), and $3F_{2g}$ of ZTO films. The Raman mode situated at 229.45 cm^{-1} is quite weak which may be caused by laser-induced plasma and can be assigned to F_{2g} [6]. On the other hand, the Raman mode at 302.50 cm^{-1} belongs to E(LO) symmetries of $ZnSnO_3$, whereas the peak at 434.6 cm^{-1} can be assigned to E_g modes. The Raman peak appearing at 669.36 cm^{-1} is the signature of the amorphous phase of ZTO and can be assigned to the A_{1g} vibrational mode. On the other hand, bending and stretching modes of ZTO appear at 620.27 and 826.01 cm^{-1}, respectively. The broadening of the Raman peaks indicate the feature of nanoscale materials. In addition, no Raman modes corresponding to ZnO, SnO_2, and SnO phase is observed, indicating the absence of any secondary phase in the film [6].

Figure 3.11 shows the combined results of AFM, EFM, and cAFM. Figure 3.11(a) depicts the schematic of working principle of EFM and cAFM. Prior to the local probe measurements, the surface morphology of ZTO films is investigated by AFM in tapping mode. Figure 3.11(b) gives the topographic information, showing the granular nature of ZTO film. The observed average grain size is found to be 56 nm having a root mean square roughness of 1.04 nm. The inset of Fig. 3.11(b) shows a zoomed part of a small region from the marked black square region in Fig. 3.11 (b), which clearly depicts the formation of grains and GBs in the film. It is well-known that charge carrier density is found to be different at grains and GBs. To directly probe the accumulation of charge carrier or to map the charge carrier density locally, EFM is a widely used technique [54]. Figure 3.11(c) depicts the EFM image of a ZTO film which provides the distribution of electrostatic force on the surface. The present EFM image is recorded using a tip voltage of -4 V. In Fig. 3.11(c), the dark contrast represents weak repulsive

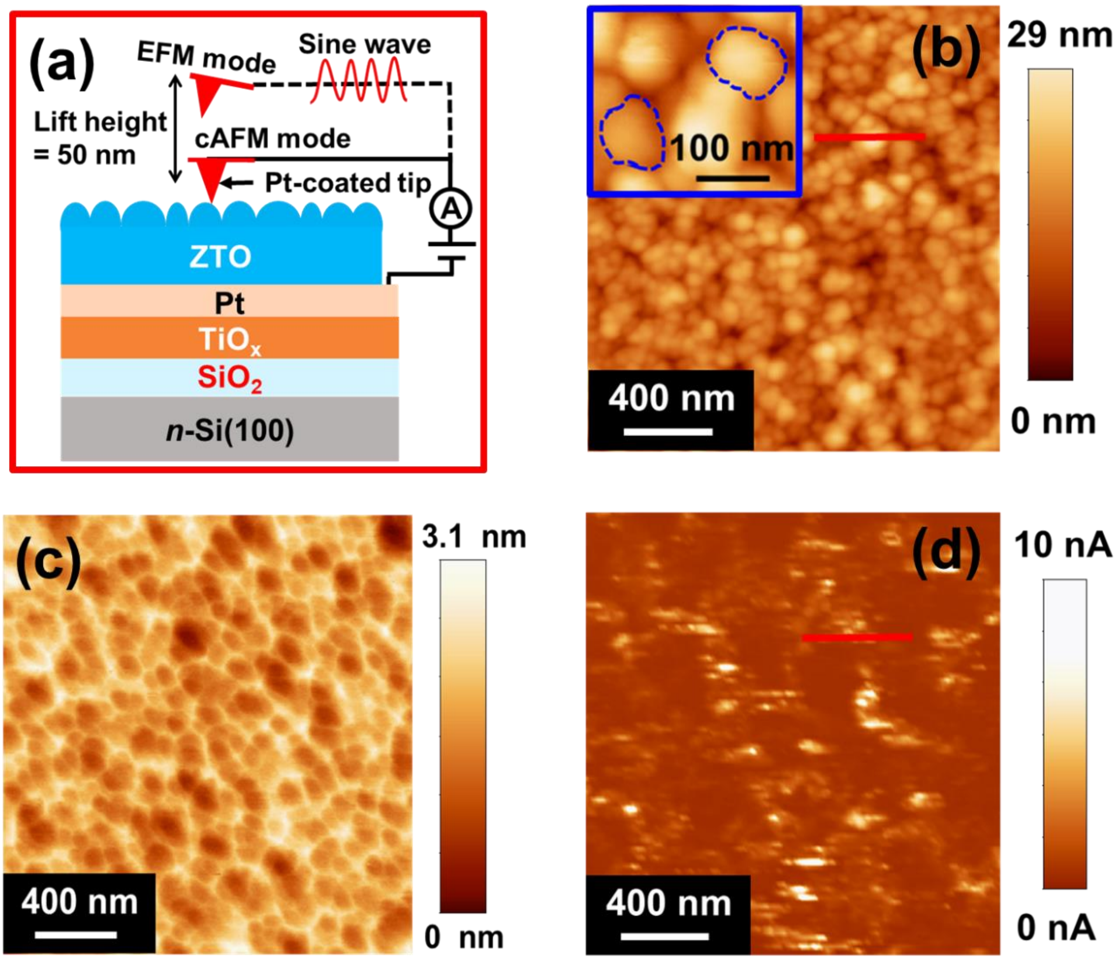

Figure 3.11: (a) Shows the schematic of the working principle of cAFM and EFM. (b) Depicts AFM topography of ZTO film taken in tapping mode, whereas the inset shows a magnified image, clearly depicting grains and grain boundaries. (c) EFM image of ZTO film corresponding to V_{tip}=-4 V, showing variation in the electrostatic interaction at grains and grain boundaries, whereas (d) shows cAFM image for V_{tip}=+6 V, depicting that bright zones are more conductive.

electrostatic interaction at the grains, while the bright contrast corresponds to the strong repulsive interaction at the GBs [69]. This variation in the intensity of ZTO films relates to the different accumulation of different amount of charges at the grains and GBs. The bright and dark regions indicate that different charge transport process takes place at grains and GBs. Generally, for the current mapping of a surface cAFM is extensively used because it can provide simultaneous information on the local current mapping and morphology of a surface with very high lateral resolution (5 nm in the topography and 1 pA in the current image) [70]. Figure 3.11(d) shows the current map of a ZTO film for a tip bias of +6 V, using cAFM technique. In the cAFM image, bright spots correspond to the current signal. Current map clearly depicts that grains have much higher current than GBs, which confirms the accumulation of charge carriers at GBs and GBs are not contributing in the current [54]. In order to further quantify the current at grains and GBs, two line profiles are drawn as shown in Figs. 3.12(a) and (b). The extracted line profiles from topography [Fig. 3.11(b)] and current map [Fig. 3.11(d)] are shown in Figs. 3.11(a) and (b), respectively which clearly depicts higher current at grains in comparison to GBs. To check the reliability, current profiles are extracted from various randomly chosen positions.

The accumulated charge carriers remain trapped at GBs and can create a space charge region, leading to a conduction band-bending at GBs [71]. Thus, in order to quantify the band-bending and to confirm the observed difference in the charge transport at grains and GBs, systematic *I-V* measurements were carried out. Using cAFM, one can perform the *I-V* measurements at any chosen place. Figure 3.12(c) shows the *I-V* characteristics measured at grain and GB using cAFM between the Pt tip and ZTO film, confirming the formation of a Schottky-like junction. The observed results further confirm a clear difference in the conductivity of a grain and GB. The current flowing through such a heterojunction shows a rectifying behaviour and *I-V* data of the same is used to calculate the barrier height. The Schottky barrier height (SBH) can be calculated using the following relation at a fixed temperature (T) [54]: $I_s \propto \exp(-\frac{\Phi}{nk_BT})$, where I_S is the saturation current, Φ is the Schottky barrier height, η is the ideality factor, and k_B is the Boltzmann constant. Using above expression, change in the barrier height ($\Delta\Phi$) can be calculated from the saturation current ratio in the forward bias by assuming that grains and GBs have similar contacts. Thus, based on the above assumption, $\Delta\Phi = nk_BT\, ln\left(\frac{I_{SG}}{I_{SGB}}\right)$, where I_{SG} is the saturation current at the grain and I_{SGB} is the saturation current at the GB. The calculated I_{SG} and I_{SGB} are found to be 54 and 32 pA, respectively from Fig. 4.11(d) and $\Delta\Phi$

turns out be 36 meV. $\Delta\Phi$ has been measured from a large number of randomly chosen places and the average value is found to be 36±12 meV. This variation in the SBH is due to grains and GBs, leading to a different electrical transport mechanism at the grains and GBs, which gets further fortified by cAFM measurements.

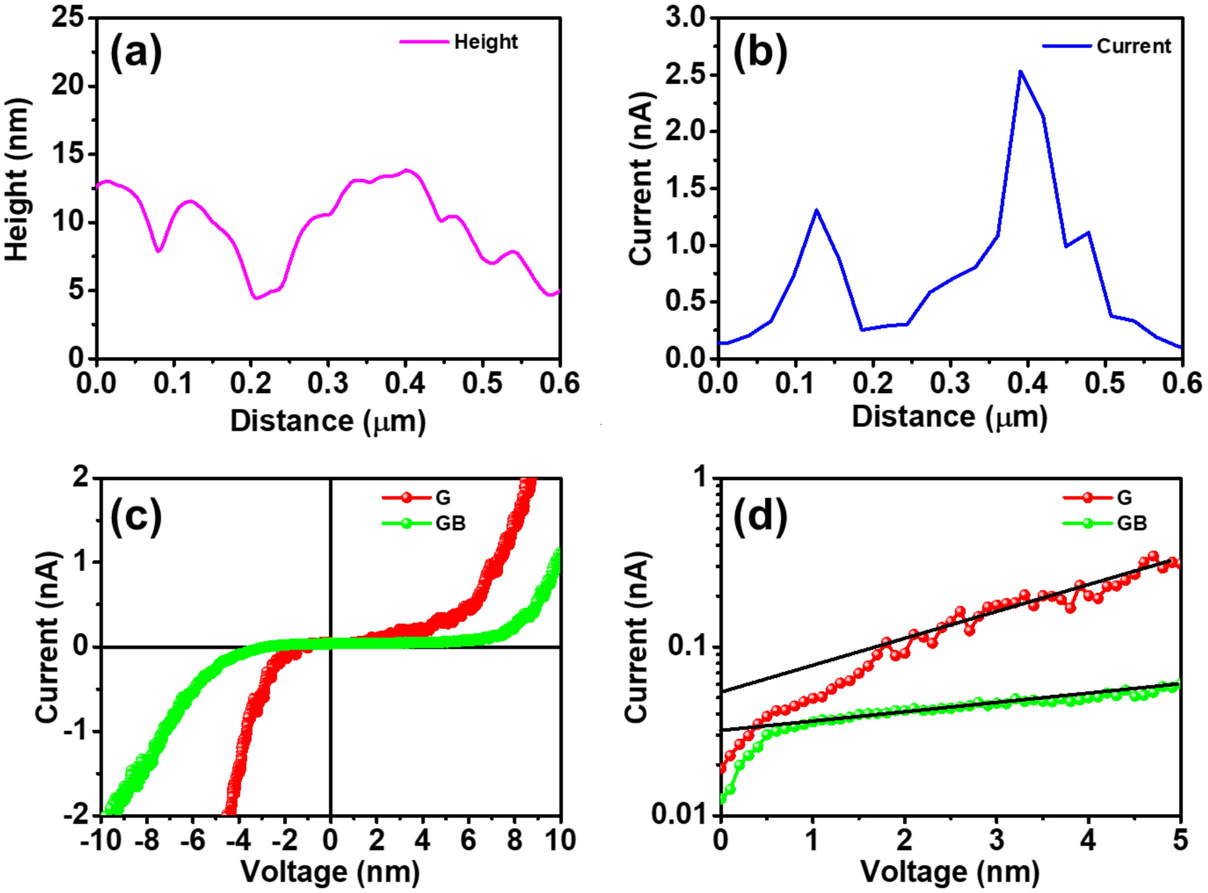

Figure 3.12: (a) and (b) Present the line profiles of the height image and the current map corresponding to Figs 3.11(b) and (d), respectively (showing higher current on grains). (c) *I*-*V* characteristics [obtained from cAFM image shown in Fig. 3.11(d)] of grain and grain boundary using cAFM tip, showing a rectifying behaviour. (d) Shows semi-log plot of forward *I*-*V* characteristics obtained from a grain and the grain boundary.

Before going for the band mapping across the junction, the surface potential of ZTO film is measured using KPFM. KPFM is known to measure the electrostatic interaction between the tip and a surface by applying an external dc bias on the sample [54,72]. This provides a contact potential difference (V_{CPD}) between the tip and a sample which is given by the following Eq. [57]: $V_{CPD} = (\Phi_{sample} - \Phi_{tip})/e$, where Φ_{sample} and Φ_{tip} are the work function of the sample and the tip, respectively. Like cAFM, this technique also provides one-to-one correlation between the surface topography and a variation in the surface potential or localized work function of the surface over a nanoscale region [66]. The topography and contact potential difference or surface potential distribution images of a ZTO films are depicted in Figs. 3.13(a) and (b), respectively.

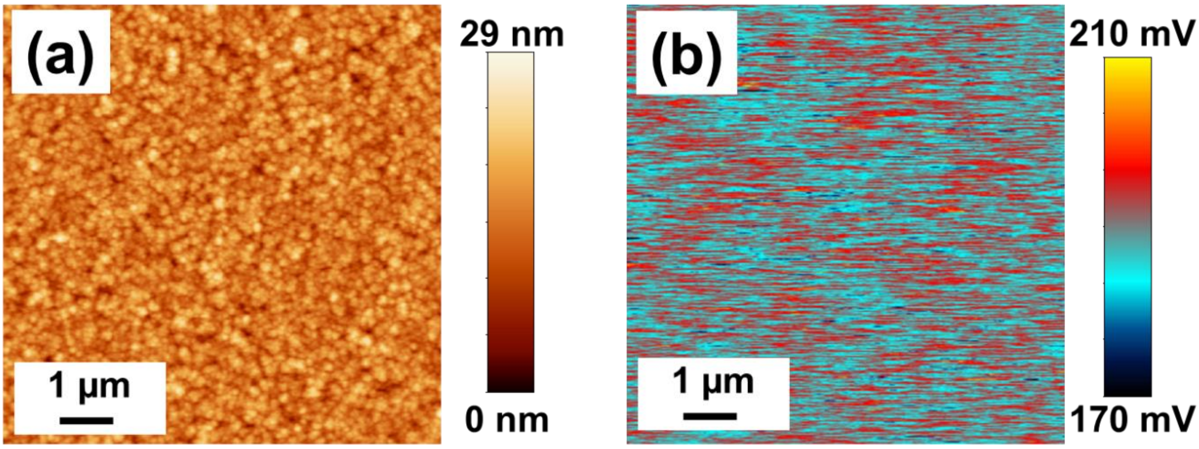

Figure 3.13: (a) and (b) depict an AFM topographical image of 180 nm-thick ZTO film and the corresponding localized surface potential difference map, respectively.

Figure 3.13(a) shows a uniform granular morphology, while Fig. 3.13(b) clearly depicts variation in the surface potential at the nanoscale. The measured work function of the ZTO film under consideration is found to be 4.98 eV. The observed variation in the local surface potential can be attributed due to the presence of grains and GBs. In the present case, it is very difficult to probe the work function at a single GB using KPFM technique due to the inherent instrumental limitation [54].

It is known that semiconductor heterojunctions are the fundamental building blocks for many device applications [10]. Thus, in order to carry out the band mapping across the junction, KPFM technique is used. Figure 3.14(a) shows an example of a ZTO heterostructure grown on the platinized-Si substrate. In this 3D AFM image, there is a sharp and uniform interface between the film and the substrate. Figure 3.14(b) depicts the band mapping across the metal-semiconductor junction. The most striking feature in Fig. 3.14(b) is the band-banding in the ZTO film near the interface.

The magnitude of the band-bending (Δ_{Bend}) is around 0.38 eV over 180 nm ZTO [as is depicted in Fig. 3.14(c)] towards the interface as shown in Fig. 3.14(d) which is very close to its theoretically calculated value of Schottky barrier height between ZTO and Pt. The line profile in Fig. 3.14(d) is obtained from the Fig. 3.14(b) (as marked by the yellow line). On the other hand, Fig. 3.14(c) shows the line profile obtained from the Fig. 3.14(a) (marked by the yellow line), i.e. the height image obtained from a 180 nm-thick ZTO films grown on a Platinized-Si substrate. In addition, the measured value of Δ_{Bend} at the interface of the metal-semiconductor junction matches very well with the conventional junction having a band-bending of around 0.3-0.4 eV [58]. The origin of the barrier height in heterostructures is due to a difference in the

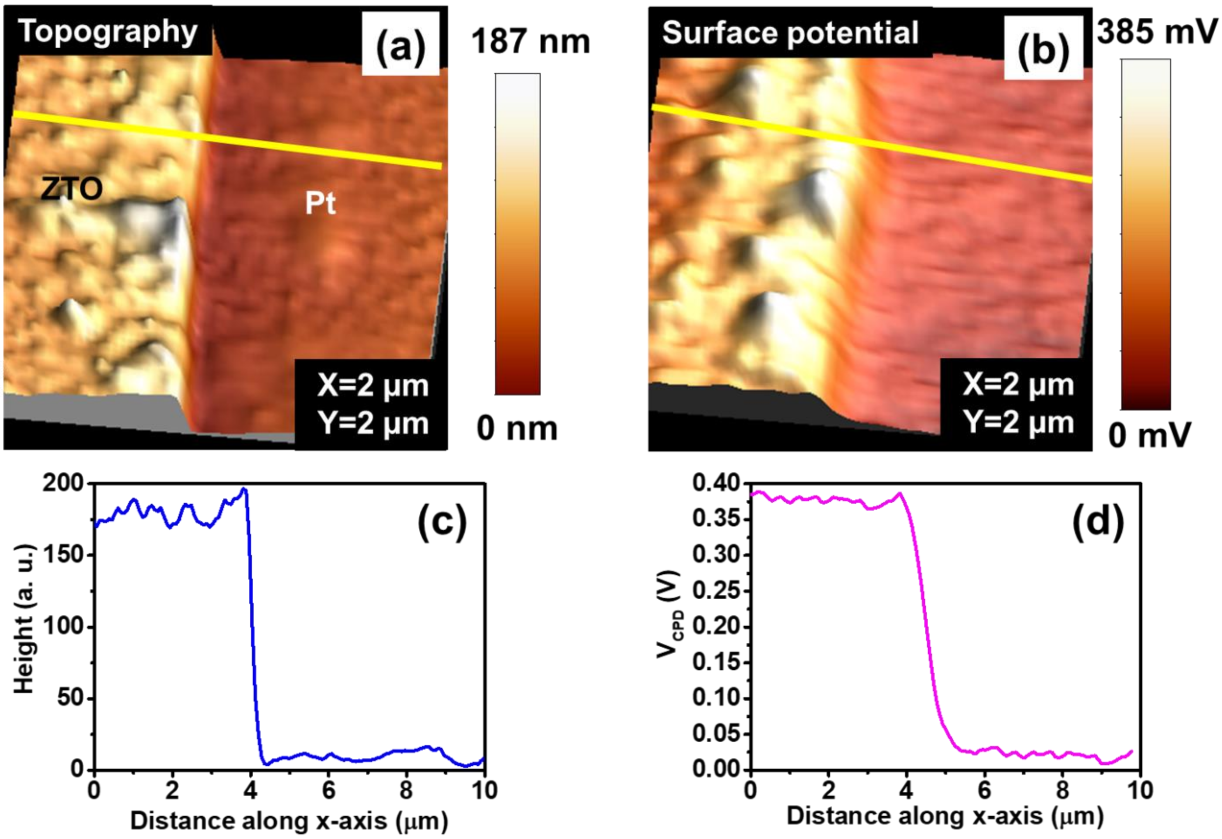

Figure 3.14: (a) Shows a 3D AFM topography of the ZTO/Pt-Si junction and (b) corresponds to band mapping at the same junction. (c) and (d) Depict line profiles of height and barrier height obtained from (a) and (b), respectively.

work function, lattice mismatch, defects, and dopants at the GBs [54,57]. To the best of our knowledge, this is the first experimental report on band mapping of a ZTO film using KPFM.

3.3.4 Conclusions

In conclusion, we have grown a junction between a ZTO film and Pt by growing ZTO films on a Platinized-Si substrate at RT using RF magnetron sputtering. Formation of such a junction is substantiated by AFM topographic and surface potential images. Using local probe measurements such as cAFM, EFM, and KPFM, we demonstrate for the first time an experimental evidence on nanoscale band-banding at RT at grains and GBs in ZTO thin films, which is further confirmed by performing local *I*-*V* measurements at a fixed point. The present observation of defect-induced potential barrier formation can be a benchmark for understanding the charge transport in amorphous semiconductor materials. In addition, we have mapped the metal-semiconductor junction across their interface using KPFM which yields a band-bending at the junction. The results show a unique method to map the barrier height at GBs and at of the junction. The present findings will be useful to design ZTO-based tailor made transparent transistors, memory devices, and solar cells.

Table 3.1: Calculated average grain size (nm) and root mean square (RMS) roughness from AFM and ideality factor (η), turn-on potential (V_{TO}), and reverse saturation current (I_s) from the current-voltage (*I*-*V*) characteristics along with barrier height (ϕ_B) from capacitance-voltage (*C*-*V*).

Sample description	Average grain size (nm)	RMS roughness (nm)	V_{TO} (V)	ϕ_B (eV)	η	I_s (µA)
S1	23	0.96	2.35	0.252	2.1	0.81
S2	28	0.99	2.08	0.183	2.39	0.98
S3	38	1.04	1.49	0.154	2.73	1.7
S4	47	1.10	1.16	0.103	3.20	83

Table 3.2: Compositional analyses of 60 and 180 nm-thick ZTO films.

Sample description	composition	Binding energy (eV)	Relative percentage (%)	Sn:O
S1:ZTO (60 nm)	Zn $2p_{3/2}$	1021.85	68.23	1:1.31
	Zn $2p_{1/2}$	1044.96	31.77	
	Sn $3d_{5/2}$	486.67	59.5	
	Sn $3d_{3/2}$	495.07	40.5	
	O 1*s* O_L	530.29	61.67	
	O 1*s* O_V	531.64	38.33	
S3:ZTO (180 nm)	Zn $2p_{3/2}$	1021.77	67.15	1:1.34
	Zn $2p_{1/2}$	1044.88	32.85	
	Sn $3d_{5/2}$	486.61	58.51	
	Sn $3d_{3/2}$	495.01	41.49	
	O 1*s* O_L	530.20	51.44	
	O 1*s* O_V	531.53	48.56	

References

[1] D. S. Ginley, H. Hosono, D. C. Paine, *Handbook of Transparent Conductors* 2011: Springer, Berlin.

[2] T. Minami, S. Takata, H. Sato, and H. Sonohara, *J. Vac. Sci. Technol. A* 13, (1995) 1095.

[3] R. Guo, Y. Guo, H. Duan, H. Li, and H. Liu, *ACS Appl. Mater. Interfaces* 9 (2017) 8271.

[4] M. Kumar, R. Singh, S. Nandy, A. Ghosh, S. Rath, and T. Som, *J. Appl. Phys.* 120 (2016) 15302.

[5] R. D. Chandra, M. Rao, K. Zhang, R. R. Prabhakar, C. Shi, J. Zhang, S. G. Mhaisalkar, and N. Mathews, *ACS Appl. Mater. Inter.* 6 (2014) 773.

[6] L. Wang, X. Zhang, X. Liao, and W. Yang, *Nanotechnology* 16 (2005) 2928.

[7] X. Shen, J. Shen, S. J. You, L. X. Yang, L. Y. Tang, Y. C. Li, J. Liu, H. Yang, K. Zhu, Y. L. Liu, W. Y. Zhou, C. Q. Jin, R. C. Yu, and S. S. Xie, *J. Appl. Phys.* 106 (2009) 113523.

[8] T. Bora, M. H. Al-Hinai, A. T. Al-Hinai, and J. Dutta, *J. Am. Ceram. Soc.* 98 (2015) 4044.

[9] E. Rucavado, Q. Jeangros, D. F. Urban, J. Holovský, Z. Remes, M. Duchamp, F. Landucci, R. E. Dunin-Borkowski, W. Körner, C. Elsässer, A. Hessler-Wyser, M. Morales-Masis, and C. Ballif, *Phys. Rev. B* 95 (2017) 1.

[10] R. Singh, M. Kumar, M. Saini, A. Singh, B. Satpati, and T. Som, *Appl. Surf. Sci.* 418 (2017) 225.

[11] K. H. Ko, H. S. So, D. H. Jung, J. W. Park, and H. Lee, *J. Appl. Phys.* 119 (2016) 135302.

[12] M. Kumar, T. Basu, and T. Som, *J. Appl. Phys.* 118 (2015) 1166.

[13] E. Chason, J. W. Shin, S. J. Hearne, and L. B. Freund, *J. Appl. Phys.* 111 (2012) 083520.

[14] F. Khan, Vandana, S. N. Singh, M. Husain, and P. K. Singh, *Sol. Energy Mater. Sol. Cells* 100 (2012) 57.

[15] G. H. Gilmer and P. Bennema, *J. Appl. Phys.* 43 (1972) 1347.

[16] S. F. Tseng, W. T. Hsiao, K. C. Huang, D. Chiang, M. F. Chen, and C. P. Chou, *Appl.*

Surf. Sci. 257 (2010) 1487.

[17] A. Sanchez-Juarez, A. Tiburcio-Silver, A. Ortiz, E.. Zironi, and J. Rickards, *Thin Solid Films* 333 (1998) 196.

[18] P. Kumar, R. Singh, and P. C. Pandey, *J. Appl. Phys.* 123 (2018) 054502.

[19] M. Kumar, A. Kanjilal, and T. Som, *AIP Adv*. 6 (2013) 092126.

[20] T. Prasada Rao and M. C. Santhosh Kumar, *J. Alloys Compd.* 506 (2010) 788.

[21] D. L. Young, H. Moutinho, Y. Yan, and T. J. Coutts, *J. Appl. Phys.* 92 (2002) 310.

[22] M. Saini, R. Singh, S. K. Srivastava, and T. Som, *J. Appl. Phys. D:Appl. Phys.* 51 (2018) 275305.

[23] T. Minami, K. Okada, T. Miyata, J. Nomoto, Y. Hara, and H. Abe, *J. Vac. Sci. Technol. A* 27 (2009) 1006.

[24] J. H. Ko, I. H. Kim, D. Kim, K. S. Lee, T. S. Lee, J. H. Jeong, B. Cheong, Y. J. Baik, and W. M. Kim, *Thin Solid Films* 494 (2006) 42.

[25] I. Horcas, R. Fernández, J. M. Gómez-Rodríguez, J. Colchero, J. Gómez-Herrero, and A. M. Baro, *Rev. Sci. Instrum.* 78 (2007) 13705.

[26] M. F. J. Vos, B. Macco, N. F. W. Thissen, A. A. Bol, and W. M. M. (Erwin) Kessels, *J. Vac. Sci. Technol. A* 34 (2016) 01A103.

[27] J. Y. Choi, K. Heo, K. S. Cho, S. W. Hwang, S. Kim, and S. Y. Lee, *Sci. Rep.* 6 (2016) 1.

[28] S. Sönmezoğlu, A. Arslan, T. Serin, and N. Serin, *Phys. Scr.* 84 (2011) 65602.

[29] R. Singh, M. Kumar, M. Saini, B. Satpati, and T. Som, *Appl. Surf. Sci.* 174 (2018) 231.

[30] D.-C. Tsai, Z.-C. Chang, B.-H. Kuo, Y.-H. Wong, E.-C. Chen, and F.-S. Shieu, *J. Alloys Compd.* 743 (2018) 603.

[31] C. M. Firdaus, M. S. B. Shah Rizam, M. Rusop, and S. Rahmatul Hidayah, *Procedia Eng.* 41 (2012) 1367.

[32] L. C. Tien, S. J. Yang, Y. H. Chen, and C. H. Ho, *Mater. Res. Express* 3 (2016) 1.

[33] B. R. Yakami, U. Poudyal, S. R. Nandyala, G. Rimal, J. K. Cooper, X. Zhang, J. Wang, W. Wang, and J. M. Pikal, *J. Appl. Phys.* 120, (2016) 163101.

[34] J. X. Wang, S. S. Xie, H. J. Yuan, X. Q. Yan, D. F. Liu, Y. Gao, Z. P. Zhou, L. Song, L. F. Liu, X. W. Zhao, X. Y. Dou, W. Y. Zhou, and G. Wang, *Solid State Commun.* 131, (2004) 435.

[35] J. I. Pankove, *Optical Process in Semiconductors* 1971: Prentice-Hall, Inc. Englewoad.

[36] P. Abbott, E. D. Sosa, and D.E. Golden, *Appl. Phys. Lett.* 79 (2001) 2835.

[37] K. Satoh, Y. Kakehi, A. Okamoto, S. Murakami, F. Uratani, and T. Yotsuya, *Jpn. J. Appl. Phys.* 44, (2005) L34.

[38] R. Sivakumar, M. Kumar, C. Sanjeeviraja, and T. Som, J. Mater. Sci. Mater. Electron. 28, (2017) 1409.

[39] D. B. Buchholz, J. Liu, T. J. Marks, M. Zhang, and R.P.H. Chang, ACS Appl. Mater. Interfaces **1**, 2147 (2009).

[40] C. G. Lee and A. Dodabalapur, *Appl. Phys. Lett.* 96 (2010) 2.

[41] S.-J. Seo, C. G. Choi, Y. H. Hwang, and B.-S. Bae, *J. Phys. D. Appl. Phys.* 42 (2009) 35106.

[42] K. Nomura, H. Ohta, A. Takagi, T. Kamiya, M. Hirano, and H. Hosono, *Nature* 432, (2004) 488.

[43] A. Rong, X. P. Gao, G. R. Li, T. Y. Yan, H. Y. Zhu, J. Q. Qu, and D. Y. Song, *J. Phys. Chem. B* 110 (2006) 14754.

[44] C.-C. Yang, W.-J. Tung, S.-P. Chang, M.-H. Hsu, W.-L. Huang, C.-H. Li, Y.-J. Fang, and S.-J. Chang, Proc. - 2018 7th Int. Symp. Next-Generation Electron. (ISNE 2018) (2018) 1.

[45] S. Hemmatzadeh Saeedabad, C. Baratto, F. Rigoni, S. M. Rozati, G. Sberveglieri, K. Vojisavljevic, and B. Malic, *Mater. Sci. Semicond. Process.* 71 (2017) 461.

[46] T.-H. Cheng, S.-P. Chang, and S.-J. Chang, *J. Nanosci. Nanotechnol.* 18 (2018) 4930.

[47] S. A. Mahmoud and O. A. Fouad, Sol. Energy Mater. Sol. Cells 136 (2015) 38.

[48] H. Q. Chiang, J. F. Wager, R. L. Hoffman, J. Jeong, and D. A. Keszler, *Appl. Phys. Lett.* 86 (2005) 2003.

[49] J.-B. Shi, P.-F. Wu, H.-S. Lin, Y.-T. Lin, H.-W. Lee, C.-T. Kao, W.-H. Liao, and S.-L. Young, *Nanoscale Res. Lett.* 9, 210 (2014).

[50] P. Schlupp, H. von Wenckstern, and M. Grundmann, *MRS Proc.* 1633 (2014) 101.

[51] T. S. Herng, A. Kumar, C. S. Ong, Y. P. Feng, Y. H. Lu, K.Y. Zeng, and J. Ding, *Sci. Rep.* 2 (2012) 1.

[52] X. Ji, Y. Zhu, M. Chen, L. Su, A. Chen, X. Gui, R. Xiang, and Z. Tang, *Sci. Rep.* 4 (2014) 1.

[53] D. Azulay, I. Balberg, and O. Millo, *Phys. Rev. Lett.* 108 (2012) 1.

[54] M. Kumar, T. Basu, and T. Som, *J. Appl. Phys.* 119 (2016) 014307.

[55] J. H. Shin, J. S. Lee, C. S. Hwang, S. H. K. Park, W. S. Cheong, M. Ryu, C. W. Byun, J. I. Lee, and H. Y. Chu, *ETRI J.* 31 (2009) 62.

[56] K. H. Lee, J. S. Jung, K. S. Son, J. S. Park, T. S. Kim, R. Choi, J. K. Jeong, J. Y. Kwon, B. Koo, and S. Lee, *Appl. Phys. Lett.* 95 (2009) 1.

[57] M. Kumar, S. Mookerjee, and T. Som, *Nanotechnology* 27 (2016) 375702.

[58] A. Bera, S. Dey, and A. J. Pal, *Nano Lett.* 14 (2014) 2000.

[59] M. Kumar, R. Singh, and T. Som, *Appl. Surf. Sci.* 428, (2018) 1006.

[60] S. M. Gheno, R. H. G. A. Kiminami, M. R. Morelli, and P. I. Paulin Filho, *J. Eur. Ceram. Soc.* 30 (2010) 549.

[61] L. S. C. Pingree, O. G. Reid, and D. S. Ginger, *Adv. Mater.* 21 (2009) 19.

[62] M. Basletic, J.-L. Maurice, C. Carrétéro, G. Herranz, O. Copie, M. Bibes, É. Jacquet, K. Bouzehouane, S. Fusil, and A. Barthélémy, *Nat. Mater.* 7 (2008) 621.

[63] O. Millo, D. Katz, Y. Cao, and U. Banin, *Phys. Rev. Lett.* 86, (2001) 5751.

[64] D. Steiner, D. Dorfs, U. Banin, F. Della Sala, L. Manna, and O. Millo, *Nanotechnology* 19 (2008) 2954.

[65] E. M. Likovich, R. Jaramillo, K. J. Russell, S. Ramanathan, and V. Narayanamurti, *Phys. Rev. B - Condens. Matter Mater. Phys.* 83 (2011) 1.

[66] E. Meyer, H. J. Hug, and R. Bennewitz, *Scanning Probe Microscopy: The Lab on a Tip* 2003: Springer, Berlin.

[67] M. Kumar and T. Som, *Nanotechnology* 26 (2015) 345702.

[68] http://www.imagemet.com/index.php.

[69] W. Wu, J. R. Guest, Y. Horibe, S. Park, T. Choi, S. W. Cheong, and M. Bode, *Phys. Rev. Lett.* 104 (2010) 1.

[70] S. A. Mollick, M. Kumar, R. Singh, B. Satpati, D. Ghose, and T. Som, *Nanotechnology* 27 (2016) 435302.

[71] V. Consonni, N. Baier, O. Robach, C. Cayron, F. Donatini, and G. Feuillet, *Phys. Rev. B - Condens. Matter Mater. Phys.* 89 (2014) 1.

[72] C. Maragliano, A. Glia, M. Stefancich, and M. Chiesa, *J. Appl. Phys.* 115 (2014) 124311.

CHAPTER 4

4. Study on CdTe absorber layer: Influence of Cu-doping

Cadmium telluride (CdTe) is a material that is particularly well suited for thin film photovoltaics and is the second most widely deployed material for PV technology in the world [1,2]. Further, perhaps more noteworthy, many believe that CdTe-based PVs can become a dominant technology in the future for renewable energy. It has a direct band gap of 1.45 eV which is well within the optimized range of 1.2 to 1.5 eV for maximum photovoltaic conversion energy (PCE) [3–6]. In addition, because of its high absorption coefficient, which is higher than *a*-Si and much higher than *c*-Si, only a few micrometers of thickness of CdTe is sufficient to absorb all the incident light [7]. As a consequence, a minority carrier diffusion length of the order of one μm is sufficient to allow all the generated carriers to be collected at the contacts [7].

Generally, CdTe exhibits a *p*-type conductivity and it is difficult to give it a high hole-density. In addition, it has a high electron affinity between 4.3 to 4.5 eV, resulting in a high back contact barrier which reduces the efficiency [8]. In general, obtaining a contact barrier height lower than 0.5 eV for CdTe requires a metal contact with a high work function (>5.5 eV) which cannot be reached if one excludes noble metals for economic reasons [9]. Thus, to reduce the back contact barrier height, there is a need to reduce the work function of the CdTe layer. In order to do so, in the present study Cu is incorporated in polycrystalline CdTe films and an attempt has been made to fabricate efficient and stable solar cells. For the growth of CdTe thin films, several physical and chemical vapour deposition techniques are used such as sputtering [10], thermal evaporation [11], pulsed laser deposition [12], close spaced sublimation [13], vapour transport deposition [14] etc. Some of these techniques, namely close spaced sublimation, vapour transport deposition requires a high growth temperature and due to high temperature deposition, there will be Cd deficiency in the CdTe thin films [12]. Sputtering has some advantages over these techniques, for instance; relatively low substrate temperature, large area deposition with accurate composition, and uniform morphology [15].

In this chapter, first we have optimized the growth angle of CdTe absorber layer. While effect growth angle-dependent structural and optical properties are studied by XRD and UV-Vis spectroscopy, the respective dependence on work function of the films is carried out by employing KPFM measurements. In addition, morphology and microstructure of CdTe films are studied by AFM and SEM. Further, we have studied the influence of Cu-doping in CdTe films by growing an ultrathin sandwiched layer of Cu between two CdTe layers of equal thickness and annealing the sandwiched structure in vacuum. Moreover, the influence of annealing temperature and in turn Cu-doping in CdTe on its work function, composition, microstructure, reflectance, morphology, and crystallinity is also studied. In particular, using KPFM, we have demonstrated that the work function of a CdTe layer can be reduced through Cu-doping, resulting in a smooth charge conduction to take place through an enhancement in the hole-density and a reduction in the back contact barrier height. The present approach is expected to yield highly efficient Cu-doped CdTe absorber layer-based PV cells without undergoing $CdCl_2$ vapour treatment which should help to avoid the end-of-life (of the cells) environmental issues since $CdCl_2$ is completely soluble in water.

4.1 Experimental details

Thin films of CdTe were deposited at RT using an RF magnetron sputtering setup at normal and different oblique angles (viz. 40°, 50°, 75°, 85°, and 87°) of incidence on Mo-coated *p*-type Si(100) (B-doped, resistivity of 0.01–0.02 Ω-cm) and soda lime glass substrates simultaneously. In this process, a silicon wafer was cut into small slices (1 cm×1 cm) which were ultrasonically cleaned in trichloroethylene, acetone, propanol, and de-ionized water for 5 min. each to remove the organic contaminations and further dried up by dry nitrogen. Mo thin films (as the back contact layer) were grown at RT (using an RF magnetron sputtering setup) on these ultrasonically cleaned Si substrates [16]. Subsequently, a trilayer configuration, viz. CdTe (500 nm)/Cu (5 nm)/CdTe (500 nm) was grown simultaneously on Mo-coated Si and glass substrates at RT using the same sputtering setup under normally incident flux. In fact, first a 500 nm CdTe layer was grown on Mo-coated Si substrates followed by deposition of a 5 nm Cu layer using a commercial 99.99% pure target (Testbourne Ltd. England) and pulsed DC magnetron sputtering (power = 100 W, frequency = 150 kHz, and reverse time = 0.4 µs) technique. Finally, a 500 nm-thick CdTe film was deposited on the Cu layer with the help of RF magnetron sputtering techique. Cu-doping was promoted through diffusion by annealing the CdTe/Cu/CdTe/Mo/Si samples at two different temperatures (e. g. 473 K and 673 K) in vacuum for 1 h. Commercially available 99.99% pure CdTe target (50.8 mm dia.×5 mm thick) (Testbourne Ltd., UK) was used as the target material. The deposition chamber was evacuated to a base pressure of 1×10^{-7} mbar. For sputtering, ultra-pure (99.99%) Ar gas was injected into the deposition chamber (base pressure: 1×10^{-7} mbar) with a flow rate of 40 sccm to maintain the working pressure of 5×10^{-3} mbar. An RF power of 100 W (Cesar, Advanced energy, USA) was supplied to the target. For the growth of CdTe films, target-to-substrate distance was kept at 80 mm and the substrate holder was rotated at a constant speed of 3 rpm to achieve a uniform films. For growth angle-dependent study, the deposition time was chosen in a way so that it yielded the same film thickness for each angle which was confirmed by thickness calibration using a surface profilometer (described earlier in section 2.2). In section 4.3, the as-deposited sample is named as S1, whereas the annealed samples at 473 K and 673 K are named as S2 and S3, respectively.

Surface morphology and the local electrical properties like work function of CdTe films (before and after annealing) were examined by *ex-situ* atomic force microscopy. In particular, morphological evaluation was carried out in tapping mode and the work function measurements were performed using KPFM in lift mode with a user-defined lift height of 50 nm (from the surface) using a conductive tip (AC240TM, Electro-lever, Olympus) having a tip radius of 15 nm, resonance frequency of 70 kHz, and the stiffness of 2 N m^{-1}. KPFM measurements were performed at large number of randomly chosen places by varying the scan speed and the scan angle of the tip by rotating the samples. However, no noticeable change in the results was found, confirming the absence of tip-related artefacts in the data. A low humidity environment was created surrounding the AFM setup to reduce the adsorption of water molecules on the surfaces of the samples. Nature of crystallinity of the films were evaluated by x-ray diffraction (XRD) under the Bragg-Brentano geometry using a Cu-K$_\alpha$ radiation (λ=0.154 nm) over a 2θ scan range of 20°-80°. In addition, microstructure of the CdTe films before and after annealing was examined by field emission gun-based scanning electron microscopy (FEGSEM) using 5 KeV electrons under the cross-sectional and plan-view geometries. For each sample, several images were collected from randomly chosen different regions to check the uniformity of films and their microstructures. For compositional analysis and evaluating the chemical nature of the films, XPS measurement was employed. Further microstructural analysis of CdTe films was carried out by cross-sectional transmission electron microscopy (XTEM) measurements on selective samples using a high-resolution transmission electron microscope equipped with an image aberration corrector. Elemental analysis was also performed (during TEM measurements) by energy dispersive x-ray spectroscopy. In addition, the linear four-probe technique (vander Pauw geometry) was used to measure the resistivity of CdTe and CdTe:Cu films. The specular reflectance measurements were performed with the help of a UV-Vis-NIR spectrophotometer using an unpolarized light.

4.2 Physical properties of CdTe thin films: Role of growth angle

4.2.1 Introduction

Thin film photovoltaic (PV) technology based on silicon [17], Cu(In, Ga)Se_2 [18], $Cu_2ZnSn(S, Se)_4$ [19], CdTe [20,21], dye-sensitized [22], and organic materials [23] have huge potential to significantly reduce the cost of power. CdTe-based PV cells offer the lowest cost in solar electricity generation and has the second largest market share after the crystalline silicon [24]. CdTe is a nearly perfect absorber material for thin film solar cells because its band gap close to 1.5 eV (at RT) which is nearly optimal for the photovoltaic conversation and has an absorption coefficient >10^5 cm^{-1} in the visible region [12]. This reveals that a layer having thickness of few micrometers is sufficient to absorb the maximum incident light.

4.2.2 Results and discussion

As a first step, CdTe films are deposited at different growth angles and their optical, structural, morphological, microstructural, and electrical properties are studied and are described below. Figure 4.1(a) depicts growth angle-dependent micro-Raman spectra of CdTe films grown on Si substrates. The Raman lines located at ~119 cm^{-1} and 139 cm^{-1} belong to $A1$ and E mode of Te, respectively [25]. On the other hand, the weak peak at ~166 cm^{-1} corresponds to CdTe longitudinal optical (LO) phonon mode. The LO phonon frequency for bulk CdTe ranges from 170 cm^{-1} to 173 cm^{-1}. It is interesting to note that the Raman peak position systematically gets shifted towards a higher wavenumber (red shift) from 118.8 (for 0°) to 120.82 (for 87°). Such optical phonon behaviours are related to strain and crystalline quality. Although, the shifts are always towards higher wavenumbers compared to the normally grown films due to less strain and dislocation density (Table 4.1) [26,27]. On the other hand, the scattering intensity increases with increasing growth angle. It is known that rough surfaces can enhance the light scattering cross-section [26]. Moreover, the Raman modes E and $A1$ of CdTe indicate that there exist Te inclusions or defects around the grain boundaries of CdTe, which may be due to deposition technique [28,29].

Figure. 4.1(b) depicts XRD data of as-prepared CdTe films grown at various deposition angles (viz. 0°, 40°, 50°, 75°, 85°, and 87°). The recorded diffractograms corresponding to different growth angles various (corresponding to a film thickness of 500 nm) show different peaks correspond to CdTe cubic zinc blende structure, indicating the polycrystalline nature of the films and the absence of any impurity peak [30]. The sharp and the strong peak at $2\theta = 23.79°$ corresponding to the growth angle of 0° matches very well with the (111) plane. However, the peak intensity reduces and the FWHM increases with increasing growth angle. It is interesting to note that the observed XRD peak gets shifted systematically from $2\theta = 23.79°$ (for 0°) to 24.03° (for 87°). The observed changes in the peak intensity, FWHM, and the shift in the CdTe (111) peak position can be attributed to variation(s) in (i) strain, (ii) dislocation density, and(iii) crystallize size. As a matter of fact, the peak shift can be associated with increasing strain in the films, the increase in FWHM value with growth angle can be due to a variation in the crystallize size (i.e. bigger to smaller). In addition, the calculated dislocation density (from the (111) XRD line) is found to increase with growth angle. The crystallize size, strain, and dislocation density for all growth angles corresponding to CdTe are presented in Table 4.1. As

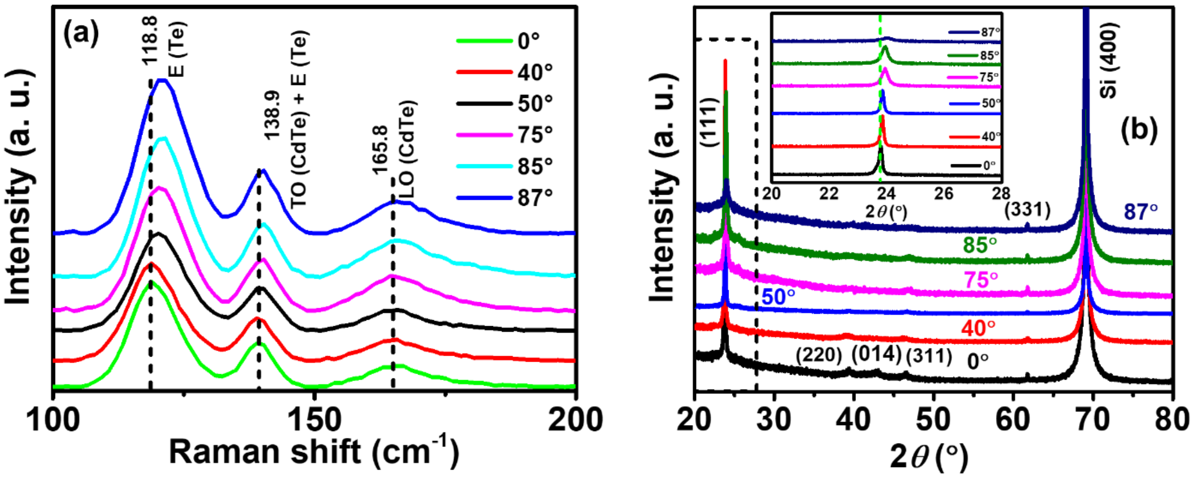

Figure 4.1: (a) Growth angle-dependent micro-Raman spectra of CdTe thin films. (b) XRD patterns of CdTe thin films sputter deposited at normal as well as various oblique angles, whereas the inset shows the magnified part of the marked region in (b).

a matter of fact, the average crystallite size (D) is calculated using the Scherrer's formula [31], $D = 0.95\times\lambda/(\beta\cos\theta)$, where λ is the wavelength of x-ray, β is the full width half maximum, and θ is the Bragg's diffraction angle. On the other hand, the dislocation density (δ) and microstrain (ε) are calculated (with respect to the CdTe (111) reflection) using the relation $\delta = 1/(D)^2$ and $\varepsilon = \beta\cos\theta/4$ [31].

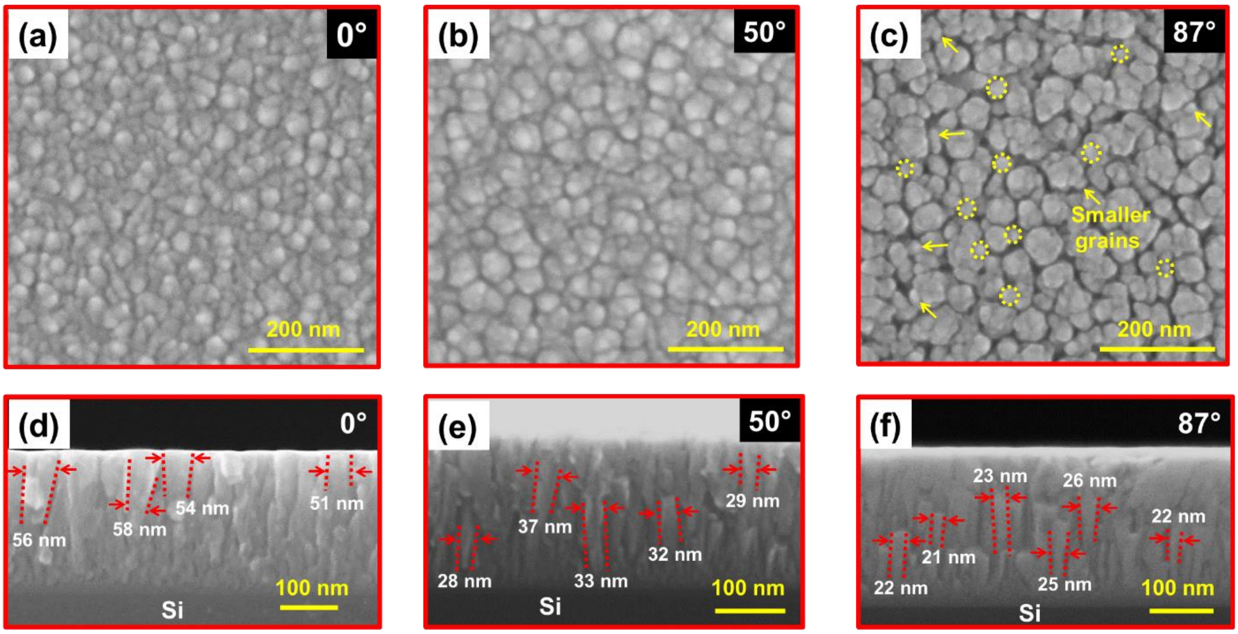

Figure 4.2: SEM images of CdTe thin films grown on Si substrates: (a)-(c) plan-view micrographs corresponding to the growth angle of 0°, 50°, and 87°, respectively, whereas (d)-(f) depict the respective high-magnification cross sectional micrographs from where the formation of columnar nanostructures are evident. The yellow dotted circles in (c) indicate the formation of smaller grains within bigger grains. On the other hand, the red dotted lines in (d)-(f) are indicative of the formation of nanocolumanr microstructures at different growth angles.

Figure 4.2 shows the SEM images which depict the angle-dependent change in the surface morphology. Figures 4.2(a)-(c) depict plan-view SEM micrographs corresponding to the films grown at 0°, 50°, and 87°, respectively. In the case of normal incidence of deposition flux [Fig. 4.2(a)], a granular microstructure is observed and the film is largely uniform. On the other hand, the films deposited at 50° and 87° show the presence of porosity [as is seen from Figs. 4.2(b) and (c)] which increases at higher growth angles [4]. As a matter of fact, with increasing growth angle the shadowing effect becomes more and more prominent and controls the granular morphology [6]. In addition, from the SEM micrograph shown in Figs. 4.2(c) it becomes evident that with increasing growth angle, smaller grains are observed to be present within the bigger grains [ref]. It is interesting to note from the respective cross-sectional micrographs of the same films (i.e growth angles of at 0°, 50°, and 87°) [Figs. 4.2(d)-(f)] that formation of vertically aligned nanocolumnar structures take place, albeit the average columnar grain size reduces from 57 nm (for 0°) to 22 nm (for 87°). It is also observed that apexes of the columnar nanostructures are wider than their bases. Such widening of the apexes of nanostructures compared to their bases occurs due to the fast rotation of substrates during sputter deposition [32].

Figure 4.3 shows AFM and KPFM images of the CdTe films deposited at two extreme growth angles of 0° and 87°. For instance, Fig. 4.3(a) represents an AFM image of the film grown under normally incident deposition flux which shows the presence of grains and tightly packed morphology. On the other hand, the AFM image of a film grown under an oblique incidence of 87° is shown in Fig. 4.3(b) which also shows granular microstructures having bigger grains. It is interesting to note that this follows the similar trend of observed apparent enhancement in grain size with increasing growth angle from the plan-view SEM images shown in Figs. 4.2 (a)-(c). However, this is in contrast to the XSEM images shown in Figs. 4.2(d)-(f). This can be attributed to the fact that the bigger grains are actually comprised of smaller grains [as are marked by dotted circles and arrows in Fig. 4.2(c)] which becomes evident from the extracted reducing value of average width of the nanocolumnar structures [Figs. 4.2 (d)-(f)]. As a matter of fact, this corroborates well with the calculated average crystallite size from the XRD data as well where we observe a steady decrease in its value with increasing growth angle (Table 4.1). Such an anomaly in AFM morphology can be arising due to the limitation of AFM tip dimensions to resolve smaller crystallites within the bigger ones [33].

Further, to understand the local electrical transport, we have undertaken KPFM studies for two-dimensional mapping of work function of the films. As discussed earlier, the work function of a sample (Φ_{sample}) is expressed as: $\Phi_{\mathrm{sample}}=\Phi_{\mathrm{tip}} - qV_{\mathrm{CPD}}$ where Φ_{tip}, q, and V_{CPD} are work function of the tip, the electronic charge, and the contact potential difference, respectively [34].

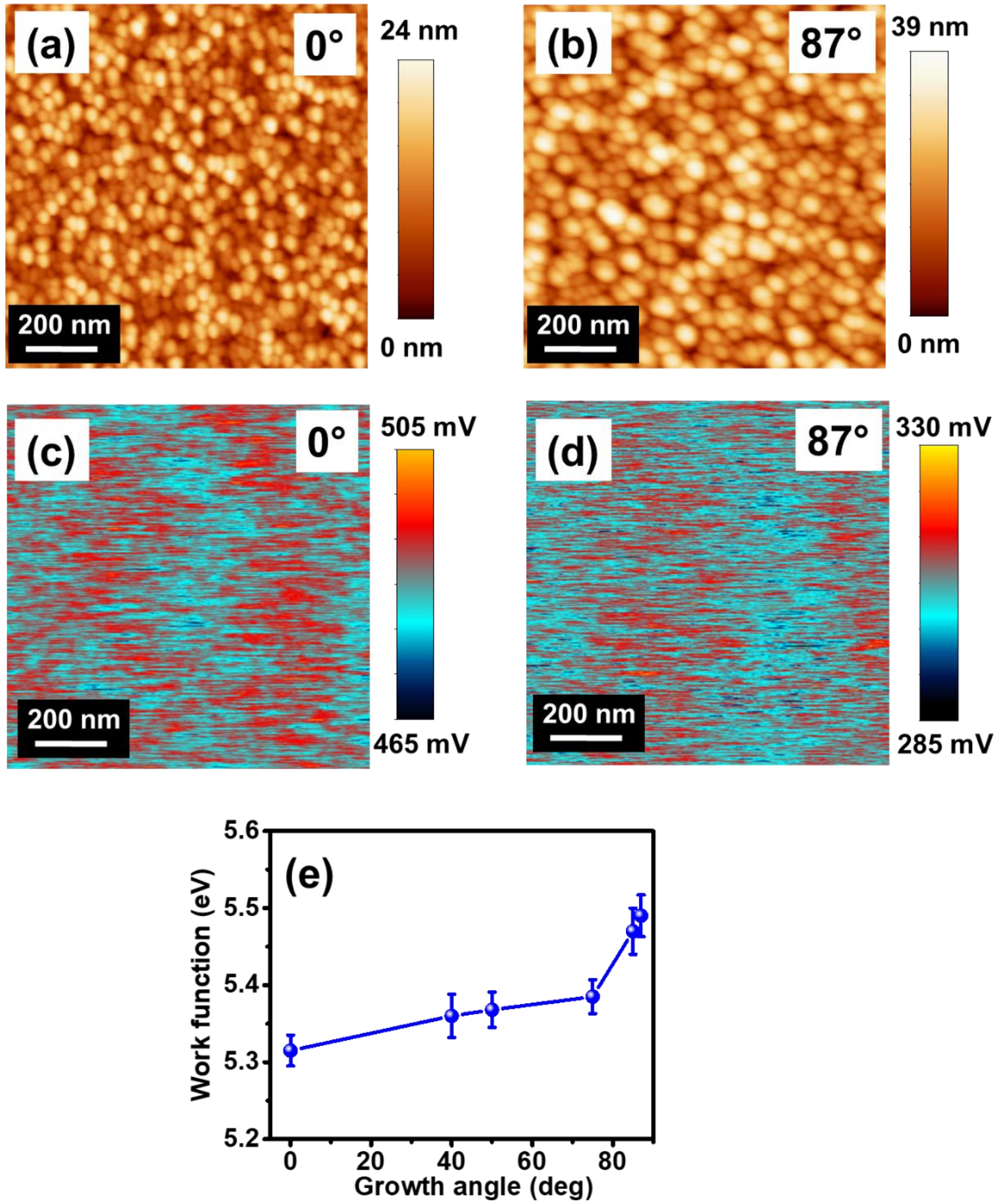

Figure 4.3: (a) and (b) AFM surface morphologies of CdTe thin films grown at 0° and 87°, respectively. (c) and (d) Contact potential difference (V_{CPD}) map corresponding to (a) and (b), respectively. (e) The growth angle-dependent variation in the work function of CdTe films.

Figures 4.3(c) and (d) depict the surface potential distribution corresponding to growth angle of 0° and 87°, respectively. The calculated work function of a CdTe film turns out to be 5.315 eV for the growth angle of 0° which gradually increases to 5.49 eV for films grown under an oblique angle of 87°. For intermediate growth angles, the values of work function are presented in Table 4.1. In fact, a low interfacial roughness and work function are desirable to obtain a smooth charge transport across a device based on a CdTe layer [35]. For the present study, the lowest roughness (4.1 nm) and work function (5.315 eV) are found corresponding to the CdTe films grown under normally deposition flux. Further, specular reflectance of CdTe films grown under different incidence angles (in the wavelength range 300 to 800 nm) is depicted in Fig. 4.4. It is interesting to note that the average specular reflectance of a CdTe film turns out to be 29.99% for the films grown under normally deposition flux which gradually decreases to 22. 83% for films grown under an oblique angle of 75°. For 85° and 87° growth angles, the average values of specular reflectance are turn out to be 23.87% and 23.41%, respectively.

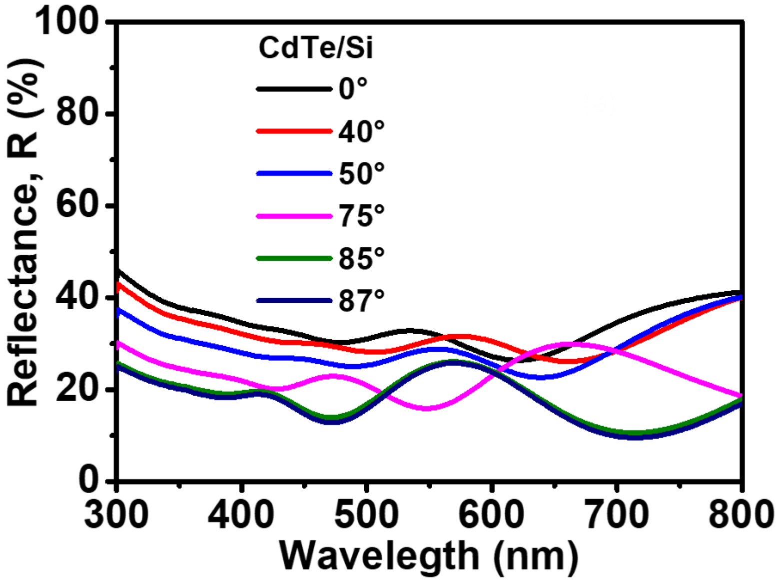

Figure 4.4: (a) Growth angle-dependent optical reflectance spectra of CdTe thin films.

4.2.3 Conclusions

Thus, for further studies, we deal with the films grown at 0° to study the role of Cu-doping in CdTe films by annealing for the fabrication of CdTe-based solar cells. It may also be mentioned that for the remaining part of this chapter, we have chosen a CdTe thickness of 1.2 µm (grown using the same experimental conditions mentioned above).

4.3 Influence of Cu-doping in CdTe layer by annealing

4.3.1 Introduction

One of the main problems in CdTe-based solar cell research is the achievement of a high hole density in the CdTe layer. As-grown CdTe thin films can exhibit *n*- or *p*-type electrical conductivity [36]. CdTe is a II-VI compound semiconductor and its physical properties can be improved by doping with some other suitable materials [37]. For instance, first-principle based simulations suggest that Cu dopants can occupy the Cd atomic sites in CdTe which act as an acceptor. On the other hand, Cu dopants work as donors at interstitial positions [38]. Cu-doping in CdTe solar cells enhances the efficiency of the PVs [20]. It is shown that CdTe-based solar cells without Cu dopants show an efficiency of <1%, whereas after Cu-doping the efficiency increases >13% [39]. Likewise, Yamamoto *et al*. have demonstrated that the Cu-doping improves the short-circuit current density and the open-circuit voltage of CdS/CdTe solar cell [13]. Recently, Kranz *et al*. have shown that the electronic properties like resistivity, hole-density, etc. can be enhanced and efficiency of the CdTe solar cells can be tuned by controlling Cu-doping in CdTe thin films [20].

Thus, Cu-doping can increase the hole density or *p*-type conductivity in a CdTe layer [14]. Cu is reported to be used as a back contact to improve the contact properties of CdTe solar cells [21]. However, high temperature processing during fabrication leads to an excessive diffusion of Cu atoms into adjacent layers and deteriorates the device performance [40]. It is also possible that Cu atoms would lead to an increase in the resistivity. Feng *et al*. have used Cu at different processing steps by dipping the cell into warm CuCl solution but efficiency remains ~7% [41]. Hence, it is very important to understand the bulk doping of Cu in a CdTe layer. In addition, the role of annealing temperature on the microstructure, electrical, and optical properties on these films are not well understood either.

In this section, we investigate the influence of Cu-doping in CdTe films and related changes in their morphology, microstructure, structural, optical, and electrical properties of CdTe films. In order to do this, an ultra-thin Cu layer, having a nominal thickness of 5 nm, is deposited between two CdTe layers of 500 nm thickness (where the bottom CdTe layer is deposited on Mo-coated Si) and subsequently its diffusion into CdTe is promoted by annealing the samples at 473 and 673 K in vacuum for 1 h. This leads to a significant reduction in the resistivity and work function of CdTe films. At a higher annealing temperature of 673 K, XTEM studies show that voids are formed and loss of columnar nanostructures is also observed. The present study will be useful to for Cu-doping induced modification in optoelectronic properties of CdTe films for making PV cells with good efficiencies.

4.3.2 Results and discussion

To study the influence of annealing temperature for Cu-doping in CdTe layers, their structural, morphological, compositional, microstructural, electrical, and optoelectronic properties are carried out. It may be mentioned that while the films grown on Mo-coated Si substrates are used to analyze their work function alongside structural, microstructural, and compositional aspects, CdTe films grown on glass substrates are utilized to study the optical and electrical properties.

X-ray diffraction (XRD) studies exhibit [Fig. 4.5(a)] that for as-deposited CdTe films (S1) all the diffraction lines appearing at 23.95°, 39.50°, 43.05°, and 46.85° correspond to reflections of (111), (220), (014), and (311), respectively which exactly match with the cubic (zinc blende structure) of CdTe data and the absence of any additional peak manifests that the films are devoid of impurities [31,42]. The sharp and the strongest peak, appearing at 2θ=23.95° indicates that majority of CdTe crystallites have a preferential orientation along (111) direction.

It is observed that the incorporation of Cu atoms in CdTe by annealing (S2 and S3) leads to even higher intensity of diffraction peaks from these samples (as compared to the as-deposited films) as is seen from Fig. 4.5.

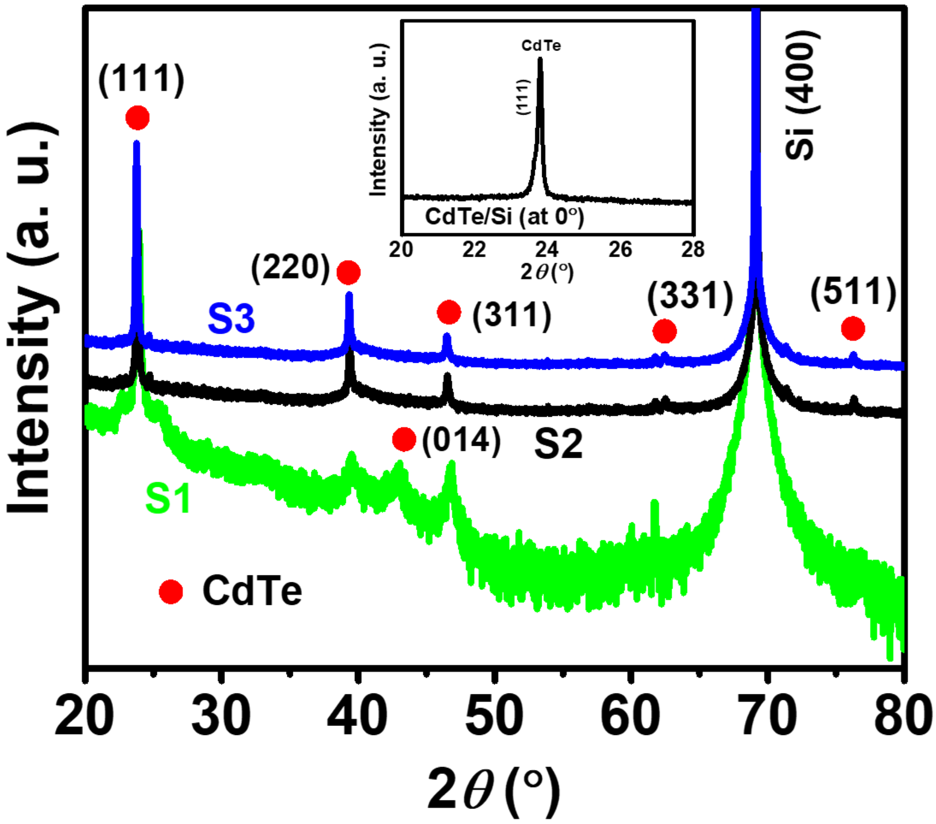

Figure 4.5: XRD spectra of S1, S2, and S3 samples, whereas the diffractogram shown in the inset corresponds to an as-grown CdTe film before the growth of Cu.

This is probably due to an increased diffusivity of atoms and the fact that (111) plane has the lowest surface energy among all the CdTe planes, allowing the growth of more CdTe grains along the (111) plane. In addition, a small shift in the position of the peaks is observed after Cu-doping. Shah *et al.* have shown that thermally evaporated CdTe films treated with Cu exhibit shift in the XRD peak positions due to a difference in the ionic radius of Cd^{2+} (0.95 Å) and Cu^{2+} (0.73 Å) [43]. The average crystallite size (D), dislocation density (δ), and microstrain (ε) are also calculated (with respect to CdTe (111) peak) [31]. The calculated structural parameters of S1, S2, and S3 are summarized in Table 4.2 which reveals that crystallite size, microstrain, and dislocation density are influenced due to Cu-doping in CdTe films. Here, it is interesting to note that the decrease in the FWHM of (111) peak of CdTe after Cu-doping is indicative of annealing induced significant reduction in dislocations present in the CdTe:Cu films [44]. Moreover, increase in the grain size can also be attributed to the improvement in the crystallinity of films upon Cu-doping.

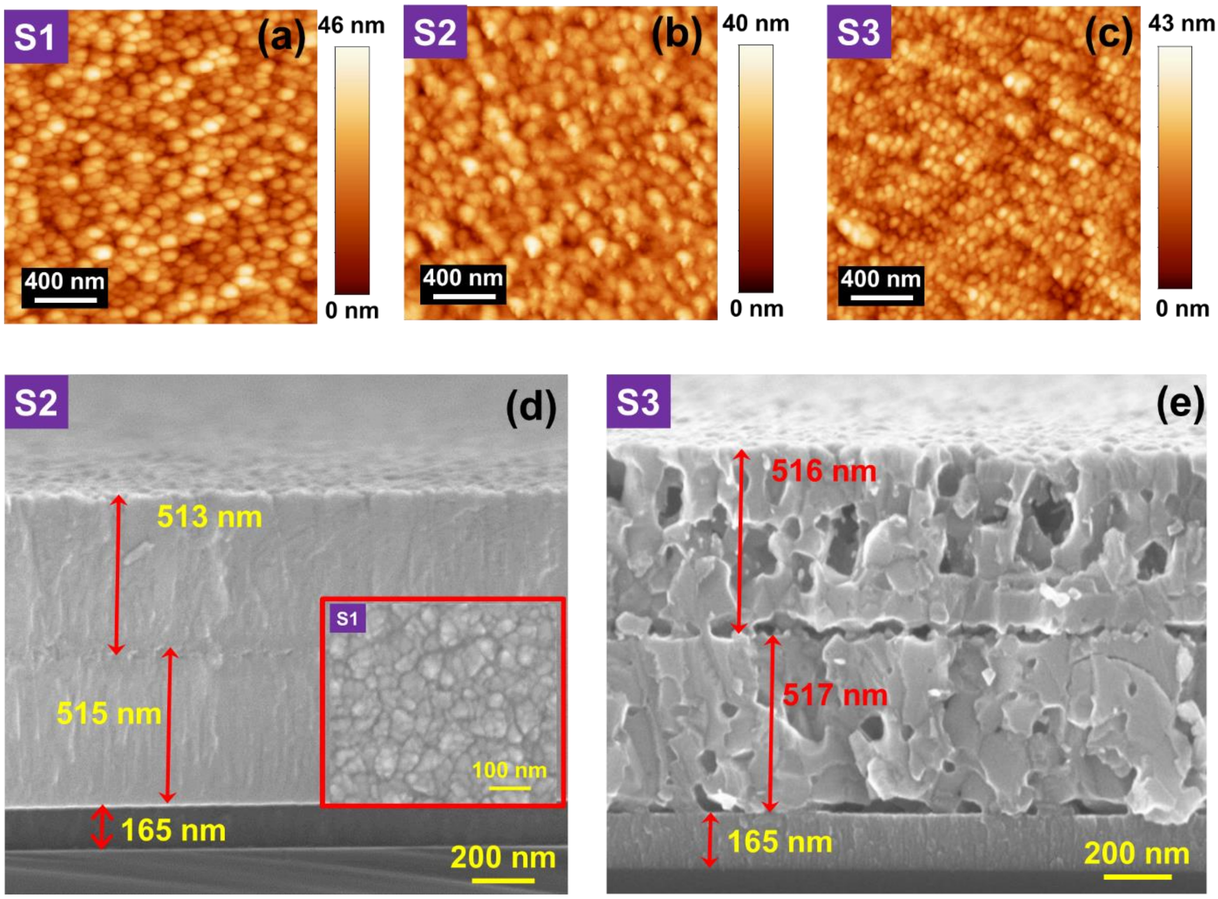

Figure 4.6: AFM images of CdTe/Cu/CdTe films grown on Mo-coated Si substrates: (a) as-deposited (S1), (b) annealed at 473 K for 1 h (S2), and (c) annealed at 673 K for 1 h (S3). (d) and (e) Depict XSEM images of S2 and S3, respectively, clearly showing the deformation of columnar nanostructures at the higher annealing temperature. The inset in (d) depicts a plan-view SEM image of S1.

Surface morphology of the films are analyzed by AFM and SEM in both plan- and cross-sectional views. Figure 4.6(a) depicts the AFM image of an as-deposited sample, whereas Figs. 4.6(b) and (c) show AFM images of S2 and S3, respectively which manifests the and granular nature of the films. These images exhibit a gradual change in surface morphology of the films with increasing annealing temperature, e.g. the average grain size increases. For instance, the average grain size is measured to be 56, 145, and 78 nm for S1, S2, and S3, respectively. Following this, the root mean square roughness is found to decrease (Table 4.2) [42]. On the other hand, Figs. 4.6(d) and (e) depict the XSEM images of S1 and S3, respectively. From these images, the formation of tightly packed and elongated nanostructures is clear. In addition, the nanostructures are observed to be tightly packed aligned normal to the surface [40]. However, after annealing at 673 K in vacuum for 1 h, void formation takes place in the films, as is shown in Fig. 4.6(e) [41].

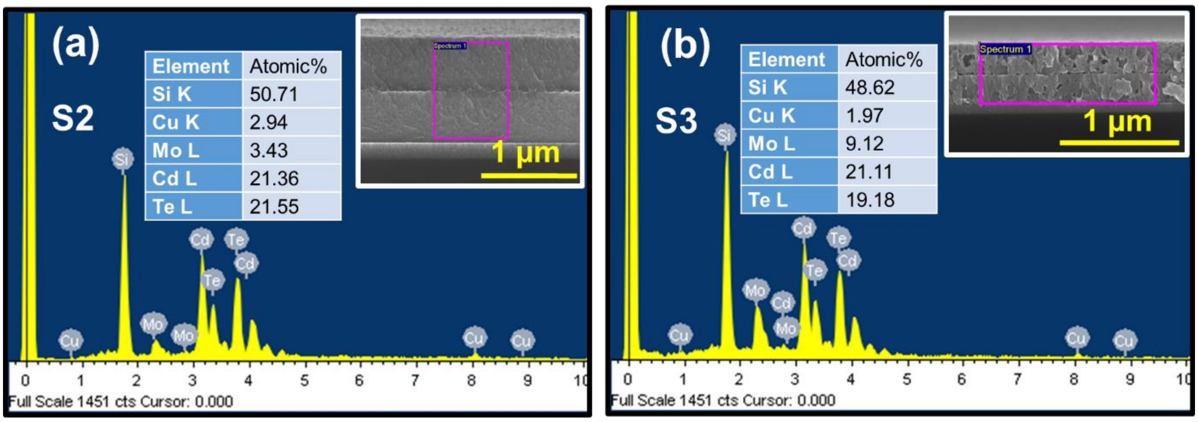

Element	Atomic%
Si K	50.71
Cu K	2.94
Mo L	3.43
Cd L	21.36
Te L	21.55

Element	Atomic%
Si K	48.62
Cu K	1.97
Mo L	9.12
Cd L	21.11
Te L	19.18

Figure 4.7: (a) and (b) depict EDX spectra of CdTe:Cu films annealed at 473 and 673 K in vacuum for 1 h, respectively. These EDX spectra are obtained from the marked region on the XSEM images which are shown as the insets of (a) and (b). The Tables in insets of (a) and (b) show percentage ratio of Cd, Te, Cu, Mo, and Si, obtained across the layers in S2 and S3.

The elemental composition of these samples is studied by energy dispersive X-ray spectrometry (EDX) analysis which does not reveal the presence of any impurity (unexpected element). The respective EDX spectrum corresponding to S2 and S3 are depicted in Figs. 4.7(a) and (b). The tables in the inset of Figs. 4.7(a) and (b) show the percentage ratio of Cd, Te, Cu, Mo, and Si. However, EDX measurements may be considered as only an indicative of the presence of different elements and hence, XPS measurements are also carried out on these samples which is described later. These results confirm that Cu-doped CdTe films are successfully formed due to thermal annealing of CdTe/Cu/CdTe films (grown on Mo-coated Si substrates) in vacuum.

In order to have a more in-depth understanding on annealing induced Cu-doping into CdTe layers, we have carried out XTEM studies on CdTe/Cu/CdTe/Mo/Si samples before and after annealing. Figure 4.8(a) shows a high-magnification XTEM micrographs of an as-deposited sample (S1) which clearly reveals the formation of columnar nanostructures which are aligned normal to the surface. In addition, a 5 nm-thick Cu layer is present between two 500 nm-thick

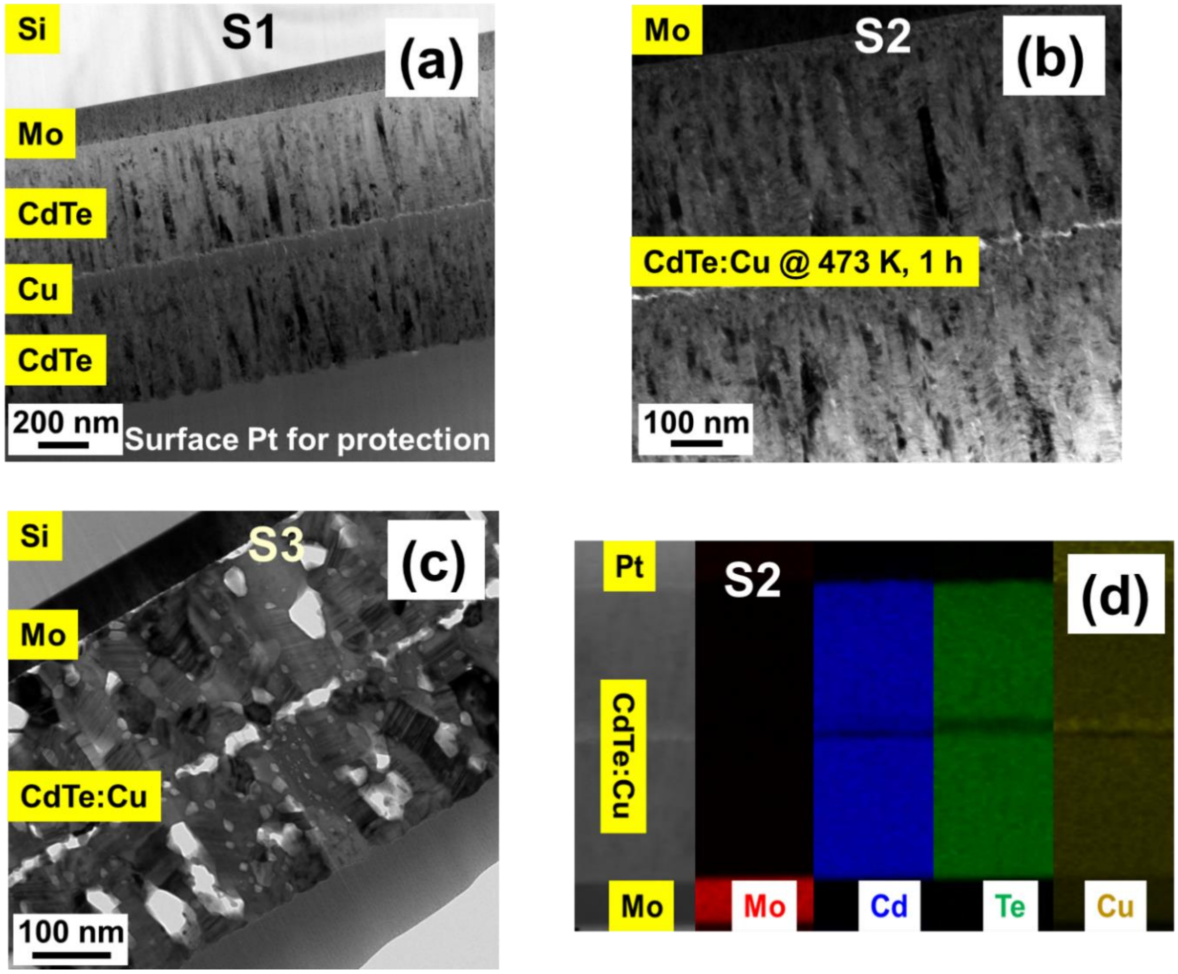

Figure 4.8: XTEM images: (a)-(c) depict high-magnification images of as-deposited CdTe/Cu/CdTe/Mo/Si sample (i.e. S1) and the ones annealed at 473 K (i.e. S2) and 673 K (i.e. S3) for 1 h in vacuum, respectively. As-deposited films reveals the presence of columnar nanostructures which remain intact for the film annealed at a lower temperature. (d) Elemental maps of Mo, Cd, Te, and Cu obtained from STEM-HAADF image of S2. The presence of a protective Pt layer in (a) comes from the focused ion beam processing TEM sample preparation [45].

(nominal) CdTe layers, as is seen from this micrograph. After annealing at 473 K in vacuum for 1 h, elongated columnar nanostructures remain intact but the formation of cavities take place in between the two CdTe layers (where the Cu layer was located originally in the as-deposited film) as is depicted in Fig. 4.8(b) [21,46]. On the other hand, Fig. 4.8(c) shows a high-magnification XTEM image of CdTe/Cu/CdTe/Mo/Si after annealing at 673 K for 1 h in vacuum (i.e. S3), depicting a significant change in the microstructure. As a matter of fact, in this case a complete loss of CdTe columnar nanostructures is observed which is accompanied by the formation of huge cavities in the CdTe layers. A dramatic change in the microstructure is also observed where the long nanocolumnar grains (as seen for S1 and S2) coalesce into irregular shapes. This indicates that to make Cu-doped CdTe films by post-annealing of CdTe/Cu/CdTe layers, temperatures more than 473 K may not be good. In addition, STEM-EDX of S2 is also carried out for elemental mapping as is shown in Fig. 4.8(d). This image not only confirms the presence of Mo, Cd, Te, and Cu but also depicts that they are uniformly distributed throughout the film.

In order to investigate the precise change in composition and the chemical nature of CdTe/Cu/CdTe films before and after annealing, XPS measurements are carried out. Figures 4.9(a)-(f) depict the XPS spectra of S1, S2, and S3 samples. The survey spectra of all the films do not reveal the presence of any impurity (spectra not shown). All the spectra are calibrated using C 1*s* core level as a reference having binding energy at 284.8 eV [47]. For all the films, respective XPS spectrum [Figs. 4.9(a)-(c)] of Cd 3*d* exhibits two main peaks corresponding to $3d_{5/2}$ and $3d_{3/2}$ levels centered around binding energies of 405.12-405.36 eV and 411.86-412.08 eV, respectively [48,49]. These peaks are consistent with the reported values of Cd bounded with Te in CdTe films. The difference in the binding energies of these two peaks is found to be 6.7 eV which is due to the spin-orbit coupling. In addition, the intensity ratio of these peaks at 405.12-405.36 eV and 411.86-412.08 eV is 1.51:1 which is very close to branching ratio of (1.5:1) of 3*d* lines [49]. On the other hand, Te 3*d* spectra are depicted in Figs. 4.9(d)-(f) which are deconvoluted into four different peaks located located at binding energies around 572.5, 576.1, 582.85, and 586.5 eV. The binding energies at 572.5 and 582.85 eV correspond to the $3d_{5/2}$ and $3d_{3/2}$ core levels of Te bound in the form of Te-Cd in CdTe, respectively. The peaks of Te $3d_{5/2}$ and $3d_{3/2}$ at binding energies of 576.1 and 586.5 correspond to Te-O bonds, respectively, which is consistent with the reported values [50]. This confirms that same amount

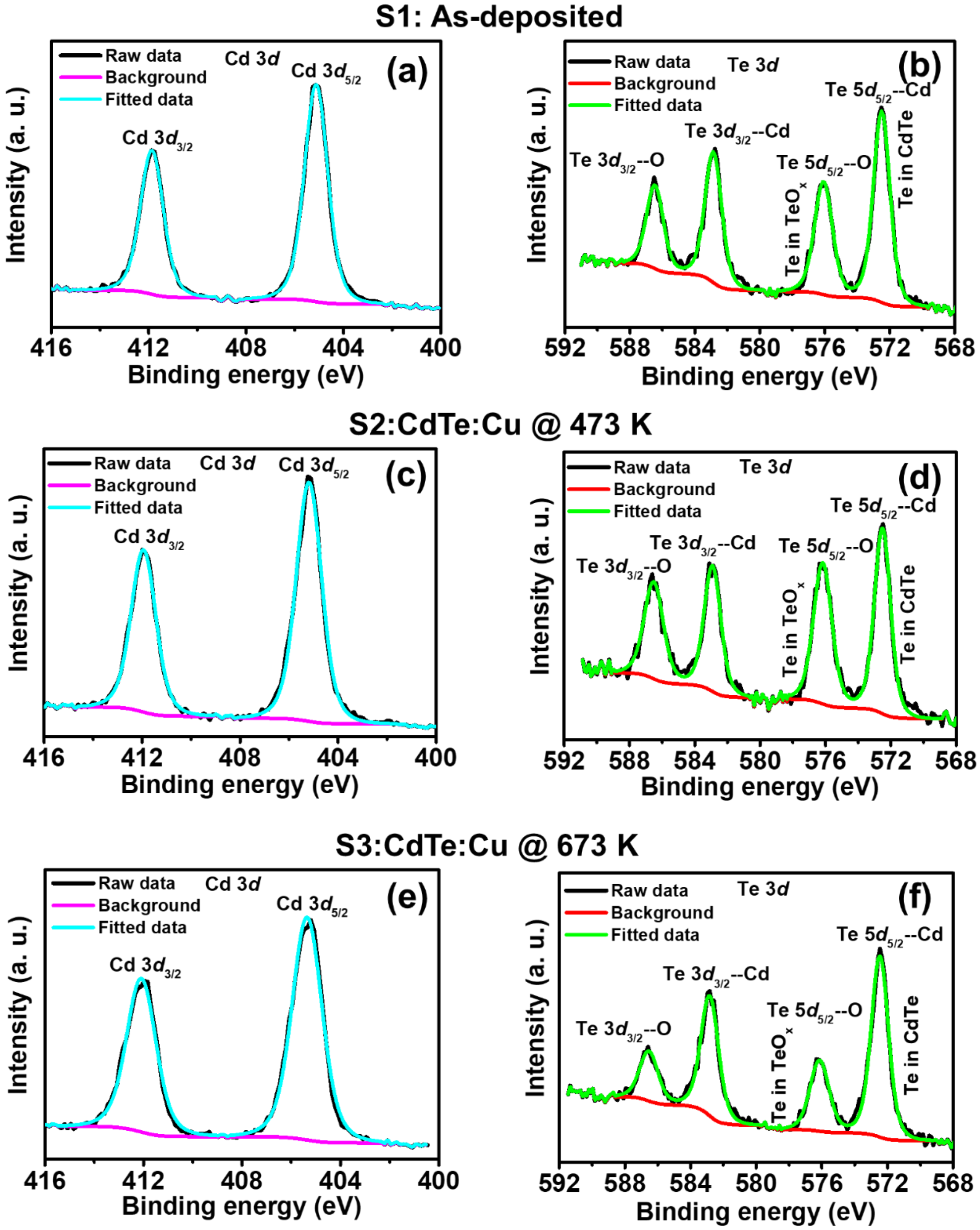

Figure 4.9: (a)-(f) Core-level Cd 3*d* and Te 3*d* spectra corresponding to CdTe/Cu/CdTe/Mo/Si (S1) and CdTe:Cu films (i.e. S2 and S3).

of Te is present in the form of tellurium oxide and CdTe. It is observed from Figs. 4.9(d)-(f) that the oxidation of Te increases for annealing at higher temperature. All the results obtained from XPS data analyses are summarized in Table 4.3.

It is well-known that CdTe has a high work function among the solar cell absorber materials which affects the cell efficiency. Thus, there is a need to reduce the work function of CdTe films. In order to test the same, we study the change in work function of CdTe films after Cu-doping (achieved through solid state diffusion) by employing KPFM technique.

Figures 4.10(a)-(c) depict the contact potential difference (V_{CPD}) maps of S1, S2, and S3, respectively. It is seen from Figs. 4.10(a) and (b) that after annealing of CdTe/Cu/CdTe films at 473 K in vacuum for 1 h the average value of V_{CPD} increases from 0.51 to 0.59 V. On the other hand, in case of S3 (annealed at 673 K for 1 h in vacuum) it decreases to 0.05 V. Here, V_{CPD} is the contact potential difference between the AFM tip and a CdTe sample. One can calculate the work function of the sample from V_{CPD} values, using the relation [34]: $\Phi_{\mathrm{sample}}=\Phi_{\mathrm{tip}} - qV_{\mathrm{CPD}}$, where Φ_{sample} is the work function of the sample, Φ_{tip} is the work function of the tip, and q is the electronic charge. The calculated value of work function (based on the HOPG reference) for S1 is 5.29 eV which decreases to 5.21 eV for S2. On the other hand, sample S3 exhibits the highest work function (5.75 eV) value among all [51,52]. It is important to note that the absolute work function values are lower compared to those reported in the literature (where is typical values are in the of 5.5 to 5.9 eV) [51]. Thus, S2 sample can be considered as the optimal one to fabricate CdTe-based PV cells due to its low work function.

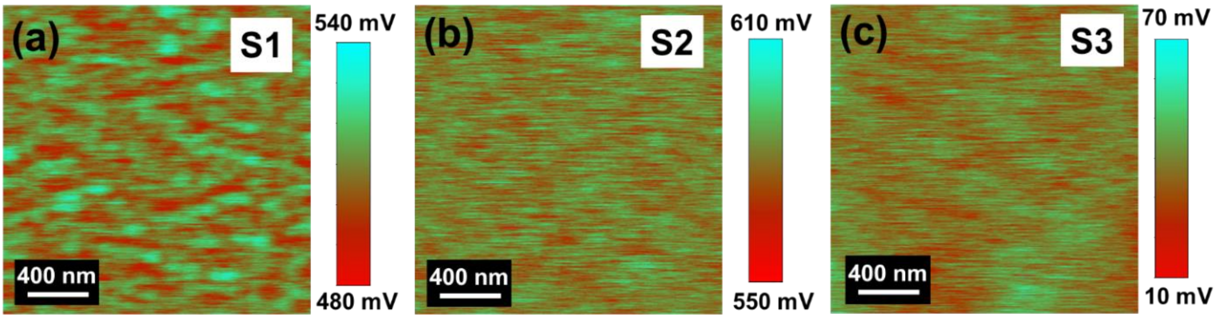

Figure 4.10: (a)-(c) Depict the surface potential maps of CdTe/Cu/CdTe films: (a) before and after annealing (b) at 473 K and (c) at 673 K in vacuum for 1 h, respectively.

In a solar cell, the optical properties of an absorbing material play a crucial role. In order to investigate the same, optical reflectance and band gap measurements of CdTe/Cu/CdTe and CdTe:Cu films are carried out. For instance, Fig. 4.11(a) depicts the optical reflectance data in the wavelength range of 300 to 800 nm for S1, S2, and S3. It is interesting to note that the specular reflectance (at 550 nm) of as-deposited and annealed samples at 473 and 673 K is 24.4, 12.1, and 6.8%, respectively. Thus, the reflectance decreases with increasing annealing temperature of CdTe/Cu/CdTe films which is the evidence of diffusion of Cu in CdTe films [12]. The very low reflectance of annealed films can be understood in light of surface features and change in their refractive index due to Cu-doping in CdTe. Further, after annealing, grain size increases which helps in absorbing more light in the annealed films. The optical band gap of CdTe and CdTe:Cu films is calculated using Tauc's Eq. $\alpha = k(h\nu - E_g)^n/h\nu$, where α is the optical absorption coefficient, $h\nu$ is the photon energy in (eV), E_g is the band gap, k is a constant, and n may have different values (in the present case, n=1/2 for direct transition). In fact, E_g is obtained from extrapolating the straight line portion of $(\alpha h\nu)^2$ verses $h\nu$ plot. Figure 4.11(b) shows the optical band gap of as-deposited and annealed CdTe/Cu/CdTe/Mo/Si films. It turns out that the as-deposited film has a band gap of 1.66 eV which decreases to 1.58 eV and 1.47 eV after annealing at 473 and 673 K for 1 h in vacuum, respectively [12]. This can be explained by higher degree of crystallinity and an increase in crystallize size of S2 [11,30]. These optical band gap values are summarized in Table 4.2 and are in good agreement with the reported values [11,12]. Further, measured resistivity values for S1, S2, and S3 are found to be 0.61 MΩ-cm, 0.56 Ω-cm, and 0.18 Ω-cm, respectively. Thus, on the basis of the above results

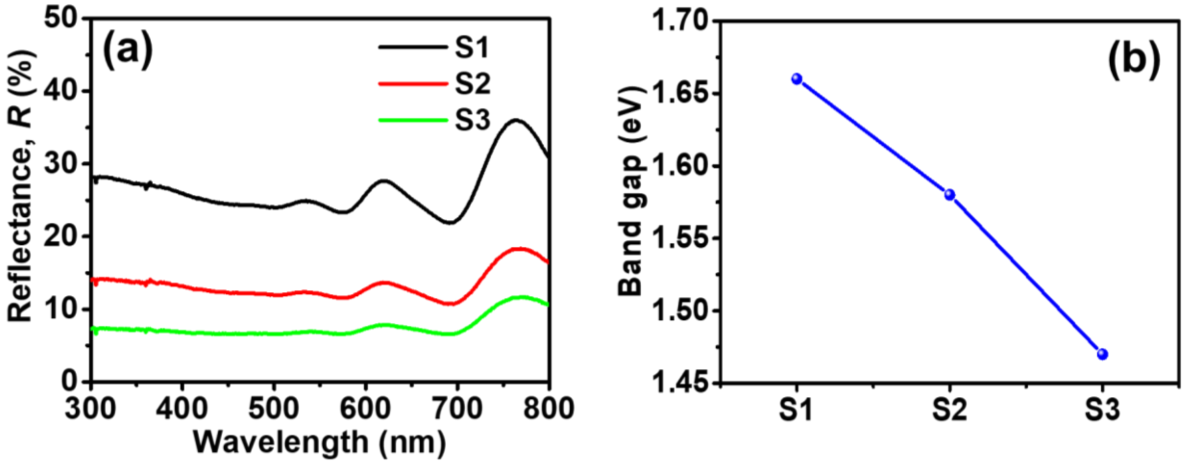

Figure 4.11: (a) Depicts the optical reflectance spectra of S1, S2, and S3. (b) Shows the variation in band gap with annealing temperature.

on structural, microstructural, composition, work function, optical reflectance, resistivity, and band gap measurements one can infer that S2 can be considered as the best optimized sample for fabricating CdTe-based PV cells in the present case.

4.3.3 Conclusions

In conclusion, CdTe films grown under normally incident deposition flux show the lowest work function and roughness values (compared to the films deposited at other growth angles) which is used for Cu-doping. Based on our experimental results, Cu-doped CdTe thin films grow in cubic phase. The microstructural, compositional, optical, electrical, and work function measurements of CdTe/Cu/CdTe/Mo/Si samples before and after annealing indicate that CdTe:Cu films prepared at 473 K will be suitable to fabricate CdTe-based solar cells. In summary, the present study opens up a new avenue to fabricate high efficiency Cl-free CdTe:Cu-based solar cells.

Table 4.1: Following parameters are determined for CdTe films deposited at different: crystallite size, microstrain, and dislocation density from XRD data, average grain size from AFM morphology, and work function from, Φ_{CdTe}, KPFM measurements.

Growth angle (°)	Crystallite size (nm)			Microstrain (°)	Dislocation density (lines/cm^2) × 10^{15}	Φ_{CdTe} (eV)
	XRD	AFM	SEM			
0	80	42	57	0.0293	0.074	5.315
40	68	49	46	0.0305	0.085	5.360
50	65	53	32	0.0342	1.22	5.368
75	35	57	29	0.0733	9.46	5.385
85	30	62	24	0.0782	11.03	5.470
87	18	68	22	0.5868	81.63	5.490

Table 4.2: Following parameters were determined for S1, S2, and S3 samples: crystallite size, microstrain, and dislocation density from XRD data; grain size and rms roughness from AFM images; average reflectance from reflectance curve; band gap from optical absorption; resistivity from current-voltage (*I*-*V*) curve and work function from contact potential difference images.

Sample name	S1	S2	S3
Crystallite size (nm)	35.3	87.3	73.8
Microstrain (°)	0.056	0.0227	0.0269
Dislocation density (lines/cm^2) × 10^{14}	8.02	1.31	1.80
Grain size (nm)	96	145	78
RMS roughness (nm)	6.58	4.91	5.21
Average reflectance (550 nm)	24.43	12.61	6.8
Band gap (eV)	1.68	1.58	1.47
Resistivity	0.61 MΩ-cm	0.56 Ω-cm	0.18 Ω-cm
Work function (eV)	5.29	5.21	5.75

Table 4.3: XPS analyses for CdTe films.

Sample name	Composition	Binding energy (eV)	Relative percentage (%)
S1	Cd $3d_{5/2}$	405.12	42.36
	Cd $3d_{3/2}$	411.86	
	Te $3d_{5/2}$ (Te with Cd)	572.48	37.94
	Te $3d_{5/2}$ (Te with O)	576.07	
	Te $3d_{3/2}$(Te with Cd)	582.85	
	Te $3d_{3/2}$ (Te with O)	586.45	
	O 1*s* O_L	530.7	19.70
S2	Cd $3d_{5/2}$	405.18	44.78
	Cd $3d_{3/2}$	411.93	
	Te $3d_{5/2}$ (Te with Cd)	572.51	33.06
	Te $3d_{5/2}$ (Te with O)	576.17	
	Te $3d_{3/2}$(Te with Cd)	582.91	
	Te $3d_{3/2}$ (Te with O)	586.51	
	O 1*s* O_L	530.6	22.16
	O 1*s* O_v	531.73	
S3	Cd $3d_{5/2}$	405.36	50.32
	Cd $3d_{3/2}$	412.08	
	Te $3d_{5/2}$ (Te with Cd)	572.46	34.44
	Te $3d_{5/2}$ (Te with O)	576.14	
	Te $3d_{3/2}$(Te with Cd)	582.83	
	Te $3d_{3/2}$ (Te with O)	586.54	
	O 1*s* O_L	530.88	15.24
	O 1*s* O_v	532.06	

References

[1] M. Raugei, S. Bargigli, and S. Ulgiati, Energy 32 (2007) 1310.

[2] V. M. Fthenakis, Renewable and Sustainable Energy Reviews 8 (2004) 303.

[3] S. M. Sze and K. K. Ng, Physics of Semiconductor Devices. 2007: Wiley-Interscience, New York.

[4] M. A. Green, Solar Cells – Operating Principles, Technology and System Applications. 1998: The University of South Wales, Wales.

[5] S. J. Fonash, Solar Cell Device Physics. 1977: Academic Press, New York.

[6] A. L. Fahrenbruch and R. H. Bube, Fundamentals of Solar Cells. 1983: Academic Press, New York.

[7] A. J. Nozik, G. Conibeer, and M. C. Beard, Advanced Concepts in Photovoltaics (RSC Energy and Environment). 2014: Royal Society of Chemistry, UK.

[8] J. Perrenoud, L. Kranz, C. Gretener, F. Pianezzi, S. Nishiwaki, S. Buecheler, and A. N. Tiwari, J. Appl. Phys. 114 (2013) 174505.

[9] N. R. Paudel, A. D. Compaan, and Y. Yan, Sol. Energy Mater Sol. Cells 113 (2013) 26.

[10] R. Kulkarni, S. Rondiya, A. Pawbake, R. Waykar, A. Jadhavar, V. Jadkar, A. Bhorde, A. Date, H. Pathan, and S. Jadkar, Energy Procedia 110 (2017) 188.

[11] G. H. Tariq and M. Anis-ur-Rehman, Mater. Sci. Semi. Proc. 30 (2015) 665.

[12] F. de Moure-Flores, J. G. Quiñones-Galván, A. Guillén-Cervantes, J. Santoyo-Salazar, A. Hernández-Hernández, M. de la. L. Olvera, M. Zapata-Torres, and M. Meléndez-Lira, AIP Adv. 2 (2012) 22131.

[13] K. Yamamoto, H. Sakakima, Y. Ogawa, A. Hosono, T. Okamoto, and T. Wada, Jpn. J. Appl. Phys 54 (2015) 08KC01.

[14] B. Biglari, M. Samimi, M. Hage-Ali, J. M. Koebel, and P. Siffert, J. Crys. Growth 89 (1988) 428.

[15] R. Singh, M. Kumar, M. Saini, A. Singh, B. Satpati, and T. Som, Appl. Surf. Sci. 418 (2017) 225.

[16] M. Kumar (Ph. D. Thesis, Institute of Physics, Bhubaneswar under Homi Bhabha National Institute, Mumbai).

[17] C. Battaglia, J. Escarré, K. Söderström, M. Charrière, M. Despeisse, F.J. Haug, and C. Ballif, Nat. Photon. 5 (2011) 535.

[18] P. Jackson, D. Hariskos, E. Lotter, S. Paetel, R. Wuerz, R. Menner, W. Wischmann, and M. Powalla, Prog. Photo.: Res. Appl. 19 (2011) 894.

[19] T. K. Todorov, J. Tang, S. Bag, O. Gunawan, T. Gokmen, Y. Zhu, and D. B. Mitzi, Adv. Ener. Mater. 3 (2013) 34.

[20] L. Kranz, C. Gretener, J. Perrenoud, R. Schmitt, F. Pianezzi, F. La Mattina, P. Blösch, E. Cheah, A. Chirilă, C. M. Fella, H. Hagendorfer, T. Jäger, S. Nishiwaki, A. R. Uhl, S. Buecheler, and A.N. Tiwari, Nat. Commun. 4 (2013) 2306.

[21] X. Wu, Sol. Ener. 77 (2004) 803.

[22] J.-H. Yum, E. Baranoff, F. Kessler, T. Moehl, S. Ahmad, T. Bessho, A. Marchioro, E. Ghadiri, J.-E. Moser, C. Yi, M. K. Nazeeruddin, and M. Grätzel, Nat. Commun. 3 (2012) 631.

[23] V. Shrotriya, Nat. Photo. 3 (2009) 447.

[24] M. de Wild-Scholten, 26th European Photovoltaic Solar Energy Conference, Hamburg, Germany, 5-9 September 2011.

[25] X. Li, D. Liu, and D. Wang, Appl. Phy. Lett. 112 (2018) 252105.

[26] S. Chandramohan, A. Kanjilal, S. N. Sarangi, S. Majumder, R. Sathyamoorthy, C.-H. Hong, and T. Som, Nanoscale 2 (2010) 1155.

[27] S. Chandramohan, A. Kanjilal, S. N. Sarangi, S. Majumder, R. Sathyamoorthy, and T. Som, Appl. Phys. A 99 (2010) 837.

[28] V. S. Vinogradov, G. Karczewski, I. V. Kucherenko, N. N. Mel’nik, and P. Fernandez, Phys. Solid State. 50 (2008) 164.

[29] J. S. W. Mak, A. A. Farah, F. Chen, and A. S. Helmy, Mater. Res. Soc. Symp. Proc. 1346 (2011) 53.

[30] P. Marwoto, D. P. N. Made, Sugianto, E. Wibowo, Z. Othaman, S. Y. Astuti, and N. P. Aryani, AIP Conf. Proc. 1555 (2013) 48.

[31] Z. Ghorannevis, E. Akbarnejad, and M. Ghoranneviss, J. Theore. Appl. Phy. 10 (2016) 225.

[32] M. Kumar, R. Singh, S. Nandy, A. Ghosh, S. Rath, and T. Som, J. Appl. Phys. 120 (2016) 15302.

[33] M. Kumar and T. Som, Nanotechnology (2015)

[34] M. Kumar, T. Basu, and T. Som, J. Appl. Phys. 119 (2016) 014307.

[35] M. Kumar, R. Singh, and T. Som, Appl. Surf. Sci. 428 (2018) 1006.

[36] A. Luque and S. Hegedus, Handbook of Photovoltaic Science. 2011: Wiely, England.

[37] U. V. Desnica, Prog. Crys. Growth Charact. 36 (1998) 291.

[38] S. H. Wei, and S. B. Zhang, Phys. Status Solidi B 229 (2002) 305.

[39] J. N. Duenow, J. M. Burst, D. S. Albin, D. Kuciauskas, S. W. Johnston, R. C. Reedy, and W. K. Metzger, Appl. Phys. Lett. 105 (2014) 053903.

[40] V. P. Singh, J. C. Mcclure, G. B. Lush, W. Wang, X. Wang, G. W. Thompson, E. Clark, Sol. Ener. Mater. Sol. Cells 59 (1999) 145.

[41] X. Feng, K. Singh, S. Bhavanam, V. Palekis, D. L. Morel, and C. S. Ferekides, IEEE Photovoltaic Specialists Conference (2012) 843.

[42] M. Thangaraju, A. Jayaram, and R. Kandasamy, App. Surf. Sci. 449 (2018) 2.

[43] N. A. Shah, J. Coat. Technol. Res. 7 (2010) 521.

[44] M. Mahanti, T. Ghosh, and D. Basak, Nanoscale. 3 (2011) 4427.

[45] M. Agati, F. Renaud, D. Benoit, and A. Claverie, MRS Conmmun. 8 (2018) 1145.

[46] Y. Yan, K. Jones, J. Zhou, X. Wu, and M. Al-Jassim, Mater. Res. Soc. Symp. Proc. 1012 (2005) 1266.

[47] R. Singh, M. Kumar, M. Saini, B. Satpati, and T. Som, Sol. Energy 174 (2018) 231.

[48] H. Jun-Feng, X. Liu, C. Li-Mei, J. Hamon, M. P. Besland, Mate. Sci. Semi. Proc. 40 (2015) 402.

[49] L. Ma, Z. Wei, F. Zhang, and X. Wu, Superlattices Microstruct. 88 (2015) 536.

[50] C. Zeng, A. Ramos-Ruiz, J. A. Field, and R. Sierra-Alvarez, J. Environ. Manage. 154 (2015) 78.

[51] W. S. M. Brooks, S. J. C. Irvine, and D. M. Taylor, Semicond. Sci. Technol. 28 (2013) 105024.

[52] I. Visoly-Fisher, S. R. Cohen, A. Ruzin, and D. Cahen, Adv. Mater. 16 (2004) 879.

CHAPTER 5

5. Selection of the hole-blocking layer

Carrier selective contact is one of the essential feature of the present photovoltaic devices (PVs) [1]. The main limiting factors in the PVs are recombination of charge carriers, optical, and thermal losses. To overcome the optical loss, different steps have been taken e.g. introduction of black-Si and chemically-prepared pyramidally textured surfaces etc. [2]. In fact, in the last few decades, the performance of PVs has improved remarkably with the introduction of a carrier selective contact sandwiched between the metal contact and buffer layers. Recently, Avasthi *et al*. have shown the hole-blocking nature of TiO_2 films and demonstrated that it helps to enhance the cell efficiency [3].The concept of hole-blocking is as follows: when a *p*- and an *n*-type semiconductors are brought together, depending on the difference in their band gaps, formation of an interfacial barrier is due to take place. Subsequently band-bending takes place at the interface which in turn leads to the blocking of charge carriers [2]. Here, we use this concept to decrease the recombination rate of charge carriers. In another report, Kumar *et al*. have fabricated a Cu-O-based solar cell using a hole-blocking TiO_2 layer whose efficiency has been demonstrated to be 5.2%. This is nine times higher compared to the one where TiO_2 has not been used as a sandwiched layer [4]. Thus, hole-blocking layer helps to increase the cell efficiency in PV cells.

In order to enhance the cell efficiency further, surface texturing can help by maximum absorption of light [5,6]. Saini *et al*. have shown the improved absorption of chemically prepared pyramidally textured-Si substrates, having an average surface reflectance of ~0.4% over a broad wide range of spectrum [7]. On the other hand, Kumar *et al*. have shown the efficacy of these pyramidally textured silicon substrates by growing a Cu_2O overlayer on the same, leading to an eight times higher efficiency compared to the one grown on an as-obtained Si substrate. Thus, textured-Si surface helps to increase the cell efficiency [8] and we study the temporal evolution of Si surface during chemical etching. In doing so, anisotropic etching of single crystalline silicon substrates is carried out for different times (in the range of 30-2400 s). This leads to the formation of randomly distributed pyramidal structures on Si surface, as is confirmed by atomic force microscopy and scanning electron microscopy. It is observed that during the early stage of etching rough surfaces evolve, whereas at longer times pyramidally textured surfaces are formed having dimensions in the range of 0.2 to 2 µm. We have carried out the surface reflectance measurements on these pyramidally textured surfaces over a broad spectral range, viz. from 300-3000 nm and observe a significant reduction in the same.

In this thesis, we have used CdTe as the main absorbing layer which has a high work function. Thus, due to a large difference in the work function between TiO_2 and CdTe films, there will be a formation of large conduction barrier height which will reduce the cell efficiency. Thus, there is a room to reduce the conduction barrier height and enhance the cell efficiency using a high work function layer such as MoO_3. In doing so, we have checked the hole-blocking properties of MoO_3 films. First, the role of deposition angle on the structural, optical, and electrical properties of radio frequency magnetron sputter deposited MoO_3 thin films on Si substrates are investigated. Following this, thickness-dependent current-voltage characteristics are carried out. The present study will be useful to improve the efficiency of a photovoltaic devices.

5.1 Experimental details

TiO_2 and MoO_3 thin films were grown on Si at RT by a RF magnetron sputtering setup at normal incidence. Pyramidally textured *p*-Si substrates were prepared through a chemical route as described in chapter 2 [2]. It may be mentioned that hereinafter chemically prepared pyramidally textured-Si substrates will be termed as *txt*-Si substrates. A 99.99% pure TiO_2

sputter target (50 mm dia×6.2 mm thick) was used for depositing TiO_2 films whereas MoO_3 films were grown using a 99.99% pure MoO_3 target having 50 mm diameter and a thickness of 5 mm in a vacuum chamber having a base pressure of 2×10^{-7} mbar. Ultra-pure (99.99%) argon gas was injected into the deposition chamber (base pressure: 2×10^{-7} mbar) with a flow rate of 30 sccm to maintain the working pressure of 5×10^{-3} mbar during deposition. An RF power of 50 and 100 W was supplied to the MoO_3 and TiO_2 target, respectively. The substrate was rotated at a constant speed of 3 rpm to achieve a uniform film thickness where the target-to-substrate distance was kept as 80 mm. Thickness of the as-grown TiO_2 and MoO_3 films were measured using a surface profilometer. Many films were grown simultaneously to check the uniformity in film thickness before making the device. Further to check the effect of crystallinity on hole-blocking, TiO_2 films were annealed at 673 K for 1 h in air. Before the deposition, a pre-sputtering was done for 20 min. to achieve a stable deposition. For MoO_3 films, deposition was carried out at different incident angles i.e. 0°, 20°, 40°, 50°, 60°, 80°, 85°, and 87° with respect to the target normal. Further, an optimized angle of 0˚ was used to grow 4, 6, 8, 10, 20, and 30 nm-thick MoO_3 films on Si and glass substrates (simultaneously) to check the hole-blocking property. In addition, effect of annealing on the hole-blocking property of MoO_3 films was also tested. Further, to check the hole-blocking nature of MoO_3/CdTe heterojunction, we have grown selective numbers of 10 nm-thick MoO_3 films on *p*-CdTe:Cu/Mo/Si.

Surface morphology of the *txt*-Si substrates and TiO_2 as well as MoO_3 films (before and after annealing) was examined by FEGSEM using 5 KeV electrons (Carl-Zeiss, Germany) under the plan- and cross sectional -views. On the other hand, surface morphology and work function measurements were studied by an *ex-situ* atomic force microscopy (AFM) setup in tapping mode using a conductive tip (AC240 TM, Electric-lever, Olympus) having a radius of curvature of ~30 nm, a stiffness of ~2 N m^{-1}, and a resonance frequency of ~70 kHz. For each sample, several images were collected from randomly chosen regions to check the uniformity and average grain size. AFM images were analyzed by WSxM software [9]. Phase identification and nature of crystallinity of the films were measured by XRD under the Bragg-Brentano geometry using a Cu-K_α radiation (λ=1.54 Å) over a 2θ scan range of 20°-80°. Micro-Raman measurements were carried out to study the vibrational properties of TiO_2 and MoO_3 films. To collect the micro-Raman spectra, 100× objective lens was used which provides 1 μm^2 laser spot on the sample surface. An argon-ion laser of 514.5 nm wavelength was used (3 mW power on the sample surface) to avoid any damage to the sample surface due to laser heating. For local microstructural analysis, cross-sectional transmission electron microscopy (XTEM) and high-resolution transmission electron microscopy (HRTEM) were used.

X-ray photoelectron spectroscopy (XPS) was also performed in a UHV chamber having a base pressure of $<5\times10^{-10}$ mbar to verify the presence of a molybdenum trioxide layer and to check the chemical oxidation state of the molybdenum. For electrical measurements, silver paste was used to make electrical contacts on the top of TiO_2 and MoO_3 films and the back side of the Si substrate. The performance of the heterostructure diodes was measured both in dark and under white light illumination and recorded using a source meter setup. The specular reflectance and transmittance were examined by UV-Vis-NIR spectrophotometer using an unpolarized light.

5.2 Growth of TiO_2 thin films on Si: Hole-blocking layer for solar cell applications

5.2.1. Introduction

Transition metal oxides are very promising materials for energy harvesting applications due to their wide band gap, photo-stability, chemical inertness, and physical stability [10,11]. As we have discussed, in a solar cell, the efficiency is affected mainly by two reasons: (a) loss due to the surface reflection [12,13] and (b) recombination of charge carriers [14,15]. To overcome the first issue, surfaces with graded refractive index can be utilized [12]. For instance, by using a TCO (e.g., AZO) on a chemically textured Si substrate, one can govern the light propagation and in turn the anti-reflection (AR) property improves due to the formation of graded refractive index [7]. On the other hand, to get rid of the second problem, a heterojunction can be made between crystalline silicon and a wide band gap semiconductor [3,16–20]. Out of the commonly used materials, TiO_2/Si heterojunction is very important since TiO_2 is considered to be a useful material for different applications such as photodiodes, resistive switching memory device, self-cleaning windows, anti-fogging glasses, gas sensors, self-sterilizing, photocatalysis, and solar cells [21–25].

Generally, TiO_2 behaves as an *n*-type semiconductor due to oxygen vacancies [26], although there are reports where it shows *p*-type conductivity as well due to acceptor-type defects in the form of Ti vacancies [27]. In photovoltaics, TiO_2 nanoparticles are known to aid electron injection and it can also be used in multi-layered structures to provide a direct electrical pathway for the photo-generated electrons to ease the electron transport by blocking the holes, leading to a higher efficiency of the solar device [28,29]. To meet the above goal, one needs to make a heterojunction with an appropriate combination of materials so that the flow of one type of charge carrier (electron or hole) can be blocked which in turn should help to increase the efficiency of a solar cell [3].

To make a TiO_2/Si heterojunction, TiO_2 thin films are prepared by different techniques, viz. sputtering [30], electron beam evaporation [31], metallo-organic chemical vapor deposition [32], pulsed laser deposition [33], and sol-gel method [34]. Among these techniques, RF magnetron sputtering process provides an easy way to integrate TiO_2 thin films since it offers the advantage of growing high quality films over large areas with tunable physical properties [30].

A lot of efforts is being put on TiO_2 thin films for last few decades and there are lot of reports on the effect of annealing on the structural, optical, and electrical properties of these films. For instance, Mathews *et al*. [34] have made nanostructured TiO_2 thin films on glass substrates by sol-gel technique and studied the effect of annealing on their structural and optical properties of these films. Likewise, Rath *et al.* [35] have deposited TiO_2 thin films on a Si substrate by sol-gel method and studied the dependence of temperature on structural, morphological, and optical properties. In fact, they observe that due to annealing at 673 K amorphous TiO_2 films undergo a transition to a crystalline anatase phase and upon annealing the films at 1073 K, it transforms into the rutile phase. Although there are some reports on *I-V* characteristics of TiO_2/Si heterojunctions [29,36,37], a detail study on the effect of annealing on the broadband AR and hole-blocking properties of an *n*-TiO_2/*p*-Si (textured-Si substrate) heterostructure is still lacking. As a matter of fact, this will be important to study following the work of Avasthi *et al.* [3] where they have reported the hole-blocking nature of an *n*-TiO_2/*p*-Si heterojunction (TiO_2 grown on commercially available silicon substrate) and its application for photovoltaics.

In this work, we study on the fabrication of self-assembled pyramidal structures on *c*-Si (100) substrates using anisotropic alkaline etching process with the help of NaOH and IPA for different times, ranging from 30 to 2400 s. It is found that with increasing etching time, the average dimension of randomly distributed pyramids on *c*-Si substrates increases from 0.2 μm to 2 μm. We also investigate the effect of crystallinity on the photo-absorption of TiO_2 thin films and the hole-blocking nature of a TiO_2/Si heterojunction (TiO_2 grown on chemically prepared, pyramidally textured *p*-Si). Microstructural analysis is carried out by field emission gun-based scanning electron microscopy and transmission electron microscopy. We show that due to a conformal growth of TiO_2 films on pyramidally textured-Si substrates (before annealing), the TiO_2 surface reflectance can be brought down to 0.2% which increases up to

0.53% after annealing at 673 K for 1 h in air. In addition, we measure the hole-blocking property of both type of heterojunctions. The present study will be useful for fabrication of solar cells based on a hole-blocking material deposited on a textured surface.

5.2.2. Results and discussion

Prior to growth of TiO_2 films, we investigate the morphological evolution of Si surfaces due to chemical etching, SEM and AFM measurements are performed before and after etching of all samples. Figures 5.1(a)-(f) show the plan-view SEM images of the microstructural evolution of Si surfaces corresponding to different etching times in the range of 30 to 2400 s. These images depict the complete coverage of the respective surface with randomly distributed pyramids having different dimensions which increase with etching time. From Fig. 5.1, it becomes evident that upon increasing the etching time, the surface increases since at higher etching times pyramids of bigger dimensions are formed. The surface coverage of these pyramids range from 27.6±2% to 85.2±4% corresponding to the etching times of 60-2400 s, as is shown in Table 5.1. The size of these pyramids range from 0.2 to 2 μm (for etching times in the range of 60-2400 s), as is confirmed from AFM images. Figures 5.2(a)-(l) show the AFM topographic and respective deflection images corresponding to the morphological evolution of Si surface subject to different etching times. The deflection images clearly show the pyramidal edges similar to the SEM images. In fact, the etching time-dependent evolution of the average size of pyramidal features are extracted from these images. It is interesting to note that for the lowest etching time (viz. 30 s), pyramid-like structures are not evident and dimension of the evolved structures are quite small. The shape of the pyramidal structures becomes prominent with increasing etching time and they start becoming sharper as well. For etching times of 1200, 1800, and 2400 s these pyramids form homogeneous surfaces and the highest surface coverage area is obtained for the ones those evolve corresponding to the highest etching time. Figures 5.3(a)-(c) show the line profiles obtained from the morphological images depicted in

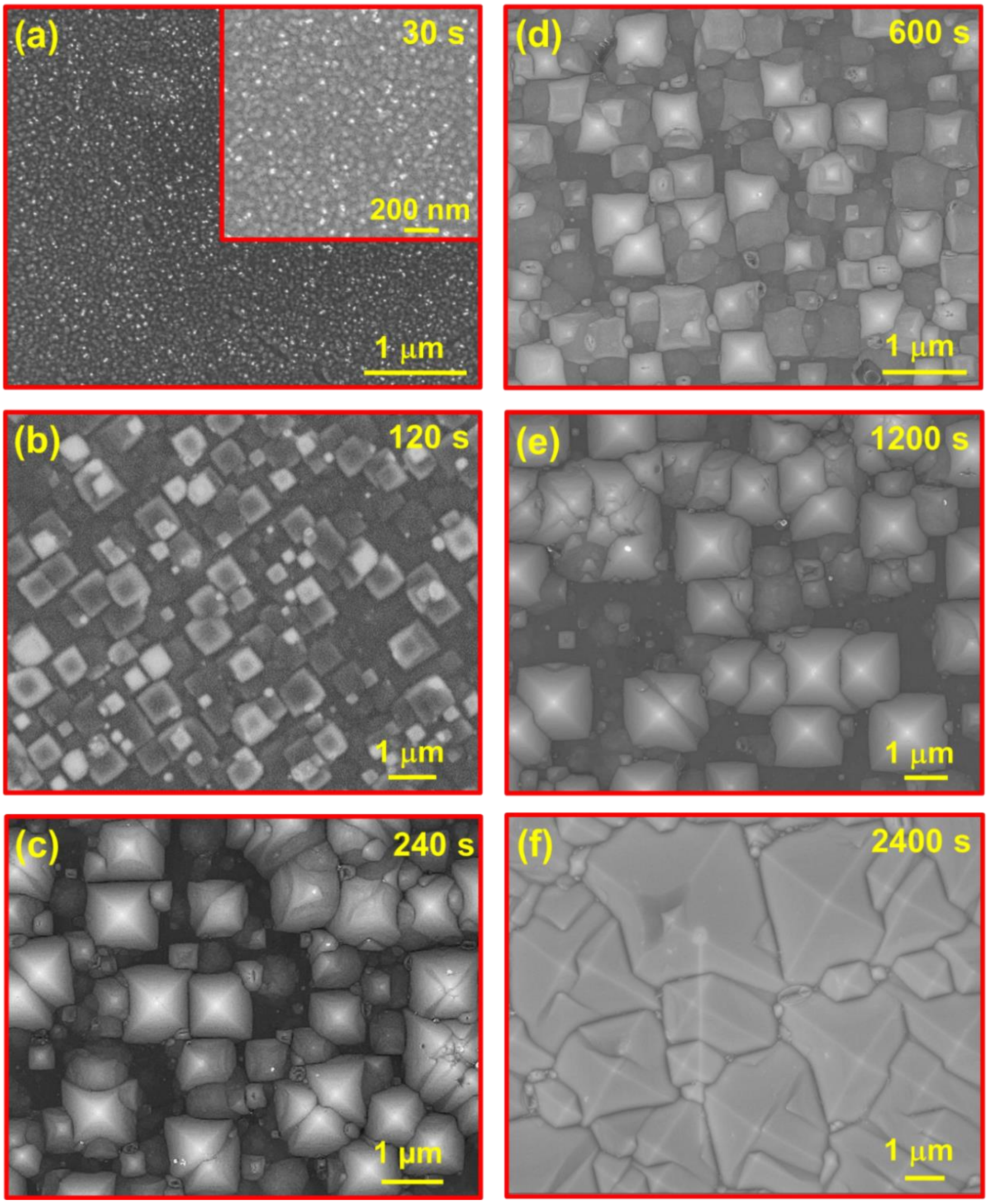

Figure 5.1: SEM images of *p*-Si(100) samples corresponding to different alkaline etching times: (a) 30 s, (b) 120 s, (c) 240 s, (d), 600 s, (e) 1200 s, and (f) 2400 s, respectively.

Figs. 5.2(a)-(c) and (g)-(i) (marked by green lines) corresponding to different etching times. For etching times up to 600 s, pyramidal structures are visible but their coverage is low (Figs. 2 and 3). On the other hand, for etching times >600 s, bigger pyramidal structures appear, having a wide distribution in size. For solar cell applications, maximum absorption of light is desirable for which the aspect ratio (*d*/*a*) of the pyramidal structures should be 2-2.5 μm and

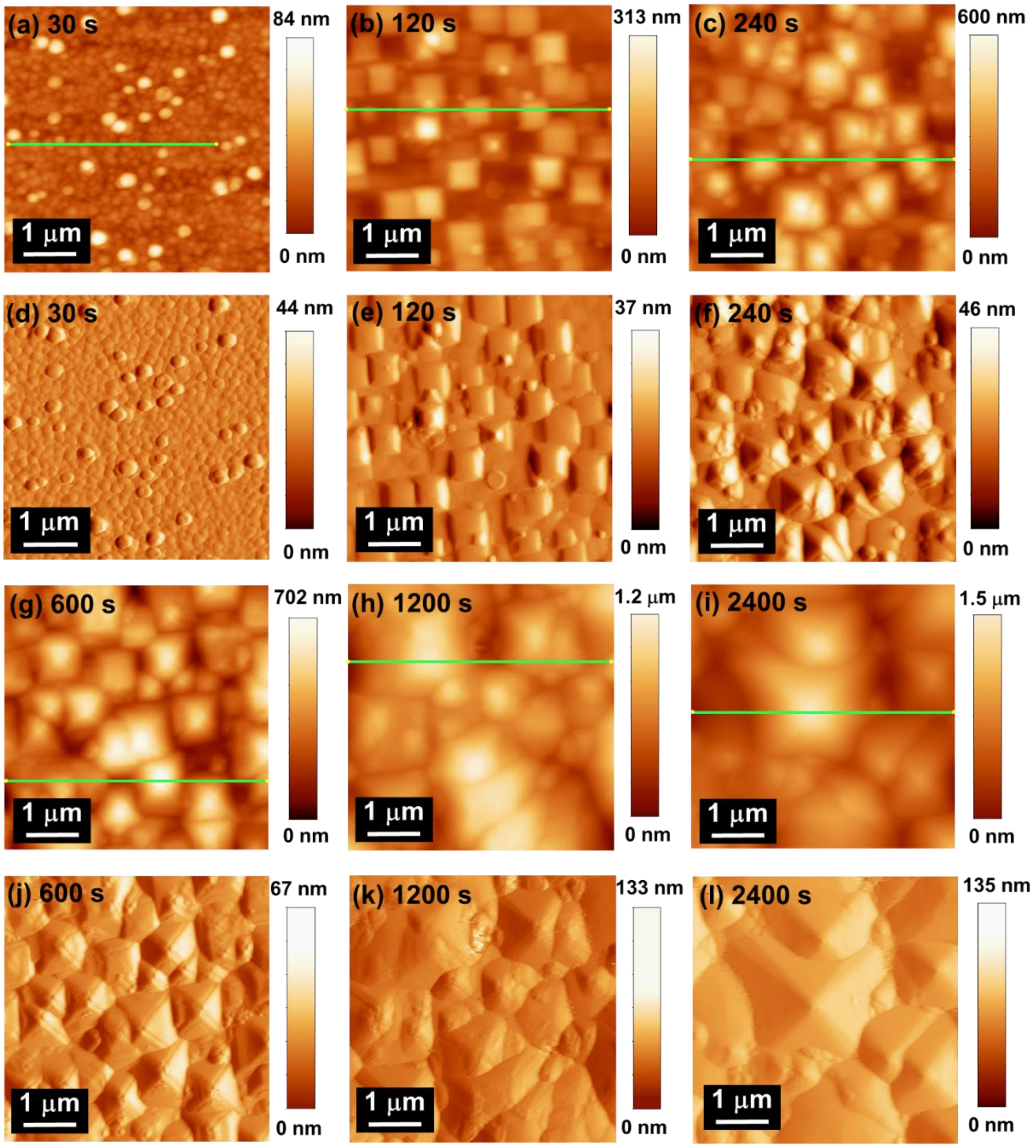

Figure 5.2: Contact mode AFM height images of chemically etched Si surfaces corresponding to different etching times of (a) 30 s, (b) 120 s, (c) 240 s, (g) 600 s, (h) 1200 s, and (i) 2400 s and corresponding deflection images: (d) 30 s, (e) 120 s, (f) 240 s, (j) 600 s, (k) 1200 s, and (l) 2400 s, respectively. The deflection images show the clear edges of pyramids. All image sizes are of 5×5 μm^2.

hence, an attempt has been made here to achieve the same.

Figure 5.3(d) shows variations in the aspect ratio and average facet angle of the pyramidal structures with etching times. This reveals a rapid decrease in the aspect ratio of the pyramidal structures (up to 600 s) which gets saturated (~2.5 μm) for higher etching times, whereas an opposite trend is observed for the facet angle of the pyramidal structures (i.e. it increases rapidly till 600 s of etching time and then shows a saturating behaviour (~45°) beyond the same.

The overall etching reaction in NaOH solution may be expressed by the following Eq. [38]:

$$Si + 2H_2O + 2OH^- \rightarrow Si(OH)_4 + 2H_2 \qquad (5.1)$$

Such a reaction proceeds at a lower rate in the absence of any one of the reactants H_2O and OH^-. In this reaction, H_2 produced is seen as bubbles which escape from the reaction vessel. These bubbles create temporary localized etch steps by sticking on the substrate and work as masks[38]. However, etching rate is a function of crystalline orientation, doping, and the etchant [38]. In the present case, surface roughening in the form of hillock formation is observed and the resulting morphology is governed by the anisotropic etching that produces

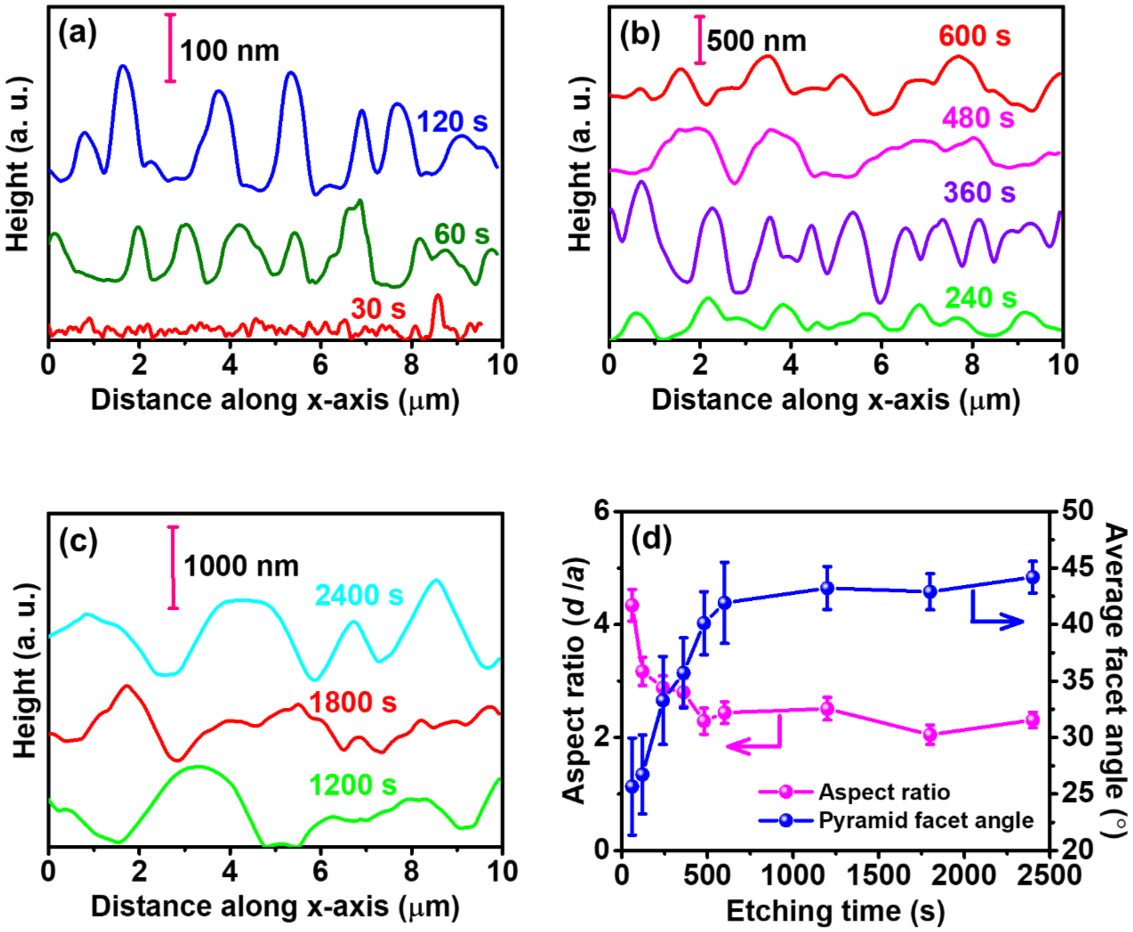

Figure 5.3: Show height distribution of pyramidal structures [(a)-(c)] and variation in the aspect ratio and average facet angle of the pyramidal structures with etching times (d).

random pyramids. As a matter of fact, for the formation of pyramids, lateral etching of the surface is very important which is achieved by the help of hydrogen bubbles formed during the etching process. During the etching of a *c*-Si substrate, Singh *et al*. have shown that the etching rate of {111} surface is lower compared to {100} or {110} surfaces and the etch ratio is ~35 for {100} to {111} surfaces [39]. This lower etching rate of the {111} plane is due to its higher activation energy in comparison to the {100} plane [40,41]. So, the pyramid formation is along the {111} plane, as is shown by an arrow in Fig. 5.1(f). For a lower etching time (i.e. 30 s), spacings between two adjacent pyramids are difficult to identify from the corresponding SEM image, although the AFM phase image [Fig. 5.2(d)] clearly manifests the nucleation of pyramidal structures on the Si surface.

In the present case, it is observed from the experimental SEM and AFM images that the height and dimension of pyramids are of the order of 1-2 μm which fulfills the criteria to achieve a significant reduction in the surface reflectance. In order to verify the same, we have carried out systematic reflectance measurements on *txt*-Si substrates, fabricated under different etching times. Figure 5.4(a) shows the specular reflectance data of *txt*-silicon samples formed under different etching times (in the wavelength range of 300 to 3000 nm) and is compared with the *pris*-Si (unetched) one. It is observed from Fig. 5.4(a) that with increasing etching time the average specular reflectance shows a decreasing trend. The surface reflectance of *pris*-Si is ~43.5%, whereas in case of lower etching times, viz. for 30 and 60 s, it reduces to 42% and 37.27%, respectively (at 550 nm) [39,42]. Thus, the observed change in the surface reflectance is minimal for lower etching times which can be attributed to less well-defined structures on Si surfaces. However, corresponding to an etching time of 120 s, there is a substantial drop in the surface reflectance (≈20%) which keeps reducing further, in a systematic manner, with an increase in the etching time. In fact, it reduces to 0.5% for an etching time of 600 s. Higher etching times up to 2400 s cause even lower (≈0.25%) reflectance value over a broad wavelength range of 300 to 3000 nm. For a better clarity, a magnified part of Fig. 5.4(a), in the wavelength range of 300 to 800 nm, is shown in Fig. 5.4(b) which depicts the reflectance data for etching times of 240-2400 s. It becomes evident that the reflectance value drops drastically to 3% for an etching time of 240 s which further reduces close to 0.25% for the highest etching time, i.e. 2400 s.

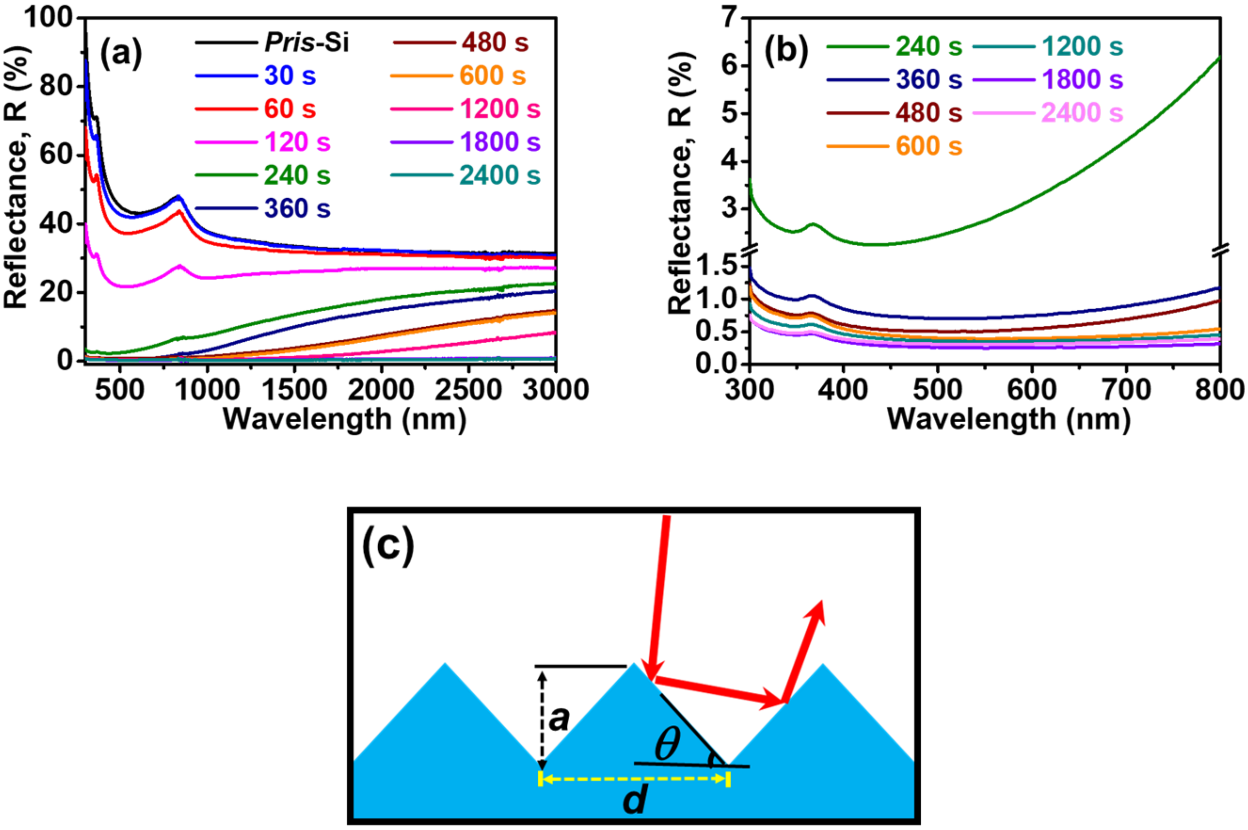

Figure 5.4: (a) and (b) Show the reflectance (*R*%) spectra of chemically prepared pyramidally textured-Si substrates for different etching times in the wavelength range of 300 to 3000 nm and 300 to 800 nm, respectively. (c) Shows the schematic optical ray diagram to demonstrate multiple reflections from a pyramidally textured-Si surface.

Recently, Imamura *et al*. have shown the effect of refractive index on the reflectance of a nanocrystalline-Si layer on pyramidally textured-Si surfaces, grown by acidic etching, and achieved a minimum reflectance in the range of 0.96 and 3.76% (in the wavelength range of 300 to 800 nm) [43]. Likewise, Jiang *et al*. [44] and Otto *et al*. [45] have shown low average reflectance for black-Si in the range of 2.4-4.7%. In another report, average optical reflectance of slantingly- and vertically-aligned silicon nanowire arrays have shown about 5 and 2.5% over the range of 300-1000 nm, respectively [46]. Thus, it is interesting to note that this hitherto unseen low optical reflectance exhibited by Si pyramids better performance sets a benchmark than the ones achieved by more sophisticated texturing approaches [44,45,47]. This reduction in the surface reflectance can be understood from the schematic optical ray diagram, as is shown in Fig. 5.4(c) where a pyramidally textured-Si surface leads to light trapping due to multiple reflections of light from the pyramids [7]. When light is incident on the top region of the pyramidal surfaces, due to low incident angle, it has highest probability of reflection. On the other hand, light incident on the bottom region of pyramid undergo multiple refection and reduces the surface reflection [39]. Likewise, each pyramid helps to reflect the light and to be incident on an adjacent pyramid. Consequently, reflectance from the front surface decreases from 43.5% to 0.25%. In addition, the low reflectance of *txt*-Si surfaces for higher etching times is due to highly dense and random distribution of pyramids having facet angle close to 45°, as is confirmed from SEM and AFM images of the same [7]. It is interesting to note that during the early etching period, the surface of silicon just starts to get roughened and at this stage dimensions of the evolved structures are quite small to trap light in an efficient manner. In fact, it is known that the reflectance is strongly influenced by the size of pyramids and light having higher wavelengths than the size of pyramidal structures cannot undergo multiple reflections [39,48]. Sai *et al*. have shown the effect of pyramid dimension on antireflection and light trapping properties of *txt*-Si surfaces using a numerical simulation based on Maxwell’s Eq. [48]. They have investigated that the surface reflection loss can be reduced significantly by using submicron Si surfaces. On the other hand, experimentally the similar trend between size of pyramids and reflectance (lowest value of reflectance is ~11% in the visible region) is observed by Singh *et al*. from *txt*-Si surfaces which are prepared in aqueous alkaline solutions [39]. As a matter of fact, reflectance of such textured surfaces changes significantly due to the size of pyramids, affecting the overall refractive index of the samples to a large extent. Thus, based on the above results, it can be inferred that pyramidally textured-Si surfaces having the right kind of aspect ratios can give rise to efficient and tunable light trapping. For further study, we have used optimized *txt*-Si substrate.

Prior to electrical measurements, structural and optical properties of TiO_2 films are carried out. Figures 5.5(a) and (b) show the plan- and tiled-view of TiO_2 grown on *txt*-Si before and after annealing, respectively, albeit granular nature of TiO_2 thin films is confirmed. For a better clarity, the insets in Figs. 5.5(a) and (b) show the high-resolution SEM images for the respective TiO_2- coated *txt*-Si surface, revealing the clear signature of granular nature of the films.

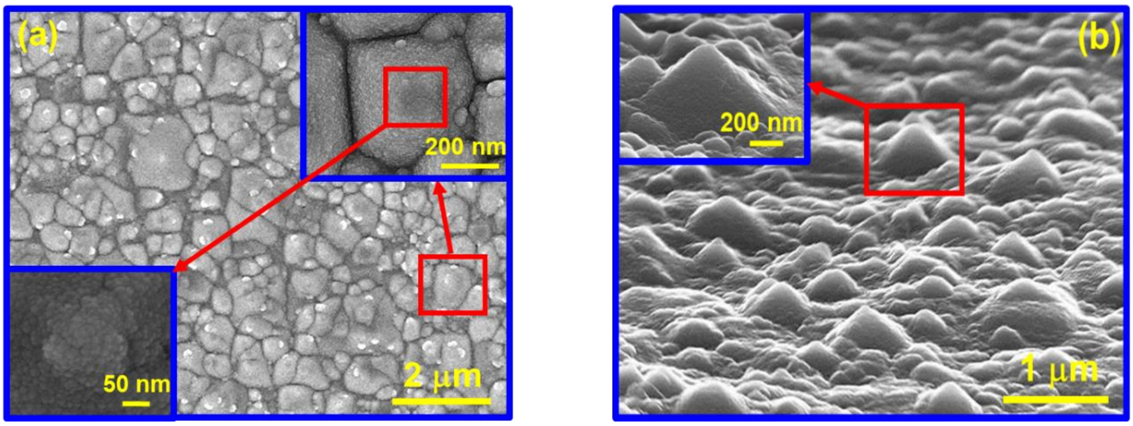

Figure 5.5: SEM images: (a) As-deposited TiO_2 film on a *txt*-Si substrate. The insets in (a) show the magnified image of a single pyramid from the marked region on (a) and a further magnified image obtained from the apex of this pyramids, confirming the granular nature of TiO_2. (b) Depicts the SEM image of the annealed (673 K for 1 h in air) TiO_2 thin film in (a) grown on a *txt*-Si substrate. Here the inset shows the magnified image obtained from the marked region in (b).

Figure 5.6(a) shows the XRD pattern of an as-deposited TiO_2 thin film grown on a *txt*-Si substrate which clearly reveals its amorphous nature [30]. On the other hand, Fig. 5.6(b) depicts the XRD pattern of the film annealed at 673 K in air for 1h. From this figure, it is evident that the annealed film becomes crystalline in nature and the peaks ($2\theta = 44.26°$ and $64.49°$) match well with that of the anatase phase [49]. Such a structural phase transition in TiO_2 under annealing was reported earlier [35].

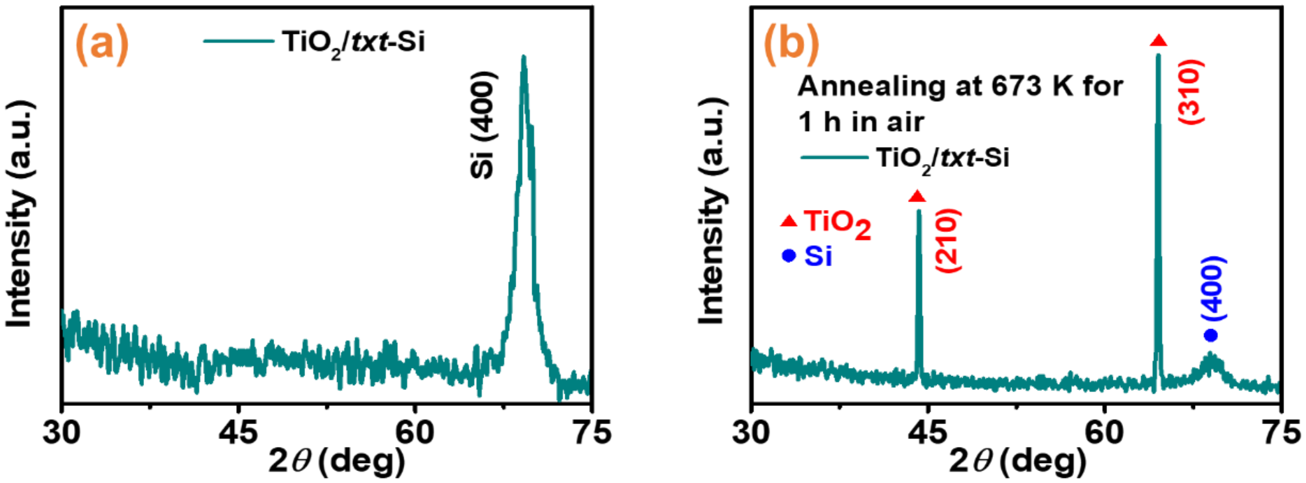

Figure 5.6: Show XRD patterns of an as-deposited (a) and the annealed (b) TiO_2 thin films grown on *txt*-Si substrates, respectively.

It is known that electrical transport property in any energy storage device is strongly influenced by the crystalline nature of the materials used in the same. Thus, in order to check the same, XTEM and HRTEM measurements are performed on our samples. Figures 5.7(a) and (b) depict the XTEM images of as-deposited and annealed TiO_2 thin films grown on *txt*-Si substrate, respectively. The inset in each case shows the corresponding HRTEM image. From the fast Fourier transform (FFT) image [inset, Fig. 5.7(a)] obtained from the marked region on Fig.

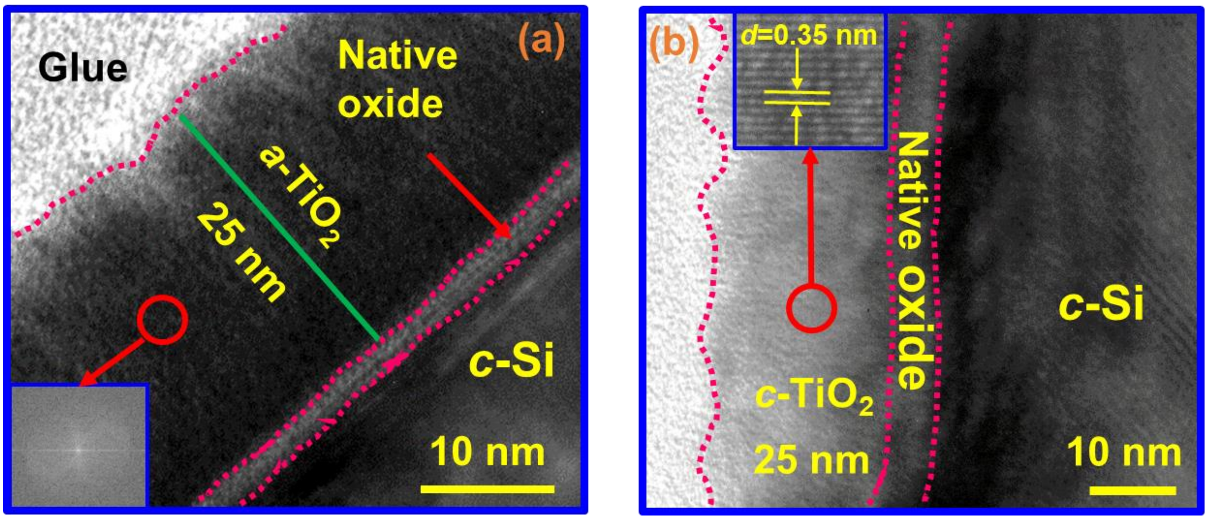

Figure 5.7: XTEM images (a) depicts an as-deposited TiO_2 thin films on *txt*-Si substrate. The inset in (a) shows the FFT image from the marked region on (a), confirming the amorphous nature of TiO_2. (b) Shows an image of the annealed (673 K for 1 h in air) TiO_2 thin film on a *txt*-Si substrate. Here the inset shows a HRTEM image obtained from the marked region on (b), confirming the crystalline nature of the TiO_2 thin film after annealing.

5.7(a), it is confirmed that the as-deposited film is amorphous in nature [50], whereas after annealing it becomes crystalline [as is seen from the inset of Fig. 5.7(b)] and the *d*-spacing (0.35 nm) obtained from the lattice image matches well with the (101) plane of the anatase phase [51]. These results corroborate well with our XRD results described above.

Since the optical properties of a material also depend strongly on its crystalline structure, we have carried out the surface reflectance and transmittance measurements on TiO_2 samples before and after annealing. Specular reflectance is measured at an incidence angle of 45° with respect to the surface normal. Figure 5.8(a) shows the specular reflectance of as-deposited and annealed TiO_2 thin films grown on *txt*-Si substrates in the wavelength range of 300 to 800 nm. It is interesting to note that the average specular reflectance of the as-deposited TiO_2 film is 0.2%, whereas upon annealing the film at 673 K in air for 1 h it increases up to 0.53%. This low reflectance of the as-deposited film is caused by its conformal growth on highly dense Si pyramids. This whole combination (granular TiO_2 on the *txt*-Si substrate) creates a graded refractive index medium (from the apex to the base of the Si pyramids), leading to the reduced surface reflectance [52]. In fact, the aspect ratio of the pyramids also plays an important role (as discussed above) in reducing the surface reflectance (like in nanowires) [48]. Thus, after annealing the surface reflectance increases up to 0.53% due to an overall decrease in the aspect ratio of the pyramids and their relatively smoother surfaces which becomes evident from the corresponding SEM image (image of the as-annealed *txt*-Si substrate not shown). In order to measure the optical band gap and transmittance, TiO_2 thin films are simultaneously deposited on glass substrates. Figure 5.8(b) shows the transmittance spectra of TiO_2 thin films under consideration (as-deposited and annealed). The as-deposited TiO_2 thin film shows ~80% transmittance which reduces to ~50% and the absorption edge gets marginally shifted towards longer wavelength [53]. In addition, there is also a sharp fall in the film transmittance in the UV region which corresponds to its optical band gap [41]. This can happen due to annealing

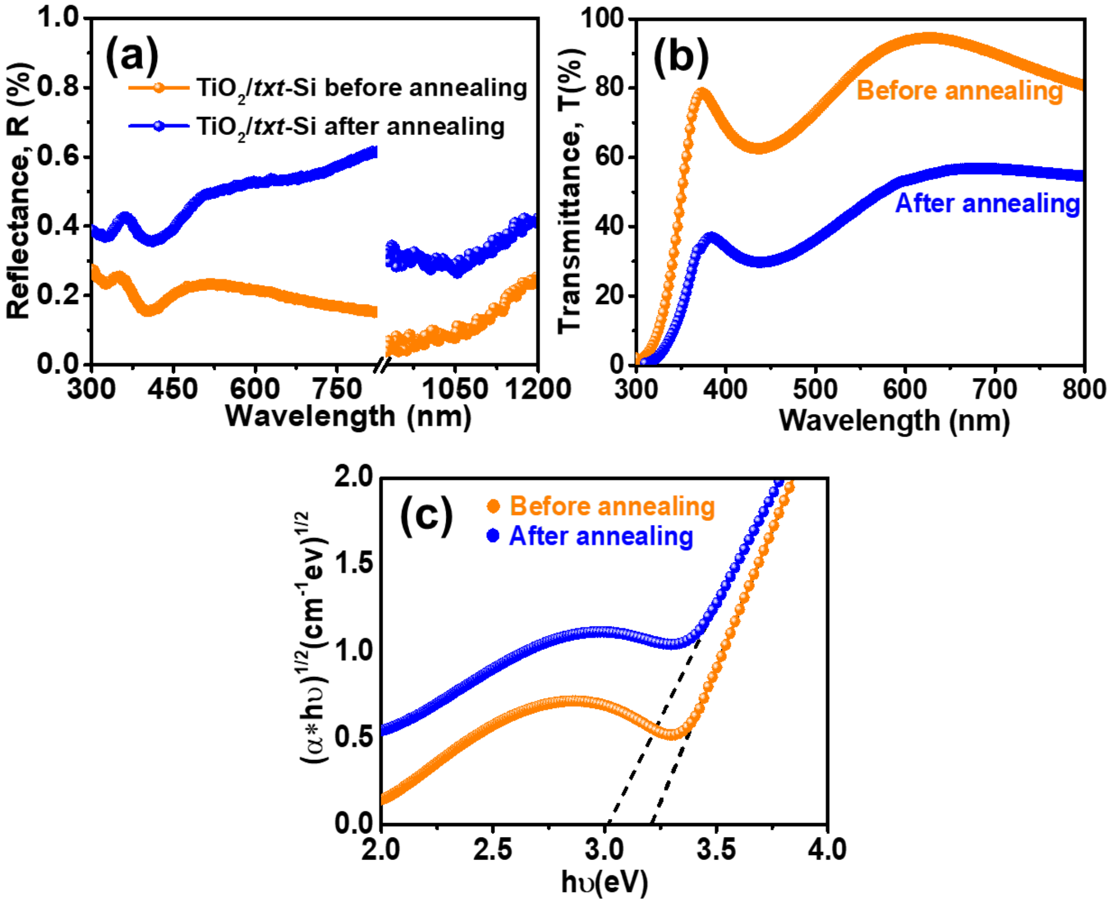

Figure 5.8: (a) Shows the reflectance (*R*%) spectra of a TiO$_2$ thin film deposited on a *txt*-Si substrate before and after annealing at 673 K in air, (b) shows the transmittance (*T*%) spectra of a TiO$_2$ thin film deposited on a glass substrate before and after annealing at 673 K, and (c) shows Tauc's plots to determine the optical band gap of TiO$_2$ thin films before and after annealing at 673 K in air for 1 h.

of the TiO$_2$ thin film, due to a change in the film density because of the variation in oxygen vacancies in the form of defects [2]. These changes are also significant due to the structural phase transition as is observed from the XRD patterns [Fig. 5.6]. The optical band gap of TiO$_2$ thin films is calculated from the Tauc's Eq. [2]:

$$\alpha = \frac{k(hv - E_g)^{\mathrm{n}}}{hv}, \qquad (5.2)$$

where α is the optical absorption coefficient, k is a constant, hv is the photon energy (in eV), and n may have different values. By extrapolating the straight line part of the $(\alpha hv)^{1/2}$ versus hv plot, one can find the value of the optical band gap. Figure 5.8(c) shows the optical band gap of as-deposited and annealed TiO$_2$ films. It is evident that as-deposited TiO$_2$ thin film has a band gap of 3.21 eV which reduces to 3.03 eV after annealing at 673 K for 1 h in air [34]. This decrease in the optical band gap of the film after annealing can be attributed to the change in the film density caused due to the structural phase transition from amorphous to anatase phase [53]. As a matter of fact, the calculated value matches very well with the band gap of anatase phase of TiO_2 thin film which is also consistent with our XRD and HRTEM results.

In order to investigate the hole-blocking nature of TiO_2/*pris*-Si and TiO_2/*txt*-Si for as deposited and annealed heterojunctions, current-voltage (*I-V*) characteristic were carried out at RT in dark condition. Based on the Anderson model, the ideal energy-band diagram of *n*-TiO_2/*p*-Si heterojunction is schematically shown in Fig. 5.9(a) [2]. For TiO_2, electron affinity (χ) and ionization energy are at about 4.30 eV and 7.45 eV, respectively below the vacuum level. On the other hand, for Si, χ and ionization energy are at about 4.05 eV and 5.17 eV, respectively below the vacuum level. At the same time, the band gap (E_g) of TiO_2 and Si are 3.15 eV and 1.12 eV, respectively. From the above values, the energy barrier for an electron, $\Delta E_c=\chi(TiO_2)-\chi(Si)=4.30-4.05=0.25$ eV and that for a hole, $\Delta E_v=E_g(TiO_2)+\Delta E_c$ $E_g(Si)=3.15+0.25-1.12=2.28$ eV [Fig. 5.9(a)] [36]. On the basis of these calculations, one can infer that there is a large barrier in the valance band which is capable to block the transport of holes from Si to TiO_2, whereas there is a small barrier in the conduction band which allows the transport of electrons from Si to TiO_2.

Figure 5.9(b) and (c) show the *I-V* characteristics of the *n*-TiO_2/*p-pris*-Si and *n*-TiO_2/*p-txt*-Si heterojunctions before and after annealing, respectively. From these figures, it is clear that no current flows for small biases (<0.3 V) for all heterojunctions, revealing that the TiO_2 film works as a hole-blocking layer in both configurations, albeit it is more prominent for the as-deposited case. This can happen since the band gap of TiO_2 decreases from 3.21 eV to 3.03 eV (due to annealing), indicating a reduction in the barrier height for holes. It may be mentioned that the concentration of oxygen vacancies can strongly modify the Fermi level which in turn

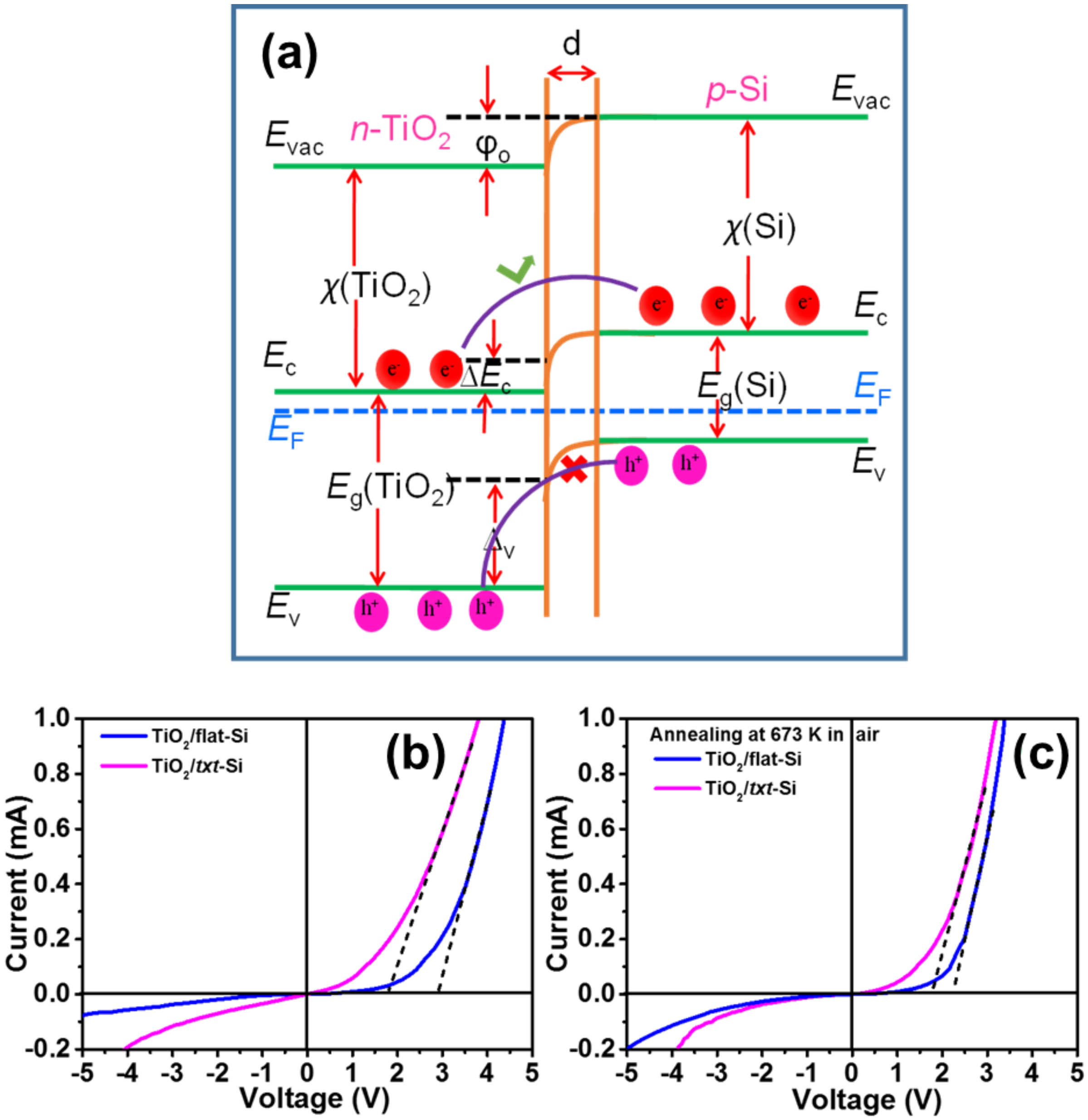

Figure 5.9: (a) Shows the energy-band diagram, based on Anderson model, of a nanostructured *n*-TiO_2/*p*-Si heterojunction diode, whereas (b) and (c) show the *I–V* plots of TiO_2/*pris*-Si and TiO_2/*txt*-Si samples before and after annealing at 673 K for 1 h in air, respectively.

changes the optical band gap of TiO_2 [31]. So the hole-blocking nature in TiO_2 is definitely affected by the crystalline nature of TiO_2 films. Such heterojunctions, based on the wide band gap semiconductors, having the ability to block one type of carrier can be widely used in future photovoltaic devices. However, in our case, MoO_3 turns out to be the most suitable one as the hole-blocking layer due to its high work function (e.g. 5.15 eV as compared to that of 4.75 eV for TiO_2), leading to a reduced interfacial barrier (3.14 eV in contrast 2.28 eV for TiO_2). The details on growth and characterization of MoO_3 layer towards optimizing its hole-blocking property is described in the next section.

5.2.3. Conclusions

In conclusion, the role of chemically *txt*-Si is very crucial for efficient light absorption in the wide range of wavelength from 300 to 800 nm, due to the formation of pyramidal-shaped structure. A structural phase transition from amorphous to crystalline anatase-TiO_2 thin film (deposited on *txt*-Si substrate) upon annealing at 673 K for 1 h in air has been demonstrated. Scanning electron microscopy measurements show a random distribution of chemically prepared pyramidal structures and the granular nature of TiO_2 thin films under both configurations (as-deposited and annealed). Specular reflectance for the as-deposited TiO_2 film (in the range of 300-800 nm) grown on a *txt*-Si substrate is found to be 0.2% which increases up to 0.53% after annealing, indicating the potential of these samples in energy harvesting applications. In addition, we show that the optical band gap of TiO_2 thin film can be tuned from 3.21 eV to 3.03 eV by annealing the film at 673 K for 1 h (in air) which in turn not only tunes the transmittance from 80% to 50% but also leads to a change in the hole-blocking ability of the film. This study will be important to fabricate a solar cell using a hole-blocking layer.

5.3 Study on hole-blocking property of MoO_3 thin films

5.3.1 Growth angle-dependent tunable structural, optical, and electronic properties of MoO_3 thin films

5.3.1.1 Introduction

Transition metal oxide (TMO) thin films have high optical transparency in the visible region, low resistivity, and tunable band gap [54,55]. Due to these interesting properties, TMOs (e.g. In_2O_3:SnO_2, SnO_2, CuO, ZnO, ZnO:Al, TiO_2, MoO_3, and WO_3) are widely used in different optoelectronic devices such as solar cells, electrochromic devices, solid-state microbatteries, display panels, ultra-violet detectors, and gas sensors [55–63]. Moreover, some of the TMOs are also used as a potential candidate for carrier selective contact(s) in solar cells and photodetectors [3,64]. Recently, Singh *et al*. have shown that TiO_2 can be used as a hole-blocking layer in solar cells [2], whereas Patel *et al*. have demonstrated that MoO_3 can be used as a hole-transporting layer in Co_3O_4 based self-powered ultraviolet photodetector [65]. In organic solar cells, MoO_3 is used as a hole-selective contact [66]. In this regard, MoO_3 is considered to be a hole or an electron-blocking layer, depending on the band-bending in the valance or conduction band. In addition, MoO_3 is regarded as an electrochromic material as it exhibits electro- and photo-chromic effect [60,67].

Generally, MoO_3 behaves as an *n*-type semiconductor due to oxygen vacancies or reduced oxidation state of Mo [15,17,18], resulting in the formation of defect levels below the conduction band which yields a large band gap (3.0-3.7 eV at RT) [66]. In addition, MoO_3 has a very high work function, ranging from 5.1 to 6.5 eV [69]. Recently, Battaglia *et al.* [64] have shown a high work function of MoO_3 (practically causing it to act as a metal) and extended its application to crystalline Si solar cell. This high work function depends on the deposition technique and oxidation state of Mo. MoO_3 films prepared by vacuum sublimation has a work function between 6.8 and 6.9 eV [70]. These insights provide guidelines for tuning the work function at nanoscale using different deposition techniques.

Various methods are used to grow MoO_3 thin films such as chemical vapor deposition, atomic layer deposition, electron beam evaporation, and sputtering [60,61,68,70,71]. Out of these, sputtering is considered to be an attractive technique because it has advantages of producing high-quality contamination-free films over a large area with uniformity and controlled growth rate having tunable physical properties [2,65,72]. It is well-known that the physical properties of transition metal oxide films grown by sputtering technique depend a lot on the working parameters such as power, deposition time, pressure, substrate-to-target distance, substrate temperature, and deposition angle [73]. Recently, Kumar *et al.* have shown that by varying the growth angle, tunable optoelectronic properties of Al-doped zinc oxide thin films can be achieved [56].

Basically, OAD is known to be an invaluable technique for growing a wide class of nanostructures [74–76]. As a matter of fact, a large number of devices are fabricated which make use of OAD-grown columnar nano/microstructures having controlled shape, size, porosity, anisotropy and/or crystallographic texture [77]. In addition, García *et al.* [78] have studied the change in porosity and water adsorption of TiO_2 thin films grown by glancing angle deposition. Likewise, Beydaghyan *et al.* have shown the photochromic behavior of nanostructured MoO_3 thin films deposited by glancing angle deposition method [79]. Further to this, organic light emitting diode performance of MoO_3 films deposited at oblique angles have been studied by Liu *et al.* [80]. Due to a wide range of usages of MoO_3 in photovoltaics applications, it has become important to carry out a detail study on the impact of growth angle on its structural and optoelectronic properties as well as work function.

In this report, we study the effect of growth angle on several physical properties, viz. morphology, crystallinity, work function, optical, and electrical properties of MoO_3 films grown at RT in a systematic manner. We have shown that the work function of MoO_3 films can be tuned from 5.6 eV to 5.26 eV by changing the angle of deposition. As a matter of fact, we show that all our films show high transmittance (>70 % in the visible region) and a blue-shift is observed in the band gap with increasing growth angle. Based on the observed results, we conclude that MoO_3 films grown under normally incident flux yields the best results for photovoltaics applications. This study is very important for MoO_3 films grown by sputtering as carrier selective contact in solar cell applications.

5.3.1.2 Results and discussion

To check the evolution of surface morphology of MoO_3 thin films grown under various deposition angles, AFM images are recorded. Figures 5.10(a)-(f) depict the morphological evolution of MoO_3 films deposited at 0°, 20°, 40°, 50°, 80°, and 87°, respectively. MoO_3 film grown at 0° shows a smooth surface with RMS roughness of 0.33 nm. However, with increasing angle of deposition from 20° to 85°, the RMS roughness increases from 0.37 to 1.85 nm and then decreases to 1.23 nm corresponding to an incidence angle of 87°. The maximum RMS roughness is 1.85 nm for the deposition angle of 85°. The values of RMS roughness are summarized in Table 5.2. The observed growth angle-dependent results are explained on the basis of growth dynamics [56,74,77] later in this section.

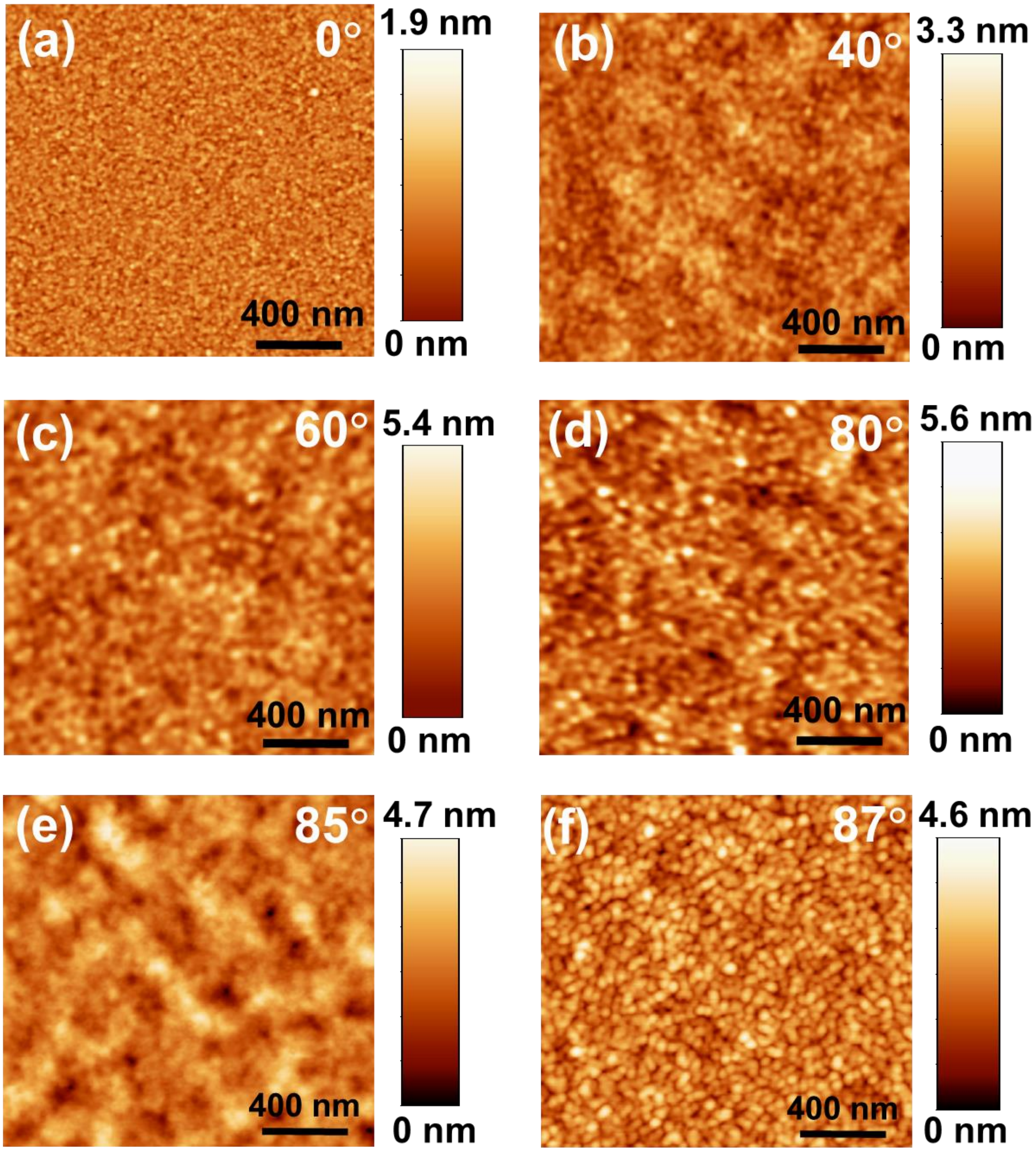

Figure 5.10: (a)-(f) depict AFM images of MoO_3 films grown at 0°, 20°, 40°, 50°, 80°, and 87°, respectively.

To have a better understanding of the evaluation of the morphological features of the film, power spectral density (PSD) curves are calculated. In fact, PSDs are calculated from Fourier transformation of the surface topographical images of MoO_3 films corresponding to different growth angles [81]. From the PSD data, it is possible to calculate the value of correlation length for each deposition angle. It is found that the film deposited at 0° has the lowest correlation length (33.1 nm) which increases for higher growth angles. Highest correlation length is 281.4 nm for 85° which again decreases (260.4 nm) for 87°. At higher growth angles the surface become rough and there is a development of large correlation length due to increase in grain size with growth angle [78]. For intermediated angles of 20, 40, 50, 60, and 80°, correlation lengths turn out to be 37.4, 49.3, 67.5, 96.1, and 115.7 nm, respectively and are presented in Table 5.2.

It is well-known that OAD technique has an influence on the crystallinity of the films [56]. To get a deeper insight into the crystal structure, XRD measurements on all MoO_3 films are performed under similar conditions (same scan speed, scan rate, scan angle, and slit width). Figure 5.11(a) shows the XRD pattern of MoO_3 films deposited at different angles ranging from 0° to 87°. It is observed that all MoO_3 films are amorphous in nature [82,83]. In order to study the vibrational properties of MoO_3 films, micro-Raman measurements are carried out. Figure 5.11(b) shows the micro-Raman spectra of MoO_3 films grown on Si under various growth angles ranging from 0° to 80°. The Raman lines apperaring at 304.94, 438.07, 619, 671, 832, and 974 cm^{-1} correspond to the characteristics Raman mode of amorphous MoO_3 films [84]. The strong Raman line observed at 521 cm^{-1} belongs to the Si substrate [3]. The Raman shifts observed in the ranges of 200-400, 400-600, and 600-1000 cm^{-1} correspond to the bending, deformation, and stretching modes, respectively. For instance, the Raman line at 304.94 cm^{-1} is associated with the bending mode of Mo_3-O and related to B_{2g}, B_{3g} [84]. The Raman line at 671 cm^{-1} (B_{2g}, B_{1g}) is assigned to the triply connected bridge-oxygen (Mo_3-O) bride (threefold bridged) entity asymmetric stretching mode along the *c*-axis [84,85]. This asymmetric mode of bridge-oxygen Mo_3-O bridge is due to the edge-shared oxygens with the three MoO_6 octrahedra. Likewise, the band appearing at 832 cm^{-1} belongs to A_g, B_{1g} mode and attributed to the symmetric stretching.

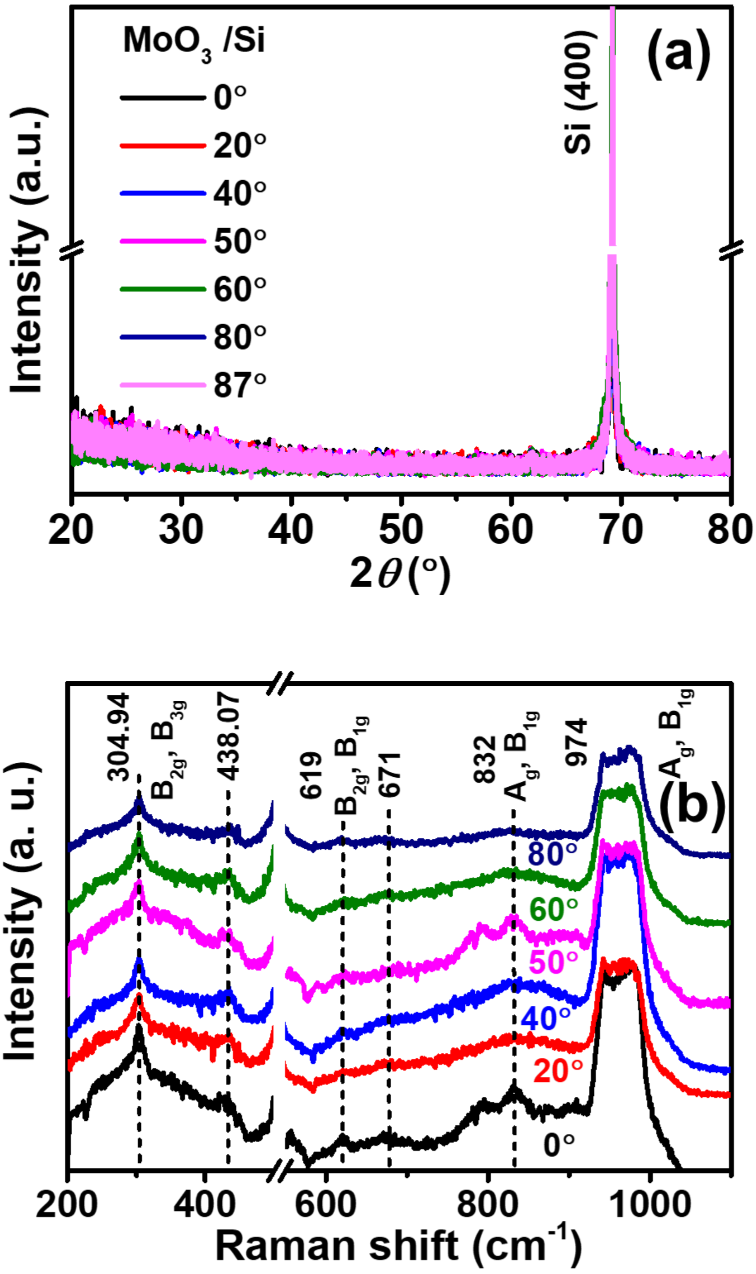

Figure 5.11: (a) Depicts the XRD patterns of MoO_3 films deposited on Si(100) substrates at different growth angles and (b) shows the Raman spectra of MoO_3 films.

This band is assigned to the terminal oxygen or doubly connected bridge-oxygen Mo-O-Mo entity which results from the corner-shared oxygen atoms with two octrahedra. On the other hand, the Raman line at 974 cm^{-1} (A_g, B_{1g}) is related to the symmetric stretching mode of the terminal atom of oxygen (Mo^{6+}=O) which is due to an unshared oxygen. Moreover, the peaks at 438.07 and 832 cm^{-1} are due to intermediate oxidation state of MoO_3, whereas the Raman lines observed at 619, 832, and 974 cm^{-1} belong to the amorphous phase of MoO_3 [84,86]. This further corroborates with the absence of any Raman peak which signifies the absence of a crystalline structure. Interestingly, width of the overlapping bands increases with increasing deposition angle. This indicates less number of vacant spaces in the films grown at higher incident angles. The observed results match very well with the XRD results described above.

It is known that optical and electrical properties are strongly influenced by structural and surface morphology of a thin film [73]. Thus, in order to correlate the same, optical transmittance measurements are carried out for simultaneously grown MoO_3 films on glass substrates, whereas reflectance measurements are performed for the films deposited on Si substrates and subsequently the band gaps are extracted for all the films deposited at various angles. Figure 5.12(a) shows the optical transmittance data for all MoO_3 films corresponding to various growth angles. It is interesting to note that the average transmittance of all MoO_3 films is higher than 70% (in the wavelength range of 400 to 800 nm) which confirms transparent nature of MoO_3 thin films in the visible region.

In addition, from the transmittance spectra it is observed that there is a sharp decrease in the transmittance around 370 nm which can be related to the fundamental absorption edge of MoO_3 [87,88]. From Fig. 5.12(a), it is found that there is a red shift in the absorption edge of MoO_3 up to a growth angle of 50° which is followed by a blue shift up to a growth angle of 87°. This shift in the absorption edge can be attributed to a change in the band gap of MoO_3 films with deposition angle. The highest transmittance (> 85 %) is observed for the film grown at 80°. This change in transmittance may be due to optical scattering effect because of change in the roughness (as confirmed by AFM) and porosity of the films [77–79].

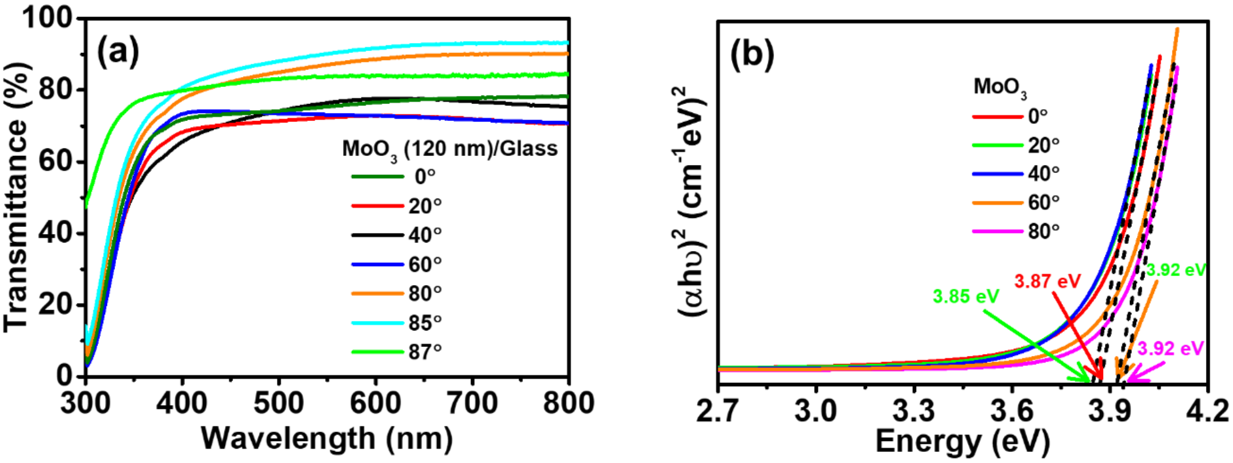

Figure 5.12: Show (a) the transmittance spectra and (b) the measured band gap (using Tauc's Eq.) of MoO_3 films grown at different angles.

At higher growth angles porosity comes into picture due to a low ratio of deposited MoO_3 particles over impinging Ar gas which in turn gives rise to a change in the film density and in turn the optical transmittance [74,89]. The optical band gap (E_g) of MoO_3 films is calculated using Tauc's Eq. 5.2. Figure 5.12(b) shows the Tauc's plot for all MoO_3 films corresponding to different grown angles. The band gap values of all MoO_3 films are presented in Table 5.2.

It is understood that nanoscale properties of thin films are influenced by growth angle [56]. Thus, to measure the change in work function of our MoO_3 films, KPFM technique is employed. A schematic representation of working principle of KPFM is shown in Fig. 5.13. Figures 5.14(a)-(g) show the contact potential difference (V_{CPD}) images of MoO_3 films deposited for 0°-87°, respectively. It is interesting to note that the results obtained from KPFM measurements corroborate well with the structural and optical properties of the films. The contact potential difference increases from 0° to 60°, whereas it decreases for films grown at higher angles of incidence (up to 87°). V_{CPD} is the contact potential difference between the AFM tip and the sample. It is known that V_{CPD} can be converted into the work function of the sample, using the following Eq. [56]:

$$\Phi_{\mathrm{sample}} = \Phi_{\mathrm{tip}} - qV_{\mathrm{CPD}} , \tag{5.3}$$

where Φ_{sample} is the work function of the sample, Φ_{tip} is the work function of the tip, and q is the electronic charge. The work function of the tip is measured with respect to a clean specimen highly oriented pyrolytic graphite (HOPG) [90]

The work function value is extracted for all the growth angles, ranging from 0 to 87°. It is observed that the measured work function decreases up to 60°, whereas it increases for the films deposited at 80° and 87° [Fig. 5.14(g)]. The maximum work function is found to be 5.58 eV corresponding to the growth angle of 0°. For other oblique angles of incidence (viz. 20°, 40°, 50°, 60°, 80°, 85°, and 87°), Φ_{sample} values turn out to be 5.5, 5.48, 5.44, 5.26, 5.41, 5.43, and 5.45 eV, respectively as is summarized in Table 5.2. Polycrystalline MoO_3 films, without exposure to adsorbents, have high work function values (5.8 to 6.8 eV) [70]. In the present case, low value of work function may be due to its crystal structure because all MoO_3 films are amorphous in nature. In addition, these MoO_3 films may have oxygen vacancies which cause a low value of work function. Greiner *et al*. have shown that metal oxides have higher work function in fully oxidized form rather than their reduced form and small changes in the oxygen content lead to significant changes in the work function of the material [70]. In addition to this, defect states within the band gap can also shift the Fermi level, causing a change in the work function [69]. From the above results, it is observed that the bulk and nanoscale properties of MoO_3 films can be tuned by changing the growth angle.

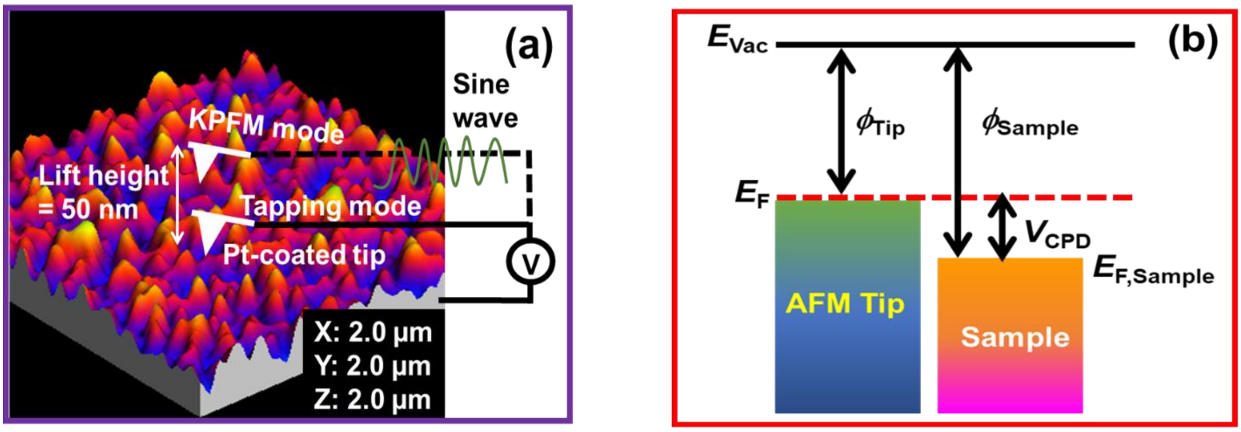

Figure 5.13: Schematic representations of KPFM technique and the contact potential difference.

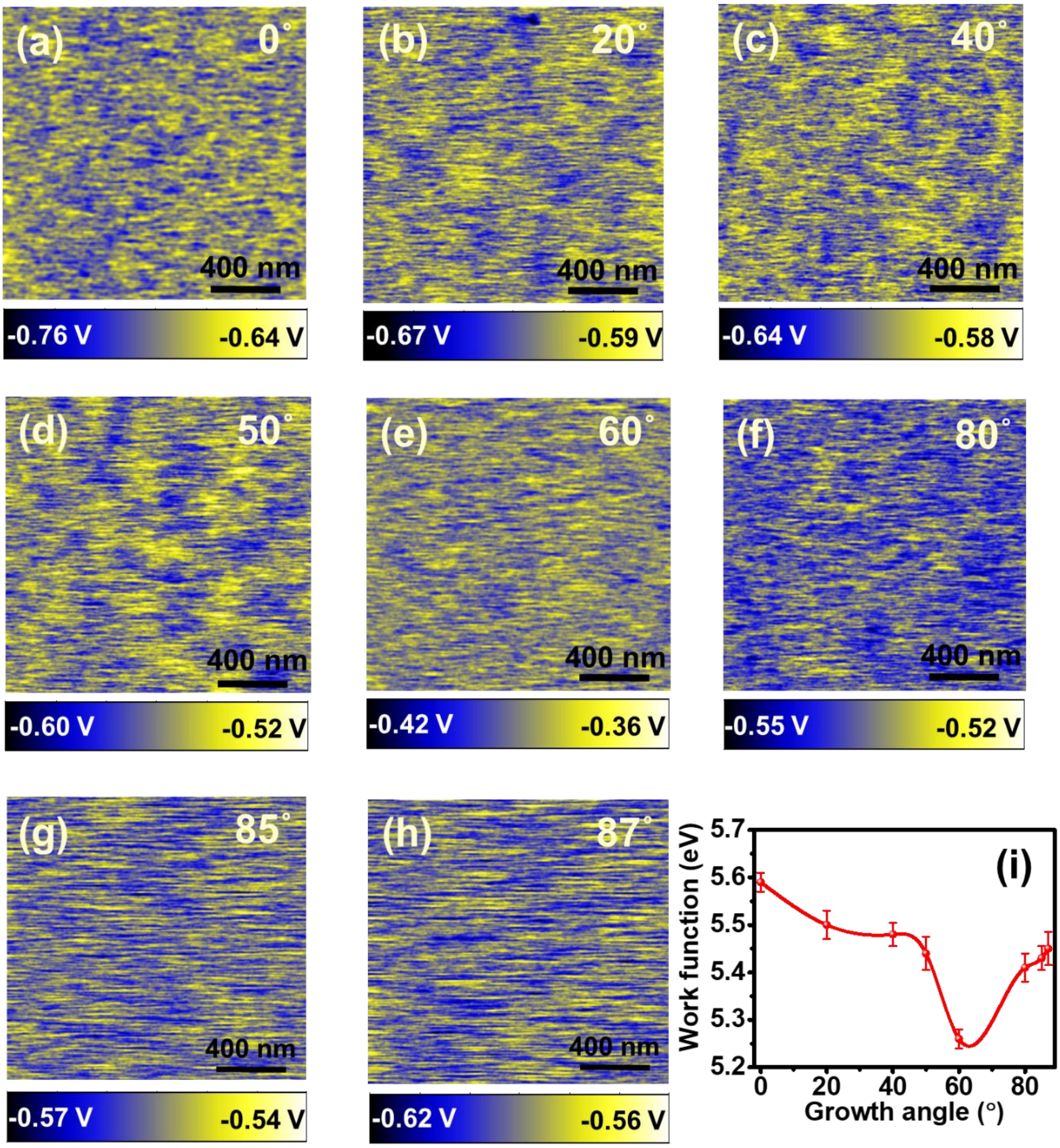

Figure 5.14: (a)-(h) V_{CPD} maps of MoO_3 films deposited at 0°, 20°, 40°, 50°, 60°, 80°, 85°, and 87°, respectively. (i) Represents growth angle-dependent variation in the work function of MoO_3 films.

The observed experimental results are explained in the framework of the growth mechanism of MoO_3 films during OAD deposition. Mainly, two mechanisms: (a) surface diffusion and (b) shadowing are operative during film growth by OAD deposition process [56,76,89,91]. For normally grown films, incoming vapour atoms and molecules arrive at the substrate surface and get quickly absorbed on the surface. In this condition, ballistic shadowing lengths are very small, resulting in a tightly packed morphology. The absorbed atoms or molecules diffuse on the substrate surface with an equal mobility in all directions [56] and mobility is gained by adatom-substrate interaction and thermal energy. Kumar *et al*. have shown that films grown under normally incident flux, the probability of diffusion is same in all directions. In this condition, nucleation boundaries create a large number of defects and diffusion process produces non-uniform nucleation with random surface distribution [56]. On the other hand, when incoming vapour atoms or molecules arrive at off-axis, the ballistic shadowing length increases due to oblique angle deposition. In oblique angle deposition, the shadowing effect increases with oblique angle and it blocks vapour condensation in the film [74,77]. Also, the asymmetric surface diffusion will take place in OAD technique. When the oblique angle of deposition is <75°, surface diffusion and shadowing lengths become comparable and shadowing may not be the dominant growth process. Films deposited in this regime show porosity and modified optoelectronic properties. On the other hand, films growth at even higher growth angles (>85°) are mainly governed by ballistic shadowing effect. So, there is a competition between surface diffusion and shadowing. In the shadowing regime, a highly porous film morphology is observed to evolve and at the same time substrate rotation dynamically controls the shadowing dynamics and leads to the evolution of columnar microstructure of the films [74]. Substrate rotation is able to control the ballistic shadowing effect and can modify the nanoscale growth dynamics. In addition, substrate rotation can change the direction of incoming vapour of atoms with respect to the columns. As a result, not only the shadowing orientation changes but also the column growth direction changes. Thus, films grown at lower oblique angles are governed by surface diffusion process and at higher oblique angles film formation process is controlled by the shadowing mechanism.

5.3.1.3 Conclusions

In the present work, we have grown MoO_3 films at different oblique angles by using an RF magnetron sputtering setup. It is demonstrated that the optoelectronic properties and work function of MoO_3 films can be tuned by varying the growth angle. AFM study reveals the existence of correlation length and also the average grain size of the films increases with increasing growth angle. All MoO_3 films are amorphous in nature as is confirmed by XRD measurements. In addition, micro-Raman measurements confirm the presence of Raman modes which belong to the amorphous phase of MoO_3. From optical transmittance data, it is found that the transmittance is more than 70% in the visible region and a red shift is observed till the growth angle increases up to 50°. Further, a continuous change in the work function is observed with growth angle and the highest observed work function is 5.5 eV corresponding to the films grown 0°. Thus, this study is very important for solar cell applications and for photochromic applications.

5.3.2 Hole-blocking molybdenum-oxide/silicon heterojunction: Carrier selective contact

5.3.2.1 Introduction

Generally, transition metal oxides are used as carrier selective contacts because of their ability to selectively block the flow of either electrons (in the conduction band) or holes (in the valence band), depending on the energy band-diagram [1,49]. Transition metal oxides are studied extensively as a hole contact for organic and inorganic solar cells, organic light emitting diode, and organic thin film transistors. Hence, there are significant improvements in the device performance and stability [17,20]. For instance, due to substantial valance band offset, TiO_2/Si heterojunction prevents the flow of holes while it allows a smooth transport of electrons and works as a hole-blocking heterojunction [2,3]. Thus, it is expected that by modulating the barrier height, the performance of PV cells can be improved further which can be achieved by choosing the appropriate transition metal oxides having high work function (e.g. MoO_3, WO_3) as a buffer layer with the substrate [94,95]. Tokito *et al*. were the first to use high work function transition metal oxide as a sandwich layer between ITO and the N,N0-diphenyl-N,N-bis(3-

methylphenyl1)1,10-biphenyl-4,40 diamine (TPD) [96]. Thus, this is very important from the point of fundamentals to check the blocking nature of charge carriers in a heterojunction having a high work function. On the other hand, it is found that the interfacial barrier height can be changed significantly with different buffer layer thickness [97]. However, to the best of our knowledge, the use of MoO_3 as a carrier selective contact and role of its thickness are still not investigated with full potential and in a systematic manner [66,98].

MoO_3 is an attractive oxide semiconductor utilized in many of the state-of-the-art electronic and optoelectronic devices due to its large band gap with an exceptionally large electron affinity (6.7 eV) and ionization energy (9.7 eV) [6,66,96]. Besides these, MoO_3 has numerous exciting characteristics including high refractive index, electrochromic properties, and relatively high chemical stability. These advantages make MoO_3 an ideal candidate for several potential applications such as transparent conductive coating, battery electrode, gas sensor, and hole-blocking layer in PV cells [66,99,100]. In organic photovoltaic devices, MoO_3 has attracted a lot of attention as a tool to enhance charge injection and charge collection [70,101]. Recently, Battaglia *et al.* have demonstrated that MoO_x can serve as an efficient transparent hole contact grown on *n*-Si [64]. So, the growing interest in MoO_3 creates an urgent need to check the effect of barrier height on hole-blocking nature of MoO_3/Si heterojunction and its applications as a photodetector.

In this section, we study the thickness-dependent hole-blocking nature of MoO_3/Si heterojunctions fabricated by RF magnetron sputtering. X-ray diffraction study reveals the amorphous nature of as-grown MoO_3 films, whereas x-ray photoelectron spectroscopy measurements indicate the formation of substoichiometric molybdenum trioxide MoO_x ($x<3$) films. All the MoO_3/Si heterojunctions show the hole-blocking nature, albeit the hole-blocking voltage decreases with increasing MoO_3 thickness. Charge transport across the *n*-MoO_3/*p*-Si junctions has been investigated using *I-V* characteristics and Kelvin probe force microscopy.

The observed results suggest that MoO_3 films can be used as a buffer layer in the solar cell for electron selective contact.

5.3.2.2 Results and discussion

Prior to study the hole-blocking properties, MoO_3 thin films are characterized by AFM, XRD, XPS, and UV-vis-NIR spectrophotometer to look for a possible correlation between its hole-blocking property and structural as well as optical properties. Figures 5.15(a)-(d) show AFM images of MoO_3 films which reveal their granular nature and exhibit a gradual change in the surface morphology with increasing thickness. It is observed that the average grain size increases with thickness [102,103]. For instance, the average grain size turns out to be 17, 24, 29, and 37 nm for 8, 10, 20, and 30 nm, respectively. In addition, AFM images reveal smooth films with a root mean square (RMS) roughness of 0.23, 0.29. 0.35, 0.37, 0.38, and

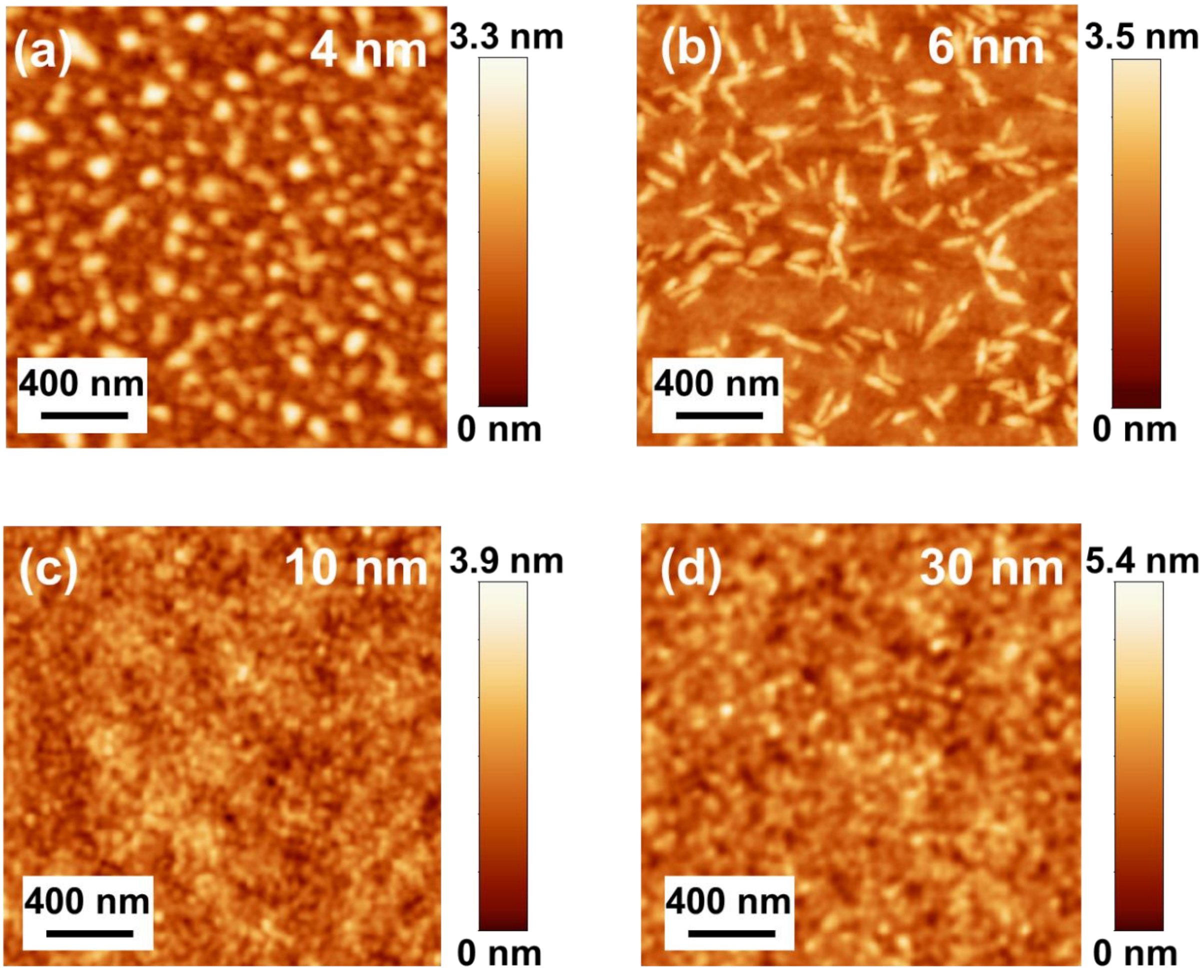

Figure 5.15: AFM images: (a)-(d) 4, 6, 10, and 30 nm MoO_3 thin films, respectively.

0.40 nm for 4, 6, 8, 10, 20, and 30 nm, respectively. Further, to check the crystalline nature of the films we have performed XRD studies on these samples. XRD data do not show any peak (data not shown), which indicates that as-prepared films are amorphous in nature in all cases. However, to reach this inference, films of higher thickness are more useful (which are grown under similar conditions like the films of smaller thicknesses), since these films also do not show any XRD peak corresponding to the all known phases of MoO_3. Generally, MoO_3 films deposited by RF sputtering at RT are found to be amorphous in nature as is reported in the literature [35,61].

Figures 5.16(a) and (b) depict the XPS spectra of MoO_3 films having thicknesses in the range of 4 to 30 nm for Mo 3*d* and O 1*s* core levels, respectively. The survey spectra of all the samples do not reveal the presence of any impurity (spectra not shown). It is known that the sputtering of MoO_3 with Ar ions causes a change in the stoichiometry of this material due to the preferential sputtering of oxygen which is well-known from the literature [105]. For this reason, XPS data in Figs. 5.16(a)-(d) are collected before sputtering. For all the layers, respective XPS spectrum [Fig. 5.16(a)] of Mo 3*d* core-level exhibits two main peaks corresponding to $3d_{3/2}$ and $3d_{5/2}$ levels centered at binding energies of 235.54-235.91 and 232.40-232.77 eV, respectively corresponding to Mo^{6+} in MoO_3, whereas for lower thicknesses (e.g. 4 and 6 nm) Mo 3*d* core-level exhibit two extra peaks corresponding to $3d_{3/2}$ and $3d_{5/2}$ levels centered at binding energies of 234.57-234.47 and 231.35-231.77 eV, respectively to Mo^{5+} in MoO_3 [10,62]. The major binding energy peaks of Mo $3d_{3/2}$ and Mo $3d_{5/2}$ are separated by 3.1±0.12 eV [10,62]. On the other hand, the high intensity peaks in the range of 529.51-533.04 eV reveal the presence of O 1*s* core level in MoO_3 films as shown in Fig. 5(b) [10,62]. It is interesting to note that oxygen vacancies increase with increasing film thickness from 4 to 30 (Table 5.3) [106]. Figures 5(c) and (d) show the XPS spectra of a 10 nm-thick MoO_3 film corresponding to Mo 3*d* and O 1*s* core level, respectively. The Mo 3*d* XPS spectra is deconvoluted using a

Gaussian curve fitting following the Shirley background subtraction [106]. The binding energy of the Mo 3$d_{5/2}$ and Mo 3$d_{3/2}$ peaks for MoO_3 are slightly higher than the other reported values, which is likely an effect of surface charging [102]. It is noted that the observed peaks are significantly different from the Mo 3$d_{5/2}$ peak of Mo^{5+} (231.5-231.2 eV) and Mo^{4+} (230.1-229.5 eV) states [102,105]. From the comparison with literature, it is evident that the Mo ions are in the 6^+ oxidation states of MoO_3 phase for a 10 nm-thick MoO_3 film [59,85]. In addition, the energy separation between Mo 3$d_{5/2}$ and Mo 3$d_{3/2}$ is found to be 2.88 eV and the calculated intensity ratio of these peaks at 235.54-235.88 and 232.40-232.77 eV is 1.52:1, which is very close to the branching ratio of 3:2, expected for the 3*d* lines [102,107]. On the other hand, Figs.

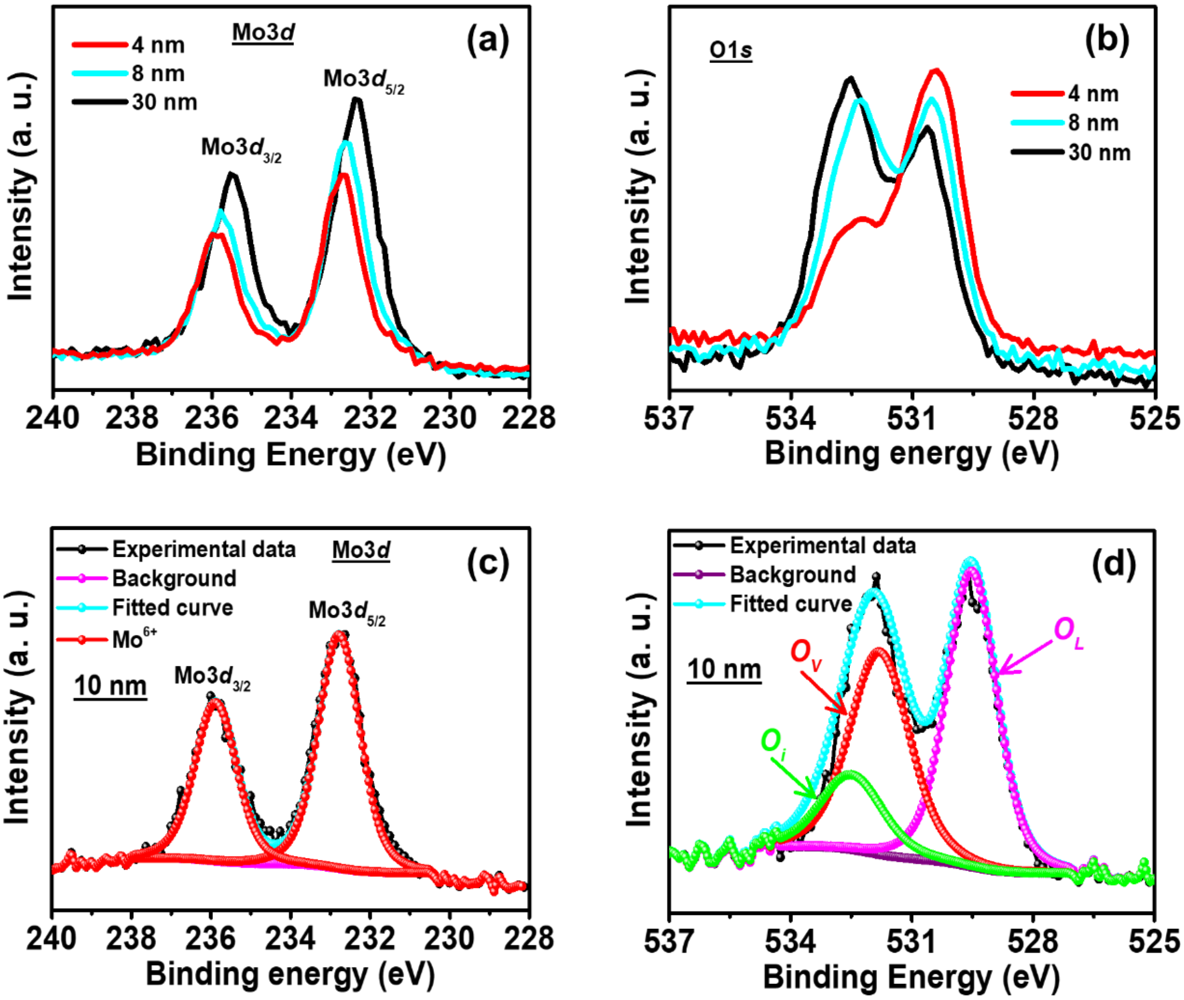

Figure 5.16: (a) and (b) Core-level Mo 3*d* and O 1*s* experimental spectra corresponding to MoO_3 thin films having different thicknesses, respectively, whereas (c) and (d) depict fitted XPS data obtained from a 10 nm-thick MoO_3 film corresponding to Mo 3*d* and O 1*s* core levels.

5.16(d) depicts O 1*s* spectrum which are deconvoluted into three different distinct curves located at binding energies of 529.5, 531.8, and 532.5 eV. The peak corresponds to the presence of O atoms at regular sites (O_L) is located at 529.5 eV. On the other hand, the second peak situated at 531.8 eV belongs to the deficiency of oxygen atoms in the MoO_3 films and intensity of this peak can vary with the concentration of oxygen vacancies. The last peak corresponding to the binding energy of 532.5 eV is related to the presence of loosely bound oxygen (O_i) atoms with absorbed H_2O or O_2 at the surface of MoO_3 films. As shown in Table 5.3, the percent concentration of O_L, O_V, and O_i turns out to be 43.06%, 35.21%, and 21.72%, respectively for a 10 nm-thick MoO_3 film. All the results obtained from XPS analyses are summarized in Table 5.3. From the obtained results it can be inferred that, with increasing MoO_3 film thickness (from 4 to 30 nm) the concentration of O_V increases. In fact, the XPS measurement confirms the presence of Molybdenum trioxide films on the surface of the Si substrate.

It is known that hole-blocking property of a material is strongly related to its optical band gap [106]. In order to address the same, we have carried out surface reflectance and transmittance measurements on all MoO_3 samples. Figure 5.17(a) depicts the specular reflectance of substrate and 4, 6, 8, 10, 20, and 30 nm MoO_3 films grown on Si substrates in the wavelength range of 300–800 nm. It is interesting to note that the average specular reflectance of MoO_3 films decreases with increasing thickness from 47.57% (for 4 nm) to 45.56% (for 6 nm) to 43.57% (for 8 nm) to 43.22% (for 10 nm) to 42.62% (for 20 nm) to 40.87% (for 30 nm) at 550 nm wavelength. It is interesting to note that from AFM measurements that with increasing thickness of MoO_3 films, grain size and RMS roughness values increase which are due to cause a reduction in their optical reflectance values [2]. It is noticed from the reflectance spectra that the reflectance minima shift towards lower wavelengths as the film thickness increases. This may be due to a change in the band gap value

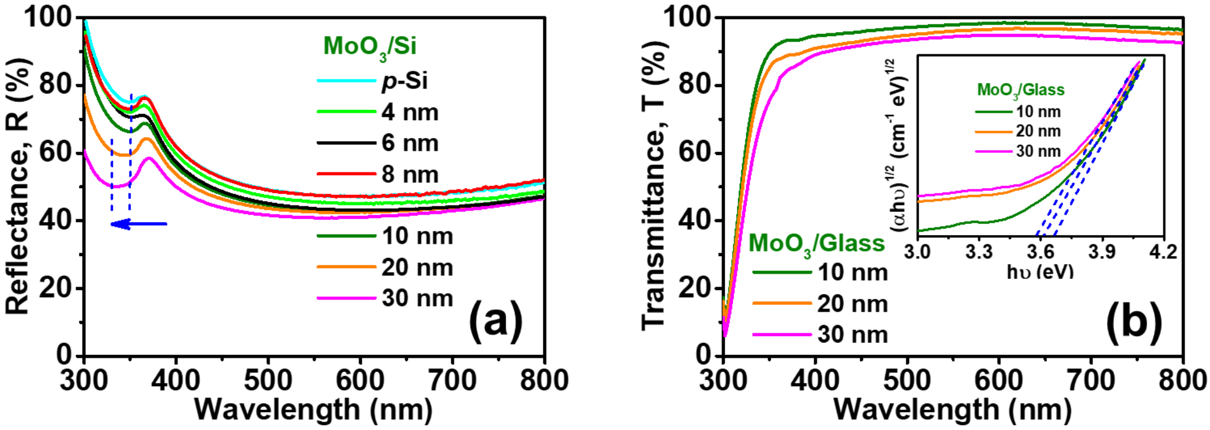

Figure 5.17: (a) Shows the reflectance spectra of 4, 6, 8, 10, 20, and 30 nm MoO_3 films deposited on *p*-Si substrate, (b) Shows the transmittance spectra of MoO_3 thin films deposited on glass substrate whereas inset of (b) depicts the measured band gap (using Tauc's method) of MoO_3 films deposited on glass substrate.

with increasing thickness [108]. To find out the reason behind this shift, transmittance data and optical band gap of MoO_3 films are measured. Figures 5.17(b) and its inset show the transmittance and optical band gap data of MoO_3 thin films, respectively. The highest transmittance is 98.3% for 4 nm-thick film which changes to 98.2% for a 6 nm-thick film and 97.9% for a 8 nm-thick film. Likewise, the transmittance value is 97.6% for a 10 nm-thick film which further reduces to 94.42% for a 30 nm-thick film in the visible region at 550 nm wavelength value and the absorption edge gets shifted towards higher wavelength with a sharp fall in the UV region [Fig. 5.17(b)] which corresponds to the optical band gap of MoO_3 films [103]. This reduction in the transmittance may be due to more light scattering arising from relatively higher rms roughness values at higher thicknesses, as is observed from our AFM studies [2]. The optical band gap of the films are calculated using Eq. 5.2. The inset of Fig. 5.17(b) shows the optical band gap of MoO_3 films which reveals that band gap value varies from 3.72 to 3. 58 eV due to an increase MoO_3 film thickness from 4 to 30 nm. This behaviour may be related to a change in the average particle size for increasing film thickness from 4 to 30 nm (as is observed from the AFM measurements). As a matter of fact, the calculated value of band gap matches well with literature [95,102]. In addition, oxygen vacancies have direct influence on the band gap [106]. For instance, oxygen vacancies increase with increasing film thickness [as obtained from XPS analyses (Table 5.3)] and band gap decreases with increasing oxygen vacancies.

The change in optical band gap with increasing film thickness can also influence the nanoscale electrical transport and it is known that the hole-blocking property of a layer depends on its work function and the carrier concentration [65]. Thus, to understand the hole-blocking property of MoO_3 films, we have employed KPFM measurements to carry out two-dimensional

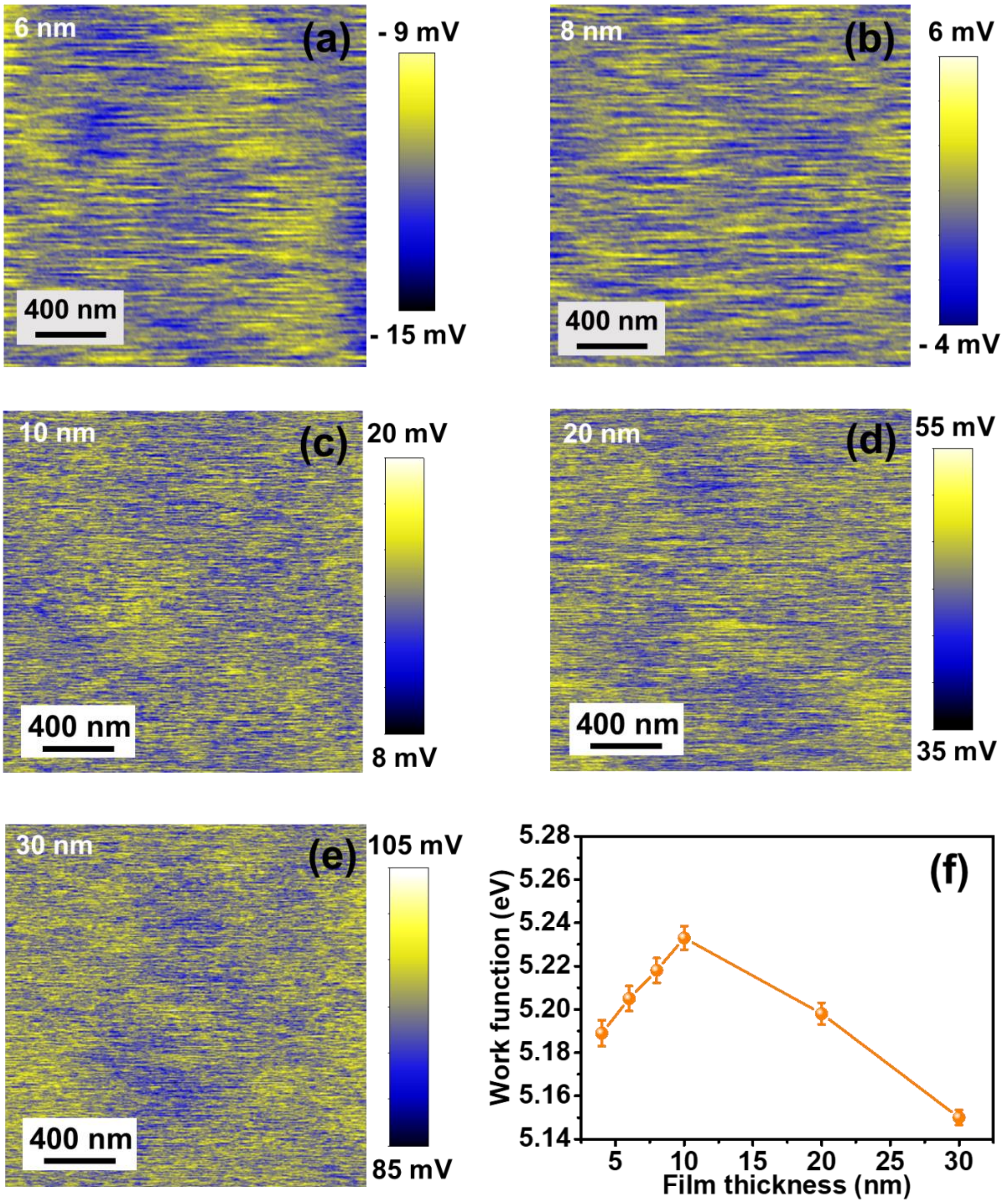

Figure 5.18: (a)-(e) The V_{CPD} maps of 4, 6, 8, 10, 20, and 30 nm-thick MoO_3 films, respectively, (f) The thickness-dependent variation in the work function of the MoO_3 films.

mapping of MoO_3 work function. The work function of the samples is calculated using Eq. 5.3. Figures 5.18(a)-(e) show the contact potential difference (V_{CPD}) map of MoO_3 thin films deposited for different thickness. Since, the work function of the tip (Si coated with Ti/Pt) is found to be [measured with respect to freshly cleaved highly ordered pyrolytic graphite (HOPG)] ~5.25 eV. It is interesting to note that similar to other results (structural and optical), V_{CPD} increases from 4 to 30 nm film thickness. So, it is known that V_{CPD} can be converted into the work function of the sample using the Eq. 5.3. The measured work function of MoO_3 films is seen to decrease from 5.19 eV (for 4 nm) to 5.15 eV (for 30 nm) and the maximum is found to be 5.23 eV corresponding to the 10 nm-thick MoO_3 film, albeit at this moment, the reason behind this behaviour is not clear to us. The observed work function values match well with the those reported in literature [101]. It is interesting to note that such thickness-dependent change in work function has been observed also in case of TiO_2 [4]. In fact, the measured nanoscale contact surface potential is found to be inhomogeneous on the mapped region and the existence of spatial inhomogeneity in the map on the MoO_3 surface leads to a variation in the barrier height which is due to affect the hole-blocking nature of MoO_3 films. For instance recently, we have shown similar intrinsic inhomogeneous barrier height in case of TiO_2 [103]. The most stricking feature of MoO_3 films is their large chemical potential up to 6.9 eV which is much higher than other substoichiometric transition metal oxides (VO_2, WO_3) [92,95,96]. In case of MoO_3, the empty (electron affinity, χ) and filled (ionization energy) band edges lie between ~4.71-5.7 eV and ~8.3-9.7 eV, respectively below the vacuum level, although these values vary with surface preparation (air/or oxygen exposed) and termination [70,101]. On the other hand, for Si, χ and ionization energy are at about 4.05 eV and 5.17 eV, respectively below the vacuum level [2]. Based on Anderson's model, the MoO_3/Si interface is expected to have a large valance band offset (ΔE_V=3.14 eV) which is capable to block the flow of holes from silicon to molybdenum trioxide, whereas there is a small conduction band offset (ΔE_C=0.66

eV) which would allow the transport of electrons from silicon to molybdenum as shown in Fig. 5.19(a) [104].

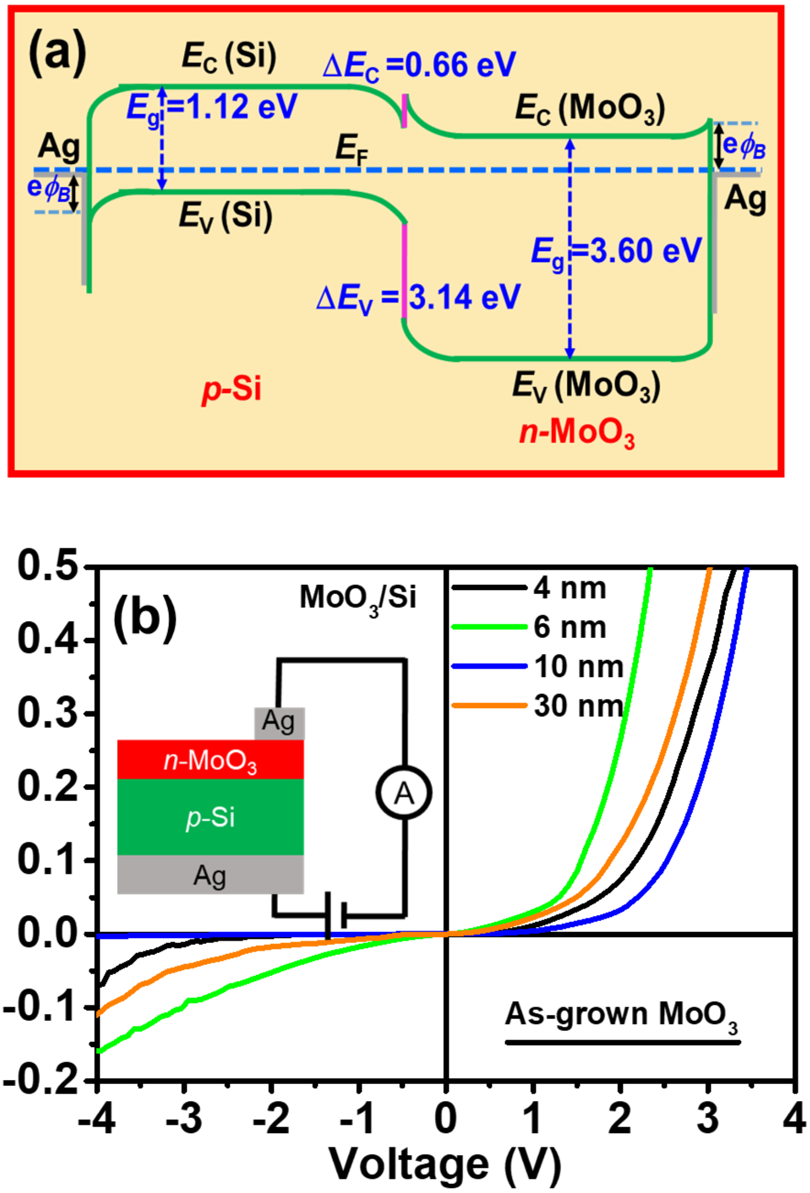

Figure 5.19: (a) Energy-band diagram of an n-MoO_3/p-Si heterojunction under equilibrium conditions and (b) depicts current-voltage (I-V) characteristics of MoO_3/Si heterojunctions for different MoO_3 film thicknesses, whereas the inset in (b) shows a schematic diagram of the device.

To check experimentally, the blocking nature of MoO_3/Si heterojunctions current-voltage (I-V) characteristics are measured for all thicknesses. The I-V measurements are carried out using the Ag/n-MoO_3/p-Si/Ag configuration, as is shown in the inset of Fig. 5.19(b). It is well-known that silver deposited on p-Si forms a Schottky junction having a very low barrier height for holes form silicon to silver [105]. Thus, introduction of a molybdenum trioxide layer between silver and silicon would block the flow of holes because it has a large valence band offset. To verify this concept, *I*-*V* characteristics of Ag/*n*-MoO_3/*p*-Si/Ag devices have been measured. Figure 5.19(b) shows the *I*-*V* characteristics of Ag/*n*-MoO_3/*p*-Si/Ag heterojunctions corresponding to MoO_3 layers of different thicknesses. The *I*-*V* characteristics turns out to be an Ohmic one for Ag/*p*-Si (data not shown), without a molybdenum trioxide layer, whereas after inserting MoO_3 layers it is clear that no current flows for small biases (<0.4 V) for all heterojunctions, revealing that the MoO_3 film works as a hole-blocking layer for all thicknesses, albeit it is more prominent for the 10 nm thick-film. For instance, the leakage current of MoO_3 films decreases from 9.1 μA (4 nm) to 5.2 μA (10 nm) and then increases to 18 μA (30 nm) and thus, the lowest is found to be 5.2 μA corresponding to the 10 nm-thick MoO_3 film. In addition, change in barrier height (as we have seen from KPFM studies) with thickness also indicates a reduction in the hole-blocking nature [64]. Moreover, as we increase the thickness of MoO_3 layer, the barrier height [which is calculated from capacitance-voltage measurements (graphs not shown)] decreases from 0.83 eV (4 nm) to 0.66 eV (10 nm) and then increases to 1.05 eV for a 30 nm-thick MoO_3 film, as is shown in Table 5.4. At higher voltages, there is a sudden enhancement in the current with voltage. The value of diode parameters like ideality factor, leakage current, barrier height, turn-on potential are calculated and summarized in Table 5.4. The high value of ideality factor may be attributed to surface defects [2]. Based on the above-obtained results, it is inferred that MoO_3 film having a thickness 10 nm offers the best hole-blocking property, although the reason behind this critical thickness exhibiting the best hole-blocking nature is not clear to us. Following this, we have annealed the MoO_3 films at 573 K for 1 h in air and carried out the *I*-*V* measurements to study the influence of annealing on their hole-blocking characteristics. However, it is interesting to note that similar to TiO_2, the hole-blocking property of all MoO_3 films degrades after annealing. Figures 5.20 and 5.21 depict the MoO_3 film morphologies and the *I*-*V* characteristics, respectively after annealing.

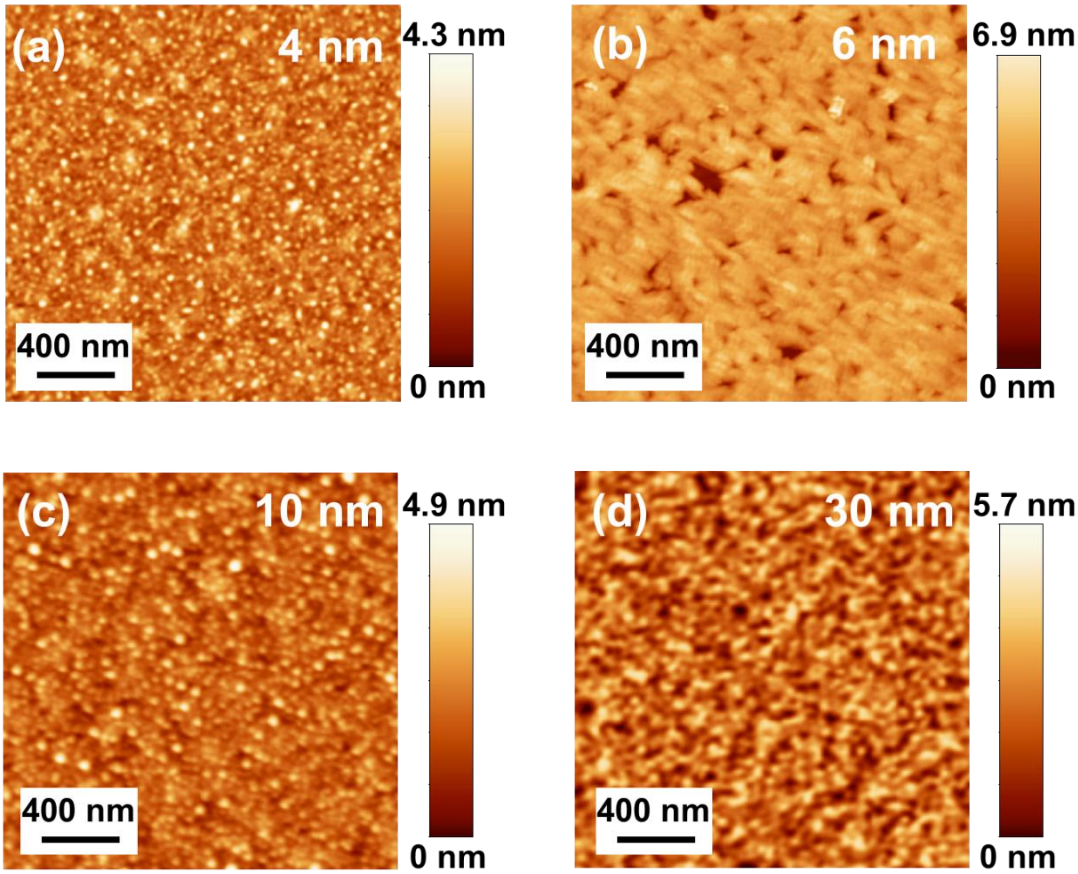

Figure 5.20: AFM images: (a)-(d) 4, 6, 10, and 30 nm MoO_3 thin films after annealing, respectively.

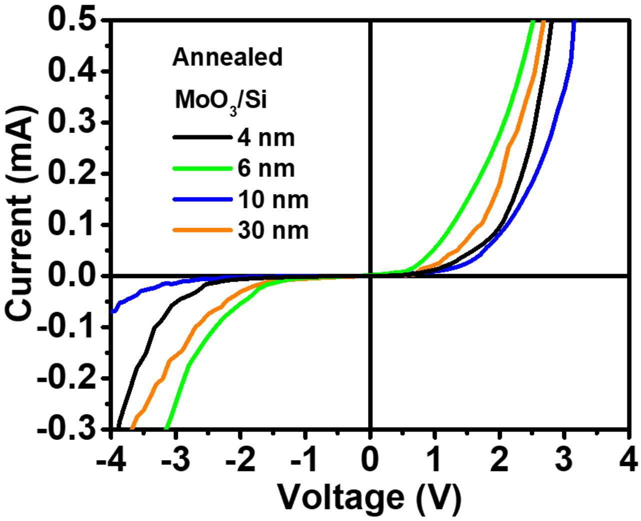

Figure 5.21: (a) Depicts current-voltage (*I*-*V*) characteristics of MoO_3/Si heterojunctions for different MoO_3 film thicknesses after annealing.

Likewise, Table 5.5 shows all the relevant extracted parameters from the *I*-*V* characteristics, corresponding to different MoO_3/Si junctions after annealing. Thus, the present study opens up an avenue to fabricate a hole-blocking solar cell using MoO_3 as the hole-blocking layer. In the context of the present thesis work, the band gap of CdTe:Cu (E_g~1.47 eV) being in the similar range to that of Si, it is expected that the MoO_3 layer should also show a good hole-blocking nature growing it on a CdTe:Cu layer [106].

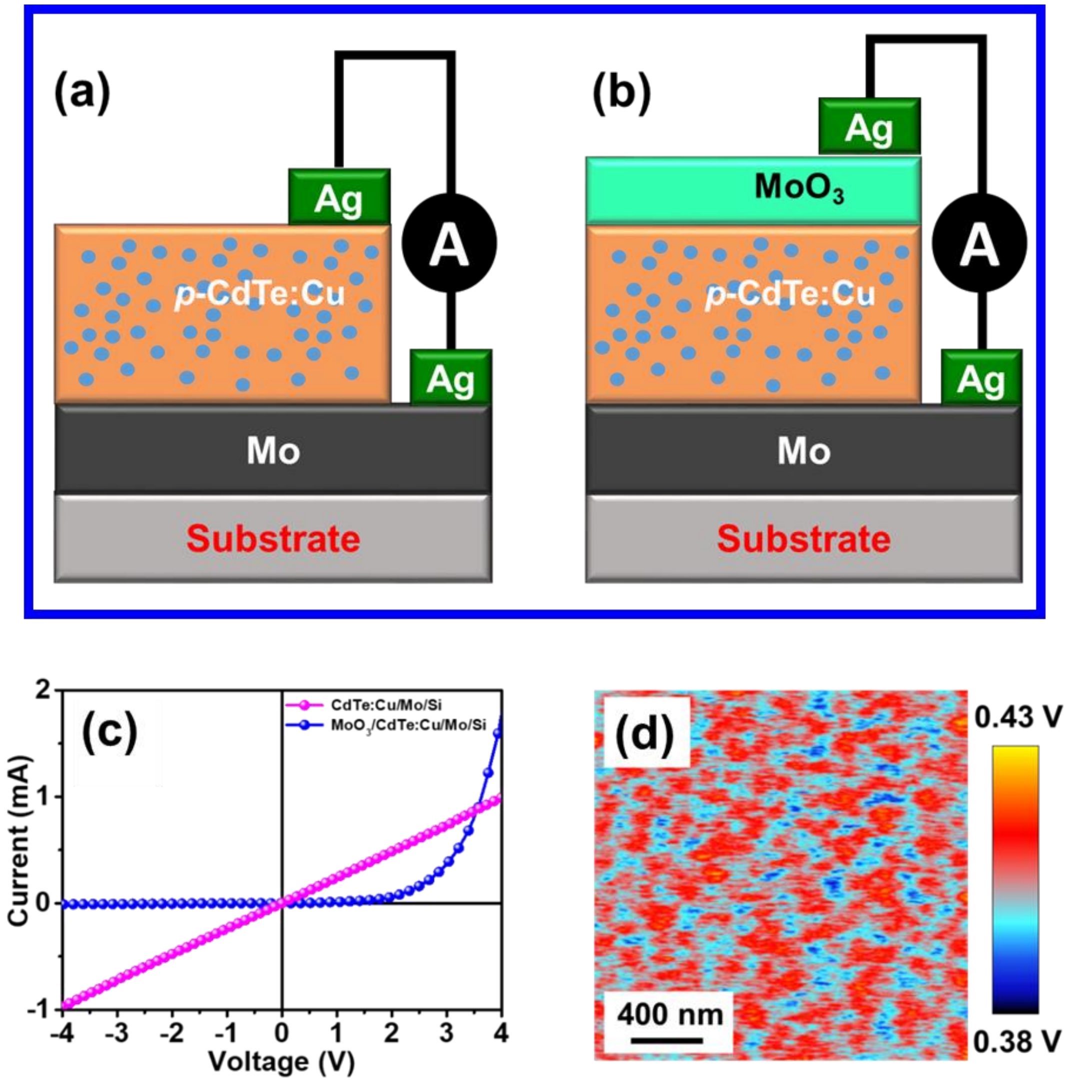

Figure 5.22: (a) and (b) show the device configuration of CdTe:Cu/Mo/Si and MoO_3/CdTe:Cu/Mo/Si heterostructures, respectively, whereas (c) depicts the current-voltage characteristics corresponding to CdTe:Cu/Mo/Si and MoO_3/CdTe:Cu/Mo/Si heterostructures, (d) KPFM map corresponding to the device configuration shown in (b).

In order to verify this, we have grown MoO_3 on a CdTe:Cu layer (1.2 µm-thick) grown on a Mo back contact coated Si substrate and have compared the *I-V* characteristics with a similar device but without having the MoO_3 layer. Figure 5.22 (c) shows the *I-V* characteristics of CdTe:Cu/Mo/Si heterojunction [as depicted in Fig. 5.22(b)] which is nearly linear, confirming the Ohmic nature of the junction. In addition, Fig. 5.22(c) also manifests a non-linear behaviour

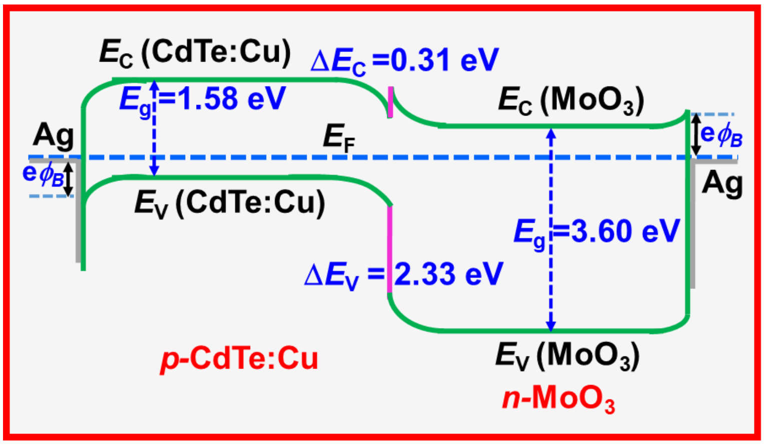

Figure 5.23: Energy-band diagram of an *n*-MoO_3/*p*-CdTe:Cu heterojunction.

in the *I-V* characteristics corresponding to the device shown in Fig. 5.22(b). This confirms the hole-blocking nature of MoO_3 film grown on a thick CdTe:Cu layer. In fact, similar to the MoO_3/Si heterojunction, MoO_3/CdTe:Cu heterojunction also blocks the flow of holes, while it allows the flow of electrons. As a matter of fact, upon depositing a 10 nm-thick MoO_3 layer on a thick CdTe:Cu layer also reveals a better hole-blocking property. In support of this fact, we have performed KPFM measurements on the MoO_3/CdTe:Cu/Mo/Si heterojunction. Based on the V_{CPD} map [Fig. 5.22 (d)] and the *I-V* data [Fig. 5.22 (c)], we have constructed the energy-band diagram for the device shown in Fig. 5.22(b) as depicted in Fig. 5.23. Based on Anderson's model, the MoO_3/CdTe:Cu interface has a large valance band offset (ΔE_V=2.33 eV) which is capable to block the flow of holes from CdTe:Cu to molybdenum trioxide, whereas there is a small conduction band offset (ΔE_C=0.31 eV) which would allow the transport of electrons from CdTe:Cu to molybdenum trioxide. Thus, it is inferred that MoO_3 film works as a hole-blocking layer and in turn it can enhance the efficiency of the PV cells.

5.3.2.3 Conclusions

In conclusion, we have studied *n*-MoO_3/*p*-Si heterojunctions having different thicknesses of the MoO_3 layer. XPS studies reveal the increasing degree of oxygen vacancy with increasing molybdenum trioxide layer thickness. These heterojunctions selectively extract the minority carriers (electron) from silicon to molybdenum trioxide while the blocking majority carriers (holes) due to a large valence band offset. The heterojunction with 10 nm-thick MoO_3 layer offers the best hole-blocking properties among all. Following this, the 10 nm-thick MoO_3 film grown on a thick CdTe:Cu layer also reveals the hole-blocking property. This heterojunction helps to block the flow of holes from CdTe:Cu to MoO_3 and in turn can increase the efficiency of the device. Thus, for the present thesis work, to fabricate a CdTe-based hole-blocking solar cell, MoO_3 film is used as a hole-blocking layer.

Table 5.1: Extracted relevant parameters from pyramidal *txt*-Si surfaces fabricated under different etching times.

Etching time (s)	RMS roughness (nm)	Aspect ratio (*d*/*a*)	Coverage area (%)	Average facet angle (°)	%*R* (at 550 nm)
30	11.34	--	73.26±2	--	42
60	35.65	4.34±0.28	27.57±1	25.66±4.3	37.27
120	46.70	3.17±0.25	38.12±4	26.73±3.5	21.69
240	101.17	2.88±0.21	42.50±1	33.28±3.9	2.7
360	148.42	2.80±0.25	49.19±5	35.72±3.1	0.70
480	165.68	2.29±0.23	53.78±2	40.12±2.8	0.53
600	198.20	2.44±0.19	58.70±6	41.92±3.6	0.39
1200	279.22	2.51±0.20	63.90±4	43.23±1.9	0.34
1800	285.43	2.35±0.17	76.33±3	42.9±1.6	0.30
2400	294.51	2.37±0.14	85.19±4	44.19±1.4	0.25

Table 5.2: Following relevant parameters are determined for MoO_3 films grown under different angles of incident flux: RMS roughness and surface correlation length scales (l) are estimated from AFM images, band gap is calculated from optical absorption data, and the work function (Φ) values are extracted from KPFM measurements.

Angle of deposition (°)	RMS (nm)	l (nm)	E_g (eV)	Φ (eV)
0	0.33	33	3.87	5.59
20	0.39	37.4	3.85	5.5
40	0.52	49.3	3.84	5.48
50	0.59	67.5	3.82	5.44
60	0.63	96.1	3.92	5.26
80	1.21	115.7	3.94	5.41
85	1.85	281.8	3.95	5.43
87	1.23	260.4	3.97	5.45

Table 5.3: XPS analyses for MoO_3 films for 4, 6, 8, 10 and 30 nm.

Sample	Binding energy (eV)	Composition	Relative percentage
4 nm	232.60	Mo $3d_{5/2}$ (Mo^{6+})	41.71
	235.77	Mo $3d_{3/2}$ (Mo^{6+})	41.67
	231.77	Mo $3d_{5/2}$ (Mo^{5+})	7.86
	234.57	Mo $3d_{3/2}$ (Mo^{5+})	8.76
	530.39	O1s, O_L	63.91
	531.83	O1s, O_V	25.03
	532.57	O1s, O_i	11.06
6 nm	232.63	Mo $3d_{5/2}$ (Mo^{6+})	43.67
	235.77	Mo $3d_{3/2}$ (Mo^{6+})	43.92
	231.35	Mo $3d_{5/2}$ (Mo^{5+})	7.40
	234.47	Mo $3d_{3/2}$ (Mo^{5+})	5.01
	530.40	O1s, O_L	53.51
	531.90	O1s, O_V	28.92
	532.69	O1s, O_i	17.56
8 nm	232.71	Mo $3d_{5/2}$ (Mo^{6+})	51.02
	235.86	Mo $3d_{3/2}$ (Mo^{6+})	48.98
	530.63	O1s, O_L	53.95
	532.27	O1s, O_V	33.49
	533.03	O1s, O_i	12.56
10 nm	232.77	Mo $3d_{5/2}$ (Mo^{6+})	53.4
	235.88	Mo $3d_{3/2}$ (Mo^{6+})	46.6
	530.66	O1s, O_L	43.06
	532.37	O1s, O_V	35.21
	533.04	O1s, O_i	21.72
30 nm	232.40	Mo $3d_{5/2}$ (Mo^{6+})	54.6
	235.54	Mo $3d_{3/2}$ (Mo^{6+})	45.4
	529.51	O1s, O_L	46.96
	531.79	O1s, O_V	38.40
	532.48	O1s, O_i	14.64

Table 5.4: Following parameters were determined for as-deposited MoO_3/Si heterojunctions: ideality factor (η), turn-on potential (V_{To}), leakage current (I_{SC}) from current-voltage measurement; barrier height (ϕ_B) from capacitance-voltage (*C*-*V*) measurement.

Sample name	η	V_{To} (V)	I_{SC} (µA)	ϕ_B (eV)
4 nm	4.51	2.21	9.1	0.83
6 nm	4.45	1.30	5.7	0.76
8 nm	4.38	1.25	5.5	0.72
10 nm	4.30	2.44	5.2	0.66
20 nm	3.99	2.31	10	0.78
30 nm	3.51	1.80	18	1.05

Table 5.5: Following parameters were determined for annealed MoO_3/Si heterojunctions: ideality factor (η), turn-on potential (V_{To}), leakage current (I_{SC}) from current-voltage measurement; barrier height (ϕ_B) from capacitance-voltage (*C*-*V*) measurement.

Sample name	4 nm	6 nm	8 nm	10 nm	20 nm	30 nm
η	4.63	4.58 2.21	4.49	4.41	4.20	3.97
V_{To} (V)	1.98	0.98	0.92	2.05	2.01	1.5
I_{SC} (µA)	21	32	35	9.1	19	28

References

[1] P. würfel and Uli würfel, *Physics of Solar cells: From Basic Principles to Advanced Concepts* 2016: Wiley, New York.

[2] R. Singh, M. Kumar, M. Saini, A. Singh, B. Satpati, and T. Som, Appl. Surf. Sci. 418 (2017) 225.

[3] S. Avasthi, W. E. McClain, G. Man, A. Kahn, J. Schwartz, and J. C. Sturm, Appl. Phys. Lett. 102 (2013) 203901.

[4] Mohit Kumar (Ph. D. Thesis, Institute of Physics, Bhubaneswar under Homi Bhabha National Institute, Mumbai)

[5] P. Spinelli, M.A. Verschuuren, and A. Polman, Nat. Commun. 3 (2012) 692.

[6] C. Battaglia, S. M. De Nicolás, S. De Wolf, X. Yin, M. Zheng, C. Ballif, and A. Javey, Appl. Phys. Lett. 104 (2014) 1.

[7] C. P. Saini, A. Barman, M. Kumar, P. K. Sahoo, T. Som, and A. Kanjilal, Appl. Phys. Lett. 105 (2014) 123901.

[8] M. Kumar A. Singh, B. Satpati, and T. Som, Sol. RRL (2018) 1700216.

[9] I. Horcas, R. Fernández, J. M. Gómez-Rodríguez, J. Colchero, J. Gómez-Herrero, A.M. Baro, Rev. Sci. Instrum. 78 (2007) 013705.

[10] C. N. R. Rao, Transition metal oxides, Annu. Rev. Phys. Chem. 40 (1989) 291.

[11] G. Bodurov, T. Ivanova, and K. Gesheva, Phys. Procedia 46 (2013) 149.

[12] S. Chhajed, M. F. Schubert, J. K. Kim, and E. F. Schubert, Appl. Phys. Lett. 93 (2008) 251108.

[13] T. Basu, M. Kumar, P. K. Sahoo, A. Kanjilal, and T. Som, Nanoscale Res. Lett. 9 (2014) 192.

[14] U. Würfel, D. Neher, A. Spies, and S. Albrecht, Nat. Commun. 6 (2015) 6951.

[15] D. Bartesaghi, I. D. C. Pérez, J. Kniepert, S. Roland, M. Tuubiez, D. Neher, and L. J. A. Koster, Nat. Commun. 6 (2015) 7083.

[16] J. C. Bean, L. C. Feldman, A. T. Fiory, S. Nakahara, and I. K. Robinson, J. Vac. Sci. Technol. A 2 (1984) 436.

[17] J. W. Agar, L. A. Reichertz, K. M. Yu, W. J. Schaff, T. L. Williamson, M. A. Hoffbauer, N. M. Haegel, and W. Walukiewicz, Photovoltaic Specialists Conference, 2008. PVSC '08. 33rd IEEE, (2008) 1.

[18] J. H. Heo, S. H. Im, J. H. Noh, T. N. Mandal, C. S. Lim, J. A. Chang, Y. H. Lee, H. Kim, A. Sarkar, M. K. Nazeeruddin, M. Gra¨tzel, and S. Seok, Nat. Photonics **7** (2013) 486.

[19] K. A. Nagamastu, S. Avasthi, G. Sahasrabudhe, G. Man, J. Jhaveri, A. H. Berg, J. Schwartz, A. Kahn, S. Wagner, and J. C. Sturm, Appl. Phys. Lett. 106 (2015) 123906.

[20] M. Kumar, A Kanjilal, and T. Som, AIP Adv. 3 (2013) 092126.

[21] D. H. Kwon, K. M. Kim, J. H. Jang, J. M. Jeon, M. H. Lee, G. H. Kim, X. S. Li, G. S. Park, B. Lee, S. Han, M. Kim, and C. S. Hwang, Nat. Nanotechnol. 5 (2010) 148.

[22] M. Maeda and T. Watanabe, Surf. Coat. Technol. 201 (2007) 9309.

[23] B. Karunagaran, K. Kima, D. Mangalaraja, J. Yia, and S. Velumani, Sol. En. Mater. Sol. Cells 88 (2005) 199.

[24] O. K. Varghese, D. Gong, M. Paulose, K.G. Ong, and C.A. Grimes, Sensors Actuators B 93 (2003) 338.

[25] S. Davíđsdóttir, J. P. Petit, M. Mermoux, R. Shabadi, S. Canulescu, K. P. Almtoft, K. Dirscherl, and R. Ambat, ACS Appl. Mater. Inter. 6 (24) (2014) 22224.

[26] M. K. Nowtony, T. Bak, and J. Nowotny, J. Phys. Chem. B 110, (2006) 16270.

[27] M. K. Nowtony, T. Bak, J. Nowotny, and C. C. Sorrell, Phys. Stat. Sol. (b) 242 (2005) R88.

[28] X. Dong, J. Tao, Y. Li, and H. Zhu, Appl. Surf. Sci. 256 (2010) 2532.

[29] L. H. Chong, K. Mallik, C H de Groot, and R. Kersting, J. Phys: Condens. Matter 18 (2010) 645.

[30] S. Chatterjee, M. Kumar, S. Gohil, and T. Som, Thin Solid Films 568 (2014) 81.

[31] A. F. Khan, M. Mehmod, S. K. Durrani, M. L. Ali, and N. A. Rahim, Mate. Sci. Semicond. Process. 29 (2015) 161.

[32] X. H. Xu, M. Wang, Y. Hou, S. R. Zhao, H. Wang, D. Wang, and S. X. Shang, Cryst. Res. Technol. 37 (2002) 431.

[33] L. E. Alarcón, E. H. Poniatowski, M. A. Camacho-Lopez, M. F. Guasti, J. J. Jarquın, and A. S. Pineda, Appl. Surf. Sci. 137 (1999) 38.

[34] N. R. Mathews, E. R. Morales, M.A. Cortés-Jacome, and J. A. T. Antonio, Sol. Energy 83 (2009) 1499.

[35] H. Rath, P. Dash, T. Som, P. V. Satyam, U. P. Singh, P. K. Kulriya, D. Kanjilal, D. K. Avasthi, and N. C. Mishra, J. Appl. Phys. 105 (2009) 074311.

[36] S. Aksoy and Y Caglar, J. Alloy Comp. 613 (2014) 330.

[37] Y. H. Chang, C. M. Liu, C. Chen, and H. E. Cheng, Nanoscale Res. Lett. 7 (1) (2012) 231.

[38] H. Seidel, L. Csepregi, A. Heuberger, and H. Boumgrtel, J. Electrochem. Soc. 137 (1990) 3626.

[39] P. K. Singh, R. Kumar, M. Lal, S. N. Singh, and B. K. Das, Sol. Energy Mater. Sol. Cells 70 (2001) 103.

[40] H. Seidel, L. Csepregi, A. Heuberger, and H. Boumgrtel, J. Electrochem. Soc. 137 (1990) 3612.

[41] M. Hong, G. D. Yuan, Y. Peng, H.Y. Chen, Y. Zhang, Z. Q. Liu, J. X. Wang, B. Cai, Y. M. Zhu, Y. Chen, J. H. Liu, and J. M. Li, Appl. Phys. Lett. 104 (2014) 253902.

[42] D. Iencinella, E. Centurioni, R. Rizzoli, and F. Zignani, Sol. Energy Mater. Sol. Cells 87 (2005) 725.

[43] K. Imamura, T. Nonaka, Y. Onitsuka, D. Irishika, and H. Kobayashi, Appl. Sur. Sci. 395 (2017) 50.

[44] Y. Jiang, H. Shen, C. Zheng, T. Pu, J. Wu, C. Rui, W. Yang, and Y. Li, Phys. Status Solidi A 214 (2017) 1.

[45] B. M. Otto, M. Kroll, T. Kasebier, S.-M. Lee, M. Putkonen, R. Salzer, P. T. Miclea, and R. B. Wehrspohn, Adv. Mater. 22 (2010) 5035.

[46] H. Fang, X. Li, S. Song, Y. Xu, and J. Zhu, Nanotechnology 19 (2008) 255703.

[47] X. Liu, P. R. Coxon, M. Peters, B. Hoex, J. M. Cole, and D. J. Fray, Energy Environ. Sci. **7** (2014) 3223.

[48] H. Sai, Y. Kanamori, K. Arafune, Y. Ohshita, and M. Yamaguchi, Prog. Photovoltaics Res. Appl. 15 (2007) 415.

[49] JCPDS - International Center for Diffraction Data 1998 Card No. 86-0147 (ICDD, Newton Square, PA).

[50] A. Lugstein, Y. J. Hyun, M. Steinmair, B. Dielacher, G. Hauer, and E. Bertagnolli, Nanotechnology 19 (2008) 485606.

[51] L. Chu, Z. Qin, J. Yang, and X. Li, Sci. Rep. 5 (2015) 12143.

[52] B. Silke L. Diedenhofen, G. Vecchi, R. E. Algra, A. Hartsuiker, O. L. Muskens, G. Immink, E. P. A. M. Bakkers, W. L. Vos, and J. G. Rivas, Adv. Mater. 21 (2009) 973.

[53] J. B. Naceur, M. Gaidi, F. Bousbih, R. Mechiakh, and R. Chtourou, Curr. Appl. Phys. 12 (2012) 422.

[54] P. Ashrit, *Transition Metal Oxide Thin Film-Based Chromogenics and Devices*, 2017: Elsevier, Oxford, United Kingdom.

[55] D. S. Ginley, H. Hosono, D. C. Paine, *Handbook of Transparent Conductors* 2011: Springer, Berlin.

[55] P. Ashrit, *Transition Metal Oxide Thin Film-Based Chromogenics and Devices* 2017:

Elsevier, Kennewick, Washington.

[56] M. Kumar, R. Singh, S. Nandy, A. Ghosh, S. Rath, and T. Som, J. Appl. Phys. 120 (2016) 15302.

[57] T. Minami, Thin Solid Films 516 (2008) 5822.

[58] S. S. Sunu, E. Prabhu, V. Jayaraman, K. I. Gnanasekar, T. K. Seshagiri, and T. Gnanasekaran, Sensors and Actuators B 101 (2004) 161.

[59] D. Xiang, C. Han, J. Zhang, and W. Chen, Sci. Rep. 4 (2014) 4891.

[60] R. Sivakumar, C. Sanjeeviraja, M. Jayachandran, R. Gopalakrishnan, S. N. Sarangi, D. Paramanik, and T. Som, J. Phys. D: Appl. Phys. 41 (2008) 125304.

[61] L. Liu, T. Zhang, L. Wang, and S. Li, Materials Letters 63 (2009) 2041.

[62] D. Gupta, D. Dutta, M. Kumar, P. B. Barman, T. Som, and S. K. Hazra, Sensors and Actuators B 252 (2015) 35.

[63] H. Kim, M. David, M. Patel, and J. Kim, Sensors and Actuators A 252 (2016) 35.

[64] C. Battaglia, X. Yin, M. Zheng, I. D. Sharp, T. Chen, S. Mcdonnell, A. Azcatl, C. Carraro, B. Ma, R. Maboudian, R. M. Wallace, and A. Javey, Nano Letts. 14 (2014) 967.

[65] M. Patel, M. Kumar, H.-S. Kim, W.-H. Park, E.H. Choi, and J. Kim, Materials Science in Semiconductor Processing 74 (2018) 74.

[66] J. Meyer, S. Hamwi, M. Kröger, W. Kowalsky, T. Riedl, and A. Kahn, Adv. Mater. 24 (2012) 5408.

[67] J. Song, X. Ni, D. Zhang, and H. Zheng, Solid State Sciences 8 (2006) 1164.

[68] S. McDonnell, A. Azcatl, R. Addou, C. Gong, C. Battaglia, S. Chuang, K. Cho, A. Javey, and R.M. Wallace, ACS Nano 8 (2014) 6265.

[69] M. F. J. Vos, B. Macco, N. F. W. Thissen, A. A. Bol, and W. M. M. (Erwin) Kessels, J. Vacuum Science & Technology A 34 (2016) 01A103.

[70] M.T. Greiner, L. Chai, M. G. Helander, W. M. Tang, and Z. H. Lu, Adv. Funct. Mater. 22

(2012) 4557.

[71] K. A. Gesheva, A. Cziraki, T. Ivanova, and A. Szekeres, Thin Solid Films 515 (2007) 4609.

[72] A. Rydosz, M. Ziabka, D. Michon, J. Kanak, W. Maziarz, and T. Pisarkiewicz, Sensor Lett. 15 (2017) 517.

[73] M. Kumar, A. Kanjilal, and T. Som, AIP Adv. 3 (2013) 092126.

[74] M. T. Taschuk, M. M. Hawkeye, and M. J. Brett, "Glancing angle deposition," in Handbook of Deposition Technologies for Films and Coatings: Science, Applications and Technology, edited by P. Martin and W. Andrew (Elsevier, Oxford, United Kingdom, 2010).

[75] M. M. Hawkeye, M. T. Taschuk, M. J. Brett, Glancing Angle Deposition of Thin Films: Engineering the Nanoscale (Wiley Series in Materials for Electronic and Optoelectronic Applications) 2014: Wiley, United Kingdom.

[76] M. M. Hawkeye, M.J. Brett, J. Vacuum Science & Technology A 25 (2007) 1317.

[77] A. Barranco, A. Borras, A. R. Gonzalez-Elipe, and A. Palmero, Progress in Materials Science 76 (2016) 59.

[78] L. González-García, J. Parra-Barranco, J. R. Sánchez-Valencia, A. Barranco, A. Borrás, A. R. González-Elipe, M. C. García-Gutiérrez, J. J. Hernández, D. R. Rueda, and T. A. Ezquerra Nanotechnology 23 (2012) 205701.

[79] G. Beydaghyan, S. Doiron, A. Hach́, and P. V. Ashrit, Appl. Phys. Lett. 95 (2009) 051917.

[80] S. W. Liu, Y. Divayana, X. W. Sun, Y. Wang, K. S. Leck, and H. V Demir, Optics Express. 19 (2011) 4513.

[81] A. L. Barabási, H. E. Stanley, Fractal Concepts in Surface Growth 1995: Cambridge University Press, Cambridge.

[82] M. Arita, H. Kaji, T. Fujii, Y. Takahashi, Thin Solid Films 520 (2012) 4762.

[83] M. Morales-Luna, S. A. Tomás, M. A. Arvizu, M. Pérez-González, E. Campos-Gonzalez, J. Allos and Compunds 722 (2017) 938.

[84] M. Diskus, O. Nilsen, H. Fjellvåg, S. Diplas, P. Beato, C. Harvey, E. van Schrojenstein Lantman, and B. M. Weckhuysen, J. Vacuum Science & Technology A 30 (2012) 01A107.

[85] N. Illyaskutty, S. Sreedhar, G. Sanal Kumar, H. Kohler, M. Schwotzer, C. Natzeck, and V. P. M. Pillai, Nanoscale. 6 (2014) 13882.

[86] K. Ajito, L. A. Nagahara, D. A. Tryk, K. Hashimoto, and A. Fujishima, J. Phys. Chem. 99 (1995) 16383.

[87] S. Y. Lin, Y. C. Chen, C. M. Wang, P. T. Hsieh, and S. C. Shih, Appl. Surf. Sci. 255 (2009) 3868.

[88] R. Sivakumar, R. Gopalakrishnan, M. Jayachandran, and C. Sanjeeviraja, Current Appl. Phys. 7 (2007) 51.

[89] P. M. Martin, Handbook of Deposition Technologies for Films and Coating (3rd edition) 2005: Elsevier, Kennewick, Washington.

[90] M. Kumar, T. Basu, and T. Som, J. Appl. Phys.118 (2015) 055102.

[91] G. H. Gilmer and P. Bennema, J. Appl. Phys. 43 (1972) 1347.

[92] J. C. Bernède, L. Cattin, and M. Morsil, Tech. Lett. 2 (2014) 5.

[93] P. würfel and Uli würfel, *Physics of Solar cells: From Basic Principles to Advanced Concepts 2016*: Wiley, New York.

[94] M. T. Greiner, M. G. Helander, W. Tang, Z. Wang, J. Qiu, and Z. Lu, Nat. Mater. 11 (2011) 76.

[95] J. Bullock, A. Cuevas, T. Allen, and C. Battaglia, Appl. Phys. Lett. 105 (2014) 232109.

[96] S. Tokito, K. Noda, and Y. Taga, J. Phys. D:Appl. Phys. 29 (1996) 2750.

[97] T. Basu, M. Kumar, and T. Som, Mater. Lett. 135 (2014) 188.

[98] T. Matsushima, Y. Kinoshita, and H. Murata, Appl. Phys. Lett. 91 (2007) 2005.

[99] J. M. Cho, S. K. Lee, S. J. Moon, J. Jo, and W. S. Shin, Curr. Appl. Phys. 14 (2014) 1144.

[100] C. Imawan, F. Solzbacher, H. Steffes, and E. Obermeier, Sensors and Actuators B 64 (2000)193.

[101] X. Li, W. C. H. Choy, F. Xie, S. Zhang, and J. Hou, J. Mater. Chem. A 1 (2013) 6614.

[102] C. V. Ramana, V. V. Atuchin, V. G. Kesler, V. A. Kochubey, L. D. Pokrovsky, V. Shutthanandan, U. Becker, and R. C. Ewing, Appl. Surf. Sci. 253 (2007) 5368.

[103] N. Usha, R. Sivakumar, C. Sanjeeviraja, R. Balasubramaniam, and Y. Kuroki, J. Mater Sci: Mater Electron 27 (2016) 7809.

[104] I. Navas R. Vinodkumar, K J Lethy, A. P. Detty, V. Ganesan V. Sathe, and V. P. M. Pillai, J. Phys. D: Appl. Phys. 42 (2009) 175305.

[105] M. F. J. Vos, B. Macco, N. F. W. Thissen, A. A. Bol, and W. M. M. (Erwin) Kessels, J. Vac. Sci. Technol. A 34(1) (2016) 01A103.

[106] R. Singh, M. Kumar, M. Saini, B. Satpati, and T. Som, Solar Energy 174 (2018) 231.

[107] Y. Mao, W. Li, X. Sun, Y. Ma, J. Xia, Y. Zhao, X. Lu, J. Gan, Z. Liu, J. Chen, P. Liu, and Y.Tong, Cryst. Eng. Comm. 14 (2012) 1419.

CHAPTER 6

6. Growth and characterization of metal back contact for CdTe-based solar cells

Thin film CdTe-based solar cells are one of the leading contenders to design efficient photovoltaic cells in terms of cost and environmental issues. In doing so, the formation of a stable, low resistance, and non-rectifying back contact to *p*-CdTe thin film is one of the major and critical challenges associated with this technology. As a matter of fact, the back contact in any solar cell not only provides a smooth charge transport but also reflects the incident light back into the main absorbing layer [1].

Here, we have studied the optimized growth conditions of Al and Mo thin films towards achieving the above-mentioned properties. Following these, the optimized metal thin films are used a as back contact to grow other necessary overlayers on *pris*- and *txt*-substrates.

6.1 Introduction

A stable back contact that is not significantly rectifying is essential for the good performance and long-term stability of solar cells. The formation of a low resistance and low barrier height back contact is one of the most challenging aspects towards fabricating of high performance CdTe based solar cells. Numerous metals such as: Au, Cr, Pd, Pt, Mo, Ag, and Al are used to form back contact for CdTe solar cells [1-4]. But for detailed growth study, we have used Al and Mo metals. Aluminium films are widely employed as a reflective layer with high conductivity and such coatings are also important for space applications [5,6]. In addition, Al is considered for making electrical contacts in different devices in comparison to other materials. Mo thin films also show high stability and good electrical conductivity and are thus, considered to be better suitable for making electric contacts in different nano-electronics applications, compared to other materials [8]. In addition, Mo is also used as a back electrode for solar cell applications where it is used not only as a conducting layer but also as a reflecting mirror [6]. As discussed earlier, using oblique angle deposition, tunable structural properties, surface reflection, and electrical transport properties have been demonstrated for wide variety of materials, including metals and semiconductors [7–12]. However, to the best of our knowledge, a systematic study on structural, electrical, and optical properties of aluminium and molybdenum thin films, deposited at oblique angles, is still lacking.

In this study, the effect of growth angle on structural, optical, and electrical properties of radio-frequency sputter-deposited Al and Mo thin films is investigated. The surface morphology of both the films is studied by atomic force microscopy and scanning electron microscopy which show an enhancement in the average grain size and root mean square roughness with increasing growth angle. Crystalline nature of the films were determined by x-ray diffraction. Since the surface morphology and crystallinity are known to play a crucial role in controlling the optical and charge transport properties of a material, we have measured the surface reflectance and resistivity of these films. In addition, we have used Kelvin probe force microscopy technique to evaluate the work function of both Al and Mo films. In fact, as a novelty, we show that the film deposited under the normally incident flux can be used as a good reflecting surface with a very low resistivity, leading to its use as a back contact.

6.2 Experimental details

In order to grow Al and Mo thin films, *p*-Si(100) and soda lime glass substrates were used. A 200 and 250 nm-thick Al and Mo films, respectively, measured by a surface profilometer, were deposited at RT using RF magnetron sputtering technique. Prior to deposition, substrates were cleaned by trichloroethylene, acetone, propanol, and de-ionized water using an ultrasonicator for 5 min. each. Commercially available (Testbourne) 99.99% pure Al and Mo targets (50.8

mm dia. meter × 6.35 mm-thick) were used for depositions. The deposition were carried out at 0^0, 30^0, 75^0, 85^0, and 87^0 angles of incidence (with respect to the surface normal). Ultra-pure (99.999%) argon gas was injected into the chamber with a flow rate of 30 sccm to maintain the working pressure of 5×10^{-3} mbar during sputtering. An RF power of 100 W (frequency = 13.56 MHz) was supplied to both the targets (during Al and Mo deposition) and the substrates were rotated at a constant speed of 3 rpm to achieve uniform film thicknesses and the target-to-substrate distance in both the cases was fixed at 80 mm. Surface morphology and microstructure of both type of films were examined by *ex-situ* AFM in tapping mode and FEGSEM (under the plan- and cross sectional-view geometries), respectively. For each sample, several AFM and SEM images were taken from a large number of randomly chosen regions to check the uniformity of the films. Work function of the films was measured by KPFM (as described in chapter 4) using a conductive tip. On the other hand, nature of the crystallinity of the films was determined by XRD, whereas the optical reflectance measurements were carried out using a UV-Visible spectrophotometer. Further, resistivity measurements were carried out by the linear four-probe technique using a source meter (Keithley, 2410) for both Al and Mo films grown at different angles.

6.3 Results and discussion

Prior to optical and electrical measurements, structural and morphological studies are carried out. Figures 6.1(a)-(d) show AFM images of Al films grown at 0^0, 30^0, 85^0, and 87^0, respectively, exhibiting a gradual change in the surface morphology with increasing growth angle [13,14]. It becomes evident that the average grain size and RMS roughness increase monotonically with increasing growth angle from 0^0 to 87^0. The variation in the average grain size and RMS roughness, as a function of growth angle, are depicted in Fig. 6.1(e). On the other hand, Figs. 6.2(a)-(d) show AFM images of Mo films grown at 0^0, 20^0, 65^0, and 87^0, respectively clearly exhibit a change in the morphology with the deposition angle. The observed change in the average grain size and RMS roughness with increasing oblique angle of deposition are shown in Fig. 6.2(e). In fact, as the deposition angle increases, the shadowing effect becomes more and more prominent which in turn controls the surface morphology [8,12]. Besides investigating the morphological evolution of Al and Mo films, as a function of deposition angle, the growth of nano-columnar structures of the films are also

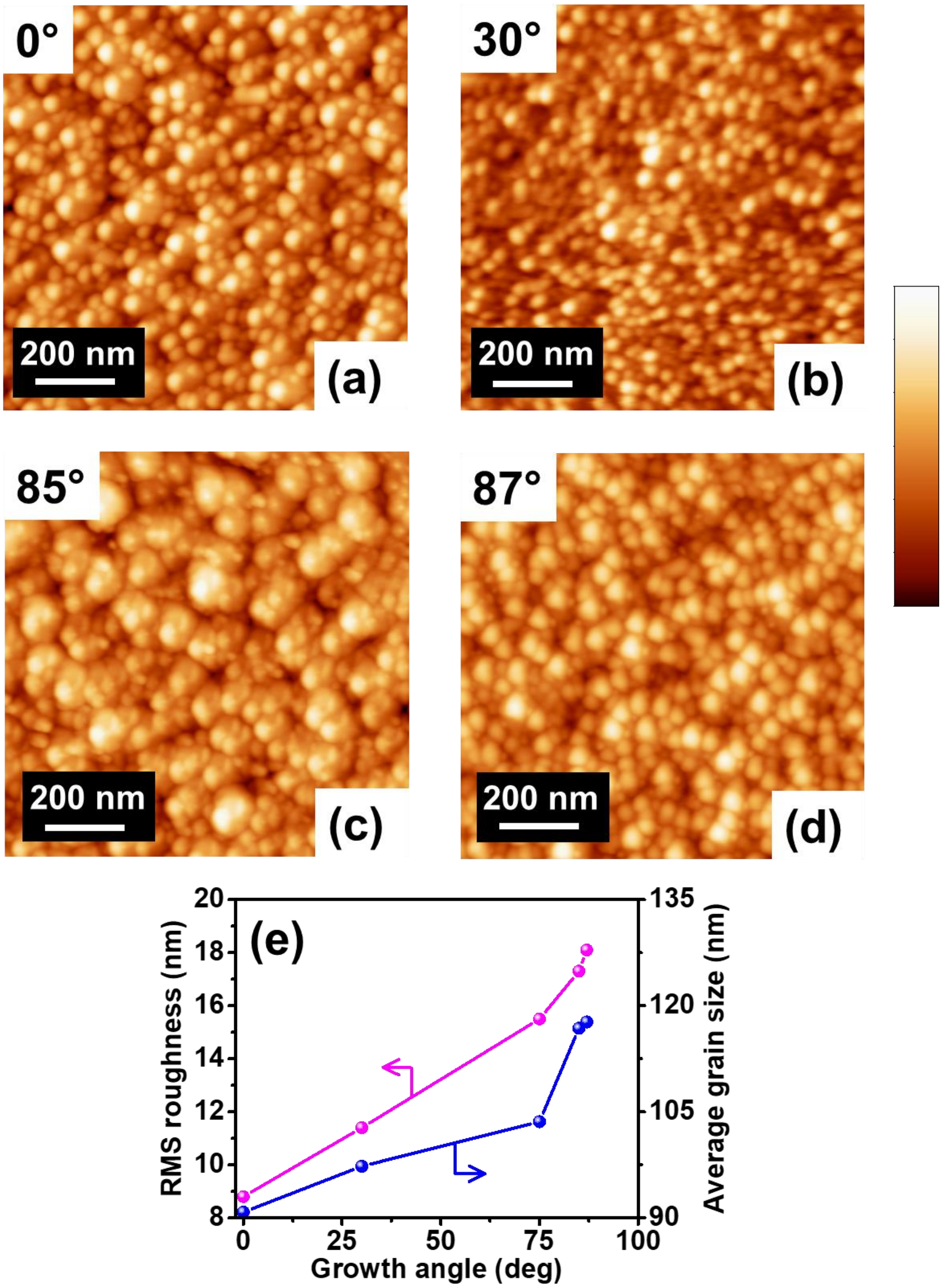

Figure 6.1: AFM images of Al films grown at different angles: (a) 0^0, (b) 30^0, (c) 85^0, and (d) 87^0 with the individual height scale of 59, 68, 76, and 79 nm, respectively. (e) Variations in the RMS roughness and average grain size with growth angle.

evident from the corresponding cross-sectional scanning electron microscopic (XSEM) images as depicted in Figs. 6.3(a)-(d) for the films grown at 0^0 and 87^0, respectively. Figures. 6.3(a) and (b) show XSEM images of Al films, whereas (c) and (d) show the microstructures of Mo films. In addition, it is interesting to note that the porosity of films increases with increasing growth angle which leads to the enhancement in the other physical properties [14].

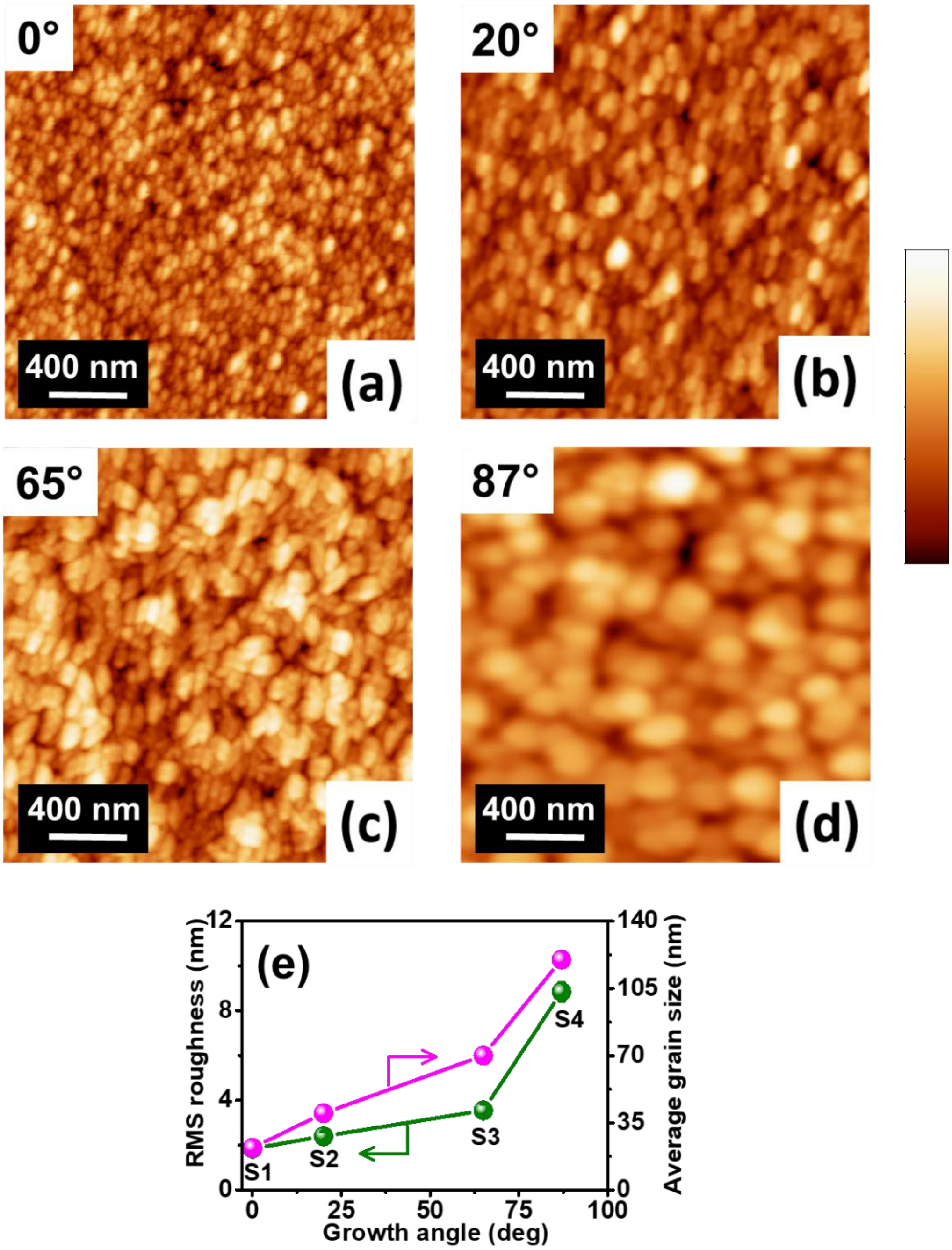

Figure 6.2: AFM images of Mo films grown at different angles: (a) 0^0, (b) 20^0, (c) 65^0, and (d) 87^0 with individual height scale of 14, 16, 22, and 73 nm, respectively. (e) Variations in RMS roughness and average grain size with growth angle.

The diffraction patterns of Al films grown under normal and oblique angles are shown in Fig. 6.4(a). There are high-intensity (111) and low-intensity (200) crystallographic peaks observed at 38.43^0 and 44.69^0, respectively [6,13]. It is interesting to note that the intensity of peaks decreases with increasing growth angle, which can be attributed to change in grain size and porosity of the films. On the hand, Fig. 6.4(b) shows XRD patterns of Mo thin films, depicting a strong peak at 40.6°. In fact, the phase identification reveals the BCC crystal structure with a

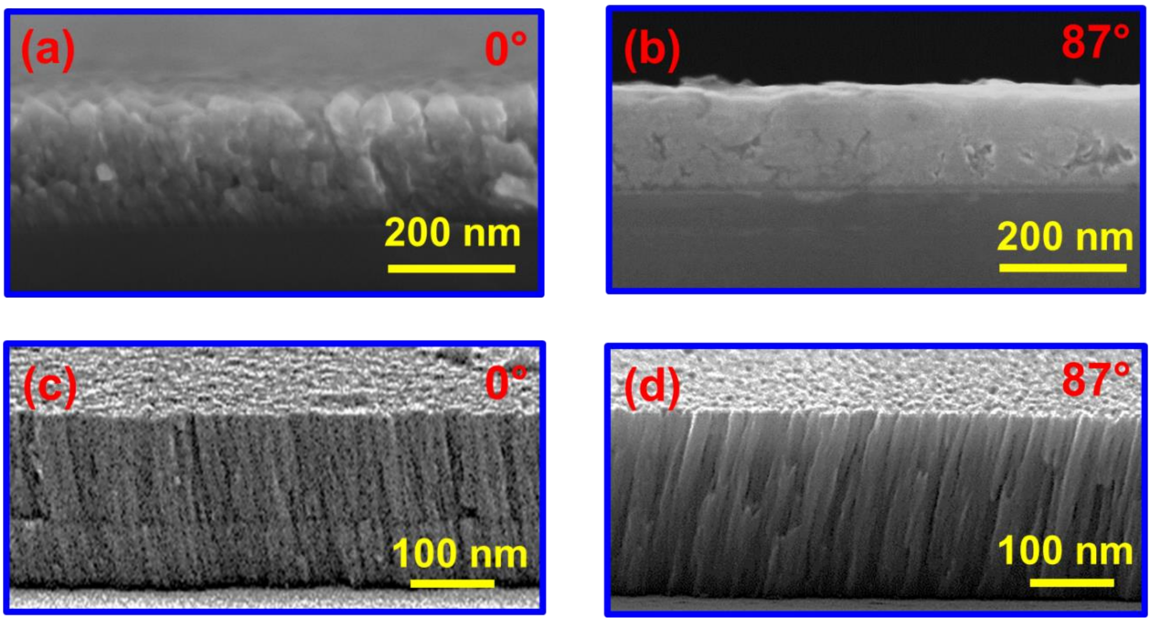

Figure 6.3: (a) and (b) Show the cross-sectional SEM images of Al films grown at 0^0 and 87^0, respectively, whereas (c) and (d) Depict cross-sectional SEM images of Mo films grown at 0^0 and 87^0, respectively.

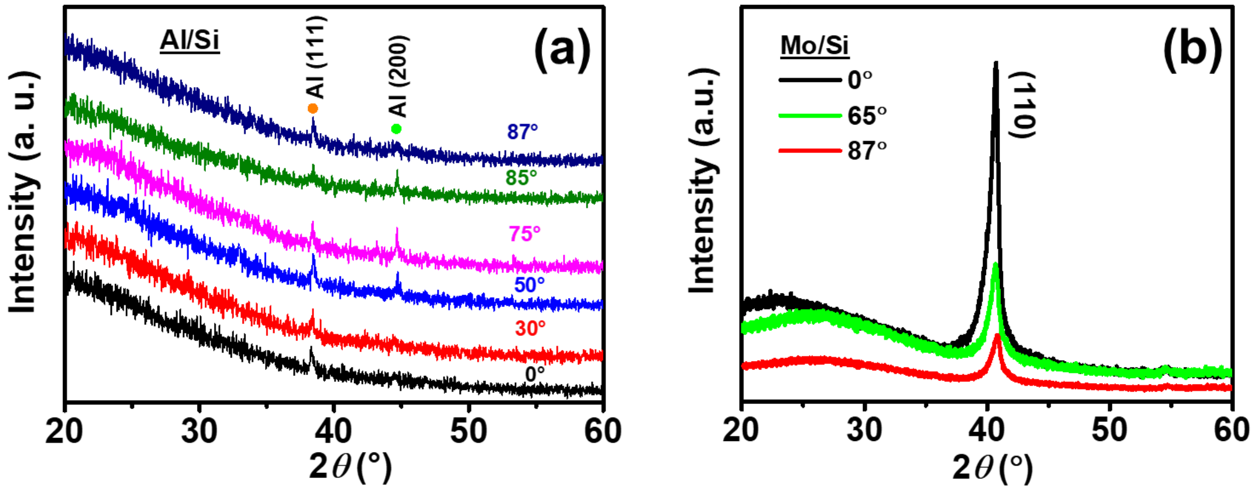

Figure 6.4: (a) and (b) Show the XRD patterns of Al and Mo films grown under different angles, respectively.

very strong [110] preferential alignment along the direction normal to the substrate. It is interesting to note that the peak position shifts towards higher angle (e.g. 44°) for the film grown at 87°, which can be attributed to the tilting of columnar nanostructures [15].

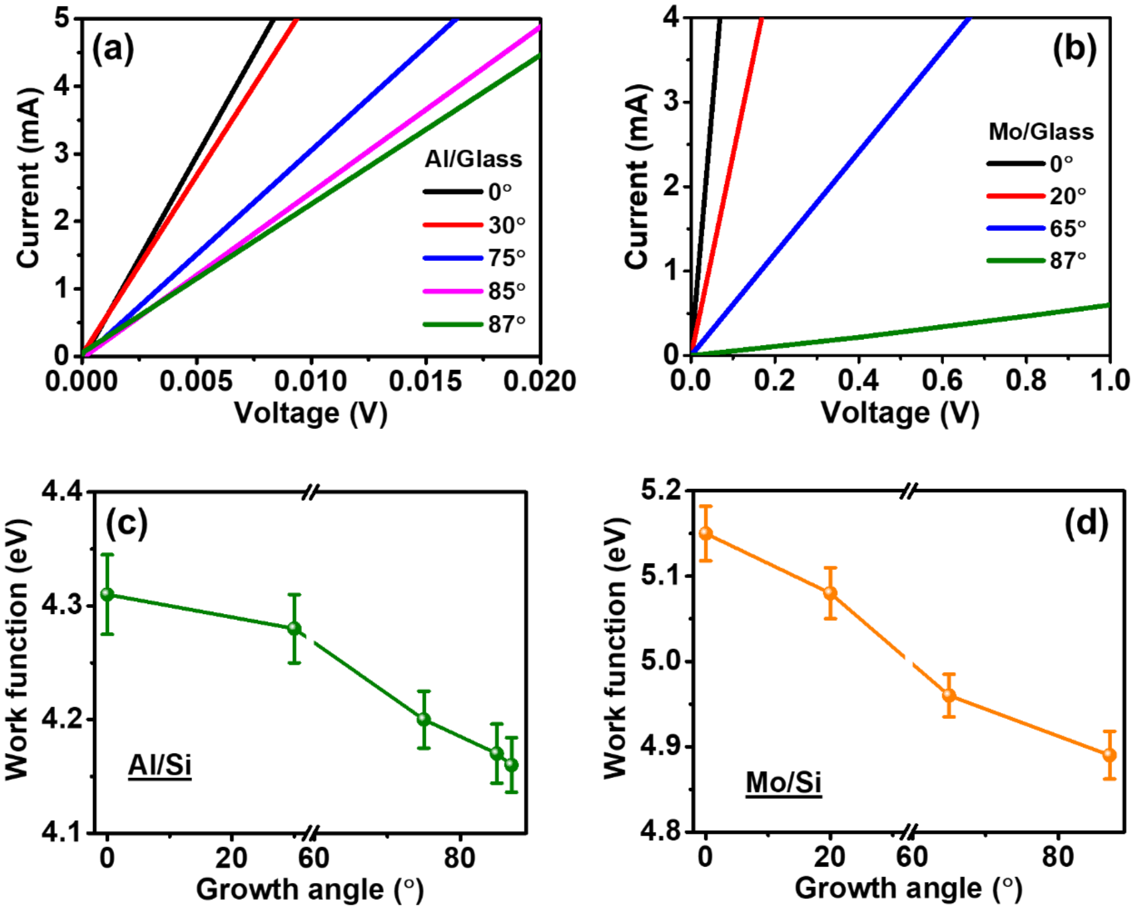

Figure 6.5: *I-V* characteristics of (a) Al and (b) Mo films, (c) and (d) show growth angle-dependent variations in work function of Al and Mo films.

Since the electrical properties of a material strongly depends on the surface morphology and crystallinity, *I-V* characteristics are recorded under similar conditions. Figures 6.5(a) and (b) depict the *I-V* characteristics of Al and Mo films, respectively measured by the linear four-probe technique. The Ohmic behaviour of the films is confirmed by the linear variation in the *I-V* characteristics [Figs. 6.5(a) and (b)]. The sheet resistance of films are calculated from the slope of *I-V* characteristics. Interestingly, a systematic increase in the sheet resistance is observed for all the films. In fact, the resistance increases by nearly an order of magnitude for the film grown at 30^0 in comparison to the one grown under normal incidence and similar enhancement takes place in resistance when one compares the case of 87^0. Moreover, resistivity is also found to increase with increasing growth angle for all films. For instance, the resistivity of Al films increases from 3.9×10^{-8} to 5.1×10^{-6} Ω-cm for growth angles of 0^0 and 87^0, respectively [14]. Thus, the resistivity increases by two orders of magnitude by increasing growth angle from 0^0 to 87^0. On the other hand, in case of Mo films, resistivity turns out to be 7.9×10^{-6}, 1.4×10^{-6}, 7.5×10^{-5}, and 8.1×10^{-4} Ω-cm for 0^0, 20^0, 65^0, and 87^0, respectively. In addition, we have measured work function of these films using KPFM technique (as discussed in chapter 5). It is observed that the work function decreases with increasing growth angle for both Al and Mo films. The maximum work function is found to be 4.31 eV and 5.15 eV corresponding to the deposition angle of 0^0 for Al and Mo films, respectively. For all other oblique angles, viz. 30^0, 75^0, 85^0, and 87^0, work function values of Al films turn out to be 4.28, 4.20, 4.17, and 4.16 eV, respectively as shown in Fig. 6.5(c) [4]. On the other hand, the work function of Mo films is found to be 5.08, 4.96, and 4.89 corresponding to the growth angle of 20^0, 65^0, and 87^0, respectively. Such a large change in resistivity and work function can be attributed to a variation in the porosity as well as surface roughness of the films with increasing deposition angle [16,17]. Porosity of thin films is known to govern not only the charge transport in the films but also has a bearing on the optical reflectance spectra [16,18]. In fact, reflectance of a film is inversely proportional to the porosity [2].

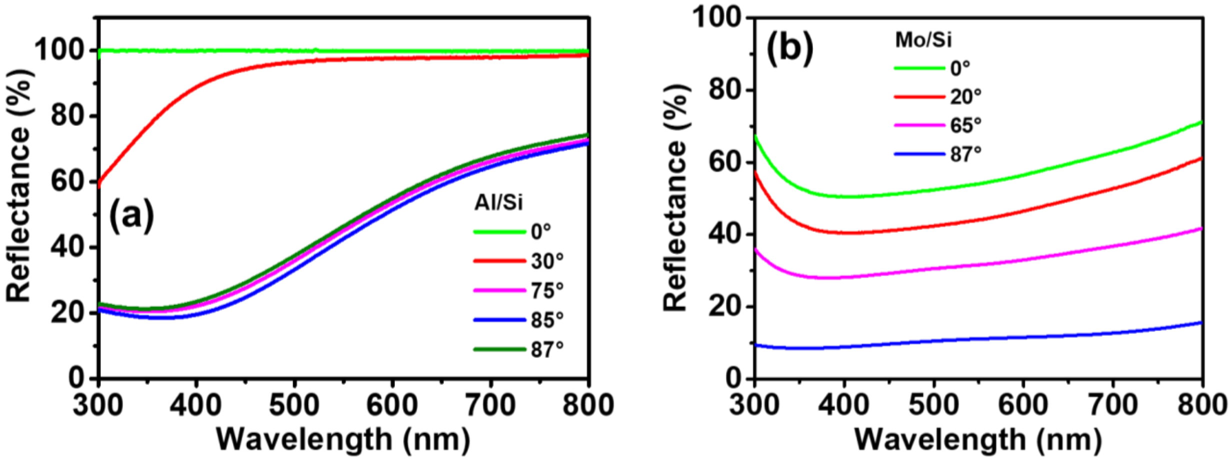

Figure 6.6: Surface reflectance of (a) Al and (b) Mo films grown at different angles.

Figures 6.6(a) and (b) show the surface reflectance spectra of Al and Mo films grown at different oblique angles. It is observed that the Al film deposited at normal incidence exhibits highest reflectance close to 99.93%. On the other hand, a decrease in the surface reflectance is observed with increasing growth angle [14]. A careful observation of these reflectance spectra reveals that the local reflectance minimum of each spectrum appears at 380 nm. For Mo films, the local reflectance minimum for each spectrum appears at 400 nm. It is also observed that the reflectance decreases in a sequential manner with increasing growth angle and the film grown at 0° exhibits highest reflectivity among others. As a matter of fact, this reduction in the surface reflectance can be attributed to the presence of porosity in the films (as discussed above). Thus, the Al and Mo films deposited at normal incidence can be used as electrical back contacts for fabricating the photovoltaic devices for the present study. However, it can be inferred that Mo is more suitable than Al due to its high work function as well as good resistivity and reflectance for the fabrication of CdTe-based PV cells. It may be noted that for the present study, we have constructed PV cells with both Al and Mo back contacts for a direct comparison on their performance as is describes in the next chapter.

6.4 Conclusions

In the present work, the tunability of work function, microstructural, electrical, and optical properties of RF sputter-deposited Al and Mo films, by changing the growth angle, have been demonstrated. Scanning electron microscopy and atomic force microscopy measurements show an increase in the average grain size and RMS roughness with the angle of deposition. A systematic increment in the resistivity and decrement in the reflectance and work function are observed with increasing growth angle. Thus, in the context of the present thesis work, it is found that both the films grown under normal incidence exhibit the lowest resistivity and the highest average reflectance and further, have been used to deposit several overlayers (including active one) to construct a CdTe:Cu-based solar cell (as described in chapter-7).

References

[1] D. L. Bätzner, R. Wendt, A. Romeo, H. Zogg, and A. N. Tiwari, Thin Solid Films 361–362 (2000) 463.

[2] M. Kumar (Ph. D. Thesis, Institute of Physics, Bhubaneswar under Homi Bhabha National Institute, Mumbai).

[3] E. Krawczak and S. Gułkowski, E3S Web of Conferences 19 (2017) 03011.

[4] C. Thu, P. Ehrenreich, K. K. Wong, E. Zimmermann, J. Dorman, W. Wang, A. Fakharuddin, M. Putnik, C. Drivas, A. Koutsoubelitis, M. Vasilopoulou, L. C. Palilis, S. Kennou, J. Kalb, T. Pfadler, and L. Schmidt-Mende, Sci. Rep. 8 (2018) 1.

[5] D. Liu, S. K. Dew, M. J. Brett, T. Janacek, T. Smy, and W. Tsai, Thin Solid Films 236 (1993) 267.

[6] H. Garbacz, P. Wieciński, B. Adamczyk-Cieślak, J. Mizera, and K. J. Kurzydłowski, J. Microsc. 237 (2010) 475.

[7] X. Jiao, J. Yang, R. Zhang, N. Zhang, H. Zhong, and Y. Shi, Mater. Lett. 124 (2014) 318.

[8 M. M. Hawkeyea and M. J. Brett, J. Vac. Sci. Tech. A 25 (2007) 1317.

[9] M. T. Taschuk, M. M. Hawkeye, M. J. Brett, P. Martin (Eds), Handbook of Deposition Technologies for Films and Coatings: Science, Applications and Technology (3rd Edition), 2010: William Andrew (Elsevier, Oxford).

[10] J. B. Sorge, A. C. van Popta, J. C. Sit, and M. J. Brett, Opt. Exp. 14 (2006) 10550.

[11] R. Singh, M. Kumar, M. Saini, A. Singh, B. Satpati, and T. Som, Appl. Surf. Sci. 418 (2017) 225.

[12] M. Kumar, R. Singh, S. Nandy, A. Ghosh, S. Rath, and T. Som, J. Appl. Phys. 120 (2016) 15302.

[13] D. V. Sidelev, A. V. Yuryeva, V. P. Krivobokov, A. S. Shabunin, M. S. Syrtanov, and Z. Koishybayeva, J. Phys. Conf. Ser. 741 (2016).

[14] M. Muralidhar Singh, G. Vijaya, K. Ms, B. K. Sridhara, and T. N. Shridhar, IOP Conf. Ser. Mater. Sci. Eng. 149 (2016).

[15] S. Chatterjee, M. Kumar, S. Gohil, and T. Som, Thin Solid Films 568 (2014) 81.

[16] J. -Q. Xi, M. F. Schubert, J. K. Kim, E. F. Schubert, M. Chen, S. Y. Lin, W. Liu, and J. A. Smart, Nat. Photo. 1 (2007) 176.

[17] F. C. Hsu, V. N. Prigodin and A. J. Epstein, Phys. Rev. B 74 (2006) 235219.

[18] A. Ghosh, P. Kant, P. K. Bandyopadhyay, P. Chandra, and O.P. Nijhawan, Infr. Phys. and Tech. 40 (1999) 49.

CHAPTER 7

7. Fabrication of a CdTe:Cu based solar cell and effect of metal back contact on its efficiency

We have discussed in the previous chapters that CdTe-based thin film solar cells have the ability to fulfil the demand of energy of world's population. Although due to its high work function it is a challenging task to fabricate a stable and non-rectifying back contact. The performance of photovoltaic devices is hindered by the presence of barrier height at the interface and junctions as well as the presence of structural defects.

The aim of this chapter is to study the impact of a back contact material on the power conversion efficiency of a CdTe:Cu absorber layer-based PV cells. Two back contact materials, viz. aluminum (Al) and molybdenum (Mo) are used to fabricate such PV cells. Following this, other necessary overlayers are grown on both *pris*- and *txt*-Si substrates. In addition, we present the structural, optical, and charge transport properties of full solar cell structures with and without the hole-blocking layer. Devices are studied through current-voltage (*I*-*V*) measurements under light. Moreover, using Kelvin probe force microscopy under dark and illuminated conditions (known as photo-KPFM), real time photoinduced charge dynamics across grains is measured. It is observed that band-bending takes place at the junctions and it also reduces under light illumination which plays a major role in charge collection.

7.1 An efficient hole-blocking CdTe:Cu-based solar cell

7.1.1 Introduction

Cadmium telluride (CdTe) is an alternative to other materials for use in thin film solar cells. Thin film CdTe based solar cells are one of the leading contenders in terms of cost and environmental issues [1–4]. Specially, heterojunction solar cells of *p*-type CdTe and *n*-type CdS are extensively employed because of their suitable band alignments [5]. In general, a *p-n* junction is needed to fabricate a solar cell where the *p*-type material works as an absorber layer and the *n*-type material generates an electric field at the junction which can be used to separate out the electron-hole pairs [6,7].

In CdS/CdTe solar cells, there is an excess amount Cd in the device and this excess Cd is not good for environment at the end of life of these cells [8]. However, for a CdTe-based solar cell, it is very difficult to achieve a high efficiency without a CdS layer because of short minority carrier lifetime, grain boundaries, impurity diffusion, interface passivation effects, high electron affinity of CdTe, and recombination of structural defects [9]. Recently, Crisp *et al.* have shown that the cell efficiency of the CdTe-based solar cell is below 5% without CdS layer which is very very far below than the maximum achieved efficiency of the same with CdS layer [10]. Thus, it is a challenging task to increase the efficiency of CdTe-based solar cell without using a CdS layer. In the present scenario, we have extensively studied the advantage of carrier-selective junction to decrease the recombination rate of photo-generated charge carriers [11] which should lead to a higher power conversion efficiency of a PV cell. For instance, Battaglia *et al.* have reported the enhancement in power conversion efficient of a Si solar cell using a carrier selective layer of MoO_3 [12]. In fact, they have demonstrated that MoO_3 thin film shows the ability to selectively block the flow of one type of charge carriers via valence or conduction band barriers depending on the band-bending [12]. Due to a mismatch in the band gaps, band-bending at the interface of MoO_3 and the neighbouring layer is formed which in turn blocks both the ionic and electronic charge carriers across the junction[12]. This property makes this material useful to replace a conventional *p-n* junction to achieve similar effects [12]. Keeping this in mind and the fact that the fabrication of a hole-blocking CdTe-based solar cell is still lacking, we have made use of MoO_3 to fabricate solar cells of this kind.

Due to the high work function of CdTe, it is very difficult to make an Ohmic back contact. Thus, back contacts show non-Ohmic behaviour in their *I-V* characteristics and the formation of Schottky barrier at the back contact takes place [13]. This Schottky barrier increases the contact resistance, thereby reducing the solar cell performance [14]. An approach to overcome this problem is to lower the schottky barrier height by decreasing the work function of CdTe. Thus, we have used different metals to check the effect of back contact on cell efficiency. In addition, we have measured barrier height at each interface of the multi-junction CdTe-based solar cell. At the interfaces, due to a difference in the work function of the adjacent layers, band-bending takes place [15]. It is worth mentioning here that to measure the barrier height, various scanning probe microscopy (SPM) techniques are employed. Among different modes of SPM, Kelvin probe force microscopy is a powerful technique to reveal the optoelectronic performance of the photovoltaic devices [15]. In fact, it allows to map the topography and the local contact potential difference (V_{CPD}) between the tip and a sample simultaneously – with nanometer resolution.

In this study, structural properties of individual layers as well as all the constructed full solar cells are studied using AFM, SEM, EDX, and XRD. In particular, AFM and SEM images of the individual layers show granular nature, while their crystalline nature is examined by XRD. We have also investigated real-time photo-induced charge carrier dynamics across ZTO/MoO_3 and MoO_3/CdTe:Cu interfaces with high lateral resolution (~20 nm) using photo-KPFM. It is observed that band-bending appears at the interfaces which plays a major role in the cell efficiency. In addition, we have measured the cell efficiency of a ZTO and CdTe:Cu heterostructure grown on *pris*- and *txt*-Si substrates with Mo as a back contact (i.e. fabricated without any MoO_3 layer) which shows 3.3% and 4.1% cell efficiency, respectively. In contrast, a significant enhancement in the efficiency is achieved after introducing a hole-blocking MoO_3 layer between the ZTO and the CdTe:Cu layers and using a Mo back contact. For instance, we observe the efficiency to be 7.0% and 8.2% on *pris*- and *txt*-Si substrate, respectively. The same configuration of cells are also fabricated using Al as a back contact. However, this yields lower cell efficiencies. Finally, it is found that the ZTO/MoO_3/CdTe:Cu/Mo/*txt*-Si hole-blocking solar cell shows the highest efficiency compared to all other configurations.

7.1.2 Experimental

Two different substrates *pris*- and *txt*-Si were used to fabricate CdTe:Cu-based multijunction hole-blocking solar cells having two different metal back contacts e.g. Al and Mo. Prior to deposition, a *p*-Si(100) wafer was cut into slices which were ultrasonically cleaned in trichloroethylene, acetone, propanol, and de-ionized water for 5 min. each to remove the organic contaminations and air dried. Subsequently, the substrates were subject to alkaline etching for 30 min. to prepare pyramidally textured *p*-Si substrates, the details of which is reported elsewhere [11,16]. Further, in order to grow multijunction solar cells, CdTe:Cu, MoO_3, and ZTO thin films having appropriate thicknesses were deposited sequentially on both *pris*- and *txt*-Si substrates (as described earlier). We also constructed cell configurations having similar thicknesses but without having a 10 nm-thick hole-blocking MoO_3 layer. Likewise, we constructed PV cells using both *pris*- and *txt*-Si substrates with both Al and Mo back contacts. Figures 7.1(a) and (b) show a schematic diagram of the studied solar cells grown on Mo-coated *pris*- and *txt*-Si substrates, respectively.

The nature of crystallinity and phase identification of the used layers were carried out by XRD studies using the Bragg-Brentano geometry. Surface morphology and microstructural evoluation after each deposition were monitored by AFM (in tapping mode) and field emission gun scanning electron microscopy (in both plan- and cross sectional-view geometries), respectively. FEGSEM-based energy dispersive x-ray EDX spectrometric analysis was performed for compositional analysis of ZTO (180 nm)/MoO_3 (10 nm)/CdTe:Cu (1205 nm)/Mo (250 nm)/*pris*-Si and ZTO (180 nm)/MoO_3 (10 nm)/CdTe:Cu (1205 nm)/Mo (250 nm)/*txt*-Si heterostructures. KPFM measurements and band mapping across the interfaces were examined by *ex-situ* AFM using a special conductive Pt/Ir-coated Si probes (ATEC-CONTPt) tilled with respect to cantilever normal, having dia.~ <20 nm, ~0.2 Nm^{-1} stiffness, and a resonance frequency of ~15 kHz and tilted with respected to cantilever normal. Further, to reveal the effect of illumination at nanoscale on band-bending, the photo-KPFM measurement was performed. For this measurement, this special Pt/Ir-coated Si probes (ATEC-CONTPt) was used, which resolves a key challenge in efforts to neutralize the shadowing to the illumination from top. The reproducibility of the KPFM measurements were tested by various lift heights, starting from 30 to 100 nm. A white light source having 8 mW cm^{-2} intensity was used to study the effect of illumination on nanoscale electric transport. All measurements were performed at large number of randomly chosen places with different scan speeds (in the range of 0.1 to 1 Hz) and at various scan angles (by rotating the samples) to rule out the possibility of tip-related artefacts in the present data [17]. All recorded images were analysed using WSxM

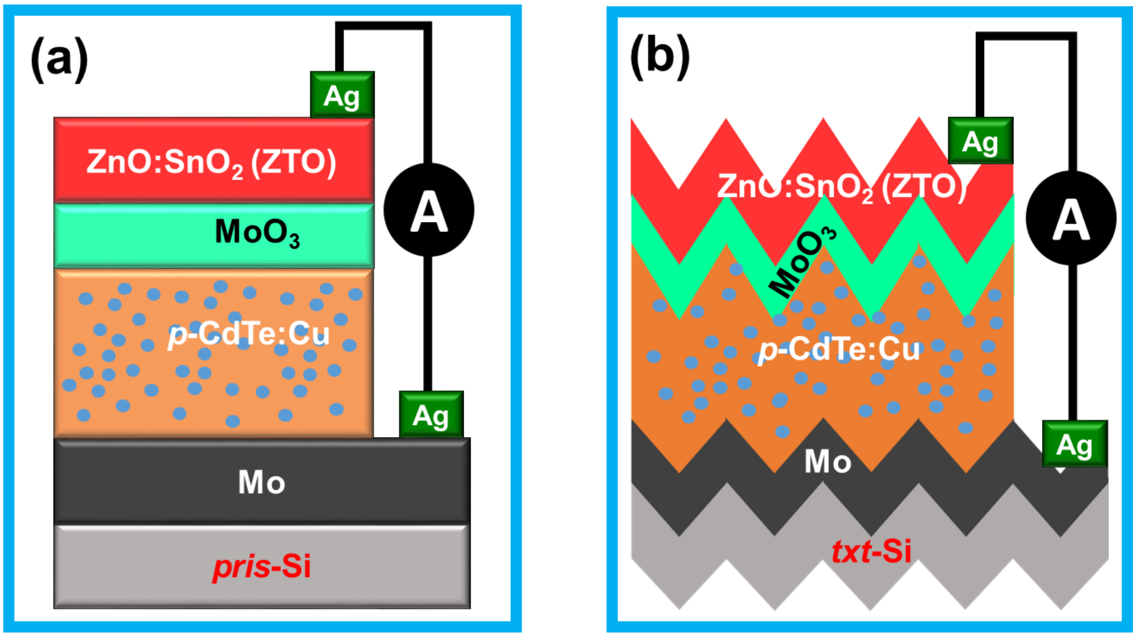

Figure 7.1: (a) and (b) Schematic diagrams of two PV cell configurations fabricated on *pris*- and *txt*-Si substrate, respectively.

software [18]. Silver paste was used to make electrical contacts on top of the ZTO layer and the metal back contact. The *I-V* data were recorded using a commercially available software (Lab-Tracer 2.0).

7.1.3 Results and discussion

In order to find out a possible correlation between the charge transport and structural properties of different layers in all the heterostructures, AFM, SEM, EDX, and XRD studies are carried out. Figures 7.2(a)-(d) show the AFM images of Mo/*pris*-Si, CdTe:Cu/Mo/*pris*-Si, MoO_3/CdTe:Cu/Mo/*pris*-Si, and ZTO/MoO_3/CdTe:Cu/Mo/*pris*-Si, respectively. It is observed that the Mo film deposited on *pris*-Si substrate [Fig. 7.2(a)] shows elongated granular structures with an average grain size of 67 nm, which increases to 123 nm after the growth of CdTe:Cu films on top of it [Fig. 7.2(b)] and the formation of spherical grains are observed. On the other hand, no significant change in the topography is observed apart from a little reduction in the average grain size after MoO_3 deposition on CdTe:Cu/Mo/*pris*-Si and this can be attributed to a low thickness of the same [Fig. 7.2(c)]. Further, it is interesting to note that after the growth of a ZTO layer on top of MoO_3/CdTe:Cu/Mo/*pris*-Si substrate further the average grain size increases as confirmed from Fig. 7.2(d). However, no other significant change takes place in the surface topography even after the deposition of ZTO thin film on top of MoO_3/CdTe:Cu/Mo/*pris*-Si substrate, confirming the conformal nature of growth. Besides investigating the topographical evolution, the growth of solar cell structures using different layers on *pris*-Si is also confirmed from the corresponding cross-sectional scanning electron microscopic (XSEM) images. Figures 7.2(e) and (f) depict the XSEM images of a PV cell grown on Mo-coated *pris*-Si without and with MoO_3 layer, respectively. The XSEM image not only confirms the intended thicknesses of the grown layers but also shows the formation of microstructures within these films. On the other hand, the inset of Figs. 7.2(e) and (f) show magnified view of the ZTO/CdTe:Cu and ZTO/MoO_3/CdTe:Cu interfaces, confirming the growth of thin MoO_3 layer between ZTO/CdTe:Cu interface. The elemental composition of the multilayer PV cell fabricated on a *pris*-Si substrate is studied by EDX spectrometric analysis

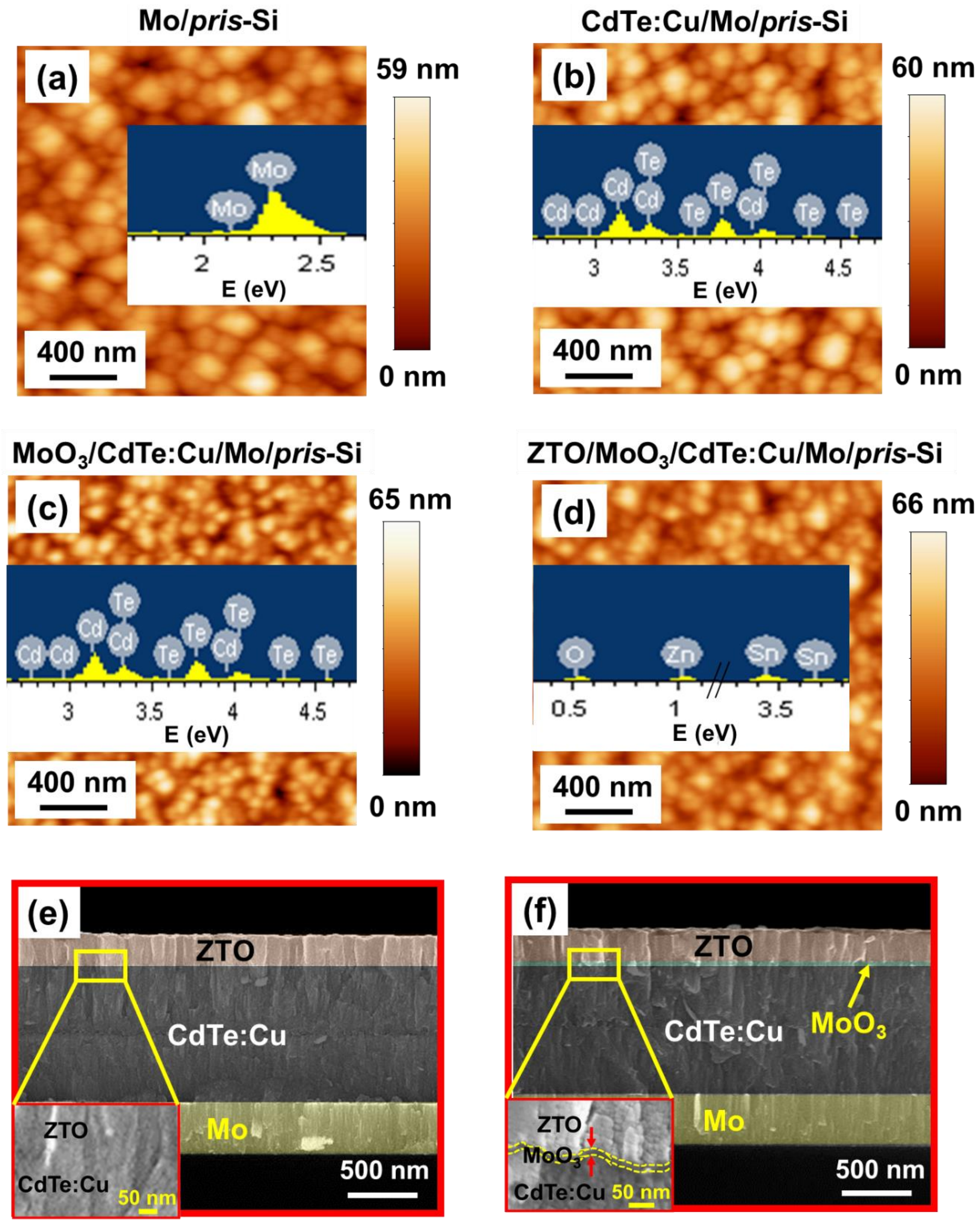

Figure 7.2: (a)-(d) Depict the AFM images of Mo deposited on *pris*-Si, CdTe:Cu deposited on Mo/*pris*-Si, MoO_3 deposited on CdTe:Cu/Mo/*pris*-Si, and ZTO deposited on MoO_3/CdTe:Cu/Mo/*pris*-Si substrate, respectively. The insets in (a)-(d) correspond to the EDX spectra, where only the layer selective elemental spectra are shown to avoid presenting the repetitive presence of all the elements arising from the bottom layers. (e) and (f) Show the cross-sectional SEM images of ZTO/CdTe:Cu/Mo/*pris*-Si and ZTO/MoO_3/CdTe:Cu/Mo/*pris*-Si, respectively where the insets in (e) and (f) depict their magnified images at the interface.

which reveals the presence of Zn, Sn, Cd, Te, Mo, and O and the absence Cu (due to its very low concentration) or of any other metallic impurity in the films [19]. EDX spectra corresponding to the individual layers of the heterostructure, grown on a *pris*-Si substrate, are depicted in the inset of Figs. 7.2(a)-(d).

In order to study the effect of a *txt*-Si substrate on the growth of Mo, CdTe:Cu, MoO_3, and ZTO films, first we study the microstructure of an as-prepared *txt*-Si substrate [as is shown in the inset of Fig. 7.3(a)] [20]. In fact, a sharp and well-defined pyramidal structures are clearly observed where the plane of observed four faces belongs to the {111} direction [11]. Figures

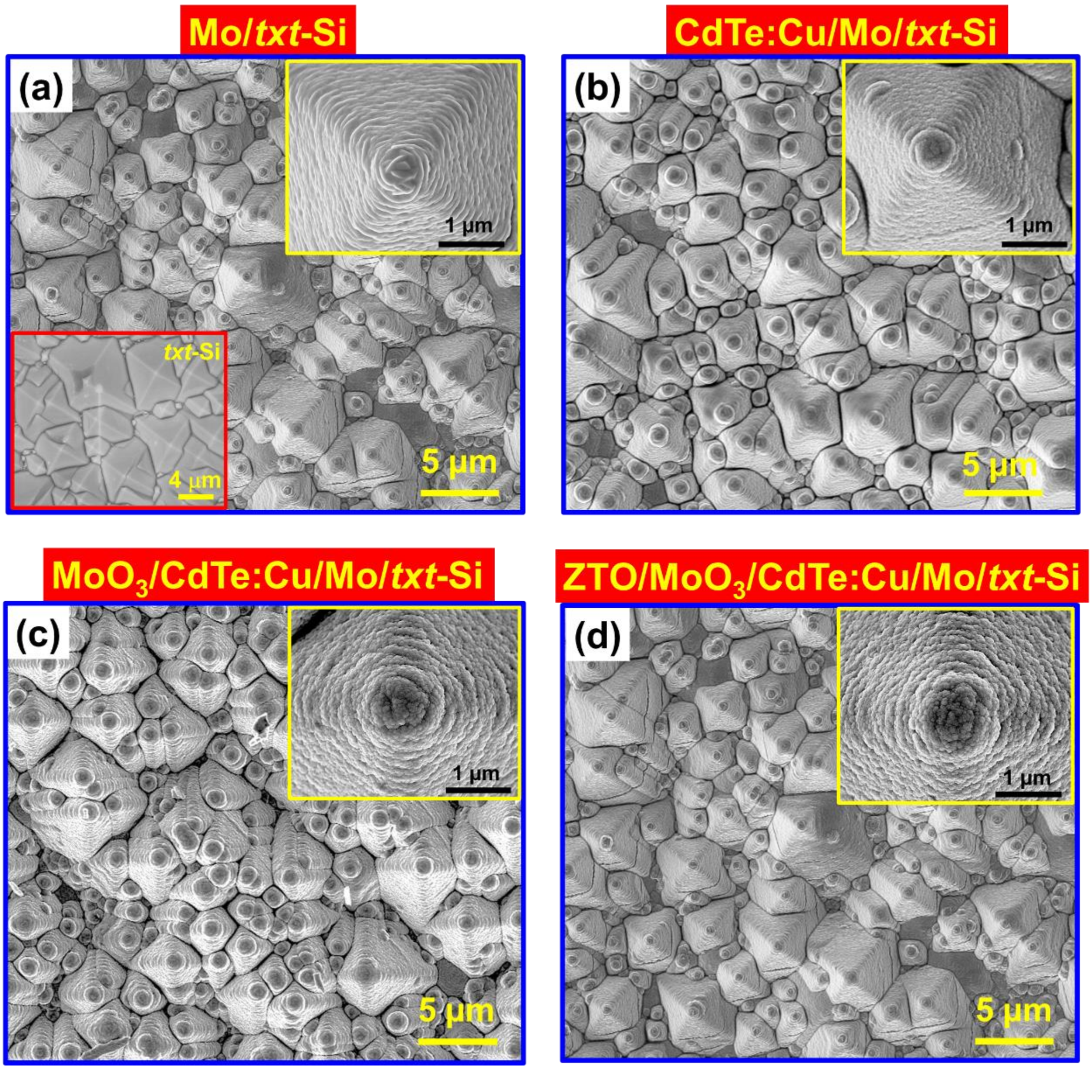

Figure 7.3: (a)-(d) Depict the plan-view FESEM images of Mo deposited on *txt*-Si, CdTe:Cu deposited on Mo/*txt*-Si, MoO_3 deposited on CdTe:Cu/Mo/*txt*-Si, and ZTO deposited on MoO_3/CdTe:Cu/Mo/*txt*-Si substrate, respectively, whereas the insets in (a)-(d) show SEM images of different magnifications and the inset in (a) for an as-prepared *txt*-Si substrate.

7.3(a)-(d) depicts the plan-view SEM images of Mo, CdTe:Cu/Mo, MoO_3/CdTe:Cu/Mo, and ZTO/MoO_3/CdTe:Cu/Mo heterostructures grown on a *txt*-Si substrate, respectively, confirming the granular nature of Mo, CdTe:Cu, MoO_3, and ZTO films with a morphology consisting of a random distribution of pyramidal structures and a very high roughness. For a better clarity, magnified plan-view SEM images of a single pyramid and close to its apex are shown in inset of Figs. 7.3(a)-(d), respectively which confirm the conformal growth and the formation of irregular shaped leaf-like nanostructures (on the pyramids) [11]. The respective

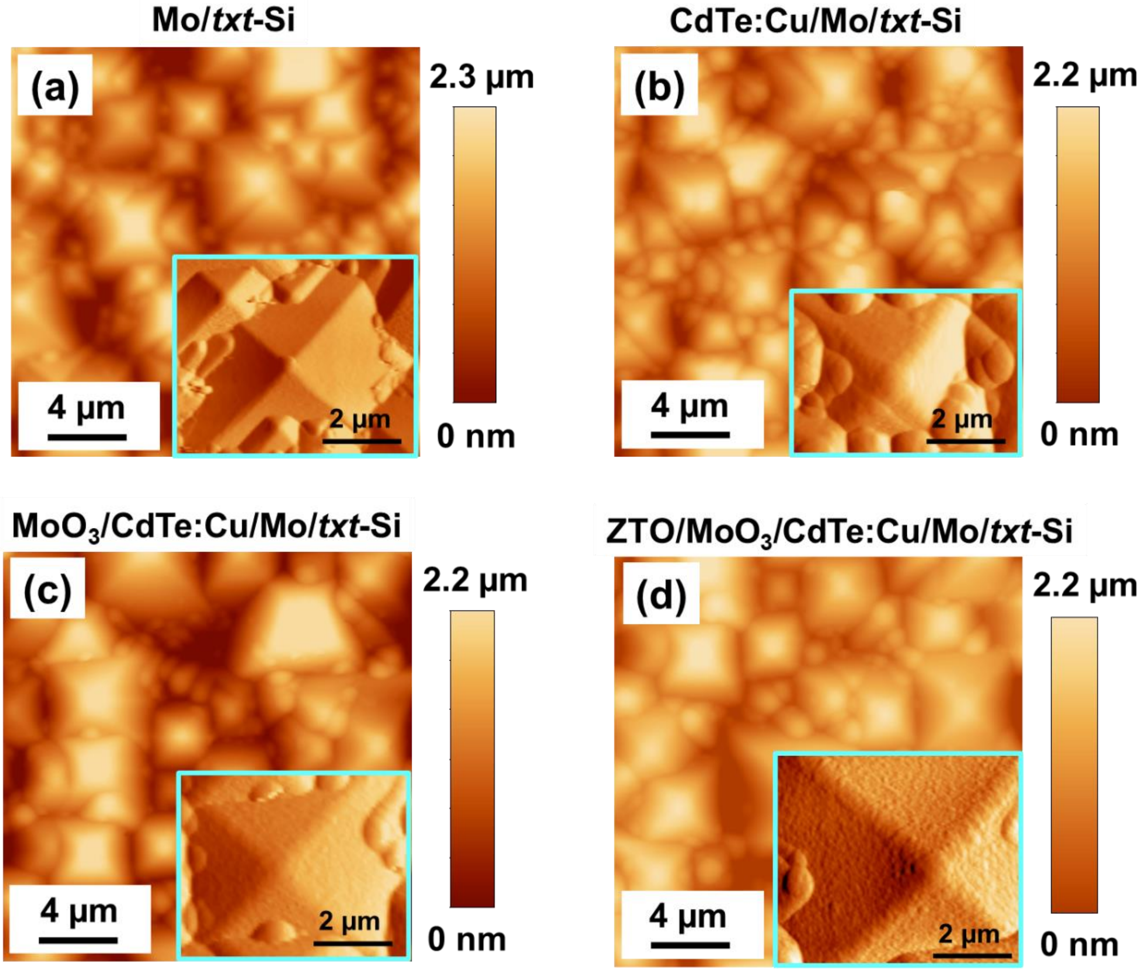

Figure 7.4: (a)-(d) Present the AFM images of Mo deposited on *txt*-Si, CdTe:Cu deposited on Mo/*txt*-Si, MoO_3 deposited on CdTe:Cu/Mo/*txt*-Si, and ZTO deposited on MoO_3/CdTe:Cu/Mo/*txt*-Si substrate, respectively where the insets in (a)-(d) depict their corresponding deflection images.

EDX measurements performed on each individual layer of the heterostructure grown on the *txt*-Si substrates also reveal the presence of Zn, Sn, O, Cd, Te, Mo, and Si (spectra not shown).

However, the absence of Cu from the CdTe:Cu layer can be attributed to its very low concentration. In order to understand to more about the surface morphology, AFM measurements on Mo, CdTe:Cu/Mo, MoO_3/CdTe:Cu/Mo, and ZTO/MoO_3/CdTe:Cu/Mo heterostructures grown on a *txt*-Si substrate are carried out, as are shown in Figs. 7.4(a)-(d), respectively. It is observed from the inset in Figs. 7.4(a)-(d) that uniformly distributed grains show an enhancement in size as the films grow. However, due to the high surface roughness, it is difficult to map the actual size of these structures. On the other hand, no significant change in the topography is observed even after the deposition of ZTO and MoO_3 thin film on top of CdTe:Cu/Mo/*txt*-Si substrates [21].

Figures 7.5(a) and (b) exhibit XRD patterns of the PV cells fabricated on *pris*- and *txt*-Si substrate, respectively. Both the samples show the presence of CdTe, Mo, and Si, whereas no peak is observed corresponding to either of ZTO and MoO_3 phases because of their amorphous nature (as described earlier in chapter-3 and chapter-5, respectively) [22,23]. It is also worth mentioning here that since Cu is doped at a very low concentration, no XRD peak appears corresponding to either metallic copper or any Cu-related secondary phase. The peaks appearing at 23.71°, 39.38°, 43.05°, and 46.47° match very well with that of CdTe (111), (220),

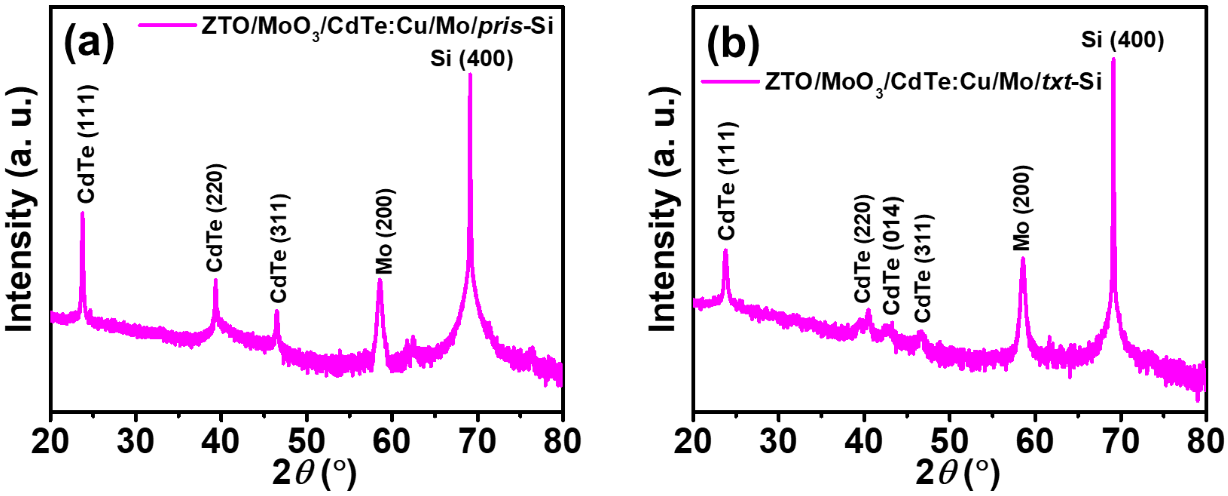

Figure 7.5: (a) and (b) Show XRD spectra corresponding to the PV cell configurations fabricated on *pris*- and *txt*-Si substrate, respectively.

(014), and (311) reflections, respectively having a zinc blende (cubic structure) [24,25]. On the other hand, the diffraction lines appearing at 58.59° and 69.12° belong to Mo and Si, respectively. It may be noted that the absence of any other peak in the diffractograms reveals that neither any impurity nor any secondary phase is present in our samples [22,23].

Prior to measuring the cell efficiency, local charge transport and interfacial band-bending (band alignment) are characterized. Figure 7.6(a) depicts a 3D AFM topography image, clearly confirming the interface between the ZTO and CdTe:Cu films. To measure the thickness of the ZTO film grown on the CdTe:Cu absorber layer, a line profile has been extracted in Fig. 7.6(b) along the line marked on the height image shown in Fig. 7.6(a). The measured average thickness is found to be 178 nm. On the other hand, variation in the vacuum-level from ZTO to CdTe:Cu is measured by KPFM under dark and illuminated conditions and are shown in

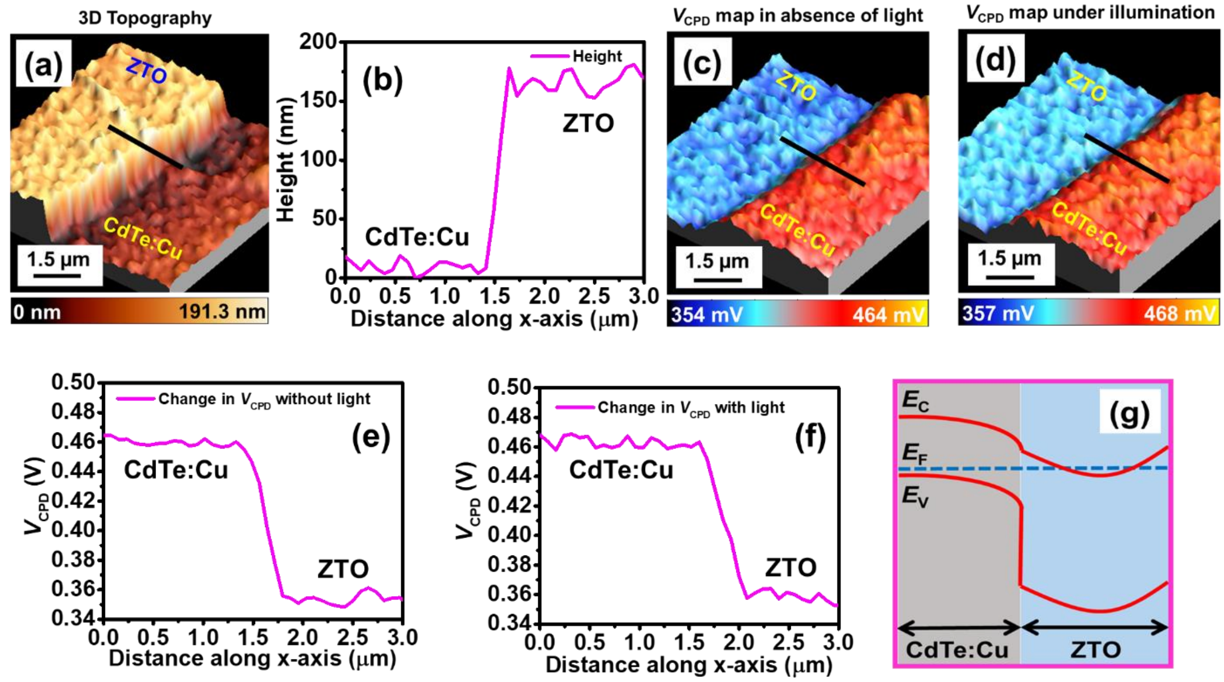

Figure 7.6: (a) Depicts 3D topography images of ZTO/CdTe:Cu interface, whereas (b) shows the line profile extracted the from marked line in (a). (c) and (d) Show the corresponding contact potential difference images of (a) under dark and light illumination (photo-KPFM), respectively, whereas (e) and (f) depict the line profiles extracted from (c) and (d), respectively (i.e. across the straight lines drawn across the respective interface). (g) Shows the schematic diagram of bend-bending at the interface of ZTO and CdTe:Cu due to the difference in their work function.

Fig. 7.6(c) and (d), respectively. These measurements help us to directly probe the energy offsets or band-bending between these two dissimilar materials [26]. A clear difference in V_{CPD} values is observed across the interface of ZTO and CdTe:Cu, as is shown in Fig. 7.6(c) which is a clear signature of band-bending, indicating that these two materials form a *p-n* junction. To measure the change in V_{CPD} value at the interface of ZTO and CdTe:Cu, a line profile is extracted from the V_{CPD} map image [along the black line drawn in Fig. 7.6(c)] and as is shown in Fig. 7.6(e). This line profile reveals a difference in V_{CPD} of 110 mV across the interface of ZTO and CdTe:Cu films. The work function of individual layers, viz. ZTO and CdTe:Cu is measured under dark, which is consistent with the existing reports. It is important to note that the difference in the work functions of ZTO (=5.05 eV) and CdTe:Cu (=5.21 eV) is found to be 160 meV which matches well with the measured difference in their work function values [obtained from Fig. 7.6(e)], viz. 110 meV [13,22].

Further, to quantify the effect of illumination on bend-bending at nanoscale, a line profile is extracted from the V_{CPD} map image [along the black line drawn in Fig. 7.6(d)] and as is shown in Fig. 7.6(f). This line profile reveals a difference in V_{CPD} of 104 mV across the ZTO and CdTe:Cu layers under illumination, whereas in case of measurements carried out in dark, the difference is 110 mV. In addition, it is interesting to note that the V_{CPD} increases for both the layers, viz. ZTO and CdTe:Cu, indicating a shift in the Fermi level after illumination. Thus, it is confirmed that after illumination smooth charge transport takes place. To understand this, a schematic diagram of band-bending across the interface of ZTO and CdTe:Cu layers is depicted in Fig. 7.6(g) which confirms that electrons can easily drift from CdTe:Cu layer to ZTO layer. This matches very well with the obtained experimental results.

Further, to check the effect on interfacial band-bending after introducing a MoO_3 layer between the ZTO and CdTe:Cu layers, photo-KPFM measurement is performed under similar conditions as-discussed above. A schematic diagram of band-bending across the interfaces

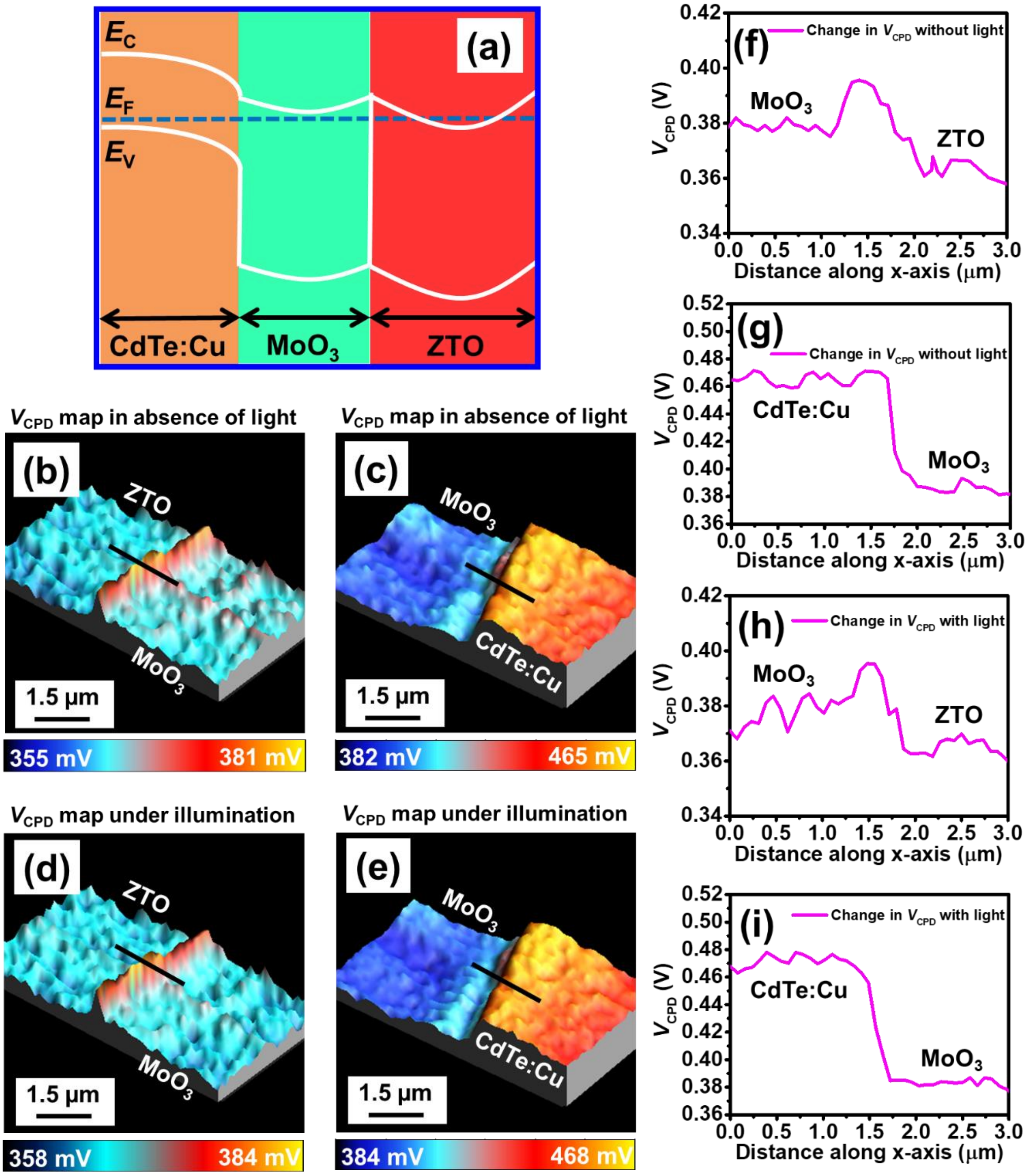

Figure 7.7: (a) Shows the schematic diagram of bend-bending at the interfaces of ZTO/MoO_3 and MoO_3/CdTe:Cu. (b)-(e) Depict the contact potential difference maps under dark and light illumination (photo-KPFM) at the ZTO/MoO_3 and MoO_3/CdTe:Cu interfaces, respectively and (f)-(i) show the line profiles extracted from (b)-(e), respectively (from the marked region by a straight line drawn across the interfaces).

after adding the MoO_3 layer is shown in Fig. 7.7(a) which confirms the smooth electron transport from CdTe:Cu layer to ZTO layer via MoO_3 layer. To check experimentally, the V_{CPD} map of both interfaces viz. ZTO/MoO_3 and MoO_3/CdTe:Cu is measured by KPFM under dark and illuminated conditions are shown in Figs. 7.7(b)-(e), respectively. A clear difference in

V_{CPD} values is observed across the interfaces of ZTO and MoO_3 as well as MoO_3 and CdTe:Cu, as are shown in Figs. 7.7(b) and (c) which is a clear signature of band-bending. To measure the change in the V_{CPD} values at the interfaces of ZTO and MoO_3 as well as MoO_3 and CdTe:Cu, line profiles are extracted from the respective V_{CPD} maps [along the black line drawn in Figs. 7.7(b)-(e)] and are shown in Figs. 7.7(f)-(i). These line profiles reveal a difference in V_{CPD} of 15 mV across the ZTO and MoO_3 films and 86 mV across the MoO_3 and CdTe:Cu films, whereas it decreases after illumination for both the interfaces and are found to be 13 and 84 mV for ZTO/MoO_3 and MoO_3/CdTe:Cu, respectively. It is important to note that the difference in the work functions of ZTO (=5.07 eV) and MoO_3 (=5.11 eV) is found close to 40 meV, whereas that for MoO_3 (=5.11 eV) and CdTe:Cu (=5.21 eV) is close to 100 meV which match well with the measured respective differences in their work function values [obtained from Figs. 7.7(f) and (g)] [12,13,22]. In fact, the difference in the work functions between the respective pair of materials forming the two interfaces create a space charge region (SCR) through the diffusion of carriers, which prevents the recombination of electron-hole from respective ZTO/MoO_3 and MoO_3/CdTe:Cu interfaces as is confirmed by measured band-bending [Figs. 7.7(f)-(i)]and schematic of the same [Fig. 7.7(a)] [27]. According to the obtained results, it can be concluded that band-bending at the interface of MoO_3 and CdTe:Cu can block the flow of the electrons towards CdTe:Cu layer and in turn helps to increase the efficiency of the cell. Certainly, light absorption generates excitons, which immediately separated out into electrons and holes under the action of built-in potential [28]. Out of theses, the holes are injected into the bottom CdTe:Cu layer, while the electrons are transferred to the top MoO_3 and ZTO layers.

To investigate the performance of ZTO/CdTe:Cu and ZTO/MoO_3/CdTe:Cu device architectures in the substrate configuration with different back contacts on *pris*- and *txt*-Si substrates, photocurrent density-voltage characteristics under white light illumination of 100 mW cm^{-2} are performed [Figs. 7.8(a)-(d)]. To briefly describe the device structure, four configurations were fabricated where light is incident through the top of the device. For these solar cells, transparent conducting oxide (TCO) layer of ZTO is used as the top electrode. These photocurrent density-voltage characteristics indicate that light absorption takes place in all the configurations but very low reflectance is observed for *txt*-Si substrate configuration (as discussed in chapter-5) [11,16,29], resulting the generation of more electron-hole pairs take place and in turn the generation of photocurrent. The ZTO/CdTe:Cu/Mo/*pris*-Si multi-junction cell shows an open-circuit voltage (V_{OC}) of 0.47 V and a short-circuit current density (I_{sc}) of 8.27 mA cm^{-2}. Subsequently, the *FF* and the power conversion efficiency (η) of this cell are found to be 34% and 3.3%, respectively. However, after adding the hole-blocking layer (MoO_3)

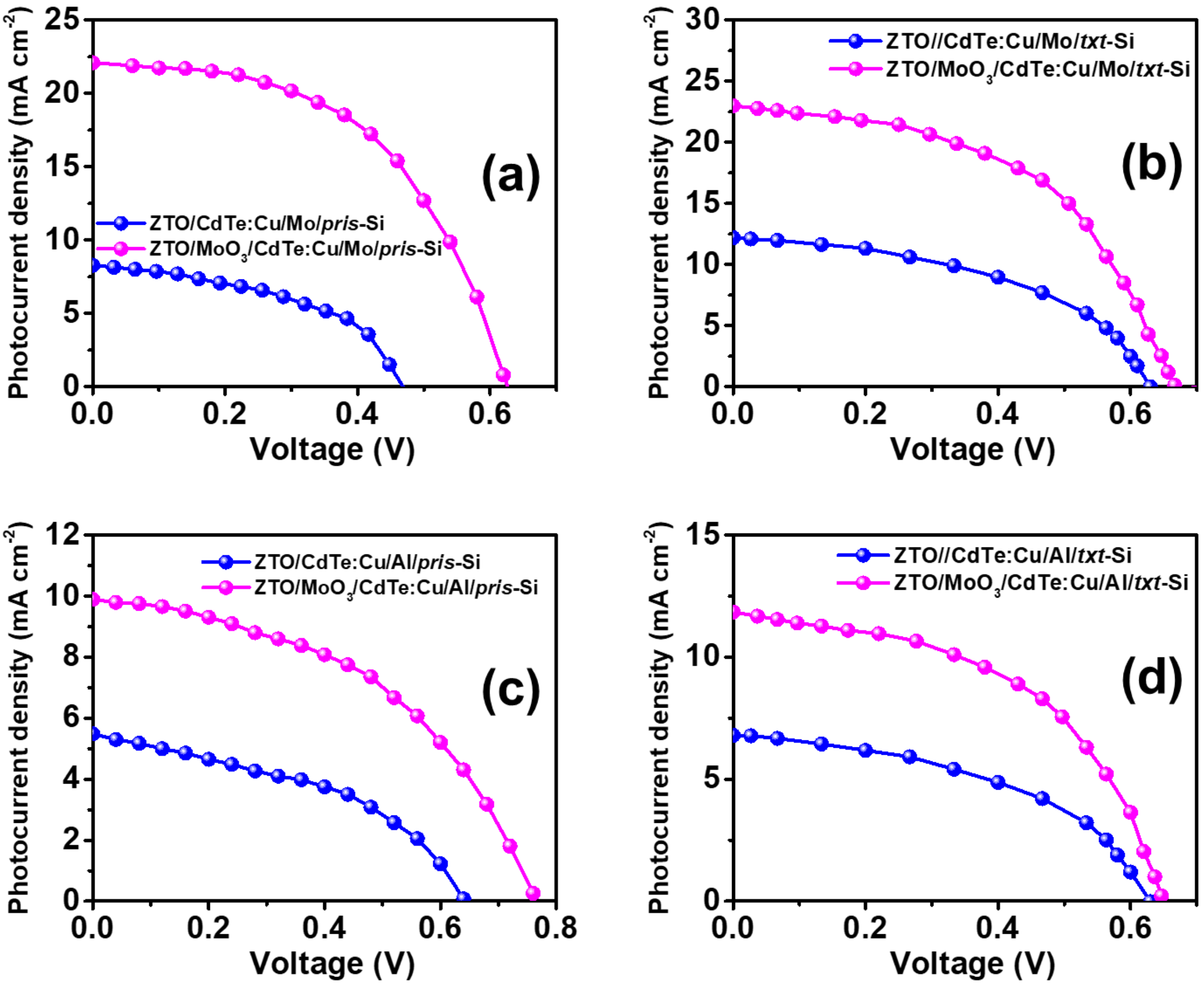

Figure 7.8: (a)-(d) Current-voltage characteristics obtained from the PV cells having different configurations and fabricated on both *pris*- and *txt*-Si substrates.

between ZTO and CdTe:Cu, all the parameters of the device, viz. V_{OC}, I_{sc}, FF, and η increase and are found to be 0.58 V, 21.68 mA cm^{-2}, 56%, and 7.01%, respectively. On the other hand, the measured V_{OC}, I_{sc}, FF, and η for the ZTO/CdTe:Cu/Mo/*txt*-Si heterojunction cell are 0.63 V, 12.2 mA cm^{-2}, 53%, and 4.07%, respectively which further increase after introducing the hole-blocking layer. For instance, the maximum measured power conversion efficiency, η, is found to be 8.2% having a FF 54%. Further, to check the effect of the back contact material, all the four configurations (described above) are fabricated on Al-coated *pris*- and *txt*-Si substrates. The measured V_{OC}, I_{sc}, FF, and η for ZTO/CdTe:Cu/Al/*pris*-Si (ZTO/CdTe:Cu/Al/*txt*-Si) heterojunction cell are 0.64 V (0.62 V), 5.50 mA cm^{-2} (6.8 mA cm^{-2}), 44% (48%), and 1.52%. (2.02%), respectively. It is interesting to note that after introducing the hole-blocking layer for both configurations, an enhancement in all parameters is observed and these values are summarized in Table 7.1. It is extremely important to note that the efficiency increases further upon using the *txt*-Si substrates as well as Mo as a back contact layer. In the present study, the maximum achieved efficiency is 8.2% corresponding to ZTO/MoO_3/CdTe:Cu/Mo/*txt*-Si multi-junction hole-blocking solar cell. This enhancement in the cell efficiency can be attributed to the hole-blocking nature of the MoO_3 layer and the much higher efficient broad-band light absorption in the case of conformally grown constituent layers on the *txt*-Si substrate. For instance, when light is incident on the devices, both the generation and recombination of electron-hole pairs take place. MoO_3 layer in between the ZTO and CdTe:Cu layers blocks the flow of holes, while it allows the movement of electrons and in turn reduces the recombination rate, resulting in an improvement in the cell efficiency. On the other hand, in case of *textured*-substrate both reflection and refraction take place, but the reflected light further falls on the next nearby pyramid and gets absorbed, resulting an increase in I_{SC} [11]. Thus, the maximum part of light is absorbed in the heterojunction, leading to the generation of more electron-hole pairs in the device and in turn the efficiency of the cell increases. To the best of our knowledge, it is the maximum achieved power conversion efficiency obtained from a Cl-free CdTe-based solar cell.

7.1.4 Conclusions

The present chapter explores the possibility of enhancing the power conversation efficiency of CdTe-based solar cells. We have examined various configurations of heterojunctions viz. ZTO/CdTe:Cu/Mo/*pris*-Si, ZTO/MoO_3/CdTe:Cu/Mo/*pris*-Si, ZTO/CdTe:Cu/Al/*pris*-Si, and ZTO/MoO_3/CdTe:Cu/Al/*pris*-Si. The same layer configurations are also grown on *txt*-Si substrates. We have studied their structural, optical, and charge transport properties. Using KPFM, bend-bending at the interfaces of ZTO/MoO_3 and MoO_3/CdTe:Cu has been measured directly and it is observed that under illumination condition, a smooth charge transport takes place across the layers. In addition, it is observed that the heterostructures fabricated with a hole-blocking MoO_3 layer sandwiched between ZTO and CdTe:Cu on both *pris*- and *txt*-Si of substrates show a much higher conversation efficiency in comparison to the ones fabricated without the MoO_3 layer. The observed results are attributed to the hole-blocking nature of MoO_3 and pyramidally textured-Si surfaces, resulting in a conformal growth of the constituent layers which yields a higher light absorption in the PV cells. Thus, these results will be very useful to design hole-blocking CdTe-based solar cells for even high power conversion efficiencies without any Cl treatment and using suitably designed constituent layers.

Table 7.1: Extracted relevant parameters from current-voltage characteristics of different solar cells.

Sample name	Fill factor (%)	Efficiency (%)
ZTO/CdTe:Cu/Al/*pris*-Si	44	1.52
ZTO/MoO_3/CdTe:Cu/Al/*pris*-Si	48	3.70
ZTO/CdTe:Cu/Al/*txt*-Si	48	2.01
ZTO/MoO_3/CdTe:Cu/Al/*txt*-Si	51	3.91
ZTO/CdTe:Cu/Mo/*pris*-Si	34	3.3
ZTO/MoO_3/CdTe:Cu/Mo/*pris*-Si	56	7.01
ZTO/CdTe:Cu/Mo/*txt*-Si	53	4.07
ZTO/MoO_3/CdTe:Cu/Mo/*txt*-Si	54	8.2

References

[1] M. de Wild-Scholten, 26th European Photovoltaic Solar Energy Conference, Hamburg, Germany, 5-9 September 2011.

[2] A. Luque and S. Hegedus (Eds), Handbook of Photovoltaics Science and Engineering, 2011: John Wiley & Sons Ltd. (Wiley, England).

[3] M. Raugei, S. Bargigli, and S. Ulgiati, Energy 32 (2007) 1310.

[4] V. M. Fthenakis, J. Renew. Sustain. Energy 8 (2004) 303.

[5] N. R. Paudel, A. D. Compaan, and Y. Yan, Sol. Energy Mater. Sol. Cells 113 (2013) 26.

[6] F. de Moure-Flores, J. G. Quiñones-Galván, A. Guillén-Cervantes, J. Santoyo-Salazar, A. Hernández-Hernández, M. de la. L. Olvera, M. Zapata-Torres, and M. Meléndez-Lira, AIP Adv. 2 (2012) 22131.

[7] S. H. Wei and S. B. Zhang, Phys. Status Solidi B 229 (2002) 305.

[8] S. J. Fonash, Solar Cell Device Physics. 1977: Academic Press, New York.

[9] J. N. Duenow, J. M. Burst, D. S. Albin, D. Kuciauskas, S. W. Johnston, R. C. Reedy, and W. K. Metzger, Appl. Phys. Lett. 105 (2014) 053903.

[10] R. W. Crisp, M. G. Panthani, W. L. Rance, J. N. Duenow, P. A. Parilla, R. Callahan, M. S. Dabney, J. J. Berry, D. V. Talapin, and J. M. Luther, ACS Nano 8 (2014) 9063.

[11] R. Singh, M. Kumar, M. Saini, A. Singh, B. Satpati, and T. Som, Appl. Surf. Sci. 418 (2017) 225.

[12] C. Battaglia, S. M. De Nicolás, S. De Wolf, X. Yin, M. Zheng, C. Ballif, and A. Javey, Appl. Phys. Lett. 104 (2014) 1.

[13] D. L. Bätzner, R. Wendt, A. Romeo, H. Zogg, and A.N. Tiwari, Thin Solid Films 361 (2000) 463.

[14] A. Niemegeers and M. Burgelman, J. Appl. Phys. 81 (1997) 2881.

[15] M. Kumar (Ph. D. Thesis, Institute of Physics, Bhubaneswar under Homi Bhabha National Institute, Mumbai).

[16] R. Singh, M. Kumar, M. Saini, A. Singh, B. Satpati, and T. Som, Sol. Ener. 174 (2018) 231.

[17] M. Kumar, T. Basu, and T. Som, J. Appl. Phys. 119 (2016) 014307.

[18] I. Horcas, R. Fernández, J. M. Gómez-Rodríguez, J. Colchero, J. Gómez-Herrero, and A. M. Baro, *Rev. Sci. Instrum.* 78 (2007) 13705.

[19] P. Marwoto, D. P. N. Made, Sugianto, E. Wibowo, Z. Othaman, S. Y. Astuti, and N. P. Aryani, AIP Conf. Proc. 1555 (2013) 48.

[20] R. Singh. S. A. Mollick, M. Saini, P. Guha, and T. Som, J. Appl. Phys. (resubmitted).

[21] V. P. Singh, J. C. Mcclure, G. B. Lush, W. Wang, X. Wang, G. W. Thompson, E. Clark, Sol. Ener. Mater. Sol. Cells 59 (1999) 145.

[22] R. D. Chandra, M. Rao, K. Zhang, R. R. Prabhakar, C. Shi, J. Zhang, S. G. Mhaisalkar, and N. Mathews, ACS Appl. Mater. Inter. 6 (2014) 773.

[23] J. Bullock, A. Cuevas, T. Allen, and C. Battaglia, Appl. Phys. Lett. 105 (2014) 232109.

[24] M. Thangaraju, A. Jayaram, and R. Kandasamy, App. Surf. Sci. 449 (2018) 2.

[25] Z. Ghorannevis, E. Akbarnejad, and M. Ghoranneviss, J. Theore. Appl. Phy. 10 (2016) 225.

[26] E. M. Tennyson, J. L. Garrett, J. A. Frantz, J. D. Myers, R. Y. Bekele, J. S. Sanghera, J. N. Munday, and M. S. Leite, Adv. Ener. Mater. 5 (2015) 1501142.

[27] J. L. Garrett, E. M. Tennyson, M. Hu, J. Huang, J. N. Munday, and M.S . Leite, Nano Lett. 17 (2017) 2554.

[28] M. Kumar, M. Patel, T. T. Nguyen, J. Kim, J. Yi, Nanoscale 10 (2018) 6928.

[29] M. Kumar, B. Satpati, A. Singh, and T. Som, Solar RRL (2018) 1700216.

CHAPTER 8

1. Summary and future scope

This thesis is devoted to fabricate efficient CdTe-based, chlorine-free hole-blocking solar cells. In order to do this, multilayers are used to make the junction and to separate out the photo-generated charge carries. For instance, ZTO is used as a transparent conducting oxide layer, MoO_3 is used as a hole-blocking layer, Cu-doped CdTe is employed as the main absorbing layer, and Mo is used as the metal back contact. Before fabricating full solar cells, we have carried out extensive experimental investigations on the growth and characterization of individual layers. Initially, we have deposited ZTO thin films at RT under various growth angles using RF magnetron sputtering and demonstrated that the optoelectronic properties of a ZTO film can be tuned by varying the growth angle from 0° to 87°. It is observed that with increasing growth angle structural changes take place and grain size increases. In addition, we have demonstrated that minimum resistivity of ZTO film can be achieved for the growth angle of 50° and resistivity increases at higher growth angles. Further, it is shown that the optical transmittance of ZTO films, in the visible region, is more than 90% and a red shift is observed till the growth angle of 70°. Using KPFM technique, work function of ZTO films is measured and a continuous change in its value is observed with the growth angle. The measured highest work function is 5.06 eV corresponding to the growth angle of 50°. Since a good electrical contact having a higher work function is desirable to construct an efficient photovoltaic cell, thus ZTO films grown at 50° can be considered to offer the best optimized optical and electrical properties as a transparent conductive electrode constructing the solar cells in the present study. In addition to above angle-dependent study, we have carried out the thickness-dependent study of ZTO films for a 50° growth angle on *p*-Si and soda lime glass substrates and achieved tunability in the optoelectronic properties of ZTO films. Using KPFM, we have demonstrated that the work function of ZTO films can be tuned from 5.04 to 4.94 eV by varying the film thickness from 60 to 240 nm which is followed by an observed grain growth with increasing thickness. Moreover, we observe a systematic red shift in the band gap and a decrease in the resistivity with increasing thickness. Further, bulk current-voltage characteristics show a systematic reduction in the turn-on potential and enhancement in the leakage current which are correlated with thickness-dependent resistivity of ZTO films. For higher thicknesses, a decrease in the resistivity takes place which is attributed to an enhancement in the grain size.

Further, we demonstrate a first conclusive experimental evidence on nanoscale band-bending at grain and grain boundaries in ZTO films. Using local probe microscopic measurements like KPFM, cAFM, and EFM, we have shown that the charge trapping at grain boundaries in ZTO gives band-bending at grains and grain boundaries. Further, band-bending is confirmed by performing local *I-V* measurements at a fixed point on grains and grain boundaries which is attributed to defect-induced electrostatic potential barrier. The present observation of the defect-induced potential barrier formation can be very important to understand the charge transport in amorphous semiconducting thin films. In addition, we have mapped band-bending across interface of the metal-semiconductor junction using KPFM.

As a next step, we have carried out the growth and characterization of the main absorbing layer (CdTe:Cu). Before fabricating Cu-doped CdTe layer, we have deposited CdTe thin films at various growth angles at RT to optimize the growth angle and demonstrated that optical, structural, morphological, and work function properties of CdTe films can be tuned by varying the growth angle. It is observed that the average grain size and roughness of the films increase with increasing growth angle. In addition, we have demonstrated that the CdTe film deposited at 0° shows the lowest work function (5.31 eV), which increases to 5.49 eV for the films grown at an oblique angle of 87°. The observed results are explained on the basis of grain growth with deposition angle. In fact, a low interfacial roughness and work function values are needed to obtain a smooth charge transport across the CdTe film. Thus, CdTe films grown under normal incidence are used for further studies in this thesis towards constructing the solar cells where it is used as an absorber layer. Since, the CdTe film deposited at 0° growth angle exhibits very high resistivity which is not acceptable to fabricate an efficient CdTe-based solar cell, to increase its conductivity, we have opted for Cu-doping in these films. To grow Cu-doped CdTe layers, we have used a sandwiched configuration of CdTe/Cu/CdTe and annealed the films at two different temperature in high vacuum to promote diffusion of Cu atoms in both the CdTe layers. Subsequently, we have studied the influences of Cu-doping and the annealing temperature on the optical, electrical, microstructural, and morphological properties of CdTe thin films. For instance, the resistivity of CdTe films decreases (5.6×10^{-1} Ω-cm) at an elevated temperature (viz. 473 K). This is accompanied by a reduction in the optical reflectance to 12.6%. Although, the film annealed at 673 K shows the lowest resistivity and optical reflectance, its work function is higher than the sample annealed at 473 K which is not good for the fabrication of a solar cell and thus, we have chosen an annealing temperature of 473 K for doping of Cu in CdTe.

Since, a carrier selective layer helps to achieve a better PV cell efficiency, we have carried out an in-depth investigation of MoO_3. In doing so, we have studied the role of deposition angle on the structural, optical, and electrical properties of RF magnetron sputter deposited MoO_3 thin films on Si substrates. The average grain size of the films increases with increasing growth angle (0° to 87°). On the other hand, the highest work function (5.58 eV) is found to correspond with the growth of 0°. Since, MoO_3 layer is deposited on the CdTe layer in the full solar cell configration and CdTe shows high work function, we have chosen the growth angle of 0° for further studies on MoO_3 films. Thus, to check the hole-blocking property of n-MoO_3/p-Si heterojunctions six different thicknesses (viz. 4, 6, 8, 10, 20, and 30 nm) of MoO_3 are deposited.

All the MoO_3/Si heterojunctions exhibit diode-like rectifying behavior measured under both dark and illuminated conditions. Interestingly, all the MoO_3/Si heterojunctions prevent the flow of holes but allow the flow of electrons. The key finding is that the 10 nm-thick film exhibits best hole-blocking properties. Further, in the context of the present thesis, the hole-blocking nature of MoO_3 is also confirmed by depositing it on *p*-CdTe:Cu thin films. As a matter of fact, this study is very important, in particular for solar cell applications, because the hole-blocking nature of MoO_3 helps to reduce the reverse leakage current.

We have discussed in the previous chapters that a suitable back contact in a solar cell is very important to enhance its efficiency and it should have a high optical reflectivity and a good charge collection efficiency. Thus, as a back contact, we have studied the growth and characterization of Al and Mo thin films compared their performances for all the presently studied cell configrations. In fact, first we have growtn Al and Mo thin films at various growth angles and studied their structural, optical, and electrical properties. It is observed that the optical reflectivity decreases with increasing growth angles and both Al and Mo films deposited under normally incident flux show the highest reflectivity and the lowest resistivity. Thus, those Al and Mo growth conditions are considered to be the optimized ones to grow the back contacts for different chosen configurations of the CdTe:Cu-based solar cell.

Finally, based on the experimental findings on individual layers, we have fabricated several solar cell, on both *pristine*-Si and chemically prepared textured-Si substrates, having the following configurations: (i) ZTO/CdTe:Cu/Mo/*pris*-Si, (ii) ZTO/CdTe:Cu/Mo/*txt*-Si, (iii) ZTO/MoO_3/CdTe:Cu/Mo/*pris*-Si, (iv) ZTO/MoO_3/CdTe:Cu/Mo/*txt*-Si, (v) ZTO/CdTe:Cu/Al/*pris*-Si, (vi) ZTO/CdTe:Cu/Al/*txt*-Si, (vii) ZTO/MoO_3/CdTe:Cu/Al/*pris*-Si, and (viii) ZTO/MoO_3/CdTe:Cu/Al/*txt*-Si. Using photo-KPFM, real time photo-induced charge dynamics across grains is measured and it is shown that local band-bending takes place at the interface which reduces under illumination. Following this, it is demonstrated that the efficiency of a CdTe:Cu-based solar cell can be increased up to 7.01% on a *pris*-Si substrate using a MoO_3 hole-blocking layer and it further increase to 8.2% by replacing the *pris*-Si by a *txt*-Si substrate. To the best of our knowledge, this is the first demonstration of a CdTe-based hole-blocking solar cell where we have achieved the best efficiency for any CdTe-based cell configuration fabricated without any $CdCl_2$ vapor treatment.

In the last chapter, we have provided a summary of the present thesis work which deals with the fabrication of chlorine-free multijunction cadmium telluride-based hole-blocking solar cell. In particular, we summarize on optimization the growth of individual layers and their bulk as well as nanoscale charge transport properties and optical properties. It is important to point out that finally we have briefed on how the comparative study on several cell configurations has yielded the best efficiency when a *txt*-Si substrate is chosen along with Cu-doped CdTe absorber layer, MoO_3 hole-blocking layer, ZTO window layer, and a Mo back contact. In addition, there are many possibilities and queries arise in the present study therefore, many other ways are possible to further increase the cell efficiency in the future. This study can be extended to the other substrates such as: ITO, FTO, etc. to further find out the role of substrate and in turn the effect on efficiency. To reduce the barrier height at the bottom electrode, the combination of different metal back contacts can be used to increase the efficiency of the CdTe-based PV cells. Moreover, other materials (for the back contact) such as ZnTe, MoOx, etc. also have potential to enhance the efficiency of CdTe:Cu-based solar cell. In addition, for Cu-doping in CdTe, ion-implantation can be used through different ion- energies and -fluence. Further, to improve in the efficiency single-axis tracking systems (which has ability to add 25% output per installed watt) can be added.